Impact of axon initial segment geometry on the electrical properties of neurons

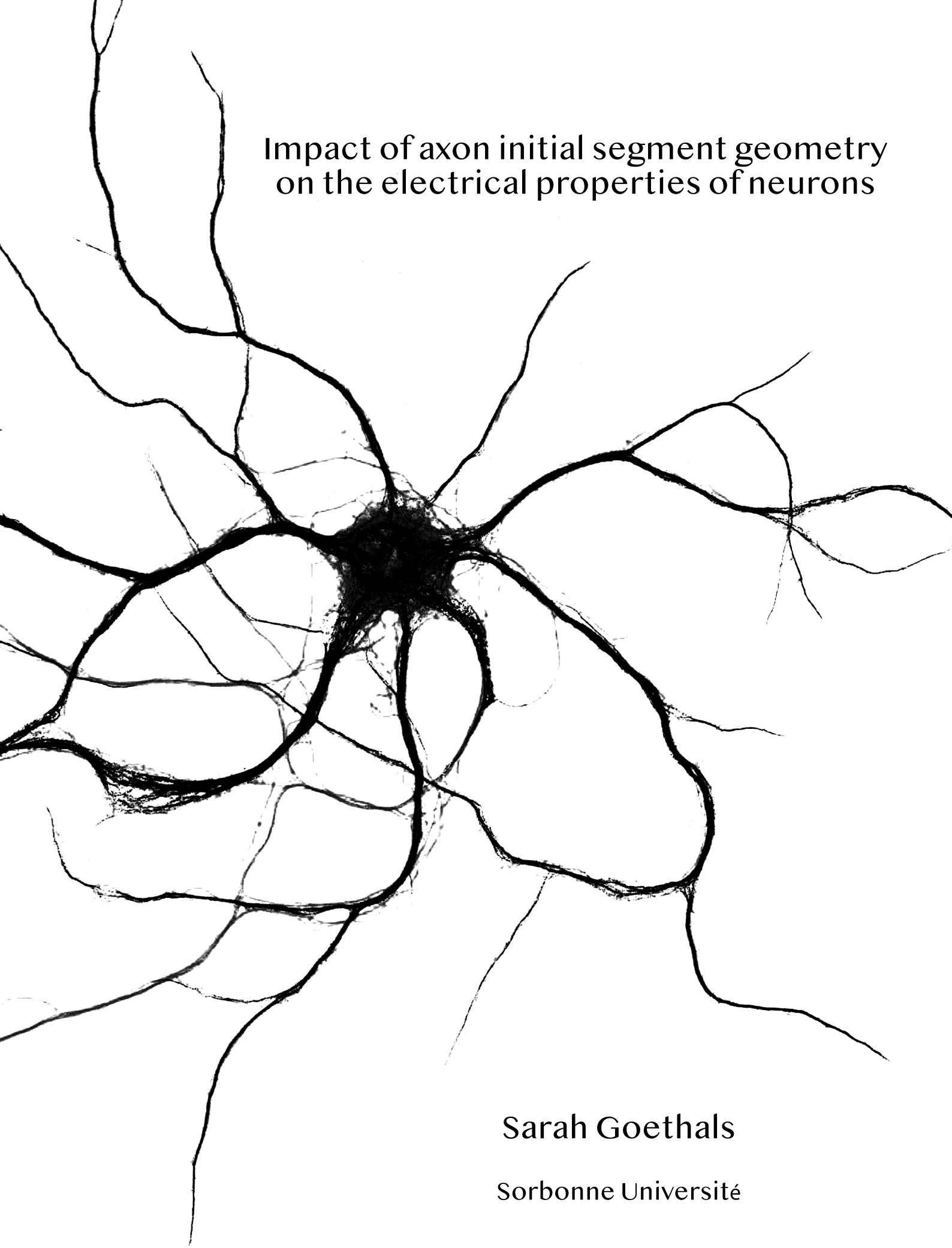

Sarah Goethals

Sorbonne Université

Cover image: Christophe Leterrier, NeuroCyto, INP CNRS-Aix-Marseille Université

SORBONNE UNIVERSITÉ

Ecole doctorale Cerveau, Cognition et Comportement

Institut de la Vision

Impact of axon initial segment geometry on the electrical properties of neurons

Par Sarah GOETHALS

Thèse de doctorat de Neurosciences

Dirigée par Romain BRETTE

Présentée et soutenue publiquement le 2 octobre 2020

Devant un jury composé de:

Pr BARBOUR Boris	Examinateur
Dr BRETTE Romain	Directeur de thèse
Pr BURRONE Juan	Examinateur
Pr DELORD Bruno	Examinateur
Dr ENGELHARDT Maren	Examinatrice
Dr NEEF Andreas	Rapporteur
Pr NIVEN Jeremy	Rapporteur

Preface

Not only is a PhD a considerable piece of work, it also consists of a human adventure as it makes you meet and work with people coming from different countries, cultures and scientific backgrounds. Before presenting the scientific achievements of my PhD, I want to express my gratitude to the many people who helped me carry out this PhD, directly or indirectly.

The person with whom I most directly worked during the last four years is my supervisor Romain Brette. I sincerely thank him for his scientific guidance, his availability and humaneness. Romain is an inspiring researcher and he not only made me discover a fascinating area of research, his advice also sharpened my critical mind. I also acknowledge his lab management, contributing to the nice atmosphere in the team.
The second person with whom I worked the most is certainly Martijn Sierksma. I warmly thank him for his invaluable guidance and help with patch-clamp experiments and confocal imaging. A human being sitting next to me in the patch room was much funnier and motivating than the sole company of granule cells. I am full of gratitude for his availability when I had a technical problem. I also thank him for his deep interest in our research project, and the long hours he spent recording sodium currents. It all ended in a fruitful scientific collaboration that would not have been possible without his passion and scientific curiosity. Ik ben echt gelukkig met onze samenwerking en ik wens je veel success in jouw academisch carrier. Hartelijk dank!
My electrophysiological adventure started earlier, and I want to thank Boris Barbour for welcoming me in his lab for a few months. He introduced me to experimental biology with great patience and availability. I consider myself very lucky to have learned the patch-clamp technique with Boris (and German Szapiro).
Along that line, I want to thank Alain Destexhe, Yann Zerlaut, Matthieu Galtier and Marco Brigham for having introduced me to computational neuroscience during my master's thesis, and given me the willingness to start a PhD in this field. In particular, Yann was for me a inspiring example of how to combine theoretical work with experimental biology in a single PhD project.
I am very thankful to Marcel Stimberg who taught me a lot about programming in Python. I thank you and all the S17 team for the friendly lab atmosphere. Pierre Yger, Baptiste Lefebvre, Charlotte Le Mouel, Maria Telenczuk, Francesco Trapani and Nissim Zerbib, you all contributed to making my everyday life at the IDV enjoyable. Olivier Marre, Matthew Chalk, Ulisse Ferrari, Semihcan Sermet, Tristan Fauvel and Danica Despotovic, I also thank you for making our lunches even more lively than they are without you, and for the interesting scientific and non-scientific discussions.
I am obliged to many other people from the Serge Picaud's team. Corentin Joffrois, Grégory

Gauvain and Antoine Chaffiol helped me a lot when I started patch clamp experiments at the Vision Institute. I thank you for your patience and time. I also thank all the team members, that kindly welcomed me, sharing their lab bench and furniture with me, despite my (sometimes dangerous) clumsiness.
Annabelle Réaux-La Goazigo patiently taught me the technique of immunohistochemistry. I warmly thank her for her time, her advice and the other people from her team for their availability and kindness.
I would also like to acknowledge the financial support I received from the École des Neuroscience de Paris. I am grateful to the administrative help of Laura Peeters, Yvette Henin and Laetitia Fillaudeau from my arrival in Paris to the end of my PhD.
And, importantly, I thank the members of my thesis committee for their time and interest in my work.

Old and more recent friends were not sitting next to me every day but their virtual or physical presence was crucial for me. Max and Pierre, all along our years at university and our PhDs, our friendship, jokes and endless skypes were a strong support. In addition, I thank both of you for proofreading part of this thesis. I heartily thank Hari for his presence next to me and his unconditional support during many years, and reminding me that I was at the right place.
Audrey, my Belgian *alter ego* in Paris, from a random Christmas Market at the Danish Church to the Caulaincourt adventure, her wise and careful presence was and is still very important to me. And thanks to her and Vincent for the precious last-minute inspection of this manuscript.
Sophie and Charlotte M., thank you for always being there, in the good and less good times.
Marie, Maud, Charlotte K. and Marianne also brought fun, life and a supportive kindness in my everyday Parisian life.
I thank T. for our stimulating discussions, his scientific advice and the numerous past and future adventures. Thanks for believing in me and making me stronger and wiser.

Last but not least, I am extremely grateful to my parents and my sister, their constant support in my projects and having given me the opportunity to be who I am today. Having a cohesive and loving family is a chance and a strength in life. My grandparents have also greatly contributed to making me who I am today and to the achievement of this work. Je les remercie de tout mon coeur.

Abstract

The action potential (AP) is the major signalling event in animal nervous systems. Although it was first recorded in the years 1940s, and a fairly accurate model was proposed in the 1950s, some characteristics of the APs recorded in mammals neuron cell bodies were still debated 10 years ago, as for example its sharp onset. Precisely understanding the shape of APs requires to consider the fact that, in many neuron types, they are generated in a small subcellular compartment located in the proximal axon, the axon initial segment (AIS). In most neurons, the AIS starts a few micro meters away from the cell body and is a few tens of micro meters long.

In this thesis we aimed at expanding our knowledge of the relationship between the precise geometry of the AIS and AP initiation. More generally, we are interested in the role of AIS geometry in neuron's electrical functions. The position of the AIS along the axon, as well as its length, vary substantially across and within neuron types, during development and can be modified in response to a change in afferent activity. How it impacts the neuron's excitability has been addressed in different studies, either experimentally or numerically, with no clear consensus on many aspects. With this work we hope to bring a new point of view as it combines a theoretical approach with experiments to shed light on the geometrical aspects of the AIS that are relevant for distinct electrical functions. In a first study we focus on excitability and develop a principled theoretical approach to relate the voltage threshold with AIS geometry and the Na^+ conductance density in the AIS. We find that the neuron is more excitable if the AIS is located further away from the soma. However, this effect is moderate and reversed if a strong hyperpolarizing current enters the AIS at AP initiation. Second, combining modelling and patch-clamp recording in retinal ganglion cells and cerebellar granule cells, we study the AP transmission to the soma by recording the axial current at spike initiation. Theory predicts that the axial current is more sensitive to a change in AIS geometry than the voltage threshold. We show that the charge transferred by the AIS at spike initiation matches the size of the soma in order to produce a sufficient somatic depolarization to regenerate the spike with local Na_v channels opening. Furthermore, we observed that threshold adapts to the membrane potential in retinal ganglion cells, and that the axial current attenuates concomitantly. This attenuation is partly compensated by current broadening to ensure the right amount of charge is transferred to the soma.

Altogether, our results show that the geometry of the AIS has a multidimensional impact, as it affects distinct electrical properties differently. More crucially, we bring additional evidence for the idea that the AIS position finely matches the geometry of the somato-dendritic

compartment to ensure AP regeneration at the soma, and thereby maintains a crucial intrinsic signalling pathway within neurons.

Résumé

Les potentiels d'action (PA) sont un moyen de signalisation électrique majeur entre les neurones du système nerveux central. Le premier enregistrement d'un PA date des années 1940 et le premier modèle décrivant les courants qui le sous-tendent fut développé au cours de la décennie suivante. Néanmoins, certaines caractéristiques des PAs enregistrés dans le corps cellulaire des neurones chez les mammifères étaient encore débattues il y a une dizaine d'années, par exemple l'initiation abrupte du PA. En effet, comprendre finement la forme des PAs nécessite de prendre en compte le fait que, dans la plupart des types de neurones, ils sont générés dans un petit compartiment sous-cellulaire situé au début de l'axone, le segment initial de l'axone (SIA). Dans la plupart des neurones, le SIA commence à quelques micromètres du soma et a s'étend sur quelques dizaines de micromètres le long de l'axone.

Cette thèse a pour but d'élargir notre connaissance sur la relation entre la géométrie du SIA et l'initiation des PAs. De façon plus générale, nous nous intéressons au rôle de la géométrie du SIA dans les fonctions électriques des neurones. La position du SIA le long de l'axone, ainsi que sa longueur, varient d'un type de neurone à l'autre, mais également au sein d'une population de neurones ou encore au cours du développement. En outre, un changement d'activité afférente au neurone peut également entraîner une modification de la géométrie du SIA. Plusieurs études ont étudié la façon dont cette modification structurelle influence l'excitabilité des neurones, sans parvenir à un consensus clair. Par la réalisation de ce travail, nous espérons apporter un nouveau point de vue sur la question, car il combine une approche théorique avec de l'électrophysiologie *in vitro* pour éclairer la pertinence des aspects géométriques du SIA pour différentes fonctions électriques des neurones. Dans une première partie, nous étudions l'excitabilité sous un angle théorique pour comprendre la relation entre le seuil d'initiation des PAs et la géométrie du SIA ainsi que la densité de canaux Na_v au SIA. Nous montrons que l'excitabilité des neurones augmente si l'AIS est éloigné du soma. Cependant, cet effet est peu marqué et peut être renversé si un courant hyperpolarisant fort est présent au SIA lors de l'initiation du PA. La deuxième partie de ce travail allie modélisation et enregistrements électrophysiologiques dans les cellules ganglionnaires de la rétine et les cellules en grain du cervelet. Nous y étudions la transmission du PA du SIA au soma en enregistrant le courant axial à l'initiation des PAs. Les prédictions théoriques prédisent que le courant axial est plus influencé par une variation de géométrie du SIA que le seuil d'initiation. Nous montrons que la charge électrique transmise du SIA au soma à l'initiation des PAs est ajustée à la taille du soma de façon à suffisamment dépolariser le soma pour y régénérer le PA grâce à l'ouverture des canaux Na_v locaux. En outre, nous avons observé que le seuil d'initiation s'adapte au potentiel de membrane dans les cellules ganglionnaires de la rétine.

Cette adaptation est accompagnée d'une atténuation du courant axial qui est elle-même en partie compensée par un élargissement du courant. De cette façon, la transmission de la charge nécessaire à la régénération du PA est maintenue.

Nos résultats démontrent que la géométrie du SIA a un impact multidimensionnel, car elle influence de façon distincte différentes propriétés électriques des neurones. En particulier, nous apportons un élément de vérification supplémentaire à l'hypothèse que la position du SIA est adaptée à la géométrie du compartiment somato-dendritique pour assurer la transmission et la régénération des PAs au soma, et par conséquent, pour maintenir un signal intrinsèque crucial au sein des neurones.

Contents

1 Introduction

1.1 Neurons and their electrical function

1.1.1 Neurons

Neurons are spatially extended cells that propagate electrical signals and transmit them to the next neuron via synapses. The intracellular and extracellular medium have different ionic compositions, causing a difference of electrical potential across the neuronal membrane. When a neuron is stimulated, short and small differences of potential are elicited that sum up and possibly convert into a larger signal able to propagate along long distances.

The electrical signalling in neurons is rather stereotypical, despite their extremely diverse morphology. The first description of neurons morphological diversity was proposed by Santiago Ramon y Cajal in the very beginning of the 20th century (y Cajal, 1995), thanks to the discovery by Camillo Golgi of a staining technique in the end of the 19th century (see e.g. Finger, 2001). Allowing to resolve the fine structure of brain cells, this technique helped Ramon y Cajal to demonstrate that nerve cells are discrete units connected through a contiguous relationship, the neuron theory (y Cajal, 1995), in opposition to the reticular theory that postulates that the brain is a single network of intricate nerves (Golgi, 1906). At the same epoch, Golgi observed that neurons have long projections, and distinguished the dendrites from the axon. In addition to providing detailed observations of different cell types, Santiago Ramon y Cajal also believed in the functional polarization of neurons.

Neurons are indeed polarized cells: different compartments have distinct functions (fig. 1.1). The central part of the neuron, the soma or cell body, is compact and small (5 µm to 50 µm in diameter) and contains the cell nucleus. Dendrites extend from the soma in projections that ramify extensively in most neurons and exhibit dendritic spines, small protrusion of the plasma membrane. In addition to the dendrites, one extension differs structurally and functionally from the dendrites, it is the axon. The axon emerges either from the soma or from a proximal dendrite and can extend over long distances (up to 1 m in humans), typically longer than dendrites. It has a diameter ranging from 0.2 µm to 10 µm (Perge et al., 2012) and ramifies less than the dendrites in most neuron types. Neurons receive stimulations from others through synapses that are predominantly located on the dendrites and the cell body. A synapse is a chemical contact between the axon terminal of the pre-synaptic neuron and a dendrite or the soma of the post-synaptic neuron. This chemical contact triggers an electrical

signal in the post-synaptic neurons, which propagates passively to the soma, where thousands of stimulation received simultaneously at different dendritic sites are added up. Dendrites are therefore termed the input compartment of neurons. Subsequently, the summation of the small dendritic signals causes the generation of a larger electrical signal in the proximal axon, the action potential. It happens at a specific region of the axon, the axon initial segment (AIS). The AIS is a subcellular compartment located a few µm away from the soma and its length ranges from 10 µm to 50 µm. The AIS has a distinct cytoskeleton and is more excitable than the rest of the cell. In many neuron types, the region of the axon starting after the AIS is covered with myelin sheets that increase action potential conduction velocity. The action potential propagates actively along the entire axon until the axon terminal, where it stimulates other neurons, therefore called the output compartment. In this way, the brain contains networks of billions of inter-connected neurons.

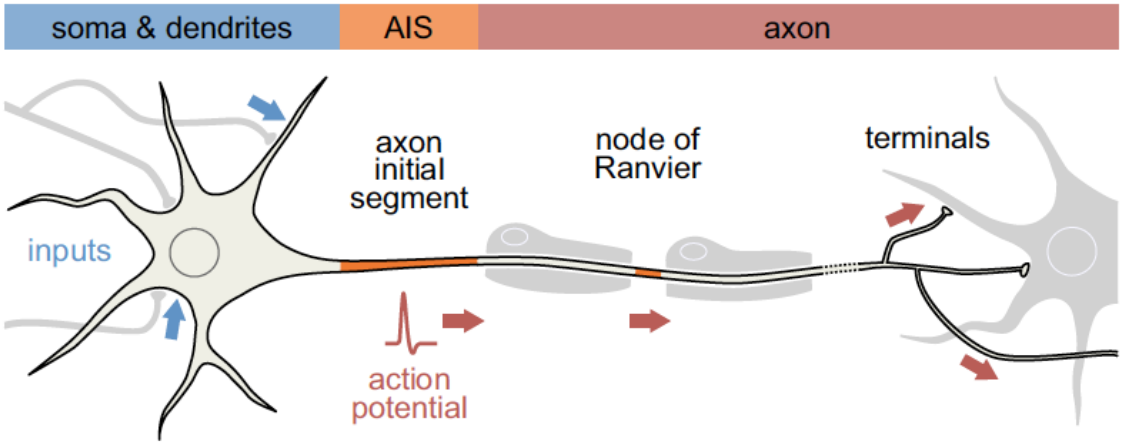

Figure 1.1: The neuron is a polarized cell: distinct compartment have specific functions (adapted from Leterrier (2016)).

In vertebrates, numerous neuron types have been studied, revealing their striking morphological diversity. For instance, the cerebellum is the most populated brain region as it incorporates 80% of the human brain neurons (Herculano-Houzel, 2009). It contains among the smallest neurons of the nervous system, the cerebellar granule cells (CGC), whose soma diameter is about 6 µm. CGCs have only 3 to 4 very short dendrites that end in rosettes (fig. 1.2 B). In contrast, the large Purkinje cell exhibit an extensively ramified dendritic arbor over a large surface (fig. 1.2 A). Both neuron types are multipolar as their soma is centralized between an arborized dendritic compartment and a single axon. Another typical multipolar neuron is the cortical pyramidal cell (fig. 1.2 C). In general, vertebrate neurons are multipolar, with the exception of sensory neurons, such as the dorsal root ganglion (DRG) cells. They are the first stage of sensory detection. A single axonal stem arises from the soma and splits in two branches, the peripheral and the central one (fig. 1.2 D). The former receives information about temperature, pain, etc. from diverse receptors and the later contacts the spinal cord. DRG neurons are called pseudo-unipolar because, even if both branches display axonal features, they are distinct on the cellular and functional levels (Nascimento et al., 2018). Despite the rather unusual character of unipolar neurons in the vertebrate nervous system, most neurons in arthropods are unipolar (Prokop, 2020; Sánchez-Soriano et al., 2005; Rolls et al., 2007). However, unlike ver-

tebrate's pseudo-unipolar neurons, they possess distinct axons and dendrites (Rolls and Jegla, 2015). Indeed, arthropod unipolar cells often display a single neurite extending from the soma, and a couple of short dendrites emerging from the proximal part of this process (Rolls et al., 2007) (fig. 1.2 E). Unlike vertebrates sensory neurons, arthropod sensory neurons are multipolar (Prokop, 2020).

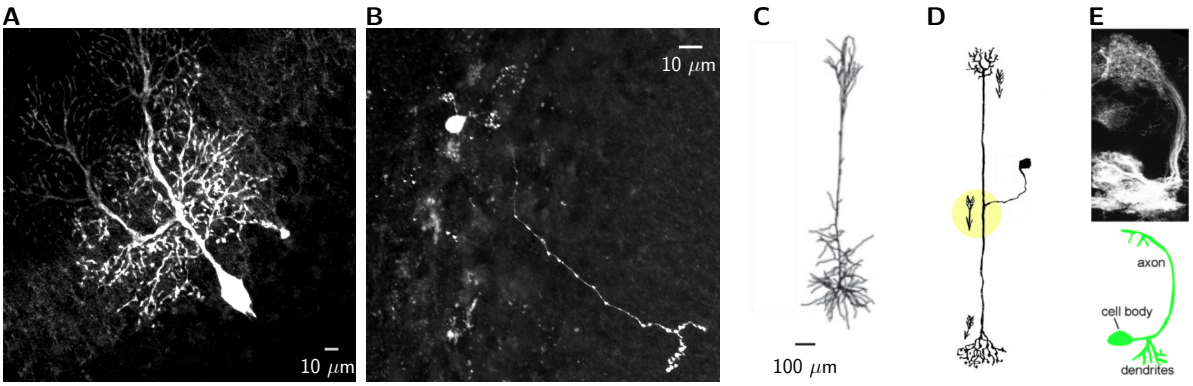

Figure 1.2: Morphological diversity of vertebrate and invertebrate neurons. **A**, a cerebellar Purkinje cell. The dendrites are numerous and highly ramified. Only the start of the axon appears on the picture, probably cut during tissue preparation. **B**, a cerebellar granule cell. Three short dendrites emerge from the small soma and end in rosettes. The axon and its terminal are clearly visible. **C**, cortical pyramidal neuron (adapted from Hamada et al. (2016)). The axon and short basal dendrite spread around the soma, while the apical dendrite extends much further away from the soma and ramifies at its end. **D**, a pseudo-unipolar neuron (adapted from Triarhou (2014) and reproduced from y Cajal and Sanchez (1915)). The soma is externalized from the main neurite by a stem process. **E**, olfactory projection interneuron from the drosophila larva (adapted from Rolls et al. (2007)). Top, fluorescence microscopy image. Bottom, schematic representation. The dendrites emerge from the main axon, and not from the soma.

1.1.2 Measuring electrical signals in neurons

General overview

The first works aiming at understanding the brain cell's electrical activity precede Ramon y Cajal and Golgi's morphological studies. Animal electricity was discovered in the 18th century by Galvani (see e.g. Whittaker, 1910). He observed that when the sciatic nerve of a frog was touched by a charged metallic scalpel, the frog's leg kicked. He thought that it was due to an electric flow through the nerve. His experiments attracted the attention of Volta who disagreed with Galvani's interpretation and proposed that the phenomenon was better explained by the electric charges in the metal (see e.g. Whittaker, 1910). Volta's ideas led to the invention of the voltaic pile and animal electricity was forgotten for a while.

Later, in the middle of the 19th century, Matteucci measured an electrical current between the cut and the intact part of a nerve and du Bois-Raymond observed that this current could change during prolonged stimulation, the so-called negative variation (see e.g. Carmeliet,

2019). In 1868, Bernstein made a major advance in improving the temporal resolution of the current measuring tool and recorded for the first time an *action potential* with 10^{-4} s precision (see e.g. Carmeliet, 2019). A few years later he proposed the first theoretical explanation of the phenomenon, in his membrane theory, based on the recently proposed Nernst equation (see e.g. Seyfarth, 2006). He hypothesized that the intracellular medium contains a higher concentration of potassium ions (K^+) than the extracellular medium and that the membrane is permeable to K^+. By diffusion through the cell membrane, K^+ ions leave the cell and accumulate on the extracellular side of the membrane, creating an electric field across the membrane by charge accumulation, which opposes diffusion. The electric potential across the membrane is called the *membrane potential*, $V_m = V_e – V_i$. When the electric field exactly opposes diffusion, an electrochemical equilibrium is reached that corresponds to the resting membrane potential of the cell (Bernstein, 1912).

In the 1930, amplifiers and electrodes started to be used to record currents in large Cephalopoda axons, as for instance the squid. In 1939, Hodgkin and Huxley recorded for the first time a squid giant axon intracellularly (Hodgkin and Huxley, 1939). The axon ($\sim 500\,\mu m$ diameter) was hanging vertically in sea water, and a micro-electrode lowered inside the axon. It consisted of a glass tube of about $100\,\mu m$ in diameter filled with sea water and a silver chloride electrode inside it. Membrane potential was recorded by connecting an amplifier on one side to the sea-water (reference electrode) and on the other side to the recording electrode. They reported an electrical event of $\sim 90\,mV$ amplitude, the action potential (AP) (fig. 1.3). A rapid increase in membrane potential is directly followed by a slower decrease that brings it to its resting value (depolarization and repolarization phase). The same researchers later discovered the underlying mechanism: the membrane is selectively permeable to ions, Na^+ and K^+, through ionic channels whose opening depends on the membrane potential, the voltage-gated channels Na_v and K_v[1] (Hodgkin and Huxley, 1952b).

In the next years, the technique, called *electrophysiology*, improved by different advances. The voltage-clamp technique allows to control the membrane potential of a cell and to record the elicited currents. In 1976 Neher and Sakmann developed the patch-clamp technique, which consists of recording currents or voltage with a glass electrode sealed to the cell membrane, allowing to record currents from single ionic channels (Neher and Sakmann, 1976). They found out that the opening of ionic channels with voltage was a discrete event (closed/open state). Nowadays the patch-clamp technique is still extensively used to study the neuron's electrical properties. Combined with high magnification microscopes, it allows to probe neurons electrical activity in many different preparations, from neurons grown in cultures, to brain slices or neurons in living animals.

The patch-clamp technique

We briefly explain the patch-clamp technique (for details see Hamill et al. (1981)), as we will extensively refer to it in this manuscript. A glass micropipette filled with a solution that resem-

[1] The subscript v is used to indicate the voltage dependence of the ionic channel gating.

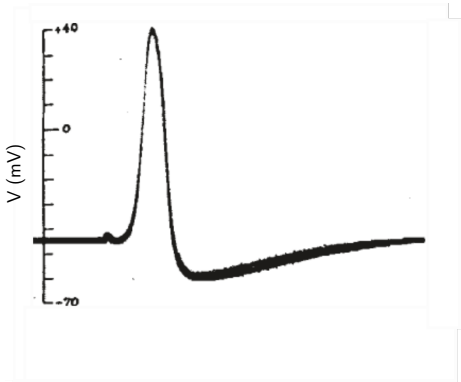

Figure 1.3: The first action potential recorded intracellularly in the giant axon of Loligo (adapted from Hodgkin and Huxley (1939)).

bles the intracellular medium and that contains a thin electrode comes in close contact with the neuron membrane (fig. 1.4 top left). The other end of the recording electrode is linked to an amplifier. A soft suction seals the membrane to the pipette tip, increasing dramatically the seal resistance. It is the *cell-attached* configuration (fig. 1.4 top centre). The high seal resistance ensures that most of the membrane patch current flows into the micro-pipette. On the one hand, pulling out the pipette and exposing briefly its tip to air breaks the membrane, leading to the *inside-out* configuration (fig. 1.4 top right). On the other hand, applying a stronger suction leads to rupture of the membrane patch delineated by the micropipette tip, giving direct access to the intracellular medium, the *whole-cell* configuration (fig. 1.4 bottom left). The tighter the seal between the pipette tip and the membrane, the less the current leak at the patch, and the more currents generated in the cell membrane we will record. From the whole-cell configuration, one can further gently retract the pipette, breaking the membrane (fig. 1.4 bottom centre) and hoping the two pieces reseal, to form an *ouside-out* patch, as if the electrode is in the extracellular medium (fig. 1.4 bottom right). In what follows, we focus on the whole-cell recording method.

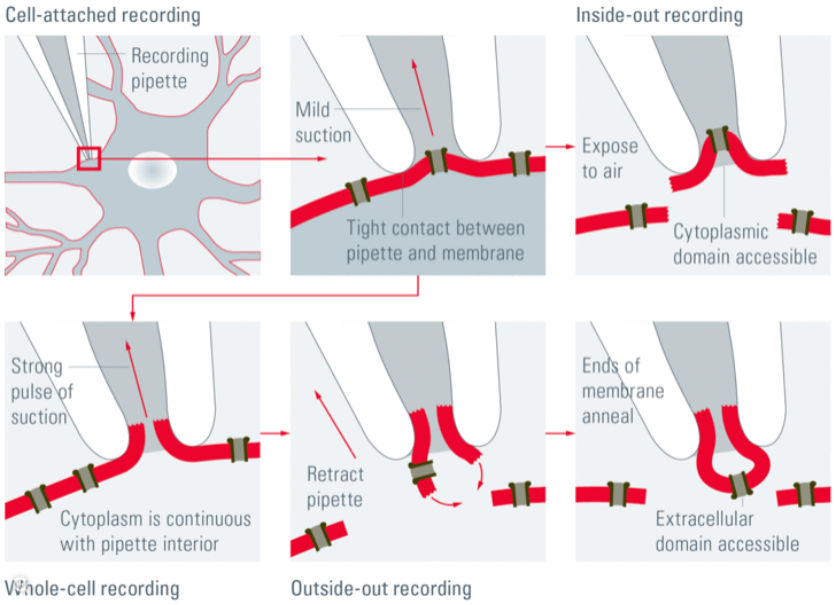

Figure 1.4: The patch-clamp techniques (adapted from Veitinger (2011)).

Having direct electrical access to the cell, one may want to inject a current pulse and record changes in the cell membrane potential, the *current-clamp* recording technique. In order to study the voltage dependence of the various voltage-gated channels, one may want to control the membrane potential of the cell and record the elicited currents, what is called *voltage-clamp* (fig. 1.5). The pipette or electrode voltage, V_p, is controlled by an operational amplifier that ensures it equals the command voltage V_c through a feedback resistor. Indeed, the cell current flowing to the amplifier has to pass through the feedback resistor, so that the output voltage V_{out} scales with the cell current. Importantly, it is the electrode voltage that is controlled and not directly the cell membrane potential V_m. Indeed, the *series resistance* R_e, coming from the electrode resistance and the interface between the glass pipette and the cell, causes a voltage drop between the membrane potential and the electrode potential when a current flows through the electrode. Moreover, the series resistance in series with the cell capacitance C_m creates a low-pass filter, distorting the recorded signal. In practice, the pipette and cell capacitances can be cancelled on-line, by injecting to the electrode the current needed to charge the capacitances. Dealing with the effect of the series resistance is more subtle as its compensation requires a positive feedback system that injects through the electrode the current needed to compensate for the effect of the series resistance. In consequence, series resistance compensation has to be performed carefully, as over- compensation causes large voltage oscillations in the feedback circuit, which often lead to cell death.

Finally, in what follows, the term *input resistance* refers to the resistance "seen" by the electrodes, so the membrane resistance R_m and the series resistance. As the membrane resistance if often 1 or 2 orders of magnitudes higher than the series resistance, the input resistance if assumed to represent the cell membrane resistance.

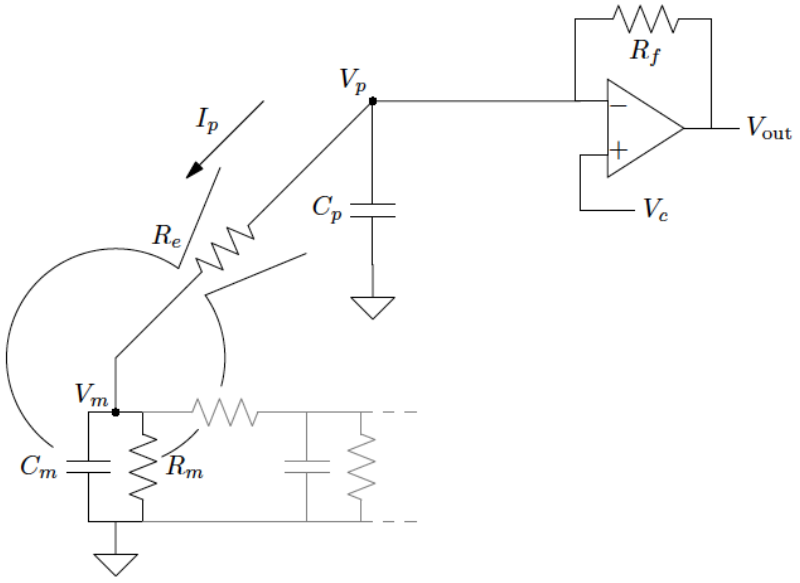

Figure 1.5: Current recording in voltage-clamp (adapted from Barbour (2014)).

1.1.3 Modelling electrical signals in neurons

Interestingly, unravelling the mechanisms underlying action potential results from an interplay between advances in electrophysiology and mathematical modelling. In 1952, Hodgkin and Huxley used a semi-empirical approach to describe the first mathematical model of the squid giant axon action potential, as a change in Na^+ and K^+ conductance with time (Hodgkin and Huxley, 1952b). Later, the progress in the patch-clamp technique, heterologous expression of cloned channels and genomic analyses enabled to uncover the many other currents underlying action potentials and explained their huge variability in shape and firing pattern (reviewed in Bean, 2007).

The action potential is a short and rapid rise in membrane potential that has a specific shape, due to the underlying currents that generate it. The cytoplasm contains a low concentration of Na^+ ions and a high concentration of K^+ ions. On the contrary, the concentration of Na^+ ions is high in the extracellular medium and the concentration of K^+ ions low. The membrane is not permeable to both these ions. If the membrane potential increases sufficiently, Na_v channels start to open, Na^+ ions enter the cell, causing a current that further depolarizes the membrane and causes more and more Na^+ ions to enter, triggering a large depolarization that becomes positive and reaches a peak. After this peak, the membrane potential falls (or repolarizes) and goes back to its resting value, because Na_v channels inactivate shortly after the AP initiation and because during the depolarization, K_v channels open, causing an outward current that accelerates the repolarization. The picture is in reality more complex, because different subtypes of channels play distinct roles during an AP. In this section we describe the original Hodgkin-Huxley model of an action potential and a model of the mechanism that makes a neuron fire.

Modelling action potentials: Hodgkin-Huxley model

Building on four seminal papers published the same year, Hodgkin and Huxley proposed in 1952 a mathematical model of an AP (Hodgkin and Huxley, 1952b). Current can be carried through a patch of membrane either by charging its capacitance, or by ions moving through resistances in parallel with the capacitance,

$$I = C\frac{dV}{dt} + I_L + I_{Na} + I_K \tag{1.1}$$

The major currents are Na^+ and K^+ currents and a small leak current is added to take into account other sources of current. Each current is described by the product of the conductance and the driving force of the ion

$$I_X = g_X(E_X - V) \tag{1.2}$$

where E_X is the reversal potential of the ion species, the potential at which the net ion flux through the membrane is zero. What needs to be described is the dependence of the conductances on time and membrane potential. Hodgkin and Huxley aimed at simple equations describing the data reasonably well but not at providing physical interpretations of them (Hodgkin and Huxley, 1952b). Indeed, it is noteworthy to remind here that at that time, the existence of gated channels across the membrane and specific to one or more ion species was not known.

The potassium conductance activates with a short delay (fig. 1.6 A), so they assumed the potassium conductance g_K is proportional to the fourth power of a gating variable n

$$g_K = \bar{g_K} n^4 \tag{1.3}$$

where $\bar{g_K}$ is the maximal K^+ conductance, and the variable n follows

$$\frac{dn}{dt} = \alpha_n(n-1) + \beta_n n \tag{1.4}$$

where α_n and β_n are transition rate between closed and open states, which can today be interpreted as the closing and opening rates of different subunits of the K_v channel. The channel is in the open position if the 4 units are in the permissive configuration. The solution of this equation is

$$n = n_\infty(n_\infty - n_0)e^{-t/\tau_n} \tag{1.5}$$

$$n_\infty = \frac{\alpha_n}{\alpha_n + \beta_n} \tag{1.6}$$

with n_∞ is the activation function of the gating variable, that describes the steady-state activation of the channel as a function of the voltage, n_0 its initial value and τ_n the time constant of activation. Hodgkin and Huxley fitted many time courses of g_K to obtain estimates for the transition rates and plotted them against V to obtain an expression for their dependence in the voltage. Another and more popular approach consists of fitting the activation curve $n_\infty(V)$ to plots of $g_K/\bar{g_K}$ against V. The steady-state activation curve is accurately represented by a Boltzmann function

$$n_\infty^4(V) = \frac{1}{1 + \exp\left(\frac{V_n - V}{k_n}\right)} \tag{1.7}$$

where V_n is the half-activation voltage of the K^+ conductance and k_n is the Boltzmann slope factor of the activation curve, that determines the sharpness of the linear part of the curve.
Similarly, the Na_v conductance is the product of the maximal conductance and of two gating variables, m and h, describing respectively the activation and the inactivation of the conductance

$$g_{Na} = \bar{g_{Na}} m^3 h \tag{1.8}$$

The dependance of m and h on time and voltage are described with the same equations as n, although the half-activation voltages and slopes are different. Here, the two gates m and h have to be in a permissive state in order for Na^+ ions to enter the cell.

The HH model enables a fairly good mathematical description of the AP (fig. 1.6 B). It is important to stress that it is a model of the squid giant axon AP, that is space-clamped and therefore isopotential. Hence the HH model is a single-compartment model and care must be taken when using it to model data recorded in neurons, where spike initiation occurs in the axon (Brette, 2015). Moreover, in mammalian neurons, AP are usually recorded at the soma and currents can flow between the dendrites and the soma, or the axon and the soma, that alter the shape of the AP. Finally, the squid giant axon is a syncytium (Young, 1936), a cell containing multiple nuclei, in sharp contrast with the uninuclear mammalian neurons. Still the HH model in one of the most popular AP models, and is extensively used nowadays, with many variations and improvements.

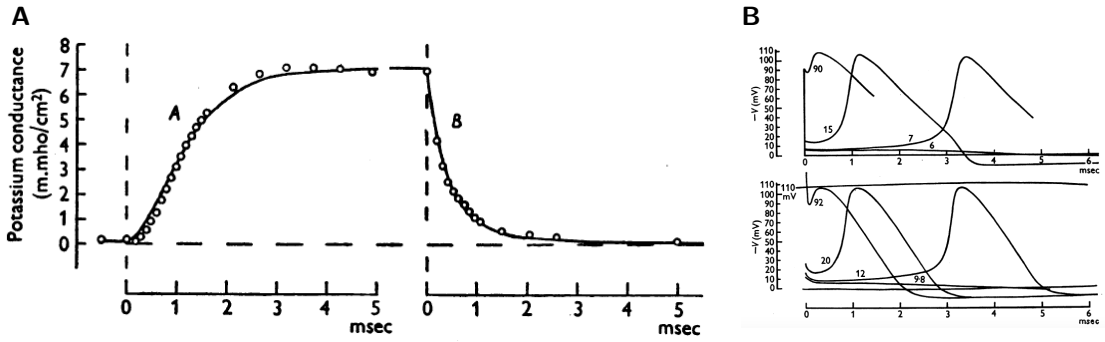

Figure 1.6: Hodgkin-Huxley model of the squid giant axon action potential (adapted from Hodgkin and Huxley (1952b)). **A**, Rise in potassium conductance in response to a 25 mV depolarization (left) and fall in response to repolarization to the resting membrane potential (right). Dots are the experimental data and the line is the model prediction. **B**, Membrane potential as a function of time. Note the unusual convention for the membrane potential, zero corresponds to the resting membrane potential. Bottom, action potential recorded in the squid axon in response to charge pulses (strength indicated next to the curves, in $\mu C\,cm^{-2}$). Top, action potential as predicted by the full Hodgkin-Huxley model, in response to depolarizations indicated next to the curves.

Modelling action potential initiation

What makes a neuron fire an AP? As described in early modelling studies of AP initiation in nerves, it corresponds to a discontinuous change of the membrane potential with the stimulus strength, in an all-or-none manner (FitzHugh, 1955). There is a critical value of the stimulation parameter, a threshold, above which the membrane potential increases suddenly. What determines this threshold, ans thereby the neuron's excitability? In this section we focus on modelling spike initiation, and not the full AP time course.

We consider a model of an isopotential membrane without external input. Its membrane potential V follows the differential equation

$$C\frac{dV}{dt} = I(V,t) \tag{1.9}$$

where $I(V,t)$ represents the voltage and time dependant underlying currents and C is the membrane capacitance. We want to know above which voltage threshold the current rapidly increases, so how I depends on V. Therefore we suppress the time dependence of I and obtain a one-dimensional dynamical system

$$\frac{dV}{dt} = F(V) \tag{1.10}$$

How do we know $F(V)$? An approach consists of using models with intrinsic spike generation mechanism, as the exponential integrate-and-fire (EIF) model (Fourcaud-Trocmé et al., 2003). Another uses experimentally determined current-voltage (IV) curves, such as the dynamic IV curve that is the average current at a specific potential recorded during white noise stimulation (Badel et al., 2008). This system has two fixed points ($F(V) = 0$) in the region where the spike initiates: the stable resting membrane potential V_r and the unstable

voltage threshold V_t (fig. 1.7 A). If the system is instantaneously brought to a potential lower than the threshold, it relaxes to V_r. If the instantaneous stimulation brings the system at V_t or above, $F(V)$ diverges towards higher values, corresponding to the triggering of a spike.

Next we add an external stimulation I_e, for instance slowly increasing long steady current pulses

$$\frac{dV}{dt} = F(V) + I_e \tag{1.11}$$

It shifts the curve $F(V)$ in fig. 1.7 A vertically. The stable fixed point is depolarized and the unstable fixed point hyperpolarized, until they collapse in a single fixed point (the minimum of the curve when it is tangent to $F(V) = 0$) and disappear if the input current further increases, corresponding to a spiking situation (Platkiewicz and Brette, 2010). The fixed point nature and number change when a parameter is varied: a bifurcation occurs with bifurcation parameter the external current. The external current at the bifurcation is the rheobase, the largest current that can be delivered to the cell without eliciting a spike. When the external current is lower than the rheobase, the resting membrane potential will increase until the bifurcation. The voltage threshold is defined as the largest membrane potential without eliciting a spike and is the solution of $F(V) = 0$ (fixed point) and $F'(V) = 0$ (bifurcation) (Platkiewicz and Brette, 2010).

To understand how the voltage threshold is determined by the underlying currents, we use a model for $F(V)$ that enables to find an analytical form for the threshold. At spike initiation, we assume that the K^+ current can be neglected because it is not significant (Hallermann et al., 2012). We further assume that the activation of Na_v channels is instantaneous, which is reasonable because at spike initiation, their activation is much faster than any other time constant. So the sources of current at spike initiation are the leak current and the Na^+ current

$$C\frac{dV}{dt} = I_L + I_{Na} + I_e \tag{1.12}$$

At spike initiation, the rapid Na^+ current increase is accurately described by a exponential function of the membrane potential (Platkiewicz and Brette, 2010; Hodgkin and Huxley, 1952b). Interestingly, Boltzmann curves are usually fitted to entire activation curves, leading to poor fitting in the initiation region, as noted in Platkiewicz and Brette (2010) (fig. 1.7 B). Fitting the Boltzmann equation or an exponential locally in the hyperpolarized range leads to a more accurate fit (fig. 1.7 B). With these approximations, the membrane equation is

$$C\frac{dV}{dt} = g_L(E_L - V) + g_{Na}(E_{Na} - V)e^{\frac{V-V_{1/2}}{k}} + I_e \tag{1.13}$$

It can be further simplified by the approximation $E_{Na} - V \simeq E_{Na} - V_{1/2}$, as $V_{1/2}$ and V are both far from E_{Na} at initiation. As $F'(V) = 0$ at the threshold, a formula can be derived with $F(V)$ being the right-hand side of equation 1.13. As a result we obtain the *threshold equation* for an ispotential neuron (Platkiewicz and Brette, 2010)

$$V_t = V_{1/2} - k\log\left(\frac{g_{Na}}{g_L}\frac{E_{Na} - V_{1/2}}{k}\right) \tag{1.14}$$

The threshold depends only on the leak conductance and on parameters describing the activation of Na_v channels ($V_{1/2}, k, E_{Na}, g_{Na}$). Increasing the Na^+ conductance decreases the threshold, making the neuron more excitable.

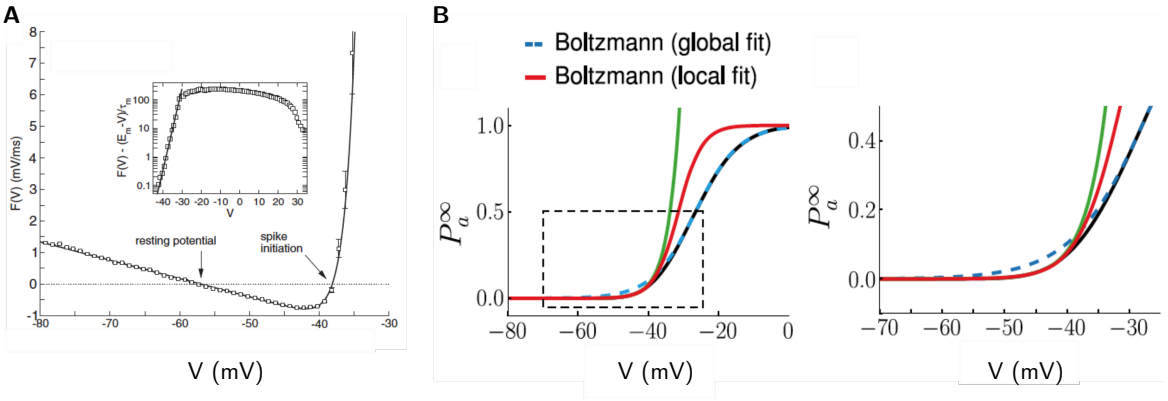

Figure 1.7: Single-compartment model of spike initiation. **A**, Dynamic IV curve. Dots are the average current (divided by the capacitance) at a specific potential recorded during white noise stimulation and the line is a fit of the EIF model. Inset: semi-log of the IV curve to show the exponential rise around spike initiation (adapted from Badel et al. (2008)). **B**, Fits of the Na_v channel activation curve (black line) to a Boltzmann function on a large voltage range (dashed blue line) and on the spike initiation voltage range (red line), compared with an exponential fit on the spike initiation range (green line) (adapted from Platkiewicz and Brette (2010)).

Modelling action potential conduction

Until this point we have considered point neuron models, representing a neuron as an isopotential patch of membrane. It is useful to model certain types of phenomena but completely misses the spatial extent of neurons. If one wants to study the impact of dendritic inputs on the somatic membrane potential or AP conduction along the axon, the spatial extent of neurons has to be taken into consideration.

Neurites are long cables filled with an intracellular electrically conducting medium (the axoplasm) and separated from another electrically conducting medium (the extracellular space) by a thin membrane. Assuming that the current flows along the direction of the cable (one-dimensional) and that the axoplam is a purely resistive medium with axial resistance per unit length r_a, one can derive the *cable equation* that describes the spread of the membrane potential V along a cylindrical piece of neurite and how it interacts with ionic currents (Tuckwell, 1988a)

$$\frac{1}{r_a}\frac{\partial^2 V}{\partial x^2} = C\frac{\partial V}{\partial t} + I_{ion} \tag{1.15}$$

The right-hand term is the membrane equation that describes the total current at a point as the sum of the capacitive current through the membrane and the ionic currents I_{ion}. The left-hand term describes the current coming from the adjacent piece of neurite. The total ionic current I_{ion} can be modelled by the HH equations.

1.2 The axon initial segment

In this chapter we focus on the axon initial segment, the site of AP initiation in neurons. First we describe its specific molecular structure and how it differs from the rest of the axon. Second we explain its role as the spike trigger zone. Finally, we provide an overview of its size and position along the axon across neuron types and how it varies under certain conditions.

1.2.1 Methods of imaging

The observation and characterization of the AIS has evolved in parallel with the development of imaging methods, in particular electron microscopy (EM) and super-resolution optical microscopy.

Developed in the 1930, EM uses a beam of electrons as the source of illumination, in contrast with optical microscopy that uses a beam of photons. Electrons can have a far smaller wavelength than visible light, depending on their velocity, allowing to probe very small structures and reach a resolution lower than 1 nm. Electron microscope use shaped magnetic fields as lenses, to focus and magnify the electron beams. A focused electron beam is targeted on the sample, and depending on its structure and composition, electrons of different energies will be transmitted, scattered or reflected by the sample. In transmission EM, an image is formed with the transmitted electron beam. In scanning electron microscopy, the surface of the sample is scanned by a focused beam of electrons and the various signals (heat, X rays, lower or higher energy electrons, light) re-emitted by the sample at each location are detected.

In Palay et al. (1968) the AIS is described as a region "somewhere between the axon hillock and the beginning of myelin sheath". Despite having been mentioned in earlier studies, the AIS structure was first characterized in EM studies in the 1960 (Conradi, 1966; Palay et al., 1968; Peters et al., 1968) by three features: "a dense layer of finely granular material undercoating the plasma membrane, scattered clusters of ribosomes and fascicles of microtubules" (Palay et al., 1968) (fig. 1.8 A, B). In addition it was noted that the AIS structure was identical whether the axon was myelinated of not. Lastly, the presence of axo-axonic synapses along the AIS was reported (Peters et al., 1968) (fig. 1.8 A, B). During the next years, the geometry of the AIS (diameter, length) in different neuron types was quantified in rats (Somogyu and Hamori, 1976; Kosaka, 1980), cats (Somogyu and Hamori, 1976; Conradi and Ronnevi, 1977; De Zeeuw et al., 1990), primates (Sloper and Powell, 1979) and humans (Sasaki and Maruyama, 1992).

One of the drawbacks of EM is that it is not appropriate to identify the molecular identity of the cytoskeleton. Coupling EM with a method of protein labelling allows to work around this lack. Immunostaining consists of using the specific binding of antibodies with antigens to target a molecule to a specific protein. In immuno-EM, gold beads are attached on proteins labelled with anti-bodies, which allows to localize them precisely. However, it is a challenging technique that presents other disadvantages.

In optical fluorescence microscopy, the samples are labelled with fluorophores that emit

light at a particular wavelength when they are illuminated with the right wavelength. Therefore different proteins can be labelled in the same sample, with fluorophores absorbing and emitting different parts of the light spectrum. In cell and molecular biology, the most common way to label proteins with fluorescent molecules is immunostaining, and more precisely immunohistochemistry. An antigen is tagged with an antibody in cells of a piece of tissue. Many AIS studies use immunohistochemistry to label specific AIS proteins, enabling to localize the AIS start and end positions (fig. 1.8 C). Moreover, it is a suited method to compare the distribution of proteins, as ionic channels, in different regions of the neuron.

Fluorescence microscopy allows to localize distinct proteins labelled with anti-bodies but is limited by the diffraction limit of optical microscopy ($\sim$ 200 nm). In neuroscience, it is therefore a valuable tool to explore brain regions, single neurons and neuron circuits, but it is of little help when it comes to exploring the sub-cellular structures. Many efforts were then taken to go beyond the diffraction limit with the development of super-resolution optical imaging techniques, as for example single-molecule-localization microscopy.

With a light microscope acquiring wide field images, all fluorophores emit light at once. In single-molecule-localization microscopy, only a few fluorophores emit light at the same time. For instance, the stochastic optical reconstruction microscopy (STORM) technique consists in activating stochastically only a few fluorescent molecules simultaneously. Light spots that have the size of optical diffraction limit are detected and the sparseness of the illumination allows to accurately locate the centre of the spot, with a 20 nm resolution. Blinking sequences of tens of thousands of frames are needed to locate all the fluorophores present in a sample and construct a complete image (Leterrier et al., 2017b) (fig. 1.8 D). Other super-resolution imaging techniques exist, based on different illuminations of the sample, as structured illumination microscopy (SIM, resolution 50 nm) or stimulated emission depletion microscopy (STED, resolution 40 nm). In neuroscience, super-resolution microscopy has produced striking images of synaptic boutons, actin dynamics in axon growth cones, vesicular content release at membranes, among other fascinating phenomena (for examples, see e.g. Igarashi et al., 2018). The nano structure of the AIS cytoskeleton was first probed with super-resolution imaging in the last decade (Xu et al., 2013; Leterrier et al., 2015) and continues to astonish researchers with its exceptional molecular organization. We detail it in the next section, starting with the mature AIS and then focusing on its assembly during development.

1.2.2 Structure

The mature AIS

Axon structure

The axonal cytoskeleton is made of 3 major constituents: microtubules, neurofilaments and actin filaments (Leterrier et al., 2017b). Microtubules (MT) are polymers arranged in cylindrical structures of $\sim$ 25 nm diameter. They are dynamic polar structures, with fast (de-)polymerisation at the plus end and slower (de-)polymerisation at the minus end. In axons, MT are exclusively oriented with the plus end towards the axon terminal, while in

dendrites, the MT are oriented in both directions (Lodish et al., 2008). In consequence, MT orientation helps determine the nature of neurites in unipolar and pseudo-unipolar neurons in invertebrates (Rolls and Jegla, 2015). The axon terminal that can be centimetres away from the soma, requiring proteins synthesized in the cell body to travel long distances. MT are responsible for the proteins and organelles transport along the axon (Lodish et al., 2008). They are stiff structures that also bring structural stability to the axon. Neurofilaments are the intermediate filaments in neurons. They consist of $\sim 10\,\text{nm}$ diameter heteropolymers forming a very stable and parallel network that fills the axoplasm in the axon (Leterrier et al., 2017b). Their principal function is structural, providing mechanical support for the plasma membrane and they are at least 10 times more abundant than MT (Lodish et al., 2008). Actin filaments are $\sim 8\,\text{nm}$ large polymers that exist with different forms in axons.

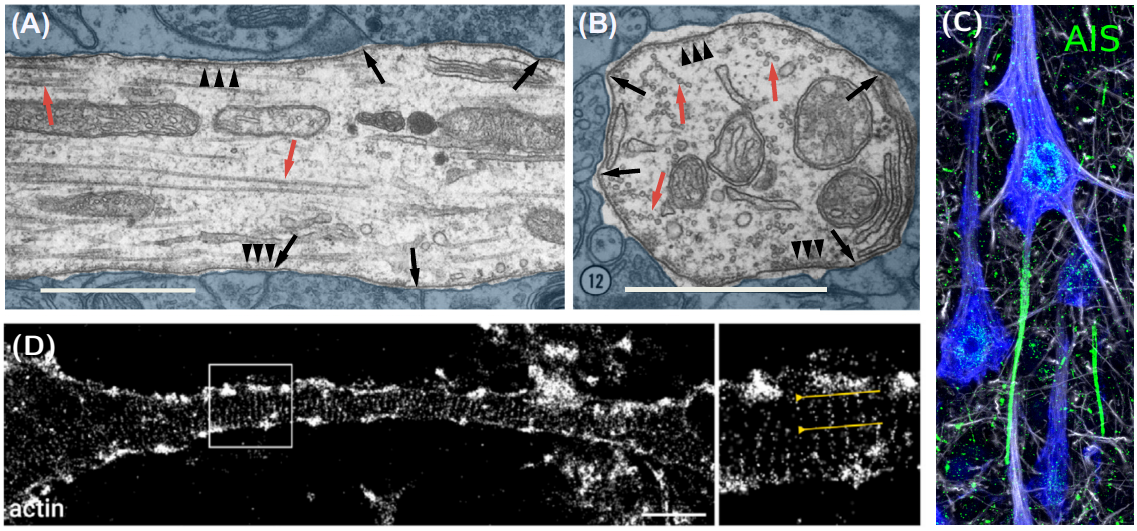

Figure 1.8: Methods of AIS imaging. **A and B**, Electron microscopy images of rat CA3 hippocampal neuron (adapted from Leterrier (2016) and reproduced from Kosaka (1980). **A**, Longitudinal section of the AIS. The electron dense membrane undercoat (black arrowheads) interrupts at the sites of axo-axonic synapses (delimited by black arrows). The microtubules are arranged in fascicles (red arrows). Scale bar: 1 µm. **B**, Cross-section of the AIS, same legend as in **A**. Microtubules are the beads linked to each other by short segments forming the fascicles (red arrows). Scale bar: 1 µm. **C**, Optical fluorescence microscopy image of a cortical layer 5 pyramidal neuron immunolabelled for NeuN (somatodendritic marker, in blue), ankyrin G (AIS marker, green) and SMI-32 (subtype of pyramidal cell marker, white) (adapted from Hamada et al. (2016)). **D**, super-resolution optical microscopy (STORM) image of the proximal axon labelled for actin (adapted from Leterrier et al. (2015)).

On the one hand, transverse actin rings, separated by 190 nm, span the entire axon (Xu et al., 2013; D'Este et al., 2015; Leterrier et al., 2015) (fig. 1.9). The exact distance between the rings is determined by the length of the βII spectrin tetramers that link the rings to each other (Xu et al., 2013) (fig. 1.9). Until recently they were thought to be composed of short and stable actin filaments capped by adducin, a protein that binds to actin filaments end and stabilize them (Leite et al., 2016; Xu et al., 2013). However, a recent platinum-replica EM study in un-

roofed neurons (Vassilopoulos et al., 2019) revealed that the actin rings are braids composed of two intertwined long actin filaments (longer than 0.5 µm). In axons, the periodic arrangement of actin rings is followed by non-muscle myosin II light chains (Berger et al., 2018; Costa et al., 2020). Non-muscle myosin II (NMII) is composed of two major parts: short light chains at the head domain, and heavy chains in the rod domain, that are head-to-tail connected in their "incompetent" form (Vicente-Manzanares et al., 2009). Upon light chain phosphorylation, the protein unfolds and assemble with another NMII protein to form filaments. The head of each NMII links to an actin filament and moves along it, generating mechanical stress in actin bundles. In axons, NMII associates with actin rings to form actomyosin rings (Berger et al., 2018) and regulate radial contractility, thereby modulating axon diameter (Costa et al., 2020). Furthermore, NMII is present longitudinally along axons, suggesting they might connect adjacent rings and have an additional scaffolding role (Costa et al., 2020).

Actomyosin rings connected by spectrin tetramers constitute the membrane-associated periodic scaffold (MPS) (Xu et al., 2013) that confers flexibility and resistance to mechanical stress from movements to axons (Krieg et al., 2014, 2017; Zhang et al., 2017). The stiffness is higher in the axon than in the soma and the dendrites, as shown by measuring the Young modulus with atomic force microscopy (Zhang et al., 2017), because spectrin filaments are held under tension (Krieg et al., 2014; Zhang et al., 2017). By comparison, spectrin tetramers are 55 nm to 65 nm long at rest (Brown et al., 2015), and 180 nm long in axons, indicating that they are held under tension like extended springs. The MPS has been observed in live neurons in all the different types where it was studied so far, from the cerebellar granule cells to the dopaminergic neurons of the midbrain and the dorsal root ganglia sensory neurons in mice, and in different invertebrate and vertebrate species (D'Este et al., 2015, 2016; He et al., 2016; Krieg et al., 2017). Interestingly, in hippocampal neurons, some dendrites contain isolated patches of MPS, in contrast to $\sim$ 25% of spines neck that displays the MPS, even in regions where the periodic structure is not present in the dendrite (He et al., 2016). This organization of stiffer actin rings connected by elastic spectrins confers a role of mechanical stability to the MPS. In C elegans, axons lacking βII spectrins break when the worms move (Hammarlund et al., 2007). In addition, spectrins are important for the maintenance of axon morphology and membrane protein organization, and have recently been shown to be involved in axonal transport (Lorenzo et al., 2019; Leterrier, 2019).

On the other hand, the deep axon contains the recently discovered focal actin "hot spots" (Ganguly et al., 2015), a site of continuous actin (de-)polymerization, putatively generating the longitudinal actin filaments (9 µm to 40 µm) that span the axon (Bearer and Reese, 1999). This phenomenon is called "actin trails" (Ganguly et al., 2015). Hence the MPS forms a stable sub-membranous mesh and the actin trails a deep dynamic structure in the axoplasm.

AIS cytoskeleton

The axon is not a uniform region, it is characterized by functionally and structurally specialized compartments, as the axon initial segment, the nodes of Ranvier and the axon terminal.

Strikingly, the AIS (and NoR) has the same cytoskeleton than the rest of the axon, but the exact isoform of several proteins are not the same and it is additionally enriched with other proteins. As in the axon, actin rings are evenly spaced with a 190 nm period but are connected by head-to-head βIV spectrins (fig. 1.9), and not βII spectrin (Zhong et al., 2014). Phosphorylated NMII light chains, the activator of NMII, are also enriched at the AIS actin rings, compared to the rest of the axon (Berger et al., 2018). In the AIS, the MPS is linked to the MTs and membrane proteins via ankyrin-G (ankG), a protein with a modular structure playing a major role in AIS assembly and maintenance. AnkG is the isoform of ankyrin specific to the AIS and was discovered in the 1990s with an anti-body against another isoform of ankyrin (Kordeli et al., 1995).

At one of its ends, the protein ankG interacts with βIV spectrin and the tail of this unstructured domain extends $\sim$ 30 nm deep in the cytoplasm, toward the microtubules (Leterrier et al., 2015) (fig. 1.9). AnkG interacts with the MTs via end-binding proteins (EB), a family of proteins usually found at the MT growing plus-end (Leterrier et al., 2011) (fig. 1.9). In contrast, in the AIS, they extend along the entire MT lattice (Leterrier et al., 2011). MTs in the AIS are not organized as in the rest of the axon, they are grouped in fascicles (Sobotzik et al., 2009) (fig. 1.8 B).

At its other end, the membrane-binding domain (MBD), ankG binds to Na_v and KCNQ2/3 channels (Garrido et al., 2003; Pan et al., 2006) to cluster them at the AIS, via a similar motif (Pan et al., 2006), thereby anchoring them tightly to the sub-membrane cytoskeleton (fig. 1.9). Even before identification of ankG, the binding to the cytoskeleton via brain ankyrin (in opposite to the isoform of ankyrin found in erythrocyte) was identified as the mechanism that reduced the mobility of voltage-gated channels at the AIS (Srinivasan et al., 1988). $K_v1.1$ and $K_v1.2$ channels are also present at the AIS but, unlike Na_v and K_v7 channels, they do not interact with ankG. They associate with other proteins (Rasband, 2010b) and their organization follows the periodic arrangement of actin rings (D'Este et al., 2016). In consequence, their location alternates with that of Na_v channels. K_v2 channels are clustered at ankG-deficient sites along the AIS, in different rat brain regions and in several mammalian species (King et al., 2014). Furthermore, ankG MBD interacts with cell adhesion molecules (CAM) like neurofascin 186 (NF186) and the specific neuronal cell adhesion molecule Nr-CAM (Leterrier, 2016) (fig. 1.9). Cell adhesion molecules bind to the extra-cellular matrix.

AIS maintenance relies on ankG, since ankG depletion prevents clustering of KCNQ2/3 channels, NF186 and NrCAM, βIV spectrin and Na_v channels (Zhou et al., 1998; Jenkins and Bennett, 2001; Garrido et al., 2003; Pan et al., 2006; Hedstrom et al., 2007; Yang et al., 2007). The cell adhesion molecules are not required for Na_v channels clustering at the AIS and neither the depletion of Na_v channels or βIV spectrin at the AIS prevents AIS assembly (Hedstrom et al., 2007; Yang et al., 2007). However, Na_v or NF186 knock-down in cultured neurons induces a cumulative reduction of ankG at the AIS, regardless of the exact membrane protein (Leterrier et al., 2017a). It suggests that the association of ankG with its membrane partners plays also a crucial role in AIS assembly and stabilization. Still, ankG is the AIS master organizer.

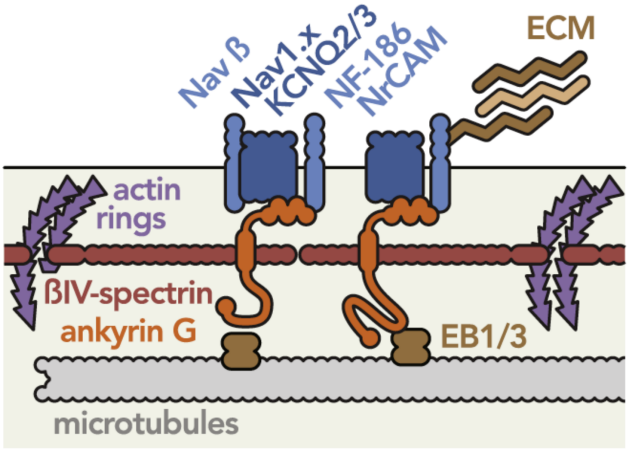

Figure 1.9: The AIS cytoskeleton (adapted from Leterrier (2016)). The AIS protein complex differs from that of the distal axon. It is characterized by a submembranous scaffold of ankG/βIV spectrin linking transversal actin rings spaced by 190 nm. The ankG membrane binding domain clusters transmembrane proteins as voltage-gated channels ($Na_v1.x$ and KCNQ2/3) and cell adhesion molecules (NF186 and NrCAM) that bind to extra-cellular matrix (ECM) components. In the axoplasm, the tail of ankG binds to microtubules via end-binding proteins (EB1/3).

Axo-Axonic synapses

As already observed in early EM studies, the pyramidal cells AIS often contains post-synaptic sites (Peters et al., 1968), whose number varies among neuron types. We now know that the pre-synaptic cells are the Chandelier cells (ChCs). Equally named axo-axonic cells, these GABAergic cortical interneurons are found sparsely in all cortical layers and in the hippocampus of different mammal species (see e.g. Howard et al., 2005). They differ from other interneuron types by an exceptional morphology. The ChC axon, which originates from the soma or a proximal dendrite, is highly ramified and these numerous terminals end form *cartridges* that contain 3-5 synaptic boutons (Inan et al., 2013). Cartridges contact exclusively AISs of pyramidal neurons (Peters et al., 1982; Somogyi et al., 1982) located in their close neighbourhood (Inan et al., 2013). These special synapses are termed *axo-axonic synapses* as both the pre- and the post-synaptic compartments are along the axon. In the primary somato-sensory cortex, each pyramidal cell is on average innervated by 4 ChCs, so in total the AIS accumulates 12-20 axo-axonic synapses (Inan et al., 2013). Strikingly, a single ChCs contacts dozens of pyramidal cells in it neighbourhood and is are therefore expected to strongly modulate the local neuron network activity. However, how this modulation occurs at the single-cell level has been intensely debated and a consensus has only recently started to emerge.

During development, the polarity of GABA transmission switches in the somato-dendritic compartment of pyramidal cells (Ben-Ari et al., 2007). Early in development, the high chloride level in pyramidal neurons makes the activation of GABA receptors (that conduct chloride) depolarizing. Later in development, the reduced intracellular chloride shifts the opening of GABA receptors to inhibitory. A body of previous work (Woodruff et al., 2010, 2009; Szabadics

et al., 2006) argues that GABAergic synapses at the AIS can either be excitatory or inhibitory, depending on the cell's resting membrane potential, the reversal potential of GABA and the threshold for spike initiation, so depending on the network state.

More recently, voltage sensors, a non-invasive technique, in contrast with the ones used in the aforementioned studies, were used to measure the effect of GABA on the activity of the post-synaptic cells (Pan-Vazquez et al., 2020). It confirmed that during synaptogenesis (post-natal day (P) 12-18), GABA can produce depolarizing response in the post-synaptic neuron but that in adult animals (P>40), it produces exclusively inhibitory responses, consistently with previous results showing that the concentration of intracellular chloride at the AIS matches that of dendrites only at early adulthood (Rinetti-Vargas et al., 2017). Interestingly, this switch in the GABA polarity is accompanied by a switch in AAS plasticity. Upon increased network activity during synaptogenesis (P14-P18), either by increasing the activity of the pyramidal cells network of directly the activity of the ChC, the number of AAS per cell formed by a ChCs decreases. The same manipulation at adulthood (P40-P46), when GABA release has an inhibitory effect, will increase the number of AAS per pyramidal cell, although the effect is less pronounced (Pan-Vazquez et al., 2020). In summary, when ChCs are likely to have a depolarizing effect on the post-synaptic cell, they will decrease their output in response to increased network activity, while when they have an hyperpolarizing/shunting effect, they will increase their output. So the ChCs adapt their stimulation intensity to the network state, depending on GABA polarity.

Finally, we mentioned earlier that $K_v2.1$ channels are detected in ankG-deficient membrane compartment at the AIS. Nonetheless, $K_v2.1$ channels are located adjacent to axo-axonal GABAergic synapses. At these sites, the cisternal organelles, a specialized intracellular organelles that is a site of calcium release, are also clustered (King et al., 2014).

Role in neuron polarization

Thanks to its tight and dense molecular structure, the AIS forms a boundary between the somato-dendritic and the axonal compartment, helping to maintain the neuronal polarity and in particular, the molecular identity of the axon (reviewed in Rasband, 2010a). Upon depletion of ankG at the AIS, the proximal axon acquires dendritic characteristics, as ectopic spines, and dendritic proteins invade the proximal axon, like MAP2, both *in vitro* (Hedstrom et al., 2008) and *in vivo* (Sobotzik et al., 2009). Two phenomena are thought to be at play in this process. First, the AIS has been shown to act as a diffusion barrier on membrane proteins (reviewed in Leterrier, 2018). Their diffusion is hampered by, on the one hand, the high density of channels and CAMs linked to the submembraneous cytoskeleton that slow other proteins movement down (Nakada et al., 2003). On the other hand, single particle tracking at the AIS revealed that the diffusion of lipid molecules on the membrane is confined by the actin rings, a submembraneous structure (Albrecht et al., 2016). So the AIS likely acts as a diffusion barrier through two processes, the slowing down and the compartmentalization of diffusion. Second, the AIS acts as a selective filter for intracellular trafficking (reviewed in Nelson and Jenkins, 2017), both cytoplasmic diffusion and active transport. The region between the soma and the

AIS start forms an exclusion zone where vesicles containing axonal proteins enter the AIS and vesicles containing dendritic proteins are excluded. The precise role of the AIS in this process has produced an extensive body of literature and is still the subject of intense debates (Leterrier, 2018).

The AIS has a tight and specific molecular structure, mastered by the scaffolding protein ankG, that is necessary for the other AIS proteins recruitment. Yet at this point we have no idea of how ankG itself is targeted to the AIS, and more generally how the AIS assembles during development.

AIS assembly

AIS assembly does not rely on extracellular mechanisms, it is an intrinsic property of neurons (Hedstrom et al., 2007; Dzhashiashvili et al., 2007), in contrast with NoR whose establishment relies on interaction with glial cells (see e.g. Rasband, 2010a). AnkG is required for both AIS assembly and maintenance (Hedstrom et al., 2008; Galiano et al., 2012) and for the maintenance of neuronal polarity (see e.g. Rasband, 2010a), but not for axon specification, i.e. establishing neuronal polarity (Galiano et al., 2012).

In rodent cortical neurons, ankG is first detected distal to the soma and a few days later, almost adjacent to the soma, suggesting a distal-to-proximal clustering of ankG at the AIS (Galiano et al., 2012). AnkG is restricted to the proximal axon by an intra-axonal boundary made of the interaction between ankB (another isoform of ankyrin), αII spectrin and βII spectrin. These proteins are present in the growth cone at the time of axon specification, before ankG clustering, and then progressively backfill the axon. Similar observations were reported in dissociated hippocampal cells. Similarly, in motor neurons, ankG first appears along the whole axon and concentrates at the AIS two embryonic days after it was first detected (Le Bras et al., 2014). A seemingly opposite mechanism was reported in dissociated hippocampal neurons. A periodic βII spectrin-actin scaffold appears just after axon specification (at days *in vitro* (DIV) 2) and before AIS assembly (Zhong et al., 2014). It emerges from the soma and subsequently progressively extends to the distal axon, in a proximal-to-distal manner. Around DIV8, ankG and βIV spectrin start to be detected at the AIS, suggesting that they are inserted in the βII spectrin lattice, and that βII spectrin is replaced by βIV spectrin at the AIS. AnkG might first accumulate at the AIS and then recruit βIV spectrin (Zhong et al., 2014).

How to combine these seemingly contradictory results? During development, βII spectrin could be initially present in the growth cone and in the proximal axon, and then extend progressively from these two ends to fill the axon (see fig. 2, M, N, O in Galiano et al. (2012)) and restrict ankG to the AIS. The formation of the periodic organization of βII spectrin and actin could be initiated in the soma and extend progressively in the entire axon. The discrepancy between the Zhong and colleagues study and that of Galiano and colleagues could also come from the different imaging techniques. The former study resolves the periodic organization of the AIS proteins with STORM imaging. The second work is based on optical confocal microscopy and therefore provides a less accurate visualization of the protein organization in

the AIS. The exact temporal organization of ankG accumulation is still unclear and debated, as discussed in Leterrier (2018) and Jones and Svitkina (2016), and needs further investigation. However, it is established that the AIS assembles in an inside-out manner: the cytoskeleton is built first and the membrane proteins (channels, CAMs, ...) are subsequently inserted in this existing structure.

Other keys to understand ankG recruitment at the AIS are provided by MTs. MTs bundling is indeed the first sign of AIS assembly during early development in cultured neurons (Jones et al., 2014). AnkG binds to end-binding molecules in the AIS, that accumulates along the microtubules and mediate the ankG - MT interactions. The EB - ankG interaction is required for proper axonal MTs organization and AIS formation and could in consequence drive the self-organized assembly of the AIS and MTs structure during development (Fréal et al., 2016). Indeed, depletion of ankG impairs EB accumulation and MT orientation at the AIS (Hedstrom et al., 2008; Sobotzik et al., 2009; Fréal et al., 2016), and conversely EB binding is required for ankG restricted localization and stabilization at the AIS (Fréal et al., 2016; Leterrier et al., 2011). A more recent study brings additional elements to the mechanism of AIS assembly after ankG has started to accumulate at the AIS (Fréal et al., 2019). The authors propose the following feedback mechanism between AIS membrane proteins and axonal MTs. First ankG targets and anchors MT fascicles to the plasma membrane, that are bundled with the help of TRIM46, a MT-associated protein found in the axon (van Beuningen et al., 2015). Second ankG facilitates the bundling of TRIM46 to the MT fascicles. In turn, TRIM46 stabilizes the MT bundles and causes the single orientation (plus-end-out) of the MT anchored to the plasma membrane in the proximal axon. Indeed, ankG is able to target MT of mixed orientations to the proximal axon. Third, NF186 is transported to the AIS. AnkG blocks NF186 endocytosis[2], thereby hindering its internalization, which confers it a role in organizing membrane micro-domains. In the absence of TRIM46, the transport of NF186 is perturbed. Finally, the stabilization of NF186 at the AIS in turn increases the accumulation of ankG and TRIM46, supporting the results of Leterrier et al. (2017a). Higher ankG concentration then strengthens the membrane anchoring of MT and facilitates TRIM46-lattice stabilization and orientation which in turn promotes efficient trafficking of NF186 to the proximal axon. In this way, the AIS achieves its tight structure through a feedback mechanism. Interestingly, this study also shows that ankG locally controls NF186 endocytosis, a mechanism that could participate in regulating AIS relocation during plasticity.

During development, phosphorylated NMII light chains (pMLC) co-accumulates with ankG at the AIS, being therefore an early marker of the AIS (Berger et al., 2018). In addition, its contractile activity is important for ankG recruitment at the AIS and, reciprocally, ankG is necessary for pMLC accumulation at the AIS.

To summarize, even if ankG is undoubtedly the AIS master organizer that recruits other AIS proteins, its stabilization and maintenance is enhanced by additional mechanisms.

[2]Upon non-specific targeting of NF186 in the entire neuron, the AIS is the only location where NF186 does not get endocytosed.

1.2.3 Role in spike initiation

Besides its major role in maintaining neuron polarization, the AIS is the site of AP initiation in neurons (see e.g. Kole and Stuart, 2012). When the summation of dendritic inputs at the soma depolarizes the somatic membrane potential to a threshold, the low-voltage-activated Na_v channels at the AIS open, triggering a spike at the AIS. The AP is then propagated along the axon to reach the axon terminal, but also back-propagated to the soma. This current will depolarize the soma until the somatic Na_v channels open and regenerate the spike that is further transmitted in the dendrite to play a role in synaptic plasticity (Stuart et al., 1997). Indeed, an AP recorded at the soma displays two components, one due to the axonal AP and the second to the somatic Na_v channels, as already noted in the 1950th (Coombs et al., 1957) (fig. 1.10 A). The two components of the AP are better illustrated by the phase plot that displays the time derivative of the membrane potential vs the membrane potential, as illustrated on fig. 1.10 B. In this section, we review the experimental evidence for AP initiation at the AIS, the role of different voltage gated channels and unconventional spike initiation.

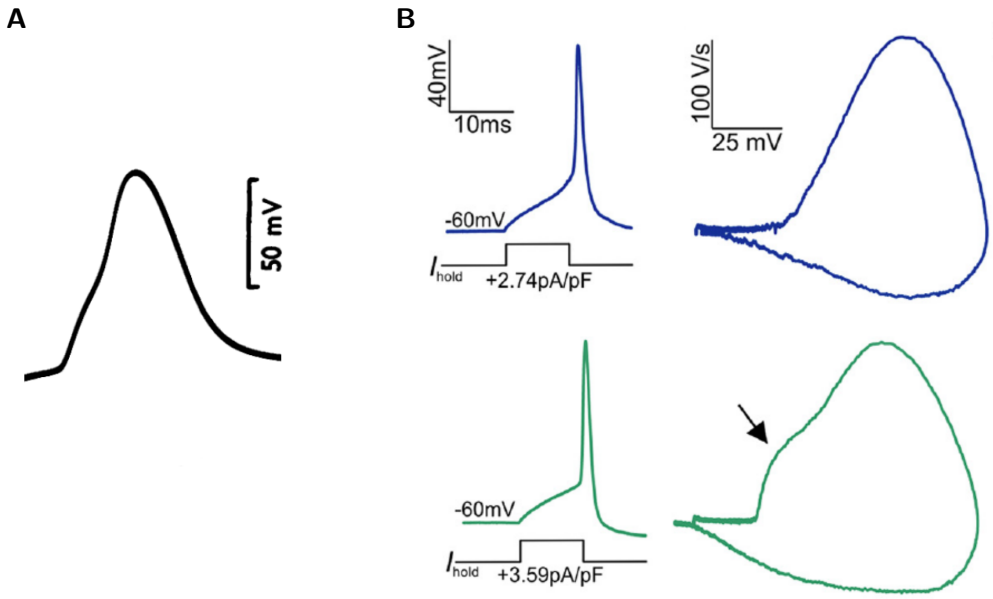

Figure 1.10: The two components of the somatic action potential. **A**, The first increase in membrane potential corresponds to the axonal spike invading the soma. The second smoother bump corresponds to somatic Na_v channels opening, so the initiation of the somatic spike (adapted from Coombs et al. (1957)). **B**, Top, action potential and phase plot (dV/dt vs. V) in axonless neuron: the action potential is monophasic. Bottom, action potential and phase plot when spikes initiate at the AIS: the AP is biphasic. The black arrow indicates the somatic spike onset (adapted from Chand et al. (2015)).

Experimental evidence

With the progress of the patch-clamp and loose patch techniques, simultaneous recording at the soma and the dendrites and/or axons became possible (Stuart et al., 1997). It was crucial in precisely locating the site of spike initiation in mammalian neurons.

Evidence for axonal spike initiation comes from comparing the latency of APs recorded at the AIS and the soma (Stuart et al., 1997; Palmer and Stuart, 2006; Kole et al., 2007) (fig. 1.11 A, B, C). Simultaneous recording at the AIS or in unmyelinated axonal blebs (Shu et al., 2006) and at the soma of rodents layer 5 pyramidal cells show that the shortest AP latency occurs on average 38 µm away from the soma, on average 120 µs before an AP is recorded at the soma (Kole et al., 2007). It supports previous reports in layer 5 pyramidal cells (Palmer and Stuart, 2006; Shu et al., 2006), confirming that spike initiation occurs in the distal part of the AIS (in layer 5 pyramidal cells, the AIS starts 0 µm to 10 µm away from the soma and ends 40 µm to 50 µm away from the soma (Hamada et al., 2016)).

Why do AP initiate in the distal part of the AIS? Different explanations have been proposed. First, early optical fluorescence imaging studies revealed that the AIS contains a higher density of Na_v channels than the rest of the axon or the soma, in retinal ganglion cells (Boiko et al., 2003; Van Wart et al., 2007), cultured spinal cord neurons (Angelides et al., 1988; Catterall, 1981, although in less than half of the neurons) and rat layer 5 pyramidal cells (Kole et al., 2008). However, immunochemistry makes no distinction between channels that are functional or not. Surprisingly, the first Na^+ currents recorded in outside-out patch at the AIS in layer 5 pyramidal cells were not larger than at the soma (Colbert and Pan, 2002), suggesting that the density of Na_v channels was in fact not higher in the AIS. It turned out that these results are explained by the tight anchoring of Na_v channels to the AIS cytoskeleton that impedes them to be drawn by the patch pipette with the membrane patch (Kole et al., 2008). Larger currents are recorded in cell-attached recordings from the AIS upon disruption of the actin cytoskeleton (Kole et al., 2008). Furthermore, $Na_v1.6$ channels density in different neuron compartment was investigated with electron microscopy and immunogold labelling, enabling extremely precise localization of $Na_v1.6$ channels (Lorincz and Nusser, 2010). The $Na_v1.6$ channel density was $150\,\mu m^{-2}$ in the AIS and $5\,\mu m^{-2}$ in the soma, predicting a 30 - fold increase in $Na_v1.6$ channels density in the AIS (Lorincz and Nusser, 2010). Assuming that a single channel has a $\sim 17\,pS$ conductance (Kole and Stuart, 2012), it gives a conductance density of $2500\,S\,m^{-2}$. In the unmyelinated axons of the dentate granule cells, outside-out patches at the soma and axon blebs[3] revealed that the Na_v conductance density is maximal close to the soma and decreases along the axon (Schmidt-Hieber and Bischofberger, 2010). The Na_v conductance density at the soma is roughly 5 times smaller than the average conductance density from 5 µm to 35 µm away from the soma. At its maximum, the Na_v conductance density is 9 fold the somatic density. Thus, in the small dentate granule cells, the density of Na_v channels at the proximal axon is only moderately higher than at the soma (Schmidt-Hieber and Bischofberger, 2010).

A second explanation comes from the properties of AIS Na_v channels (Colbert and Pan, 2002). In neocortical layer 5 pyramidal cells, the proximal part of the AIS contains a majority of the $Na_v1.2$ subtypes, while the distal region of the AIS contains prominently $Na_v1.6$ channels (Hu et al., 2009). The recorded Na^+ current also increases with the distance from the soma and similarly the ratio between somatic and AIS Na_v density ranges from $1/24$ to $1/37$, confirming previous studies. In addition, the half-activation voltage of Na_v channels in the AIS is lower

[3]The cytoskeleton is presumably disrupted at axon blebs.

in its distal part than in its proximal part, consistent with the $Na_v1.2$ subtype activating at a higher voltage than the $Na_v1.6$ channels (Rush et al., 2005) (fig. 1.11 D). Therefore, the site of initiation accumulates low-threshold $Na_v1.6$ channels, that activate at more hyperpolarized membrane potential ($\sim 15\,mV$) than somatic Na_v channels. The proximal AIS contains higher activation threshold $Na_v1.2$ channels (Hu et al., 2009). Within the AIS, the half-activation voltage progressively decreases from roughly $-35\,mV$ to $-44\,mV$, and reaches a steady value in regions beyond the AIS (Hu et al., 2009) (fig. 1.11 D). In dentate granule cells unmyelinated axons, axonal Na_v channels activate and inactivate at more negative potential than the somatic Na_v channels (Schmidt-Hieber and Bischofberger, 2010). It is consistent with the observation that the $Na_v1.6$ subtype dominates in granule cells AIS (Kress et al., 2010). Moreover, both activation and inactivation kinetics of axonal Na_v channels are faster in the range $-50\,mV$ to $-10\,mV$, corresponding to the spike initiation voltage range (Schmidt-Hieber and Bischofberger, 2010). Finally, computational modelling supports that the fast kinetics of Na_v channels in the proximal axon is necessary to reproduce the experimental findings (Schmidt-Hieber and Bischofberger, 2010).

Lastly, as suggested in early modelling studies (Mainen et al., 1995), the distal AIS might be a preferred site for initiation because of its electrical isolation from the capacitive load of the soma, so that less current is required to depolarize its membrane. The two explanations detailed above support the idea that spikes are initiated in the distal AIS because the Na^+ current is the highest there. This view was challenged by high-speed Na^+ imaging along the AIS (Baranauskas et al., 2013), showing that the maximal Na^+ influx during the axonal spike occurs in the middle of the AIS, in a region starting from $8 \pm 3\,\mu m$ away from the soma and extending over $14 \pm 5\,\mu m$ (fig. 1.11 E). The Na^+ flux in the distal AIS is on average one fourth of its maximal value in the AIS. Loose-patch recordings confirmed that AP are initiated in the distal AIS and therefore that there is a spatial mismatch between the initiation site and the region of maximal Na^+ flux. It supports the idea that AP initiate in a site electrically isolated from the large soma and not at the location of maximal Na^+ influx. This mismatch can be explained by the resistive coupling theory, developed originally to explain the sharpness of spike initiation (Brette, 2013) and will be addressed in more details in Appendix B. Incidentally this theoretical study also supports the idea that electrical isolation from the soma promotes distal initiation site, because the threshold for spike initiation decreases with the axial resistance between the soma and the initiation site (Brette, 2013). Furthermore, a recent modelling and experimental study in cultured hippocampal neurons lacking βIV spectrin suggests that high Na_v channel density is not necessary to define the site of spike initiation (Lazarov et al., 2018). Even if the density of Na_v channels at the soma and the AIS are identical, AP still initiate in the AIS. At the end of this introduction, it will become clear that the important features defining the initiation site are low-activating Na_v channels and electrical isolation from the large capacitive load of the soma.

Voltage gated channels involved in spike initiation

We detail the major subtypes of voltage-gated channels involved in spike initiation at the AIS, as most often reported by immunostaining studies.

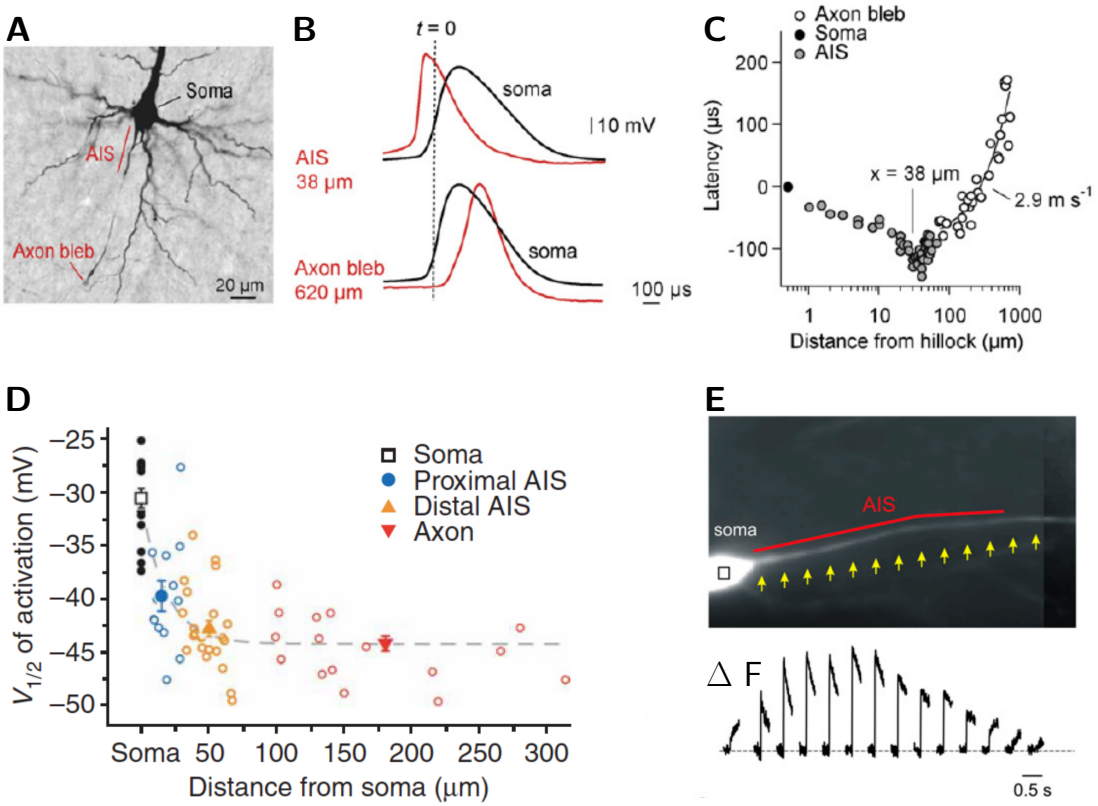

Figure 1.11: Spike initiation in the distal AIS (A, B, C are adapted from Kole et al. (2007)). **A**, The different recording sites for simultaneous recordings at the soma, AIS and axon. **B**, AP recorded at the AIS (top red, 38 µm away from the soma) occur earlier than AP recorded at the soma (black) whereas AP recorded in an axon bleb occur later (bottom red, 620 µm away from the soma). **C**, The latency relative to the somatic spike is minimal 38 µm away from the soma, in the distal AIS. **D**, The half-activation voltage of Na_v channels decreases strongly in the proximal axon and remains low in the axon beyond the AIS (adapted from Hu et al. (2009)). **E**, AP evoked Na^+ influx along the proximal AIS (adapted from Baranauskas et al. (2013)). Top, fluorescence was recorded at the points indicated by the square and the yellow arrows. Bottom, average change in fluorescence evoked by a single AP in the regions indicated above.

Sodium channels

Voltage-gated Na_v channels are proteins made of one α subunit and one or more β subunits. The α subunit consists of 4 domains that each contains 6 trans-membrane segment and is the voltage-sensing part of the channel. Ions are allowed through the channel when one of these segments moves, forming a pore. Auxiliary β subunits regulate the voltage dependence of gating and kinetics (see e.g. Catterall, 2000). Na_v channels can activate, inactivate and deactivate, as revealed by early voltage-clamp studies (Hodgkin and Huxley, 1952a). There are nine subtypes of voltage-gated Na channels, not all of them expressed in the brain. We will focus on the $Na_v1.1$, 1.2 and 1.6 subtypes as they are found in the AIS and involved in AP initiation.

The most prominent Na_v channel subtype present at the AIS is $Na_v1.6$. In pyramidal neurons of the neocortex and hippocampus (Layer 5, II/II, CA1, CA3), as well as in cortical and cerebellar interneurons, $Na_v1.6$ are expressed in a large portion of the AIS but excluded from the most proximal region of the AIS. $Na_v1.2$ span the proximal region of the AIS in neocortical pyramidal neurons (Lorincz and Nusser, 2008; Hu et al., 2009; Debanne et al., 2011) and the entire AIS of the retinal ganglion cells unmyelinated axon (Boiko et al., 2003). The RGC axon is unmyelinated in the retina and becomes myelinated only after it enters the optic nerve. In adult rats, $Na_v1.2$ are found all along the unmyelinated part of the axon, while $Na_v1.6$ are found only at NoR (myelinated optic nerve) and AIS (Boiko et al., 2001, 2003). The proximal region of the AIS (defined based on ankyrin-G staining) contains in addition $Na_v1.1$ channels and no (small diameter axons) or very few (large diameter axons) $Na_v1.6$ (Van Wart et al., 2007). This pattern of channel subtype expression changes during development. $Na_v1.2$ are detectable since early in development but $Na_v1.6$ progressively add up to $Na_v1.2$ in the AIS. On the contrary, in NoR of the myelinated part of the RGC axons, $Na_v1.6$ replace $Na_v1.2$. During the period in which $Na_v1.6$ start to substantially appear at the AIS, the firing of RGC also changes. In developing rat retina, RGC typically fire a single AP during a sustained depolarization (Wang et al., 1997). Between P7 and P24, the fraction of cells that fire repetitively increases progressively (Wang et al., 1997). It could be attributed to the $Na_v1.6$ channels.

The proximal $Na_v1.2$ have a higher threshold for activation and are responsible from AP propagation to the soma (Rush et al., 2005; Hu et al., 2009). The zone of high $Na_v1.6$ channels density in the distal AIS corresponds to the site of spike initiation, so they are believed to be mostly responsible for AP initiation (Royeck et al., 2008; Hu et al., 2009). In cultured CA1 pyramidal cells lacking the $Na_v1.6$ subunit, spikes are still initiated at the AIS, but with a higher initiation threshold and the activation of the large transient current is shifted towards higher values (Royeck et al., 2008). In mice lacking the gene encoding the $Na_v1.6$ in a small region of the cortex (if $Na_v1.6$ are KO in the entire brain, the mice do not survive), there is a complete loss of $Na_v1.6$ at the AIS, that is compensated for by the expression of $Na_v1.2$ channels (Katz et al., 2018). These cells display a biphasic phase plot and a higher threshold for SI than wild type mice (Katz et al., 2018). It indicates that the exact subtype of channel is not crucial for AIS spike initiation, as long as its activation threshold is low enough, and that the geometrical arrangement of the soma and the AIS might be more important.

The $Na_v1.1$ subtype is mostly found in the proximal AIS of GABAergic interneurons of the cortex, cerebellum and hippocampus (Lorincz and Nusser, 2008; Ogiwara et al., 2007). In retinal ganglion cells, they also span the proximal part of the AIS (roughly first third), a region from which $Na_v1.6$ are excluded (Van Wart et al., 2007). The only cell type that was reported expressing $Na_v1.1$ along its entire AIS is the short-axon cells of the external plexiform layer of the olfactory bulb (Lorincz and Nusser, 2008).

Potassium channels

The voltage-gated potassium channels are made of 1 to 4 α subunits and of a variable number of auxiliaries β subunits (see e.g. Trimmer, 2015). This high number of possible combinations and the large amount of paralogous genes encoding the α subunit result in a large diversity of K_v channels but we will here focus on the subtypes involved in spike initiation. Among the voltage-gated K_v channels, only subtypes 1, 2, 3, 4 and 7 are expressed in neuron membranes. The 5, 6, 8, 9, 10, 11 and 12 subtypes are either found intracellularly or were not reported. In general, K_v2 channels are present in the proximal dendrites and the soma and the K_v4 family in distal dendrites.

$K_v1.1$ and 1.2 subunits are detectable at the AIS of excitatory and inhibitory neurons and tend to be located more distally than $Na_v1.6$ channels in most neuron types (Lorincz and Nusser, 2008), but not in neocortical L5 pyramidal neurons. In RGC, $Ka_v1.2$ are excluded from the proximal region of the AIS (they have a similar distribution as $Na_v1.6$ channels) (Van Wart et al., 2007). K_v1 channels are responsible for the repolarization phase of the AP and their variable density along the AIS modulates the shape of the AP (Kole et al., 2007; Shu et al., 2007). In layer 5 pyramidal cells, the duration of the AP increases along the proximal AIS, concomitantly with the amplitude of DTX-sensitive[4] currents recorded in the proximal AIS (Kole et al., 2007). In contrast, the spontaneously firing Purkinje cells lack K_v1 channels at the AIS (Lorincz and Nusser, 2008). The K^+ current is considerably smaller than the Na^+ current at spike initiation, indicating that the K_v channels are not substantially open at that time and thereby do not influence spike initiation importantly (Hallermann et al., 2012).

The other K_v channels subtypes expressed at the AIS of many neuron types are the $K_v7.2$ and 7.3 subunits (KCNQ2/3) (Devaux et al., 2004; Battefeld et al., 2014). They carry the M-current that activates slowly at low voltages and does not inactivate, so that these channels are open at rest (Cooper, 2011). Their hyperpolarizing effect is important for stabilizing the resting membrane potential, thereby regulating Na_v channels availability and preventing a large persistent Na_v^+ current and spontaneous firing (Battefeld et al., 2014). Indeed K_v7 channels are responsible for a 3 mV hyperpolarization of the AIS resting membrane potential relative to the soma in layer 5 pyramidal cells (Hu and Bean, 2018). In layer 5 pyramidal cells, the K_v7 channels are located in the distal AIS (Battefeld et al., 2014). Consistently, recording the M-current in the cell-attached configuration along the proximal axon shows that the conductance density of the M-current increases 10-fold at the distal end of the AIS, compared to the soma (Battefeld et al., 2014).

Unconventional spike initiation

In most multipolar neurons, AP are triggered in the distal AIS. However some neurons have no AIS or even no axon. Where do spikes initiate in such unusual morphologies? Do unipolar neurons contain an AIS and if not, what is the spike initiation zone? AP triggering mechanisms

[4]Dendrotoxin (DTX) is a toxin that selectively blocks $K_v1.1$, $K_v1.2$ and $K_v1.6$ channels.

are in fact diverse and can depend on a neuron specific morphology and function.

The mammalian retina and olfactory bulb comprise axonless neurons. In the retina, the main type of axonless neuron is the AII amacrine cell, a compact neuron (length on the order of 100 µm) that has an elaborate dendritic tree and no axon (Veruki et al., 2010). AII amacrine cells receive inputs from the rod bipolar cells and excite retinal ganglion cells. Their spikes are small (<10 mV) and long (>5 ms). An AIS-like region has been identified by accumulation of $Na_v1.1$ channels, ankG and NF186 on a dendritic process, despite no axon (Wu et al., 2011). This region is the site of spike initiation (Wu et al., 2011) and is located electrotonically far from the soma, on a thin neurite that branches from a proximal dendrite close to the soma (Cembrowski et al., 2012). Therefore the small somatic AP is an attenuated version of the large dendritic spike initiated distally (Cembrowski et al., 2012). A substantial proportion of the dopaminergic interneurons of the olfactory bulb is axonless. The axonic cells have a larger soma and dendritic tree than the axonless ones (Chand et al., 2015; Galliano et al., 2018) and are exclusively born during embryonic development whereas the axonless neurons are generated postnatally, and undergo neurogenesis throughout adulthood (Galliano et al., 2018). In contrast to AII amacrine cells, no AIS-like region was identified in the olfactory bulb axonless neurons (Chand et al., 2015; Galliano et al., 2018). Consistently, axonic neurons display biphasic spikes and have an AIS, while the spikes of axonless neurons are monophasic, indicating somatic spike initiation (Galliano et al., 2018) (fig. 1.10 B). The fact that the latter neurons and AII amacrine cells have no dedicated output compartment could be related to their local function within a neuron population (Goaillard et al., 2019).

In invertebrate neurons, spike initiation can occur in diverse locations. Particularly striking are the big arthropod neurons. In snails, the B2 neuron soma is located in the buccal ganglion and innervates the salivary gland, 10 mm to 11 mm further away. Removing the ganglion and cutting the axon peripheral end does not prevent the axon to spontaneously fire APs, suggesting that it is able to generate spikes in the absence of a soma and a trigger zone (Maratou and Theophilidis, 2000). Multiple spike initiation zones were reported in the arborized axon of the crayfish (Calabrese and Kennedy, 1974). The lateral gastric motor neuron of the crab stomatogastric nervous system has its large soma located in the stomatogastric ganglion and projects to the periphery to innervate a serie of muscles (Meyrand et al., 1992). Spike initiation can occur close to the soma or in the periphery, and the different initiation zones are associated with distinct types of muscle contraction (Meyrand et al., 1992).

Most insects neurons are unipolar, with the soma externalized from the main neurite. To our knowledge there is no experimental evidence for a distinct AIS. However, in drosophila, an AIS-like region was identified as containing a specific isoform of ankyrin (Trunova et al., 2011; Rolls et al., 2007; Spurrier et al., 2019). Whether this region is functionally similar to the mammals AIS still needs to be determined.

Within the (rare) mammals pseudo-unipolar neurons, the dorsal root ganglion neurons initiate AP at its peripheral end (Nascimento et al., 2018). A proximal segment located in

the stem process and accumulating the same proteins (ankG, NF186, Na_v channels) than the multipolar neurons AIS was reported in cultured embryonic DRG neurons (Zhang and Bennett, 1998; Dzhashiashvili et al., 2007). However there is to date no evidence for a proximal segment in adult DRG neurons *in vivo* (Nascimento et al., 2018).

Until recently, the mechanism of AP initiation in the peripheral pseudo-unipolar sensory neurons remained poorly understood. Goldstein and colleagues newly shed light on this phenomenon in corneal nociceptive neurons. Their soma is located in the trigeminal ganglion. The peripheral process receives noxious signals from the cornea and the other targets the central nervous system to transmit sensory information. The spike initiation zone (SIZ) is spatially removed from the peripheral process terminal ending, despite a analogous Na_v channels density (Goldstein et al., 2019). The Na_v channels at the terminal ending are in a slow inactivate state, making them unavailable for depolarization-induced initiation (Goldstein et al., 2019). Upon corneal inflammation, the availability of Na_v channels increases, so that the SIZ shifts towards the terminal ending. A computational model suggests that it increases the terminal's excitability (Goldstein et al., 2019).

1.2.4 Geometry

The AIS molecular structure is exquisitely specialized. Fortunately it enables to localize precisely the start and end positions of the AIS. In the following we use the term "AIS geometry" to refer to its start position, length and, when specified, diameter. AIS geometry is surprisingly variable across and within neuron types, and more strikingly its structure is plastic. In consequence, the distance from the soma to the spike initiation zone varies, putatively impacting the neuron's electrical functions. In this section we describe AIS geometry diversity.

Variability across and within neuron types

We present a table of the AIS start position and length in the neuron types where it has been measured to date to our knowledge (table 1.1). We aim at highlighting the variability in AIS geometry across the brain. Particularly interesting cases of variability within neuron types are discussed below: related to axon origin, tonotopy and development.

Diversity of axon origin

As already noted in early morphological studies, in some neurons, the axon emerges from a primary dendrite instead of from the soma (y Cajal, 1995; Peters et al., 1968; Sloper and Powell, 1979; De Zeeuw et al., 1990) (fig. 1.12 right), increasing the variability of the soma-AIS distance. In an important proportion of neurons in diverse brain regions, the axon originates from a proximal dendrite (fig. 1.12 right). In the hippocampus, 52% of the CA1 pyramidal cells have an axo-dendritic axon, 28% of the CA3 pyramidal cells and 21% of the subiculum neurons (Thome et al., 2014). Similarly, one third of the neocortical thick-tufted layer 5 pyramidal cells have an axon originating from a dendrite (Hamada et al., 2016) (table 1.1). More impressive, the midbrain dopaminergic neurons of the substantia nigra pars compacta are spontaneously active, firing AP even in the absence of synaptic inputs, the so-called pacemaking regime.

Their axon emerges from a primary or secondary dendrite (Häusser et al., 1995). Consequently, the position of the AIS in these neurons is extremely variable (González-Cabrera et al., 2017; Meza et al., 2018; Moubarak et al., 2019): the AIS start position ranges from 20 µm to 120 µm in rats (Moubarak et al., 2019) (table 1.1). In the cerebellum, 40% of the cerebellar granule cells have an axo-dendritic axon (Houston et al., 2017). Lastly, in the visual cortex, approximately 50% of pyramidal neurons, 44% of interneurons and 60% of the Martinotti cells have an axon originating from a dendrite (Höfflin et al., 2017).

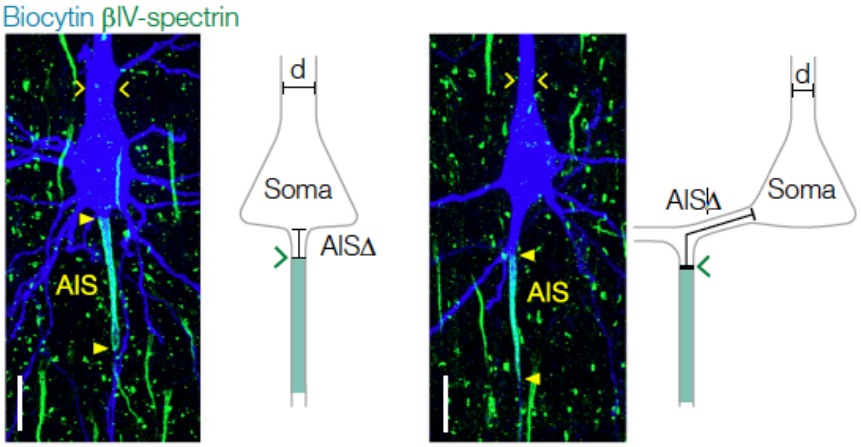

Figure 1.12: Axon origin in cortical layer 5 pyramidal neurons (adapted from Hamada et al. (2016)). Neurons were filled with biocytin (blue) during patch-clamp recordings and subsequently labelled for βIV spectrin (green) to localize the AIS. Left, axo-somatic neurons: the axon emerges from the soma. Right, axo-dendritic neuron: the axon originates from a basal dendrite.

Related to tonotopy

In the auditory system, neuronal processing of auditory information starts at the cochlear nucleus. In chicks, neurons of the cochlear nucleus project through the auditory nerve to the nucleus magnocellularis (NM), the second nucleus. NM neurons generate precisely timed spikes at specific sound frequency that are transmitted bilaterally to the nucleus laminaris (NL). NL neurons detect the coincidence of synaptic inputs from both ears and encode interneural time differences for sound localization (fig. 1.13 A).

NM neurons are tuned to a characteristic frequency (CF) of sound and are arranged along a spatial gradient depending on their specific frequency, a spatial organization termed *tonotopy* (Smith and Rubel, 1979). They have a very few, one or no dendrites, independently on the tonotopic arrangement (Jhaveri and Morest, 1982) (fig. 1.13 B). On the contrary, AIS geometry varies along the tonotopic axis. The AIS start position is similar in low, middle and high frequency neurons, whereas low CF neurons have a longer AIS containing a higher Na_v channels density (Kuba and Ohmori, 2009) (table 1.1).

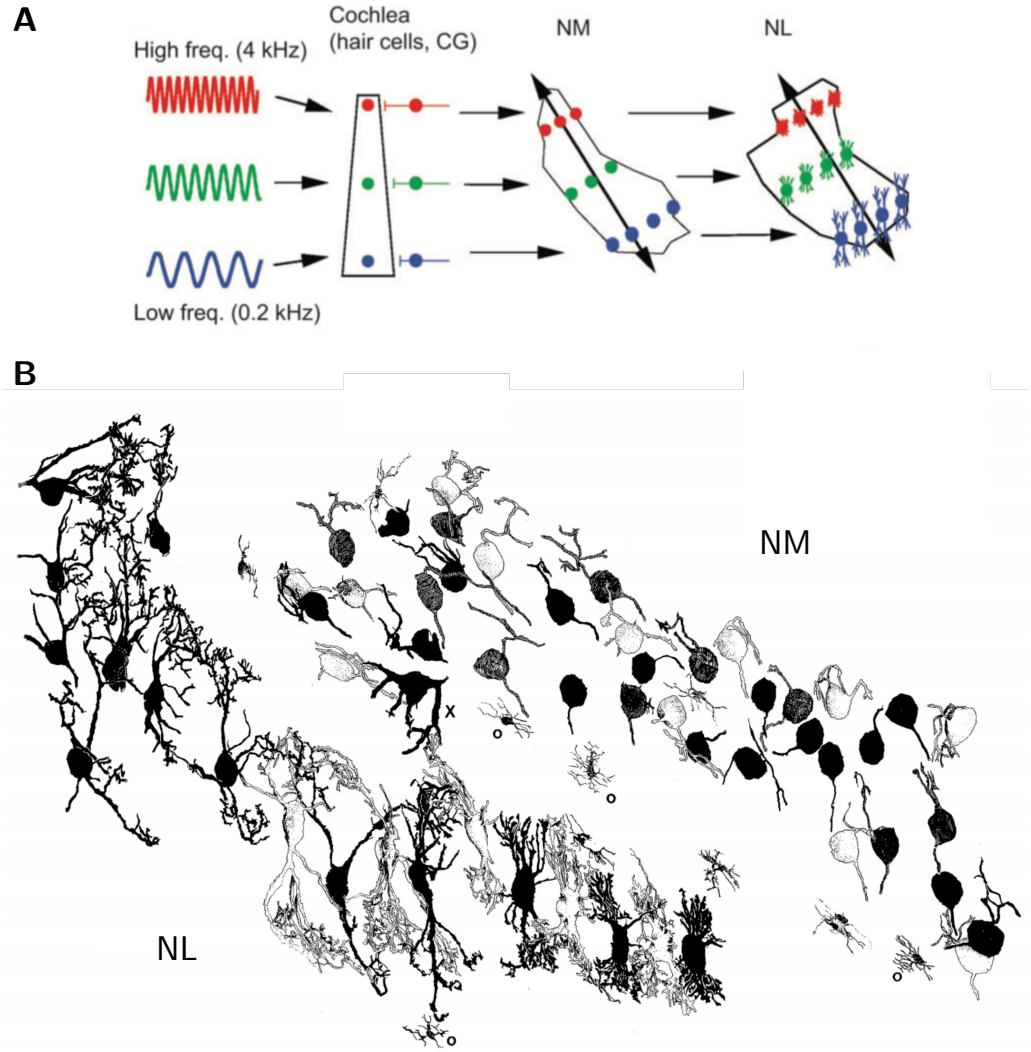

Figure 1.13: Tonotopic arrangement of the avian auditory system. **A**, Schematic representation of the auditory pathway in chicken (CG: cochlear ganglion) (adapted from Kuba (2012)). **B**, NM neurons have no or a very small amount of dendrites, unrelated to tonotopy (right). In NL neurons (left), the dendritic arbor morphology varies along the tonotopic axis. High CF neurons (bottom) have short and numerous dendrites whereas low CF neurons (top) have long and few dendrites (adapted from Jhaveri and Morest (1982)).

NL neurons are analogously tuned to a specific frequency of sounds and tonotopically arranged (Smith and Rubel, 1979), a specification that occurs after hearing onset. The dendritic arbor shape depends on the position along the tonotopic axis (fig. 1.13 B): high CF neurons have many short unbranched dendrites starting at the soma, while low CF neurons have longer dendrites branching further away from the soma (Smith and Rubel, 1979; Jhaveri and Morest, 1982; Kuba et al., 2005). In addition, the electrophysiological properties vary importantly along the tonotopic axis. Consistently with the morphological observations, the input capacitance of low CF neurons is higher than for middle and high CF neurons (Kuba et al., 2005). In low CF neurons, the amplitude and maximal rate-of-rise of APs are 2 to 3 times bigger than in middle and high CF neurons (Kuba et al., 2005).

Neuron type	Δ (µm)	L (µm)	Reference
	Visual system		
Rat visual cortex			Höfflin et al. (2017)
Pyramidal neurons	13.5 ± 12.6	28.5 ± 10.7	
supragranular, AS [1]	12.2 ± 11.2	31.1 ± 11.9	
infragranular, AS	13.5 ± 11.9	25.1 ± 7.5	
Interneurons	14.3 ± 10.9	25.7 ± 11.1	
Rabbit retinal ganglion cells			Fried et al. (2009)
DS cells	22.95 ± 6.55	28.68 ± 4.79	
Alpha cells	27.66 ± 5.75	39.72 ± 6.61	
Other subtypes	19.05 ± 9.61	26.07 ± 8.82	
Mouse retinal ganglion cells	20 ± 7.1	16.82 ± 0.25	Schlüter et al. (2019)
Mouse V1			Schlüter et al. (2019); Gutzmann et al. (2014)
Layer II/III	2.3 ± 1.5	33	
Layer V	2.3 ± 1.5	-	
	Auditory system		
Chicks nucleus magnocellularis			Kuba and Ohmori (2009)
Low CF [2]	9.13	18.31	
Middle CF	9.26	15.34	
High CF	9.78	13.18	
Chicks nucleus laminaris			Kuba et al. (2006)
Low CF	7.31	24.38	
Middle CF	21.30	14.55	
High CF	46.50	9.88	
Mouse auditory brainstem (MNTB [3])			Kim et al. (2019)
Low CF	6.2 ± 0.24	19.9 ± 0.37	
High CF	10.4 ± 0.34	15.1 ± 0.23	
	Hippocampus		
Rat CA1 pyramidal neurons			Thome et al. (2014)
Axo-dendritic	-	34.2 ± 0.5	
Axo-somatic	-	32 ± 0.5	

Table 1.1: AIS start position Δ and length L in different species and neuron types (continued on next page). [1] AS = axo-somatic. [2] CF = characteristic frequency. [3] MNTB = medial nucleus trapezoid body. [4] SNc = substantia nigra pars compacta.

Neuron type	Δ (µm)	L (µm)	Reference
	Cortex		
Mice dopaminergic neurons	-	13-62	Meza et al. (2018)
Rat dopaminergic neurons SNc [4]	20-125	20-55	Moubarak et al. (2019)
Rat thick-tufted L5 pyramidal neurons			Hamada et al. (2016)
Axo-dendritic	9.8 ± 0.79	46.5 ± 1.3	
Axo-somatic	3.71 ± 0.42	45.7 ± 1	
Rhesus monkeys motor and somato-sensory cortices, pyramidal cells	-	43	Sloper and Powell (1979)
Mouse primary somato-sensory cortex			Jamann et al. (2020)
Layer II/III	-	22	
Layer V	-	19	
	Cerebellum		
Purkinje neurons			Somogyu and Hamori (1976)
Cat	-	17.3 ± 1.3	
Rat Purkinje	-	17.1 ± 2	
	Other		
Young cats spinal motoneurons	-	17.36 ± 3.38	Conradi and Ronnevi (1977)
Cat medial accessory olive	19 ± 2	35 ± 3	De Zeeuw et al. (1990)
Olfactory bulb dopaminergic interneurons			Chand et al. (2015)
Rat	15.2 ± 8.5	11.7 ± 4.9	
Mice	17 ± 11.4	14.3 ± 7.5	

Table 1.1: AIS start position Δ and length L in different species and neuron types (continued). [1] AS = axo-somatic. [2] CF = characteristic frequency. [3] MNTB = medial nucleus trapezoid body. [4] SNc = substantia nigra pars compacta.

In the NL, the site of spike initiation is located at a position that depends on the characteristic frequency of the neuron (Kuba et al., 2006). The AIS is shorter and more distally located from the soma with increasing tuning frequency (table 1.1). Accordingly, high CF neurons have a distal and short AIS, associated with many short unbranched dendrites and a smaller soma. Low CF neurons have a long and proximal AIS, associated with long branched dendrites and a bigger soma. Patch-clamp recordings revealed that in high and middle CF neurons, there is no cell-attached Na^+ current at the soma, suggesting that Na_v channels are absent from the cell body (Kuba et al., 2006). In low CF neurons, there is a small cell-attached Na^+ current at the soma. In whole-cell recording condition, the Na^+ current is roughly 5 times larger in low-CF neurons than in high or middle CF neurons, suggesting a difference in Na_v conductance density (Kuba et al., 2006).

Interestingly, at early developmental stage (before hearing onset at embryonic day (E) 12), the distribution of Na_v channels at the AIS is the same independently of the tonotopic region. At E15, the AIS shape begins to differ between tonotopic regions. The AIS shortens importantly in high-CF neurons, moderately in middle-CF neurons and almost not in low-CF neurons, forming the AIS length tonotopic gradient of mature animals. At the same time, the AIS starts to shift distally from the soma: substantially in high-CF neurons, modestly in middle-CF neurons and almost not in low-CF neurons (Kuba et al., 2014). The subtype of Na_v channels changes concomitantly, from $Na_v1.2$ to $Na_v1.6$. In consequence, a negative correlation appears between the AIS length and start position at P3-7 (Kuba et al., 2006) (fig. 1.14 B). AIS development is associated with differences in action potential shape. From E15, the AP threshold and rise time decrease for both high- and low-CF and the spike amplitude increases, as well as the max dV/dt in low-CF region.

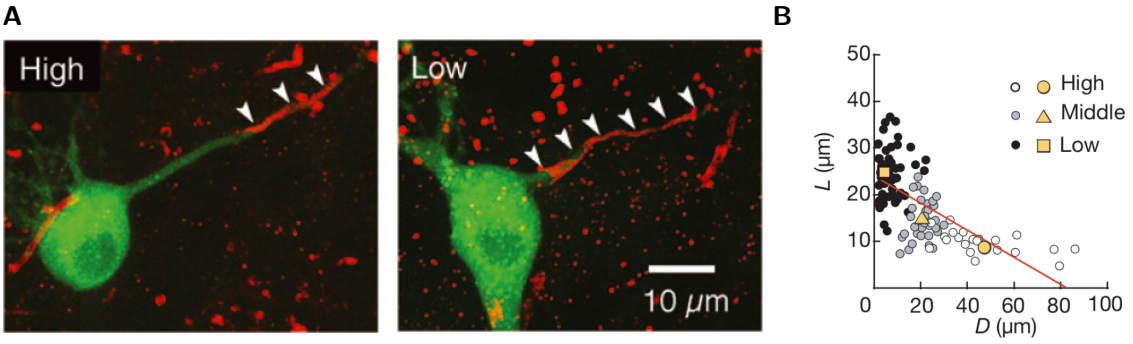

Figure 1.14: AIS geometry in the nucleus laminaris. **A**, High CF neurons have a distal and short AIS (left, white arrowheads) and low CF neurons have a proximal and long AIS (right, white arrowheads) (adapted from Kuba (2012)). **B**, The AIS length L correlates negatively with the soma-AIS distance D in the NL (adapted from Kuba et al. (2006)).

The neurons of the medial nucleus of the trapezoid body (MNTB) in the mice auditory brainstem are also arranged tonotopically, and the morphology of the AIS changes accordingly (Kim et al., 2019). The AIS in high CF neurons is located more distally and is shorter than low CF neurons, although the difference is not as marked as in chicks. This differentiation starts to appear after hearing onset (P12), high CF neurons AIS shorten by a distal shift of the AIS start

position while the AIS of low CF neurons remains roughly unchanged. By P40, the AISs have their final configuration (Kim et al., 2019).

The AIS tonotopic arrangement in auditory systems provides a first impression of how exquisitely the AIS geometry can be organized.

During development

AIS geometry evolves during development in the chicks and mice auditory system. As examined in the following, it is not unusual and rather a common feature across the brain.

In the mouse visual cortex, pyramidal neurons have a longer AIS than interneurons whereas the soma-AIS distance is similar on average (table 1.1). In layer II/III and V pyramidal cells of the visual cortex, AIS development is triphasic. First, it elongates steadily until eye opening (P14), then it shortens rapidly until P28, and finally elongates again to reach its final length around P35 (Gutzmann et al., 2014). Visual deprivation for more than two weeks prevents the AIS compression (Gutzmann et al., 2014).

In retinal ganglion cells, the AIS undergoes a dynamic change of length during development (Schlüter et al., 2019). The AIS is long until eye-opening and then shortens to reach its constant length approximately one week later, from 25 µm to 17 µm on average. In adults, the AIS is located rather distally from the soma. Rearing mice in the dark until adulthood prevents AIS maturation, so that adult animals have a longer AIS, as juvenile mice. The AIS start position is not affected by dark-rearing (Schlüter et al., 2019). Rabbit retinal ganglion cells also have a rather distal AIS, although different subtypes have distinct AIS geometries (Fried et al., 2009).

A similar change in AIS geometry during development has been reported in the whisker-to-barrel system of the mice, in the primary somato-sensory cortex. The AIS of layer II/III and V pyramidal cells elongates progressively until the onset of active whisking behavior, around P12 (Jamann et al., 2020), reaching a maximal value of 30 µm on average. It then shortens and reaches a stable value at adulthood (table 1.1). Two weeks of sensory deprivation by whisker trimming results in AIS lengthening in layer II/III neurons (Jamann et al., 2020). In contrast, one hour in an enriched environment is sufficient to trigger AIS shortening in layer II/III neurons (Jamann et al., 2020).

At the first stage of sensory information processing, AIS morphology is strongly shaped by the incoming inputs. Before the onset of sensory stimulation, the AIS has a canonical morphology, that is later accurately shaped to the neuron function, as beautifully illustrated in the chicks auditory system. Discussing the link between changes in geometry and the neuron's electrical function will be the core of this thesis.

Structural plasticity

As exemplified in the previous section, the AIS is not a static structure, its length and location along the axon can vary on the time scale of hours to days during development. However, the first studies revealing dynamic changes in AIS geometry were performed in adult neurons.

Structural and intrinsic changes

Structural changes in AIS geometry were first reported in 2010, in dissociated excitatory hippocampal neurons (Grubb and Burrone, 2010) and *in vivo* in chicks (Kuba et al., 2010). In the former situation, 2 days of chronic depolarization (from 12 to 14 DIV) with elevated extracellular K^+ concentration or elevated photostimulation shifted the AIS away from the soma, leaving its length unchanged (Grubb and Burrone, 2010). The AIS start position shifted from 3.5 µm to 10.4 µm on average. This change is reversible and not observed in the inhibitory neurons in the same cultures. Distal relocation of the AIS is associated in these neurons with an increase in current threshold and current threshold density and a strongly decreased input resistance at the soma. The later accounts for almost half of the current threshold augmentation (Grubb and Burrone, 2010).

The second seminal study investigated the effect of removing the cochlea on NM neurons, the second order nuclei in the auditory pathway. The cochlea is removed at post-hatch day 1, ten days after hearing onset. Seven days later, the AISs in the deprived side were significantly longer than in the intact side (16.8 ± 0.2 µm vs. 12.1 ± 0.2 µm) whereas the AIS start position did not move. Both the distribution of $Na_v1.6$ channels (there are no $Na_v1.2$ in NM neurons) and ankG are affected. Removing the cochlea later has the same effect, indicating that plasticity happens after development. Interestingly, AIS elongation was important in HF and MF neurons, and less marked in LF neurons, thereby almost annihilating the difference in AIS length due to tonotopy in the MN. Functionally, AIS elongation is associated with a larger Na^+ current coming from the AIS and a lowered voltage and current threshold for AP initiation (Kuba et al., 2010, 2015). It is likely that the longer AIS contains more Na_v channels, increasing the AIS Na^+ current and therefore decreasing the AP initiation threshold. This structural plasticity occurs in parallel to a switch in ion channels expressed at the AIS. In control NM neurons, it contains a large amount of $K_v1.1$ channels at its distal end and a diffuse distribution of $K_v7.2$ along the AIS (Kuba et al., 2015). In deprived neurons, AIS elongation is accompanied by a strong reduction in $K_v1.1$, and a prominent increase of $K_v7.2$ expression (Kuba et al., 2015). In deprived neurons, blocking $K_v7.2$ channels lowers the voltage threshold for AP initiation, indicating that they stabilize excitability (Kuba et al., 2015), as reported in other neuron types (Kole et al., 2007).

What happens to the third nucleus when the cochlea is removed? We know that in the NL, AIS geometry changes along the tonotopic axis and that the gradient is established progressively after hearing onset. Removing afferent activity to NL neurons before hearing onset results in a strong AIS elongation in high CF neurons (from 12.5 ± 0.6 µm to 21.5 ± 0.8 µm) and a moderate AIS elongation in low CF neurons (from 24.3 ± 1.1 µm to $27.6 \pm$

1 µm), reducing the difference in AIS length due to tonotopy. The AIS start position remains unchanged, so the elongation is explained by a distal shift of the AIS end position (Kuba et al., 2014).

In addition to these long-term changes in AIS geometry, rapid variations have subsequently been reported. Focusing on dissociated dentate gyrus granule cells[5], Evans and colleagues have shown that 3 hours of patterned optogenetic stimulation or 3 hours of chronic depolarization is sufficient to shorten the AIS (from 19.2 $\pm$ 0.7 µm to 15.7 $\pm$ 0.6 µm) (Evans et al., 2015). It is driven by a large proximal shift in AIS end position and a smaller proximal shift in AIS start position. As for the long-term change in AIS position, it is not observed in inhibitory neurons. Assuming a fixed Na_v channels density, AIS shortening is expected to reduce excitability, since it decreases the total Na_v conductance[6]. Surprisingly, WC recordings in control and high K^+ conditions show no difference in single spike features nor in firing rates (Evans et al., 2015). Indeed, depolarization activates the phosphatase calcineurin that in turn dephosphorylate $Na_v1.2$ channels at the AIS, therefore increasing their functional density. Decreasing the activity of calcineurin and boosting the activity of the kinase PKA after the 3 hours of depolarization keeps the AIS shortened but re-phosphorylates the Na channels. In that condition, the recorded Na^+ current is indeed lower in shortened AIS (Evans et al., 2015). To sum up, rapid AIS shortening is associated with lowered excitability in multiple spike firing but this effect can be offset by the modulation of Na_v channels properties. As in NM neurons, the structural transformation happen in parallel with a change in ionic channel distribution.

AIS plasticity in inhibitory neurons was first investigated in a subpopulation of olfactory bulb (OB) GABAergic interneurons, that are also dopaminergic (Chand et al., 2015). In rats dissociated cultures, within this neuron subpopulation, only 20% have an AIS, that is short and located distally, with high variability (start position: 15.2 $\pm$ 8.5 µm, length: 11.7 $\pm$ 4.9 µm) (Chand et al., 2015). The same trend was reported in mice dissociated cultures (Chand et al., 2015). In both rat and mice OB cultures, one day of chronic depolarization is sufficient to elicit a proximal shift and a moderate elongation of the AIS, caused by a marked proximal shift of the AIS start position towards the soma (6.8 µm on average) and a smaller proximal shift of the AIS end position (4.3 µm on average) (Chand et al., 2015). In mice, no significant changes in AP shape or firing pattern are observed concomitantly with AIS plasticity. It might be due to the high baseline variability in AIS geometry within this population of neurons, or to other parallel intrinsic changes, as in cultured dentate gyrus granule cells.

Blocking ionic current can also trigger AIS plasticity. In CA1 hippocampal neurons *in vitro*, 4 hours of acute blocking of the M-current moves the distribution of Na_v and K_v7 away from the soma, by 3.5 µm on average but on this time scale, the distribution of ankG remains unchanged (Lezmy et al., 2017). In cultured hippocampal neurons, the ankG distribution shifts away from the soma after 2 days of drug exposure (Lezmy et al., 2017). Recording the same cell

[5]In cultured neurons, the axon is not myelinated. The dentate gyrus granule cell axon is unmyelinated in vivo.

[6]A change in Na_v channel density is difficult to assess precisely with immunohistochemistry but no change in fluorescence intensity was reported in this study.

over 3 hours reveals rapid changes in threshold current, RMP and firing rate upon M-current blocking, that go back to normal values after 3h of exposure. It suggests that the ionic channels relocation works to reset electrical properties to baseline values. However, it should be kept in mind that patch-clamping a cell for 3 hours might have a substantial effect on its electrical properties. Na^+ imaging revealed that the Na^+ dynamics associated with spike generation is also affected by M-current inhibition. It elicits a distal relocation of the axonal Na^+ flux associated with AP initiation. This relocation occurs rapidly (30 min to 45 min) after drug application start. The start of the Na^+ flux does not move but its distribution becomes wider, thereby shifting the position of maximal flux away from the soma. The spatial mismatch between maximal Na^+ influx and the AP trigger zone is therefore conserved, because the latter zone also shifts away from the soma after drug application (Lezmy et al., 2017).

The Tau protein is a micro-tubule associated protein able to modify MT stability and that, in neurons, is expressed prominently in the axon (Götz et al., 2019). Upon hyperphosphorylation, Tau proteins dissociate from MT, thereby destabilizing them and possibly the entire AIS cytoskeleton (Sohn et al., 2016). In consequence, the neuron polarization is disrupted and Tau can invade the soma (Sohn et al., 2016). Deficit in Tau protein polarized distribution is an early key marker of neurodegenerative diseases as frontotemporal dementia and Alzheimer's disease (Götz et al., 2019). In a mouse model of Tau pathology, the AIS is located further away from the soma than in wild type mice in CA1 pyramidal neurons, which is associated with decreased firing rate and higher voltage threshold (Hatch et al., 2017). Mimicking Tau hyperphosphorylation in cultured CA1 neurons results in a distal relocation of ankG, Nav1.6 and βIV spectrin, without any change in length (Hatch et al., 2017).

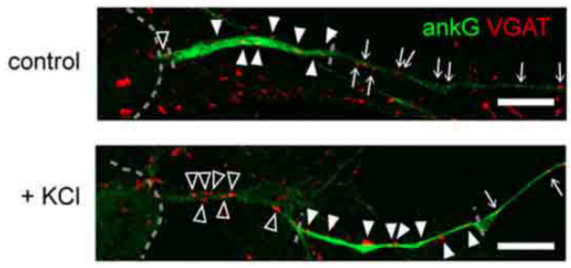

Figure 1.15: Axo-axonic synapses location remains fixed upon AIS plasticity (adapted from Muir and Kittler (2014)). Top, control condition. Axo-axonic synapses (red dots) along (white arrow heads) and beyond the AIS (white arrows, AIS in green). Bottom, increased extracellular K^+ concentration. Axo-axonic synapses are now present before (empty white arrowheads), within (white arrowheads) and beyond (white arrows) the AIS (green). Scale bar, 10 µm.

Finally, what happens to the axo-axonic synapses when the AIS shifts along the axon? In organotypic slices of the hippocampus, optogenetic stimulation of CA1 neurons leads to a distal shift of the AIS (Wefelmeyer et al., 2015). It is accompanied by a reduction in input resistance, an increase in current threshold density and both RMP and voltage threshold are depolarized. Strikingly, the position of AAS along the AIS are not affected. As AAS are also present in the

axon beyond the AIS, the number of synapses within the AIS is importantly modified (Wefelmeyer et al., 2015). Conversely, the number of AAS increases in the segment between the soma and the AIS (Muir and Kittler, 2014; Wefelmeyer et al., 2015) (fig. 1.15), thereby raising GABAergic inputs in this region (Muir and Kittler, 2014; Wefelmeyer et al., 2015). How this multiplied amount of inhibitory synapses between the soma and the AIS influences spike initiation still needs to be investigated.

Mechanisms

Understanding the mechanisms underlying AIS plasticity is an ongoing work that is attracting more and more attention. Parts of the signalling pathway at play have already been deciphered. Long-term AIS relocation and short-term AIS shortening in cultured hippocampal cells is triggered by calcium entry through L-type voltage-gated calcium channels (VGCC) and downstream activation of the phosphatase calcineurin is necessary for depolarization-induced AIS plasticity (Evans et al., 2013, 2015). The activity of calcineurin is in part counteracted by another protein, CDK5, that tends to maintain AIS length (Evans et al., 2015). Surprisingly, L-type VGCC and calcineurin are not at all concentrated at the AIS. L-type VGCC predominantly distribute in the somatodendritic compartment (Evans et al., 2013), suggesting that AIS relocation is triggered in the somatodendritic compartment. The kinase CDK5 has been implied in AIS plasticity in olfactory bulb dopaminergic neurons and in drosophila neurons (Chand et al., 2015; Trunova et al., 2011). Lastly, not surprisingly, the protein kinase CK2 that regulates the interaction between ankG and Na_v and K_v7 channels at the AIS, is necessary for M-current mediated plasticity (Lezmy et al., 2017).

How is the AIS cytoskeleton modified during plasticity? Contractile activity of pMLC has an important role in AIS assembly, so putatively in AIS plasticity too. Upon depolarization with either increased K^+ concentration or optogenetic stimulation, pMLC is lost preferentially and early from the AIS after increased activity (15 min), but MLC did not decrease, indicating that the loss in pMLC comes from dephosphorylation (Berger et al., 2018). Consistently with previous results, calcium chelation and inhibition of VGCC prevented AIS disassembly and pMLC reduction. Stabilizing the actin cytoskeleton blocks the activity-dependent loss of ankG but not that of pMLC, indicating that actin destabilization occurs downstream of pMLC level reduction and is a late-stage event that underlies activity-dependent AIS disassembly (Berger et al., 2018). End-binding (EB) proteins, that link ankG to MTs in the AIS, have recently been shown to play a role in regulating AIS length in pathological conditions (Sohn et al., 2019). A mutation in the gene encoding the MT-associated protein Tau increases the level of EB at the AIS, which shortens the AIS and prevents depolarization-induced AIS shortening (Sohn et al., 2019). Reducing the EB level elongates the AIS and restores plasticity. The mutated Tau colocalizes with EB at the AIS and the mutation enhances Tau's binding affinity to EB. So it might indicate that enhanced Tau-EB binding promotes the recruitment of EB at the AIS, thereby stabilizing even more the ankG-MTs link. It shows that EB has a critical role in regulating AIS length but how it interacts with the calcium pathway is not elucidated yet. In summary, both the acto-myosin rings and the MTs are involved in AIS relocation/lengthening.

An important question that remains to be elucidated is whether, upon AIS relocation, the entire structure shifts along the axon or whether material is removed at one end and added at the other end.

1.3 Resistive coupling theory

In this chapter we are interested in modelling AP initiation in a two-compartment model. We previously considered one-compartment models of spike initiation (section 1.1.3) but they miss the fact that APs are triggered in the distal AIS, a compartment electrically remote from the soma, where spikes are usually recorded.

1.3.1 Spike initiation in a two compartment model: observations

The one-compartment Hodgkin-Huxley model reproduces correctly APs recorded in the squid giant axon (fig. 1.6 B). In sharp contrast with AP recorded in mammalian neurons *in vivo* and *in vitro*, the squid giant axon AP initiates smoothly with the membrane potential (compare fig. 1.6 B with fig. 1.16 B (black arrow)). Indeed, mammalian AP recorded at the soma display a very abrupt increase in membrane potential at spike onset (Naundorf et al., 2006; McCormick et al., 2007), as if Na_v channels would open at once (fig. 1.16B).

In isopotential models of spike initiation, spikes have a smooth onset because Na_v channels open gradually as a function of the membrane potential (Naundorf et al., 2006), with a Boltzmann slope close to 6 mV (Kole et al., 2008) (fig. 1.16A). To explain this discrepancy, Na_v channels have been proposed to cooperate, opening therefore at once (Naundorf et al., 2006). This hypothesis has received a lot of criticism and few support, as recordings of AP at the AIS never reported cooperativity (discussed in Telenczuk et al., 2017) and, importantly, spikes recorded at the AIS initiate smoothly (Kole and Stuart, 2008; Palmer and Stuart, 2006; McCormick et al., 2007) (fig. 1.16 C and fig. 1.11 B). Even more crucial, in the model used by Naundorf and colleagues to support their hypothesis, AP initiate at the soma.

In a multiple compartment HH model, adjusting Na_v channels density and activation properties at the soma and the AIS is sufficient to induce AIS spike initiation and observe both sharp onset at the soma and smooth onset at the AIS (McCormick et al., 2007; Yu et al., 2008). Subsequently, it was proposed that spikes sharpen while propagating actively from the distal AIS to the soma, helped by more Na_v channels opening as the AP travels along the axon (McCormick et al., 2007). It assumes that the portion of axon between the soma and the AIS contains Na_v channels. In this view, sharpening is not a feature of spike initiation, but rather of an electrical signal propagating actively along a cable, which is in contradiction with several lines of evidence (Brette, 2013, 2015). For instance, the IV curve recorded in voltage-clamp at the soma is sharp too (Milescu et al., 2010; Barrett and Crill, 1980) (fig. 1.19). Another major problem of this idea is that, in a cable model, the sharpening occurs on distances larger than the soma-AIS distance, approximately 2 mm in their model (Yu et al., 2008). If the soma is now larger than the AIS, sharpening of the spike onset occurs on shorter distances, comparable to the soma-AIS distance (Yu et al., 2008; Telenczuk et al., 2017). However, even this observation is artefactual

as it comes from an incorrect way to measure sharpness (Telenczuk et al., 2017). Finally, active backpropagation is not necessary to observe sharp initiation at the soma, as initiation is sharp at the soma even in models without Na_v channels in the region between the soma and the AIS (Brette, 2013; Telenczuk et al., 2017). In summary, the cooperativity hypothesis nor the backpropagation hypothesis are satisfactory to explain sharp spike initiation at the soma. A third hypothesis based on the geometry of the spike initiation system was later proposed, the *resistive coupling theory* (Brette, 2013).

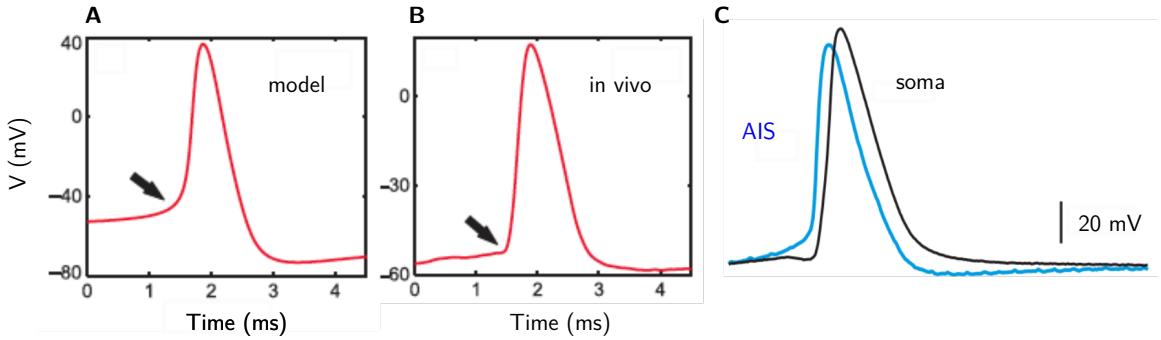

Figure 1.16: Sharpness of spike initiation (**A** and **B** adapted from Naundorf et al. (2006)). **A**, Smooth spike onset (black arrow) in an isopotential neuron model. **B**, Sharp spike onset (black arrow) recorded in current-clamp *in vivo*. **C**, Simultaneous current-clamp recordings at the soma and the AIS. Spike initiation is sharp at the soma (black) and smooth at the AIS (blue) (adapted from Kole and Stuart (2008)).

1.3.2 Resistive coupling theory

The resistive coupling theory (RCT) provides a geometrical explanation for the sharpness of spike initiation, based on the observation that in most neuron types, the soma is considerably larger than the axon (Brette, 2013). For instance, cortical pyramidal cells have a soma of 30 µm diameter and their AIS is 1 µm to 1.5 µm large (Hamada et al., 2016; Höfflin et al., 2017). The small cerebellar granule cells have a soma of 6 µm diameter (Delvendahl et al., 2015) and an AIS of 0.2 µm to 0.3 µm diameter (Wyatt et al., 2005; Perge et al., 2012). In the following we first present the passive response of the spike initiation system (soma-AIS) as explained by RCT, then how spike initiation occurs in the RCT framework and finally address AP backpropagation to the soma.

Passive response of the spike initiation system

We consider a simple neuron model consisting of a big spherical soma and a thin long cylindrical axon, without voltage-dependent ionic channels (fig. 1.17). We are interested in the passive response of this system to a current that enters the proximal axon, because we ultimately aim at describing spike initiation which occurs through Na^+ current entering the AIS. First, as the soma is very big, its membrane potential clamps the membrane potential at the start of the axon. Indeed, most of the time, the membrane potential is roughly the same at the soma and in the proximal axon (Stuart et al., 1997) (fig. 1.17 A), although it can be slightly different in certain neuron types (Hu and Bean, 2018). Second, the input resistance at the site

where the current enters is lower towards the soma than towards the distal axon (Tuckwell, 1988a). The input resistance towards the soma R_{prox} is proportional to the distance between the soma and the injection site (0 µm to 50 µm in most neurons (table 1.1)) while the input resistance towards the distal axon R_{axon} is proportional to the axon space constant, that can be 500 µm in layer 5 pyramidal cells (Kole et al., 2007). Therefore, most of the injected current flows towards the soma that acts as a current sink on the injection site (fig. 1.17 B). In addition, because of its big capacitance, the soma charges much more slowly than the axon, and its response happens at a different time scale than that of the proximal axon. Consequently, a voltage gradient ΔV develops very quickly between the soma and the injection site, equal to the input resistance times the current (fig. 1.17 B). On a short time scale, the time scale of spike initiation, the input resistance is essentially the axial resistance R_a between the soma and the injection site. On a longer time scale, the resistance of the soma should be taken into account. In a cylindrical geometry with constant diameter d and AIS position Δ, $R_a = 4R_i\Delta/\pi d^2$ where R_i is the intracellular resistivity. It follows that when the injection site moves away from the soma, the input resistance at the injection point is larger and the voltage gradient increases. This will make the neuron more excitable when the injection site is further away from the soma because less current is needed to produce a given depolarization (Brette, 2013).

In the resistive coupling regime, spike initiation occurs through a global current loop that encompasses the soma and the AIS (Telenczuk et al., 2017; Brette, 2013). At spike initiation, the large Na^+ current that enters the AIS (current source) flows towards the soma (current sink), leaves the soma as a capacitive current, and returns to the AIS through the extracellular space.

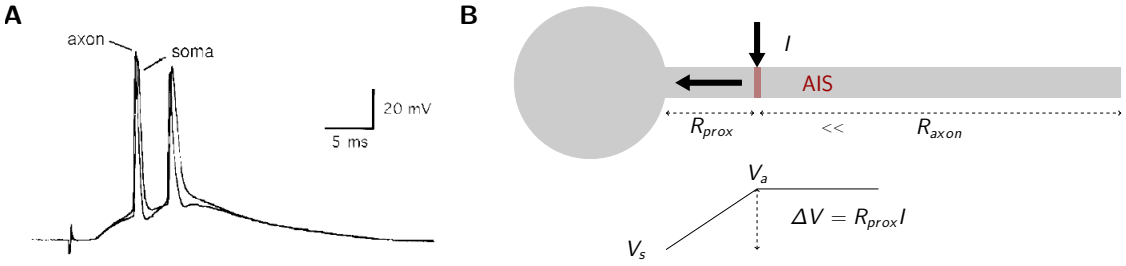

Figure 1.17: Resistive coupling theory. **A**, Simultaneous recording from the soma and proximal axon at 23 µm away from the soma edge (adapted from Stuart et al., 1997). **B**, A current entering the AIS produces a linear voltage gradient between the soma and the injection site. The gradient depends on axial resistance R_a and therefore on the soma-AIS distance.

Spike initiation

The resistive coupling regime is characterized by a fast response at the AIS, that depends on the axial resistance of the region between the soma and the AIS. We focus on the huge Na^+ current that enters the AIS at spike initiation. As the soma acts as a current sink, the Na^+ current has to match the axial current that flows to the soma (fig. 1.18 A, B). The Na^+ current at the AIS $f(V_a)$ is determined by the membrane potential at the initiation site V_a, while the axial current is determined by Ohm's law

$$\frac{V_a - V_s}{R_a} = f(V_a) \tag{1.16}$$

where V_s is the clamped somatic membrane potential. It results that, at any time, the membrane potential at the AIS is determined by the membrane potential at the soma through a non-linear equation. The fixed points of this equation are represented on (fig. 1.18 C), as the intersections between the black lines (axial current for increasing V_s) and the red curve (Na^+ current). At rest, the membrane potential at the soma and the AIS are similar, corresponding to the left region of fig. 1.18 C where there is a single intersection (stable fixed point, fig. 1.18 C full green dots). When the somatic membrane potential increases, three intersections suddenly occur, but the system remains in the stable state, which is the resting state, because the next FP is unstable (fig. 1.18 C, empty green dots). If V_s further increases and reaches a critical value, a unique fixed point exists, corresponding to the spiking situation. The membrane potential at the AIS suddenly jumped to a higher value (fig. 1.18 C). The change in the number (3 to 1) and nature of the fixed points is a bifurcation whose parameter is the somatic membrane potential (fig. 1.18 C half-filled circle). When it changes slightly, the system moves in a very different state. At the bifurcation, there is a loss of voltage control of V_s on V_a. It occurs because the response of the AIS is a lot faster than the response of the soma.

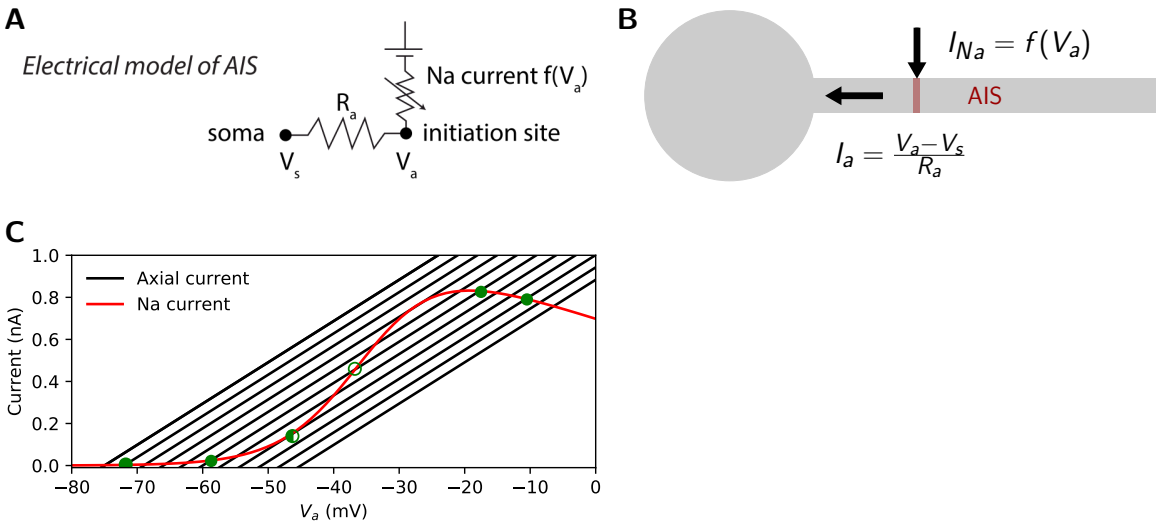

Figure 1.18: Spike initiation in the resistive coupling regime (**A** and **C** adapted from Brette (2013)). **A**, The two-compartment electrical model of the spike initiation system, R_a axial resistance, V_s somatic membrane potential, V_a membrane potential at the AIS. **B**, Current equality at spike initiation: the Na^+ current $f(V_a)$ matches the axial current I_a. **C**, Bifurcation at spike initiation. Axial current (black line) for different V_s (from $-75\,\text{mV}$ to $-45\,\text{mV}$) and Na^+ current (red line) as a function of the axonal membrane potential V_a. The stability of the solutions (green dots, filled:stable, empty: unstable, half-filled: bifurcation) changes with V_s.

In other words, when the somatic membrane potential attains its critical value, Na_v channels at the AIS, that have a lower threshold for activation than somatic Na_v channels, open, producing a huge current at the AIS. The resistive coupling between the two compartments causes a loss of voltage control: the membrane potential at the AIS rises, not clamped by the soma anymore, and the Na^+ current flows to the soma as an axial current. The membrane potential at the soma therefore increases very steeply due to this large current, which corresponds

to first component of a spike recorded at the soma (fig. 1.10). Finally, spike initiation is sharp at the soma because Na_v channels at the AIS open abruptly as a function of the somatic membrane potential, as illustrated by IV curves recorded in voltage-clamp at the soma (fig. 1.19). The AIS membrane potential evolves smoothly, determined by the activation curve of the AIS Na_v channels, this is why spike initiation at the AIS is not sharp.

Excitability

The critical value of the somatic membrane potential above which a spike is triggered at the AIS is the *somatic voltage threshold for spike initiation*. It is the highest value of V_s at which we can clamp the soma without eliciting a spike at the AIS. Crucially, this analysis reveals that it is the membrane potential at the soma that controls AP initiation at the AIS, through the coupling resistance. In this view, the parameter that determines if a neuron is more or less excitable is the somatic threshold for spike initiation at the AIS.

What determines this threshold in a two-compartment model? The threshold equation for an isopotential model (eq. (1.14)) and the preceding explanations suggest that the parameters describing Na_v channels activation as well as the Na_v conductance at the AIS should play a role. To derive a threshold equation for the two-compartment model, we consider a simple theoretical model. The axon is a cylinder voltage-clamped at its left end, corresponding to the soma. Non-inactivating Na_v channels are clustered at a single location in the proximal axon (point AIS). K_v channels are not included in the model. The Na^+ current at the AIS is approximated by an exponential function of the AIS membrane potential (eq. (1.13)). At the bifurcation, the red and black curves on fig. 1.18 are tangent, so differentiating the current equality we have

$$1 = R_a f'(V_a) \tag{1.17}$$

Using again the approximation $E_{Na} - V_a \simeq E_{Na} - V_{1/2}$, eq. (1.17) becomes the threshold equation for spike initiation at the AIS (Brette, 2013)

$$V_t = V_{1/2} - k - k \log \left(R_a g_{Na} \frac{E_{Na} - V_{1/2}}{k} \right) \tag{1.18}$$

Notably, the somatic threshold depends only on parameters describing the AIS Na_v channels (activation curve: $V_{1/2}$, k; conductance: g_{Na}) and on the axial resistance between the soma and the AIS (R_a). The threshold decreases logarithmically with both the Na_v channels conductance and the axial resistance. It predicts that either increasing the Na_v conductance, shifting the AIS away from the soma or reduce AIS diameter should decrease the threshold and thereby make the neuron more excitable.

The threshold equation eq. (1.18) was empirically tested by varying the axon diameter d. The axial resistance R_a scales quadratically with the diameter: $R_a = 4R_i\Delta/\pi d^2$. In cortical layer 5 pyramidal neurons, the proximal axon was pinched with two glass micro-pipettes located at each side of the axon (putatively before the AIS start location), to reduce d and therefore increase the axial resistance (Fekete, 2018). In 7 out of 14 neurons, axon pinching led to reduction in spike threshold, of 4 mV on average. No parallel change in resting membrane

potential or input resistance was observed. Despite the small number of samples, the results of this experiment provide a direct empirical support for the theoretical prediction that increasing the axial resistance between the soma and the AIS hyperpolarizes the threshold for spike initiation (Fekete, 2018).

Recordings at the AIS show that the spike onset at the AIS is higher than at the soma. It might seems counter-intuitive since Na_v channels at the AIS open at a lower voltage than at the soma. In fact what is called the spike onset at the soma corresponds to the onset of the axonal spike that invades the soma. The onset of the somatic spike, underlain by somatic Na_v channels, is much higher and corresponds to the start of the second component of the phase plot (difference: 6 mV to 8 mV, Kole and Stuart (2008)) (fig. 1.10). Blocking the Na_v channels at the AIS with localized TTX[7] puffing and eliciting a spike indeed shows that the threshold for the initiation of the SD spike is higher than the threshold at the AIS (Kole and Stuart, 2008). RCT also predicts that the membrane potential at the AIS at spike initiation, the *axonal threshold* V_t^a is higher than the somatic voltage threshold. Using the currents equality (eq. (1.16)) and the threshold condition (eq. (1.17)), we obtain

$$V_t^a = V_t + k \tag{1.19}$$

The axonal threshold is a few mV higher than the somatic threshold, depending on the value chosen for the Boltzmann slope k. Using $k = 6\,\text{mV}$ matches the experimental observations (Kole and Stuart, 2008).

Incidentally, RCT supports the idea evoked above that spikes are initiated at the distal end of the AIS because it is electrically isolated from the large capacitance of the soma, allowing to a very fast raise in the membrane potential.

Action potential backpropagation

The AIS properties and the axial resistance set the threshold for axonal spike initiation at the soma. The axial current that flows from the AIS to the soma has to be large enough to depolarize the soma up to the threshold for somatic spike initiation. Indeed the somatic membrane potential has to reach the threshold for the opening of the somatic Na_v channels. Experimentally, the axial current at spike initiation corresponds to the large uncontrolled event recorded above a certain threshold in voltage-clamp (peak axial current on fig. 1.19). A distal AIS is advantageous for excitability because it hyperpolarizes the threshold for spike initiation. But how does it influence the amplitude of the transmitted current?

Spikelets

Spikelets are spike-like events (all-or-none) of small amplitude recorded at the soma in various neuron types, that might be due to AP propagation failure (Michalikova et al., 2017; Hu et al., 2009). Although their origin has been debated and can be multiple *in vivo*, recent evidence and computational modelling (Michalikova et al., 2017) show that in most cases

[7] Tetrodotoxin is a toxin that selectively blocks the Na_v channels.

spikelets are axonal spikes passively propagated along the axon, that fail to activate the somatic Na_v channels and therefore to trigger the somatic spike. So the axial current that invades the soma at initiation in the AIS has to be sufficient in order to depolarize the soma to that threshold. In cortical pyramidal cells, if the soma is hyperpolarized and spikes are elicited by current injection at the axon, different responses are observed (Hu et al., 2009). If the soma is sufficiently hyperpolarized, a full AP is recorded at the AIS, while a spikelet is recorded at the soma (Hu et al., 2009) (fig. 1.20). In view of the variability in AIS position, a natural question that emerges is whether it influences backpropagation failure or success.

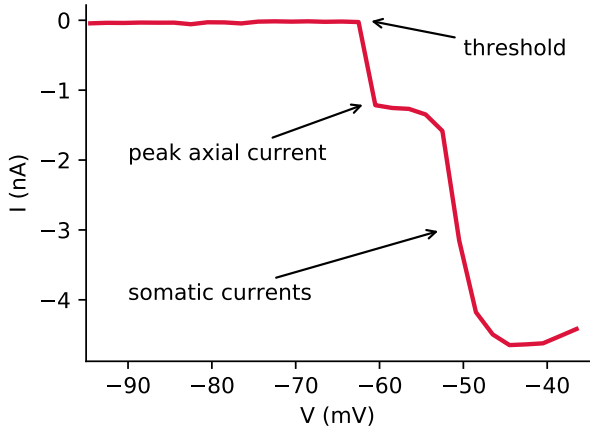

Figure 1.19: Current-voltage relationship in a cerebellar granule neuron. The peak current recorded at every voltage step is represented as a function of the command potential.

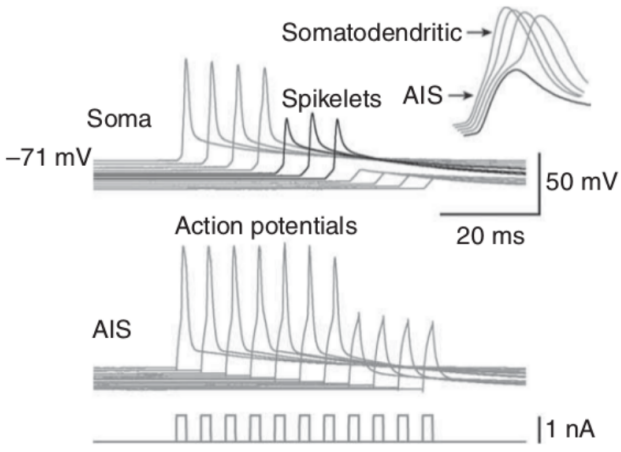

Figure 1.20: Spikelets as backpropagation failure (adapted from Hu et al. (2009)). **Bottom**, Current injected in the axon while the soma is voltage-clamped. **Middle**, Membrane potential recorded at the axon for different somatic holding voltage. **Top**, Membrane potential at the soma. When the soma is hyperpolarized below a critical value, an AP is still elicited at the AIS but spikelets are recorded at the soma. If the soma is further hyperpolarized, axonal current injection is not sufficient to trigger an AP at the AIS.

Peak axonal current (Hamada et al., 2016)

To address the previous question we study the *peak axonal current* I_p, the axial current at the peak of the axonal spike, in a theoretical model. It consists of two cylinders: a large somato-dendritic compartment that represents the soma and proximal dendrites and a thin axonal compartment (fig. 1.21 A). The AIS contains non-inactivating Na_v channels. To start we consider the simplest situation of a point AIS located at Δ. In the RCT regime, the region between the soma and the AIS is purely resistive, so the peak axonal current follows Ohm's law. We further assume that at the peak of the spike, the Na_v channels clamp the AIS membrane potential at their reversal potential (infinite conductance, $V_a = E_{Na}$). It results that if the AIS is located further away from the soma, less current flow towards the soma at spike initiation

$$I_p = \frac{V_a - V_s}{R_a} = \frac{E_{Na} - V_s}{R_a} \propto \frac{1}{\Delta} \tag{1.20}$$

The point AIS situation and assuming $V_a = E_{Na}$ are rather drastic approximations. In reality, there is a finite density of sodium channels in the AIS, that are not all open and therefore do not completely clamp the axonal membrane potential at E_{Na}. Let us consider a more realistic situation of an extended AIS that starts at a distance Δ from the soma and has a length L. It contains a constant density of Na_v channels g_{Na}. To study the axial current flowing to the soma at spike initiation we solve the cable equation (eq. (1.15)) in the AIS under a few approximations. First, in the RCT regime, the time-dependent term can be neglected. Second, we assume that at the peak of the axonal spike, all the Na_v channels are open, so that $f(V_a) = g_{Na}(E_{Na} - V_s)$. Third, the axon diameter is constant. The cable equation reads

$$\frac{1}{r_a}\frac{d^2V}{dx^2} = -g_{Na}(E_{Na} - V) \tag{1.21}$$

and the boundary conditions are 1) the soma is voltage-clamped: $V(0) = V_s$, 2) no current flows towards the distal axon: $V'(\Delta + L) = 0$. As the voltage is linear in the region between the soma and the AIS, the first boundary condition rewrites $V(\Delta) = V_s + V'(\Delta) \cdot \Delta$. Solving the problem, we obtain a formula for peak axonal current

$$I_p = \frac{V'(\Delta)}{r_a} = \frac{1}{r_a}\frac{(E_{Na} - V_s)}{\Delta + \left(\sqrt{\frac{4R_i g_{Na}}{d}}\tanh(\sqrt{\frac{4R_i g_{Na}}{d}}L_{ais})\right)^{-1}} \tag{1.22}$$

that can be simplified because, for realistic AIS geometries,

$$\tanh\left(\sqrt{\frac{4R_i g_{Na}}{d}}L\right) \simeq 1 \tag{1.23}$$

and therefore we obtain a simplified expression

$$I_p \simeq \frac{1}{r_a} \cdot \frac{(E_{Na} - V_s)}{\Delta + \delta} \tag{1.24}$$

with $\delta = \sqrt{\frac{d}{4R_i g_{Na}}}$. The axial current is the slope of the voltage profile along the axon in the region between the soma and the AIS. The effect of the finite Na_v conductance at the AIS is increasing the effective distance between the soma and the AIS of an amount δ, and making the

voltage profile less steep (fig. 1.22). Indeed, the membrane potential in the proximal part of the AIS is lowered by the clamp at the soma. The formula for the peak axonal current (eq. (1.24)) predicts a strong impact of the AIS start position on the current, and no influence of the AIS length. It is well matched by the results of simulations in more complex models (fig. 1.21 C).

Measuring the peak axonal current - AIS start position relationship empirically would require to record the axial current at the soma in voltage-clamp. However, in most neurons, the axial current at spike initiation can be a few tens of nA, which poses several problems. First, in single-electrode voltage-clamp, recording large currents prevents successful clamp. Second, typical patch-clamp amplifiers are not able to record large currents (Molecular Devices, 2008). For these reasons, most supra-threshold voltage-clamp recordings at the soma are performed with the application of a small dose of TTX (Milescu et al., 2010), even in very small cells as cerebellar granule cells (Goldfarb et al., 2007).

Soma size - AIS geometry relationship (Hamada et al., 2016)

The peak axonal current invading the soma at spike initiation then leaves as a capacitive current. At that time, other currents are negligible compared to the large peak axonal current. In consequence, mainly the latter determines the speed of the somatic AP

$$C\frac{dV_s}{dt} = I_p \tag{1.25}$$

The capacitance C has to be understood as the effective capacitance on the time scale of spike initiation. The peak axonal current is larger when the AIS is proximal (eq. (1.24)). Consequently, the AP speed at the peak of the axonal spike, the initial speed[8], should depend on the AIS start position. The closest the AIS, the faster the AP at the peak of the axonal spike. As the derivative of V_s at the peak of the axonal spike is easier to measure than the peak axonal current, eq. (1.25) provides an indirect verification of the relationship between the peak axonal current and the AIS start position. Assuming that C is roughly conserved across a neuron population, we would expect that neurons with a distal AIS have a slower initial speed (fig. 1.21 C).

However, in thick tufted layer 5 pyramidal neurons, the initial speed is independent of the AIS start postion. One third of this neuron population has its axon originating from a basal dendrite, rather than from the soma. Axo-dendritic neurons have a thinner apical dendrite, a smaller soma and a longer soma-AIS distance. Unexpectedly, the AP initial speed is similar across neurons. Theoretically, if we assume that the initial speed is conserved, the peak axonal current has to scale with the capacitance (eq. (1.25)). Thick-tufted pyramidal neurons have a big apical dendrite and the axonal current is transient, thus we assume that the effective capacitance corresponds to that of the apical dendrite, which is modelled as a cylinder (fig. 1.21 A). The capacitance of a cylinder scales with its surface. It results that the peak axonal current is larger if the apical dendrite is bigger

$$\left.\frac{dV_s}{dt}\right|_{initial} = \frac{I_p}{C} \Rightarrow I_p \sim C \sim \text{SD surface} \tag{1.26}$$

[8]It corresponds to dV/dt at the first plateau of a biphasic phase plot (fig. 1.10 B bottom, black arrow).

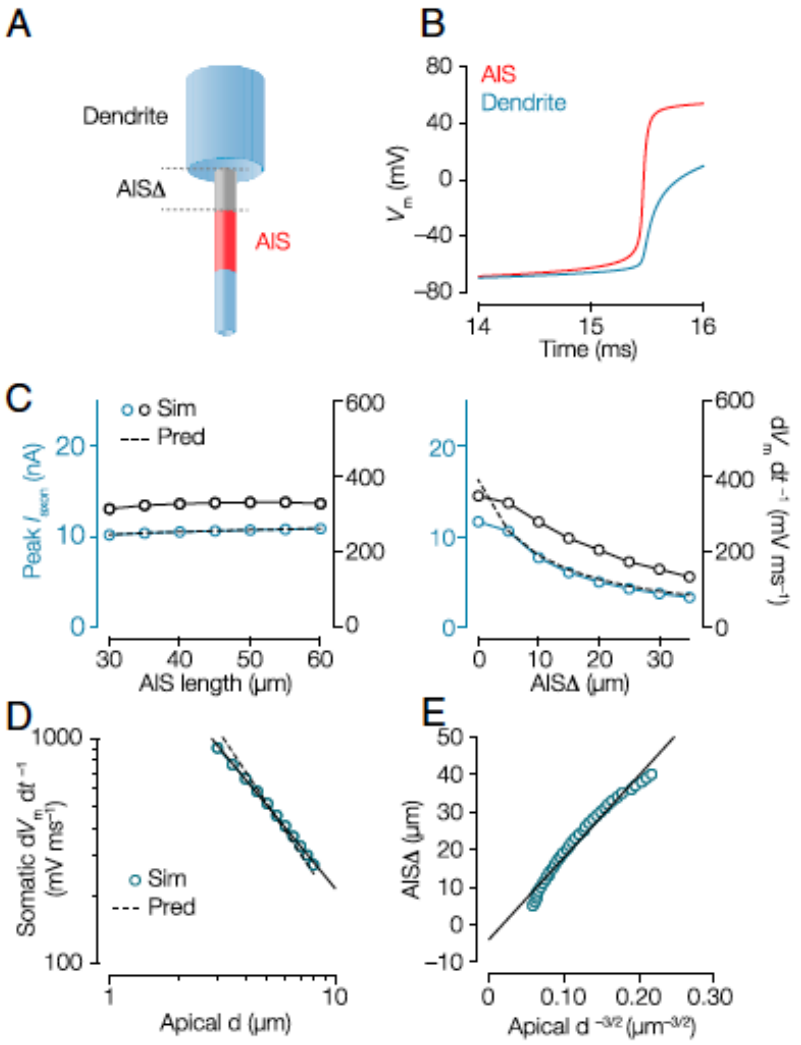

Figure 1.21: Numerical simulations in a two-cylinder model of a thick-tufted pyramidal cell (adapted from Hamada et al. (2016)). **A**, The large cylinder represents the soma and the proximal dendrites, the somato-dendritic (SD) compartment, and has a capacitance C. The thin cylinder represents the axon. The AIS starts at a distance Δ from the soma and has a length L. **B**, Membrane potential at the AIS (red) and at the soma (blue, the interface between the two cylinders). As Na_v channels inactivation and K_v channels are not included in the model, repolarization is lacking. **C**, Initial speed (black) and peak axonal current (blue) in simulations of a simple spike initiation model and as predicted by the theory (dashed black). Left, the peak axonal current is not influenced by the AIS length. Right, the AIS start position strongly reduces the peak axonal current. **D**, Initial speed plotted as a function of the apical dendrite diameter in log-log scale (blue circles). The relationship is plotted with a power law function with exponential -1.22 (black line) and compared with the theoretical prediction with exponent -1.5 (dashed line). **E**, AIS start position is adjusted to obtain a fixed value of the initial speed for apical dendrite diameters between 2 µm to 8 µm. AIS start position is plotted as a function of $d^{-3/2}$ and the line represents the linear regression.

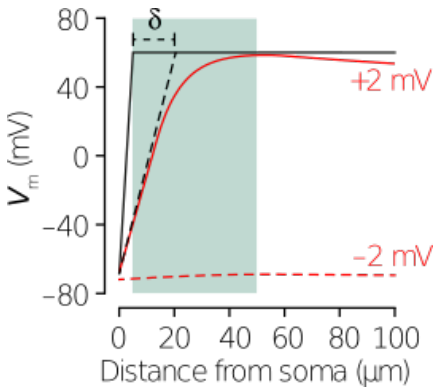

Figure 1.22: Effect of finite Na_v conductance density at the AIS in a simple model of spike initiation (adapted from Hamada et al. (2016)). Voltage traces along the axon when the soma is voltage-clamped 2 mV below (red dashed line) and above (red line) the AP threshold. The black line is the theoretical voltage profile obtained if the AIS Na_v channels clamp the AIS membrane potential at E_{Na}. The difference in axial current between this profile and the simulation is equivalent to shifting Δ by a few micrometers δ.

Finally, as a larger current requires a closer AIS (eq. (1.24)), the AIS start position correlates inversely with the apical dendrite diameter. The detailed peak axonal current formula (eq. (1.24)) allows to predict more precisely the relationship in eq. (1.26). In particular, the AIS start position scales inversely with the apical dendrite diameter raised to the $3/2$

$$\Delta \simeq K d_{SD}^{-3/2} - \delta \tag{1.27}$$

where K is a constant term. We indeed observed that the position of the AIS covaries with the diameter of the apical dendrites in thick tufted pyramidal cells (fig. 1.23). Moreover, simulations in the more complex model shows that the covariation between the apical dendrite diameter and the AIS start position is sufficient to normalize the initial AP speed (fig. 1.21 D and E). Varying the apical dendrite diameter and tuning the AIS start position in order to fix the initial speed results in a relationship that closely matches the theoretical prediction (fig. 1.21 D and E). It suggests that in this neuron type the AIS start position matches the geometry of the SD compartment in order to ensure enough current to activate the Na_v channels at the soma and regenerate the spike. Spikes regeneration and back-propagation in the dendrites is observed in many neuron types and has crucial functions (Stuart et al., 1997). It provides a internal feedback mechanism that enables AIS-dendrites communication. Moreover, AP back-propagation could serve as a gating mechanism for dendritic processes. For instance, it plays an important role in long-term potentiation in CA1 pyramidal neurons (Magee and Johnston, 1997). Finally, it may help coincidence detection.

Other examples of covariation of soma-AIS geometry

The literature provides additional examples for both the idea that the AIS geometry is tuned to normalize the AP at the soma and more generally that it matches the geometry of the soma and the proximal dendrites.

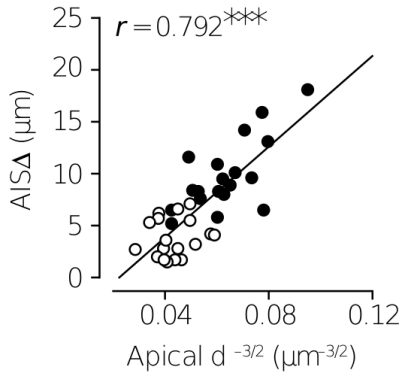

Figure 1.23: The AIS starts position scales linearly with the apical dendrite diameter raised to the -3/2 in tick-tufted layer 5 pyramidal neurons (adapted from Hamada et al. (2016)).

In the NL, neurons are tuned to a specific frequency of sounds. They are arranged tonotopically depending on their tuning frequency, high, middle or low. The AIS of high CF neurons is short and located far from the soma, while the AIS of low CF neurons is longer and located close to the soma. But early during development, before hearing onset, the AIS has the same position and extent in the three neuron types (Kuba et al., 2014). Later the AIS shortens/moves distally depending on the tonotopic region. Interestingly, in high-CF neurons, the distal shift and shortening of the AIS is associated with a decrease of the capacitance measured from patch-clamp recordings (Kuba et al., 2014). This effective capacitance is exactly the parameter that we considered in our theoretical development. The observation that the AIS shifts away from the soma while the capacitance decreases supports the idea that the AIS and the SD geometry could covariate.

A similar relationship was reported in dentate granule cells: the capacitance of the soma-dendrites correlates with the AIS length (Evans et al., 2015). In layer 5 pyramidal neurons, a bigger soma also seems to be associated with a longer AIS (Battefeld et al., 2014).

1.4 State of the art and objectives of the thesis

This thesis focuses on understanding the relationship between AIS geometry and neurons electrical properties, such as excitability or spike transmission to the soma. Since the first works on AIS plasticity, a number of experimental and numerical studies tackled this problem, but, to date, no clear picture emerged. Investigating the relationship AIS geometry and neurons electrical functions experimentally and numerically is difficult for several reasons.

Empirically, the different preparations, conditions and measures of excitability make the comparison between different studies uneasy. The most studied electrical property in this literature is excitability, or how the threshold for spike initiation changes with AIS plasticity. AIS distal shift in cultured hippocampal neurons is accompanied by an increase in the current threshold density, in parallel with a decrease in input resistance, which accounts for roughly one third of the change in current threshold (Grubb and Burrone, 2010). The short-term AIS shortening in dentate granule cells is accompanied by a non-significant decrease in the thresh-

old and the latter correlates inversely with the AIS length (Evans et al., 2015). AIS elongation in NL neurons is associated with a 4 mV decrease in voltage threshold, but whether this change comes from variations in geometry itself or from an increase in total Na_v conductance[9] is not known (Kuba et al., 2010). The large proximal shift accompanied by a moderate elongation in the dopaminergic neurons of the olfactory bulb is not associated with any change in voltage threshold (Chand et al., 2015). The threshold equation (eq. (1.18)) for a point AIS predicts that the proximal shift should depolarize the threshold, while the elongation[10] should decrease it. The absence of threshold variation could be explained by a compensatory effect. In the NL neurons during development, high-frequency neurons undergo a large distal shift and an important AIS shortening, while the AIS of low frequency neurons slightly shift proximally and shorten moderately. Accordingly, we can compare their electrical properties at different stages of development, assuming that the eventual changes in channels distribution are the same in the high and low CF (Kuba et al., 2014). Interestingly, at every developmental stage, the somatic threshold is on average always higher in low frequency neurons than in high frequency neurons (E15: low: -28.5 mV, high: -30.2 mV; P3-7: low: -41.2 mV, high: -44.5 mV) (Kuba et al., 2014). According to the threshold equation, it is consistent with more distal AIS in high frequency neurons.

To sum up, having a clear picture of the effect of AIS plasticity on electrical properties is not straightforward for several reasons. First, different measures of excitability are used: current density (Grubb and Burrone, 2010; Kuba et al., 2010), voltage threshold (Kuba et al., 2010, 2014; Chand et al., 2015) or current density threshold (Grubb and Burrone, 2010). However, RCT predicts that the measure of excitability that appropriately captures the AIS properties is the somatic voltage threshold for spike initiation. More support for this assumption will be provided in the thesis. Second, intrinsic changes occur in parallel to AIS plasticity. The functional density of Na_v channels at the AIS can be altered in the conditions that trigger plasticity (Evans et al., 2015), the subtype of K_v channels at the AIS can change (Kuba et al., 2015) as well as the input resistance at the soma (Grubb and Burrone, 2010; Kuba et al., 2014) or the input capacitance at the soma (Kuba et al., 2014). Putatively, many more intrinsic changes can occur that have not been identified yet.

Numerically, a few studies have investigated the effect of AIS shift on diverse electrical functions. For instance, one study has shown that in small neurons that have few dendrites, shifting the AIS away from the soma decreases excitability (rheobase current), whereas the opposite is reported in large neurons that have many dendrites (Gulledge and Bravo, 2016). RCT is based on the idea that the soma is much larger than the AIS and predicts that shifting the AIS away from the soma increases excitability, so which regime is physiological still needs to be determined. In another model, the way the current threshold changes with the AIS position also depends on the ionic channels included at the AIS (Lezmy et al., 2017). With only Na_v channels at the AIS, the threshold decreases with more distal location. If K_v7 channels are added, the opposite is reported (Lezmy et al., 2017). In summary, the results of the simulations seem to de-

[9] Assuming that the Na_v channels density remains constant.

[10] Increase in total Na_v conductance, assuming that the Na_v conductance density remains constant.

pend on the model itself, which indicates complex non-linear interactions between parameters.

A theoretical description of the relationships between AIS geometry and electrical properties could help understand them. Until now, the theory of excitability including spike initiation at the AIS exists for a point AIS that contains only non-inactivating Na_v channels (Brette, 2013). The effect of AIS length on excitability is not described yet, nor the effect of K_v channels at the AIS or Na_v inactivation[11]. The AIS accumulates axo-axonic synapses and their impact on spike initiation has not been investigated theoretically either. **The first objective of this thesis is to include the AIS extent, Na_v inactivation and K_v channels within a theory of excitability with an AIS**.

The second electrical property that was mentioned previously is AP backpropagation to the soma and it has been described theoretically in an extended AIS (Hamada et al., 2016). Surprisingly, AP backpropagation is not examined in plasticity studies. The inverse relationship between AIS start position and peak axonal current has been indirectly tested empirically but lacks a direct proof. To our knowledge, no one has, in the same neuron, labelled the AIS and recorded the axial current in voltage-clamp without pharmacologically reducing the Na^+ current at the AIS (Milescu et al., 2010; Goldfarb et al., 2007). A major difficulty for recording the axial current with single electrode voltage-clamp arises from the large current amplitude that hinders proper clamp. For instance, the axial current coming from the AIS recorded with two-electrode voltage-clamp in cat motoneurons (Barrett and Crill, 1980) ranges from 30 nA to 80 nA. In the large pyramidal cells, postulating $R_i = 100\,\mathrm{M\Omega}$ and using $d = 1.5\,\mu\mathrm{m}$, the axial resistance per unit length is $r_a = 0.57\,\mathrm{M\Omega\,\mu m^{-1}}$. Assuming that at the peak of the axonal spike, $\Delta V = 100\,\mathrm{mV}$ and that the AIS start 5 µm away from the soma, eq. (1.20) predicts that the axial current is roughly 35 nA. **The second objective of this thesis is to test empirically the inverse relationship between the peak axonal current and the AIS start position in small neurons.**

In thick-tufted layer 5 pyramidal cells, AIS start position matches the apical dendrite size in order to normalize the shape of the axonal spike invading the soma (Hamada et al., 2016). Could such a relationship be observed in other neuron types? If not, is the AIS geometry tuned to preserve another electrical function? For instance, in the NL neurons, the spike is not regenerated at the soma, so it is unlikely that the AIS geometry is tuned to preserve the somatic spike. **The third objective of this thesis is to investigate other geometrical relationships that preserve an electrical function.**

[11] Although the two latter have briefly been addressed in (Brette, 2013).

2 Theoretical relation between axon initial segment geometry and excitability

This work was published exactly as it is reported here in Elife in March 2020 (Goethals and Brette, 2020).

2.1 Abstract

In most vertebrate neurons, action potentials are triggered at the distal end of the axon initial segment (AIS). Both position and length of the AIS vary across and within neuron types, with activity, development and pathology. What is the impact of AIS geometry on excitability? Direct empirical assessment has proven difficult because of the many potential confounding factors. Here we carried a principled theoretical analysis to answer this question. We provide a simple formula relating AIS geometry and sodium conductance density to the somatic voltage threshold. A distal shift of the AIS normally produces a (modest) increase in excitability, but we explain how this pattern can reverse if a hyperpolarizing current is present at the AIS, due to resistive coupling with the soma. This work provides a theoretical tool to assess the significance of structural AIS plasticity for electrical function.

2.2 Introduction

Historically, the theory of neural excitability was developed on the space-clamped giant squid axon (Hodgkin and Huxley, 1952b), which stems from a syncytium (many cells merging their axons into a giant one) (Young, 1936). Spike initiation occurs in a different configuration in vertebrate neurons: spikes generally initiate in the axon initial segment (AIS), a small structure next to the soma (Bender and Trussell, 2012). Although this fact has been known for a long time (Coombs et al., 1957), it has been generally neglected in theory (Koch, 2004; Tuckwell, 1988b). Recently, its potential functional significance has been emphasized by a number of studies showing that both the position and length of the AIS can vary not only across cells (Hamada et al., 2016; Höfflin et al., 2017; Kuba et al., 2006), but also with activity (Grubb and Burrone, 2010; Jamann et al., 2020). These observations raise the possibility that AIS movements could be involved in the regulation of excitability.

Variations of AIS geometry indeed co-occur with changes in excitability, but also with many other factors (Kole and Brette, 2018), such as changes in input resistance (Grubb and Burrone, 2010; Hatch et al., 2017; Lezmy et al., 2017; Wefelmeyer et al., 2015), phosphorylation of voltage-gated sodium (Na_v) channels (Evans et al., 2015), redistribution of voltage-gated

potassium (K_v) channels (Kuba et al., 2015), or changes in cell capacitance (Kuba et al., 2014). In some studies, distal displacement of the AIS is associated with decreased excitability (Grubb and Burrone, 2010; Hatch et al., 2017; Lezmy et al., 2017; Wefelmeyer et al., 2015). In others, neurons with more distal AIS have an identical (Thome et al., 2014) or slightly hyperpolarized threshold (Hamada et al., 2016). Thus, it is challenging to experimentally isolate the specific contribution of AIS geometry to excitability changes.

Modeling studies have also produced mixed results. Theoretical work proposed that increased electrical isolation of the AIS from the large soma should result in increased excitability (Baranauskas et al., 2013; Brette, 2013; Telenczuk et al., 2017). However, several numerical studies have reported decreased excitability when the AIS is moved distally, depending on cell morphology (Gulledge and Bravo, 2016) or on the expression of K_v channels in the AIS (Lezmy et al., 2017). These findings indicate that the relation between AIS position and excitability is highly nonlinear, since even the direction of change depends on model parameters.

Finally, differences in excitability have been reported using various measures: rheobase, current density threshold or voltage threshold at the soma. It has also been argued that a more relevant quantity is the axonal threshold, since spikes initiate in the AIS (Yu et al., 2008). Thus, it is unclear how excitability should be characterized in order to capture the contribution of AIS geometry.

Here we develop a principled theoretical analysis to address these issues and disentangle the different factors relating AIS geometry and excitability. In the first part, we examine the relation between cell geometry and passive properties of the soma-AIS system. When the axon is small compared to the somatodendritic compartment, an axonal current produces a larger local depolarization when it is applied further from the soma, while the converse holds when the axon is large. We show with neuroanatomical and electrophysiological data that the physiological situation is the former one. In the second part, we show that excitability changes caused by changes in the AIS are captured by the somatic voltage threshold (and not, perhaps counter-intuitively, by the AIS threshold). In the third part, we theoretically analyze the excitability of a spatially extended AIS with sodium channels, and in the fourth part we consider the impact of non-sodium channels of the AIS (for example K_v7 channels). From this analysis, we derive a parsimonious mathematical expression for threshold variations as a function of AIS geometry, Na_v conductance density and non-sodium current at the AIS. We find that, when the AIS is moved away from the soma, the cell becomes slightly more excitable, unless a strong hyperpolarizing current is present at the AIS. In the fourth part, we discuss the role of axon morphology, and finally in the fifth part we examine the relation with experimental observations.

2.3 Results

2.3.1 Passive properties

At spike initiation, a Na^+ current first enters the AIS, producing a local depolarization. How does this depolarization vary with the position of the injection site? As several studies have pointed out, the answer depends on the relative sizes of the soma (or somatodendritic compartment) and axon (Brette, 2013; Eyal et al., 2014; Michalikova et al., 2017; Telenczuk et al., 2017). In the following, we consider a current passing through the membrane of a passive cylindrical axon attached to the cell body, and we analyse two extreme cases: a very small soma, and a very large soma. We then show that at the time scale of spike initiation, the latter case approximates the physiological situation in many neuron types.

Small soma, or sealed end condition

We start with the theoretical case of a soma and axon of the same size, meaning that the neuron is simply a cylinder. In cable theory, this is called the "sealed end condition": one end of the axon is sealed and no current passes through it (Tuckwell, 1988a). A current is injected at a distance x from the soma, in an axon of space constant λ, typically about 500 µm in cortical pyramidal cells (Kole et al., 2007). The ratio between local depolarization and current is by definition the *input resistance* R. How does the input resistance vary with x? Part of the current flows towards the soma (proximal side), and the rest flows towards the distal axon. Thus, the input resistance decomposes into $R(x)^{-1} = R_{proximal}^{-1} + R_{distal}^{-1}$ (for a long axon only the proximal resistance varies with x). The proximal segment is highly resistive because its end is sealed. Specifically, if x is small ($x << \lambda$), which is the physiological situation when a current is injected at the distance of the AIS, we have $R_{proximal}/R_{distal} \approx \lambda/x$, a large number (see Methods). This means that the current flows mostly towards the distal axon (as seen in the uniform voltage response between soma and injection site, fig. 2.1 A). In addition, the input resistance is approximately the distal resistance, and therefore the position of the injection site has little effect on the electrical response. More precisely, we can calculate that $R(x) \approx r_a(\lambda - x)$, where r_a is axial resistance per unit length (fig. 2.1 B). Thus, moving the AIS away from the soma should make the cell slightly less excitable. This is consistent with the findings of Gulledge and Bravo (2016), who observed numerically that when the somatodendritic compartment is small, the neuron is most excitable when the AIS is next to the soma.

Large soma, or killed end condition

Suppose now that the somatodendritic compartment is so large that the axial current has negligible effect on its potential. This is the "killed end" condition (as if the membrane were open) (see Methods). In this case, when $x << \lambda$, $R_{proximal}(x) \approx r_a x$, which means that only the axial resistive component is significant. We then have $R_{proximal}/R_{distal} \approx x/\lambda$, a small number (the exact inverse of the sealed end condition). Thus, current flows primarily towards the soma and $R(x) \approx R_{proximal}(x)$. We express this fact by stating that the soma is a *current sink*. This is illustrated on fig. 2.1 C with a thin axon (diameter 1 µm) attached to a large spherical soma (100 µm). The current I flowing towards the soma produces a linear depolarization between

the soma and the injection site, with a total voltage difference $\Delta V = r_a x I$. It follows that the input resistance increases with the distance of the injection site, which would tend to make the cell more excitable when the AIS is moved away from the soma, since less Na^+ current is then required to produce the same depolarization.

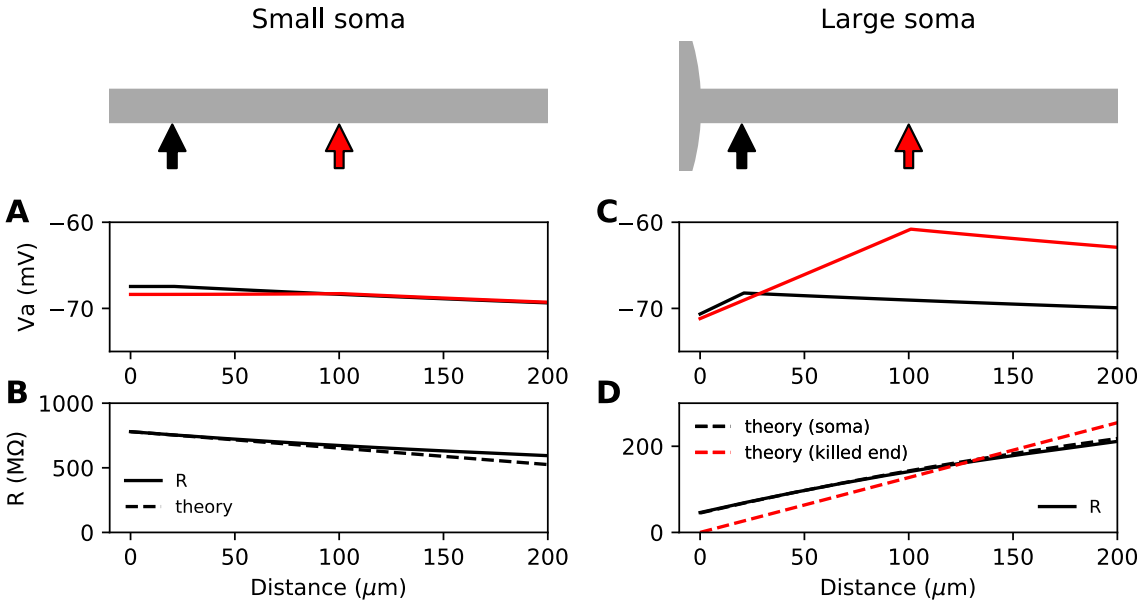

Figure 2.1: Steady-state passive response of the axon ($r_a = 1.3\,\mathrm{M\Omega\,\mu m^{-1}}$, $\lambda = 612\,\mu\mathrm{m}$, $E_L = -75\,\mathrm{mV}$). **A, B**: with a very small soma. **C, D**: with a large soma. **A**, Voltage response along the axon for a 10 pA current injected at 20 µm (black) and at 100 µm (red). **B**, Input resistance as a function of distance, as numerically measured (solid) and according to the simplified theoretical formula ($R(x) \approx r_a(\lambda - x)$, dashed). **C**, Same as A for a large soma (diameter: 100 µm, current: 100 pA). **D**, Same as B for a large soma, with the simplified theoretical prediction for the killed end condition ($R(x) \approx r_a x$, dashed red) and the full theoretical prediction for a finite soma ($R^{-1} = (r_a x + R_{soma})^{-1} + (r_a \lambda)^{-1}$, dashed black; $R_{soma} = 47.7\,\mathrm{M\Omega}$).

This simplified formula ($R_a(x) = r_a x$) differs from the actual input resistance in two ways, as illustrated in fig. 2.1 D. First, some current flows towards the distal side, which becomes substantial at long distances from the soma. Second, with a finitely large soma instead of a killed end, the current also charges the soma, which makes the input resistance increase approximately by the somatic membrane resistance R_{soma}. However, this difference holds for the stationary response. On a short time scale, the somatic depolarization is negligible because the soma charges much more slowly than the axon. This is illustrated in fig. 2.2 A, where a current pulse is injected at the axon and measured at the injection site (red) and at the soma (black). The difference between the two responses, which is the voltage gradient between the soma and the injection site, essentially follows Ohm's law: $\Delta V = R_a I$ (fig. 2.2 B), where $R_a = r_a x$ is the *axial resistance* of the axon between soma and injection site (thus, $R_{proximal} \approx R_a + R_m$). Since on a short time scale the soma is not substantially depolarized, the local depolarization mainly reflects the ohmic voltage gradient across the proximal axon. In fig. 2.2 C, we show the input resistance at time $t = 300\,\mu\mathrm{s}$, $(V_{axon}(t = 300\,\mu\mathrm{s}) - V_0)/I$, as a function of distance x (red): it is essentially the same as $\Delta V(t = 300\,\mu\mathrm{s})/I$, because the somatic

response $(V_{soma}(t = 300\,\mu s) - V_0)/I$ is negligible (black). This plot shows quantitatively that the axon indeed charges faster than the soma, for a broad range of distances of the axonal stimulation site.

To summarize, the case with a large soma is characterized by two key properties: 1) a current injected at the axon produces a resistive voltage gradient between the soma and injection site, proportional to the axial resistance R_a of that piece of axon; 2) the axonal site charges much faster than the soma. We call this regime the resistive coupling regime (Brette, 2013; Kole and Brette, 2018; Telenczuk et al., 2017).

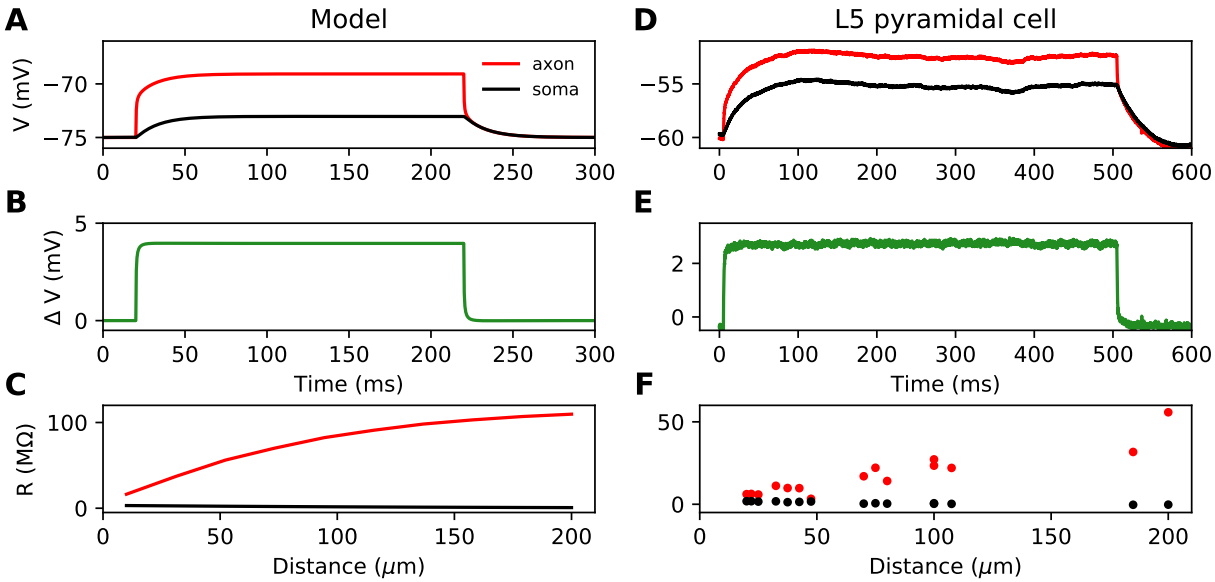

Figure 2.2: Time scale of responses to axonal current injection in a model with large soma (**A-C**) and in layer 5 pyramidal neurons (**D-F**). **A, D**, Voltage response at the axonal injection site 75 µm away from the soma (red) and at the soma (black). **B, E**, Difference between the two responses. **C, F**, Input resistance measured 300 µs after the start of current injection as a function of the distance of the injection site (red), compared to the resistance obtained from the somatic voltage response at the same time (black).

Cortical cells

Which regime applies to neurons? Clearly, the soma of neurons is smaller than in the simulations shown in fig. 2.2 A-C, but the axonal current must also charge the capacitance of the proximal dendrites (thus we call the compartment connected to the axon the somatodendritic compartment). We start by examining experimental recordings from layer 5 cortical pyramidal neurons, where a current pulse is injected in the axon and simultaneously recorded at the soma (Hu and Bean, 2019). These neurons have a soma of about 30 µm diameter attached to a large apical dendrite and an AIS of about 1 µm to 1.5 µm diameter (Hamada et al., 2016; Höfflin et al., 2017) – note that these are optical measurements, which have limited precision. Strictly speaking, the experimental situation is not exactly the same as the physiological situation

because currents are injected in axonal blebs, and therefore the resistance of the distal axon is replaced by the resistance of the bleb. However, recordings of action potentials in intact AIS appear very similar to recordings in blebs (compare Yu et al. (2008) with Kole et al. (2008)).

Figure 2.2 D shows the response to a current pulse injected at 75 µm away from the soma, in the soma and at the axonal injection site. As in the theoretical case described above, a voltage gradient develops very quickly between the soma and injection site (fig. 2.2 E). Note that the resting potential is different at the two sites; we will come back to this issue in a later section. As noted by Hu and Bean (2018), the axonal input resistance increases with distance of the injection site. When measured 300 µs after the start of the pulse, the axonal input resistance increases steeply with distance, while the soma barely responds (fig. 2.2 F). Therefore, the passive properties of these neurons follow the resistive coupling regime, rather than the small soma regime (compare with fig. 2.1 B).

Dimensional analysis

Could it be that large neurons follow the resistive coupling regime while smaller neurons such as granule cells do not? Consistently with this hypothesis, in simulations, Gulledge and Bravo (2016) noted that large neurons are more excitable when the AIS is distal whereas small neurons are more excitable when the AIS is proximal. However, those simulations were performed with a constant AIS diameter of 1.5 µm. As noted in Telenczuk et al. (2017), cerebellar granule cells, which have a small cell body of about 6 µm (Delvendahl et al., 2015) also have very thin axons, of diameter about 0.2 µm (Perge et al., 2012; Wyatt et al., 2005), and as a result they still follow resistive coupling theory because the soma remains large compared to the axon.

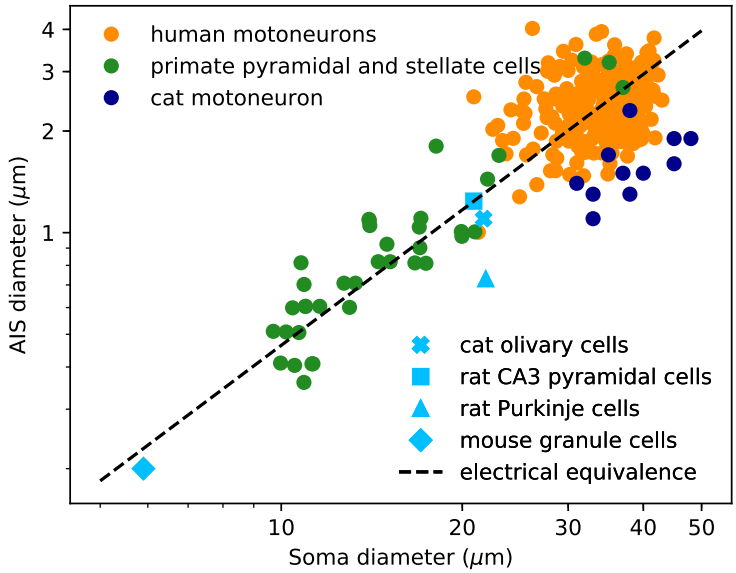

Figure 2.3: AIS diameter vs. soma diameter in a variety of cell types. Four points are averages over many neurons of the same type (light blue symbols), other points are individual measurements (dots). Electrical equivalence is represented by the dashed line.

We now examine the relation between soma and axon diameter empirically. Figure 2.3 shows minimum AIS diameter (generally measured at the distal end of the AIS) vs. soma diameter measured with electron microscopy in several cell types, plotted in logarithmic scale. We have excluded optical microscopy measurements because small AIS diameters approach the diffraction limit. The figure includes three sets of measurements on individual neurons: human spinal motoneurons (Sasaki and Maruyama, 1992), cat spinal motoneurons (Conradi and Ronnevi, 1977) and pyramidal and stellate cortical cells of primates (Sloper and Powell, 1979) (dots). It also includes average AIS and soma diameters of four other cell types: cat olivary cells (Ruigrok et al., 1990; De Zeeuw et al., 1990) ; rat CA3 pyramidal cells (Kosaka, 1980; Buckmaster, 2012); rat Purkinje cells (Somogyu and Hamori, 1976; Takacs and Hamori, 1990); mouse cerebellum granule cells (Delvendahl et al., 2015; Palay and Chan-Palay, 2012; Wyatt et al., 2005).

The data show that smaller neurons also tend to have a smaller AIS. The correlation between AIS and soma diameter appears both within and across cell types (the best power law fit across all merged data has exponent 1.14 ± 0.05, bootstrap standard deviation, but the exact number is not very meaningful because the regression is done on groups of different sizes).

To interpret this relation, we now ask what relation between soma and axon diameter preserves electrical properties. We use the dimensional analysis that Rushton (1951) applied to the scaling of conduction velocity with axon diameter. For this analysis, we consider a simplified model consisting of a spherical soma of diameter d_s with no dendrites and a cylindrical axon of diameter d_a. First, the somatic input resistance scales as $R_s \propto d_s^{-2}$ (inverse membrane area), while the distal axonal resistance scales as $R_{distal} \propto d_a^{-3/2}$ (input resistance of a semi-infinite cylinder). For the resistance of the proximal axon, we must determine the injection point. To preserve electrical properties, its position should be constant in units of the space constant λ, which gives $R_a \propto \lambda / d_a^2 \propto d_a^{-3/2}$. Thus, for all resistances to scale in the same way and therefore to preserve electrical properties, we must have $d_s^{-2} \propto d_a^{-3/2}$, which means: $d_a \propto d_s^{4/3}$, that is, a power law exponent of about 1.3. This relation is represented by the dashed line on fig. 2.3: all lines parallel to it correspond to electrical equivalence – this is of course approximate since it does not take into account the scaling of dendrites.

In summary, small neurons also have a thin AIS, such that electrical properties are preserved. This indicates that the passive properties of the soma-AIS system should generically follow the resistive coupling regime. We will now show that in this regime, the appropriate measure of excitability for studying the effect of AIS structural plasticity is the somatic voltage threshold.

2.3.2 Measuring excitability

A simple biophysical model of spike initiation

We first present a minimal biophysical model of spike initiation that will be compared with theoretical predictions. We aimed for a simple model with as few parameters as possible (see Methods for details). The morphology consists of a spherical soma, a large cylindrical dendrite and a thin cylindrical axon (fig. 2.4 top). The AIS is a section of the proximal axon with a high uniform density of inactivating sodium and non-inactivating potassium channels. The rest of the neuron contains a lower density of both channels. On this figure, the AIS is $L = 30\,\mu m$ long and is positioned at a distance $\Delta = 5\,\mu m$ from the soma.

For channels, we chose simple Hodgkin-Huxley-type models with just three interpretable parameters: half-activation (or inactivation) voltage $V_{1/2}$, slope k and maximum time constant τ^{max}. The equilibrium value of gating variables is shown on fig. 2.4 A. The activation slope factor of the Na_v channel was rounded at 5 mV. We modeled the K_v channel in the same way, but we used 8 gates (n^8) as in Hallermann et al. (2012). This was important so that the K_v channel activates with a delay. The dynamics of the gating variables during a spike are shown at the distal end of the AIS in fig. 2.4 B.

Our goal was to reproduce the essential phenomenology of action potentials recorded in cortical neurons. First, a high amplitude action potential initiates first in the AIS where it rises quickly ($dV/dt > 1000\,V\,s^{-1}$), then appears in the soma with a distinct kink and a biphasic phase plot (fig. 2.4 C,D) (Kole and Stuart, 2008; Kole et al., 2008; Naundorf et al., 2006; Stuart et al., 1997; Yu et al., 2008). Second, Na^+ and K^+ currents have little overlap at spike initiation (fig. 2.4 E,F) Hallermann et al. (2012), which implies that K_v channels are more involved in repolarization than in spike initiation.

How to measure excitability?

Excitability changes associated with changes in AIS geometry have been reported using various measures: rheobase, the minimal constant current required to elicit a spike (Lezmy et al., 2017), or minimal transient current (Raghuram et al., 2019); threshold current density, which is rheobase divided by input capacitance (Grubb and Burrone, 2010; Wefelmeyer et al., 2015); somatic potential at spike onset (Kuba et al., 2014, 2015).

All these quantities are related to each other. However, an issue with both rheobase and current density threshold is that they vary not only with changes in the AIS but also with the neuron's input resistance. For example, Grubb and Burrone (2010) reported an increase of about 50% in threshold current density after long-term depolarization associated with a distal displacement of the AIS. To infer the specific effect of changes in the AIS, they had to discount the estimated effect of an observed reduction of input resistance (about 1/3). This issue is illustrated in fig. 2.5 A and B: the rheobase varies when the total Na_v conductance G is varied at the AIS, but also when the somatic leak conductance g_L is varied. Thus, changes in rheobase reflect excitability changes due to factors in the AIS and elsewhere.

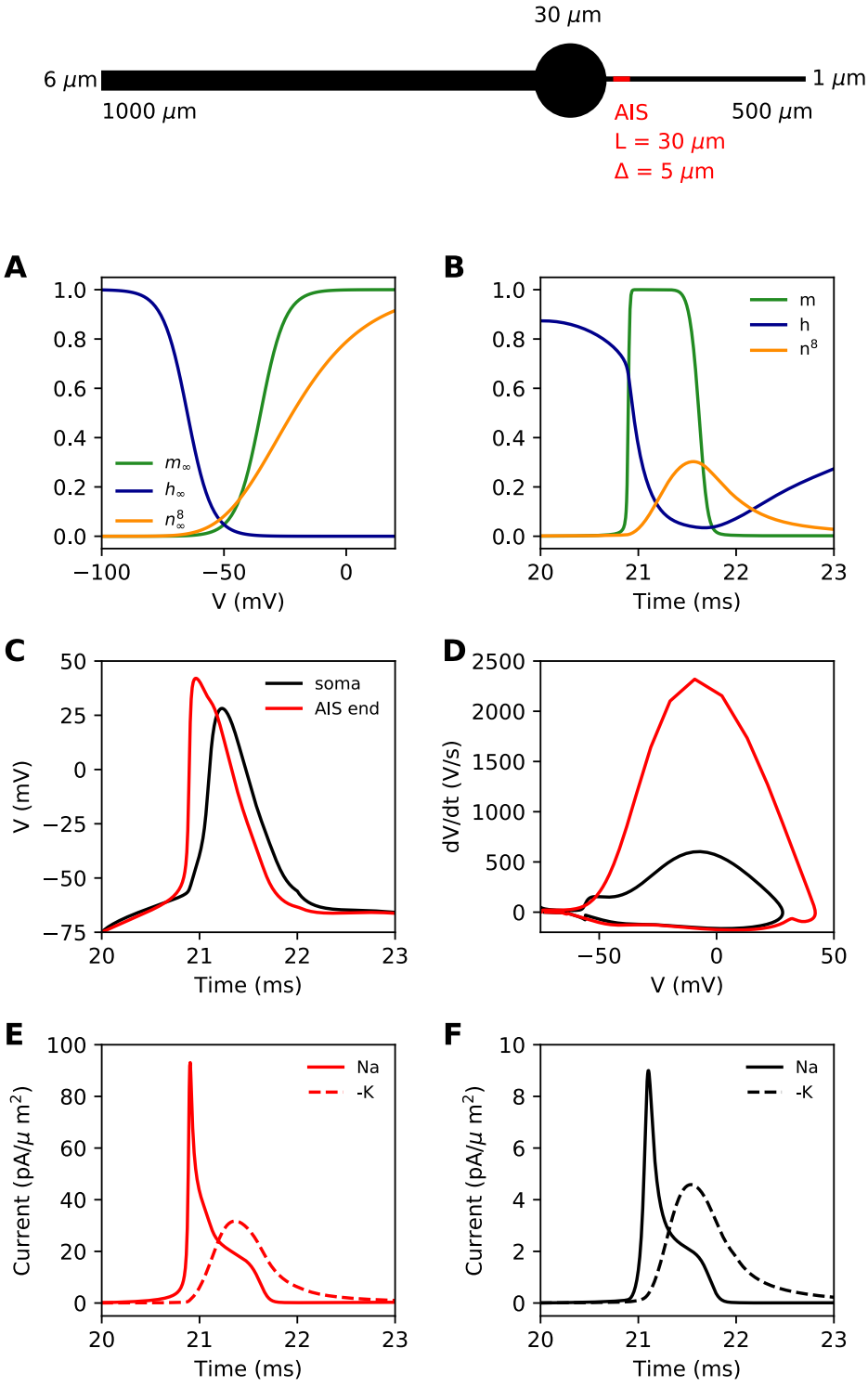

Figure 2.4: Simple biophysical model of spike initiation. **Top**, morphology of the neuron. **A**, Equilibrium functions of the gating variables m, h, and n^8. **B**, Time course of the gating variables at the distal end of the AIS during an action potential. **C**, Action potential observed at the end of the AIS (red) and at the soma (black). **D**, The same action potential shown in a phase plot. **E**, Absolute value of Na^+ and K^+ currents at the AIS during a spike. **F**, Same as E, at the soma.

In the resistive coupling regime, the somatic voltage threshold is a measure of excitability that depends only on axonal factors. It is defined as the maximum somatic membrane potential that can be reached without triggering a spike (Brette, 2013). This is illustrated in fig. 2.5 A and B: the voltage threshold varies with G in the same way as the rheobase (more precisely, $V_{threshold} - V_0$ is proportional to the rheobase), but it does not vary with g_L. The reason is the separation of time scales between somatic and axonal dynamics, due to the size difference: when the Na^+ current enters the AIS, it depolarizes the AIS very rapidly, while at the time scale of spike initiation the soma does not get charged significantly. This is shown in fig. 2.2 C and F, which compare the somatic and axonal responses at time t = 300 µs after current injection in the axon. It follows that at the relevant time scale, the somatic potential acts as a fixed boundary condition for the axon. Therefore, the initiation of a spike depends only on the somatic potential and properties of the axon, but not on properties of the soma or dendrites (an exception is the axon-carrying dendrite of some neurons (Kole and Brette, 2018)). In terms of dynamical systems theory, the somatic potential is a bifurcation parameter (see below).

It could be argued that a better measure of excitability is the voltage threshold at the AIS, rather than at the soma, since spikes are initiated in the AIS (Yu et al., 2008). To show that this is not the case, we inject a constant hyperpolarizing current at the distal end of the AIS, while still triggering spikes with a somatic current (fig. 2.5 C). As a result, the somatic voltage threshold is raised in proportion of the hyperpolarizing current. This change does represent a reduction of excitability, because the rheobase also increases - we note that the rheobase increases both because the voltage threshold increases and because the resting potential also decreases substantially (see final section). In contrast, the voltage threshold at the AIS changes in the opposite direction (fig. 2.5 C): it does not capture the change in excitability due to this particular change at the AIS, but on the contrary it is misleading. We will analyze this perhaps counter-intuitive phenomenon in the last part of the manuscript. We note for now that the somatic voltage threshold specifically captures the axonal factors of excitability.

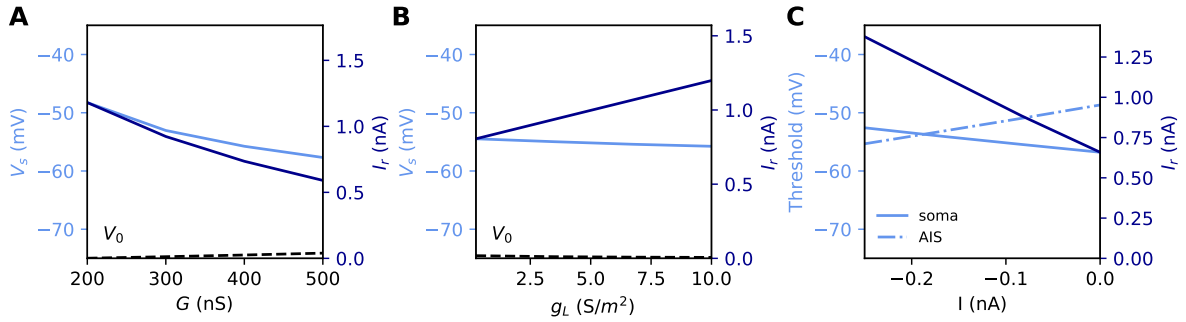

Figure 2.5: Measuring excitability in the biophysical model. **A**, Rheobase (dark blue) and somatic voltage threshold (light blue) as a function of total Na_v conductance in the AIS G (d_s = 30 µm). The resting potential also changes slightly (dashed). **B**, Rheobase and somatic voltage threshold as a function of leak conductance density (G = 350 nS). **C**, Voltage threshold at the soma (solid light blue) and AIS (dashed light blue) as a function of a hyperpolarizing current injected at the AIS end. The rheobase is shown in dark blue.

2.3.3 Relation between excitability and AIS geometry

General theoretical framework

We now develop a theoretical analysis of the relation between AIS geometry and excitability as measured by the somatic voltage threshold. To develop the theory, we make a number of strong approximations. First, we neglect the axial current towards the distal axon because the soma acts as a current sink for the AIS. Second, we neglect axonal leak currents because the resistance through the membrane is much larger than the axial resistance towards the soma. For a length x of axon, the membrane resistance is $R_m/\pi dx$ (d is axon diameter and R_m is specific membrane resistance); for example, with $d = 1\,\mu m$, $x = 100\,\mu m$ and $R_m = 15\,000\,\Omega\,cm^{-2}$, we obtain about $4.8\,G\Omega$. In contrast, with the same parameter values and $R_i = 100\,\Omega\,cm$ we obtain an axial resistance $R_a = 4R_i x/(\pi d^2) \approx 127\,M\Omega$. Third, we neglect the time-varying K^+ current responsible for repolarization because it is small compared to the Na^+ current at spike initiation, at least in layer 5 pyramidal cells (Hallermann et al., 2012) (see fig. 2.4 E). Fourth, we further assume that Na_v channel inactivation plays no role, except for setting the proportion of initially available Na_v channels. Finally, we neglect all time-varying processes. This drastic approximation is justified by the following arguments: first, the somatic membrane potential should not vary substantially at the time scale of spike initiation because the somatodendritic compartment is large; second, the axonal capacitive current should be small because we are considering the situation near threshold (i.e., where dV/dt is not very large) and the axonal capacitance is relatively small; third, the activation time constant of Na_v channels is very short (about $100\,\mu s$ at room temperature (Schmidt-Hieber and Bischofberger, 2010)).

With this set of approximations, the theory then considers just two currents: the axial resistive current, and an instantaneous axonal Na^+ current (in the last part we will consider the effect of a static non-sodium current). Theoretical predictions will be compared with simulations in the biophysical model, which does not make these approximations. We address increasingly complex situations, starting with a point AIS.

A point AIS

The idealized case where all Na_v channels are clustered at a point AIS has been treated theoretically in (Brette, 2013). We briefly summarize the result. When the somatic potential is increased, the axonal potential also increases. Under some condition, there is a somatic potential above which the axonal potential suddenly jumps to a higher value, which corresponds to spike initiation. This is called a bifurcation and the voltage at the bifurcation (the spike threshold) has been calculated analytically (see Methods). A simple (but not rigorous) way to obtain the result is the following. The axial current is resistive, and therefore scales inversely with axial resistance R_a. At spike initiation, we therefore expect: $I_{axial} \propto 1/R_a$. The Na^+ current changes approximately exponentially with voltage below threshold (Baranauskas et al., 2013; Hodgkin and Huxley, 1952b): $I_{Na} \propto G\exp(V/k)$, where G is the total available Na^+ conductance and k is the Boltzmann slope factor of Na_v channels (typically 4 mV to 8 mV (Angelino and Brenner, 2007; Platkiewicz and Brette, 2011)). The two currents must match (the Na^+ current entering the axon then flows towards the soma as a resistive current), therefore the somatic

spike threshold is:

$$V_s = \text{constant} - k \log(R_a G) \tag{2.1}$$

where the constant depends on Na_v channel properties. For an axon with constant section (e.g. cylindrical), the axial resistance R_a is proportional to AIS position Δ. Therefore, the formula can be expressed as

$$V_s = \text{constant} - k \log(\Delta) - k \log(G) \tag{2.2}$$

We did not include the AIS diameter d in this formula, which would contribute an additional term $2k \log(d)$ (because R_a is inversely proportional to d^2; see Discussion). Figure 2.6 A and B illustrate this formula for $k = 5\,\text{mV}$. To show that the analysis is correct, we first show numerical results in a simplified cable model that includes neither Na_v channel inactivation nor K_v channels (see Methods). The soma is voltage-clamped and the command potential is increased until a spike is triggered in the AIS. This situation is close to the approximations used for the theory, but includes leak currents, axonal capacitive currents and Na_v activation dynamics. Figure 2.6 C and D show that the formula is essentially correct in this case.

We now examine this relation in the biophysical model where a spike is elicited in current-clamp. Several factors make this situation much more challenging: first, the somatic potential is no longer assumed to be clamped at spike initiation, and second, the model includes Na_v channel inactivation and K_v channels, both of which can interfere with spike initiation. To ensure that the same proportion of Na_v channels is initially available when x and G are varied, we use the following protocol: the somatic potential is held at $V_0 = -75\,\text{mV}$, then a current step of varying amplitude is injected. The voltage threshold is defined as the maximal somatic potential reached in a non-spiking trial. Thus, the value of G represents the total non-inactivated conductance, which can potentially vary with the initial potential (see Platkiewicz and Brette (2010, 2011) for a theory); in practice, this variation was small in our simulations.

The numerical results show quantitative differences with the theoretical predictions (fig. 2.6 E and F), namely, the spike threshold is more sensitive to Na_v conductance than predicted (logarithmic slope of about 9 mV instead of $k = 5\,\text{mV}$). Nonetheless, theory correctly predicts that 1) shifting the AIS distally or increasing total Na_v conductance lowers spike threshold on a logarithmic scale, 2) the two logarithmic factors interact linearly (meaning the plotted lines are parallel). The relation between threshold and AIS position is also quantitatively well predicted (logarithmic slope of about 6 mV to 7 mV).

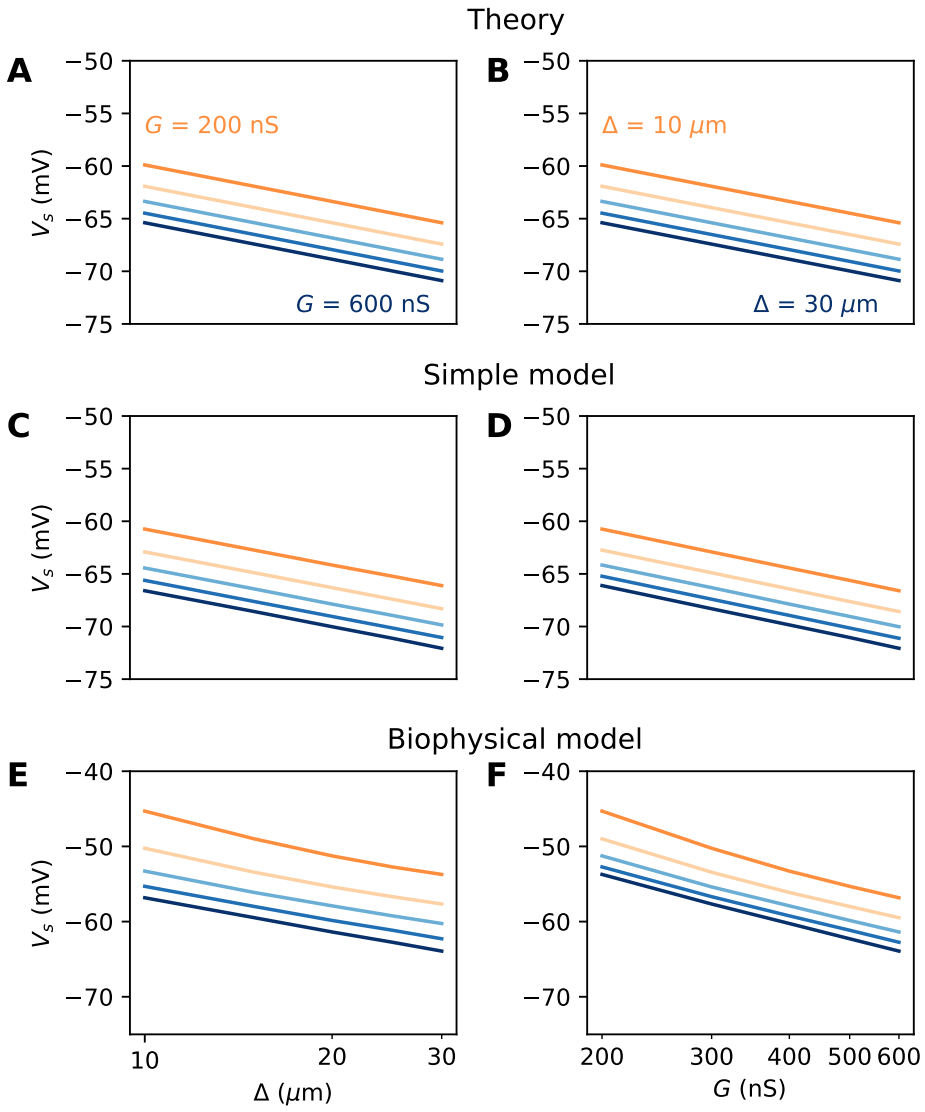

Figure 2.6: Spike threshold vs. AIS position and Na_v conductance with a point AIS. **A**, Theoretical prediction of spike threshold vs. AIS position in logarithmic scale, for different total Na_v conductances (from 200 nS to 600 nS). **B**, Theoretical prediction of spike threshold vs. total Na_v conductance for different AIS positions (from 10 µm to 30 µm). **C**, Spike threshold in a simplified model measured in somatic voltage clamp, vs. AIS position. The regression slope is about 5 mV for all curves. **D**, Spike threshold in the simplified model vs. total Na_v conductance. The regression slope varies between 5.3 mV ($\Delta = 10$ µm) and 5.3 mV ($\Delta = 30$ µm). **E**, Spike threshold vs. AIS position in the biophysical model in current clamp. Regression slopes vary between 7.7 mV ($G = 200$ nS) and 6.5 mV ($G = 600$ nS). **F**, Spike threshold vs. total Na_v conductance in the biophysical model. Regression slopes vary between 10.5 mV ($\Delta = 10$ µm) and 9.3 mV ($\Delta = 30$ µm).

A spatially extended AIS

We now turn to the more difficult case of a spatially extended AIS, which requires new theory. Figure 2.7 shows the relation between AIS geometry and voltage threshold in the biophysical model, when the surface conductance density of Na_v channels is maintained constant. As expected, the threshold is lowered when the AIS is moved away from the soma (fig. 2.7 A). However, the relation is less steep than in the case of a point AIS. The threshold is also lowered when the AIS is extended (fig. 2.7 B). This is not surprising, but the quantitative relation cannot be easily extrapolated from the point AIS theory: when the AIS is extended, the total Na_v conductance increases in proportion of the length, but the spike initiation site also moves.

We developed an analytical strategy to derive a formula for the extended case (illustrated in fig. 2.7 C, D). We first consider an AIS of length L starting at the soma. We solve the cable equation in the resistive coupling regime, that is, where all time-varying effects as well as leak currents are neglected and the somatic potential is held fixed. The cable equation then becomes an ordinary second-order differential equation:

$$\frac{d^2V}{dx^2} \propto -ge^{V/k} \tag{2.3}$$

where g is the surface conductance density of (available) Na_v channels, and the proportionality factor includes axon diameter, resistivity and Na_v channel properties. This equation simply expresses the fact that the Na^+ current entering the axon (right hand-side) equals the axial diffusion current (left hand-side). This equation can be solved with the two boundary conditions: $V(0)$ is the somatic potential ($V(0) = V_s$) and no axial current flows towards the distal axon ($V'(L) = 0$; see Methods). A simple rescaling argument shows that the spike threshold varies as

$$V_s = \text{constant} - k\log(G) - k\log(L) \tag{2.4}$$

where G is the total Na_v conductance ($G = \pi dL$ for a cylindrical axon). Remarkably, this is the same formula as for a point AIS placed at position $\Delta = L$ and with the same total number of Na_v channels. The only difference is the constant term. By solving the differential equation analytically, we find that this difference is $0.87\ k$ (about 4.3 mV with $k = 5$ mV), as illustrated on fig. 2.8 A (dashed vs. solid black). Note that in the point model, the threshold is not defined anymore (no bifurcation or "kink") when AIS distance is lower than 2.25 µm (Brette, 2013). This limit is more difficult to calculate in the extended model.

An equivalent and more intuitive way to understand this result is to note that a threshold shift of $0.87\ k$ is equivalent to a displacement of the AIS by a factor $e^{-0.87} \approx 0.42$. In other words, the spike threshold of the extended AIS is almost the same as for a point AIS with the same number of channels placed in the middle of the AIS (fig. 2.8 A, green curve):

$$V_s = \text{constant} - k\log(G) - k\log(x_{1/2}) \tag{2.5}$$

with $x_{1/2} = L/2$, the midpoint of the AIS, and the constant in this formula differs from the constant for the point AIS by about 0.9 mV (see Methods). This analysis shows that extending the AIS lowers the spike threshold by two mechanisms: by increasing the number of Nav

channels and by moving the initiation site away from the soma. As G and $x_{1/2}$ are both proportional to L, each factor contributes a shift of $-k\log(L)$.

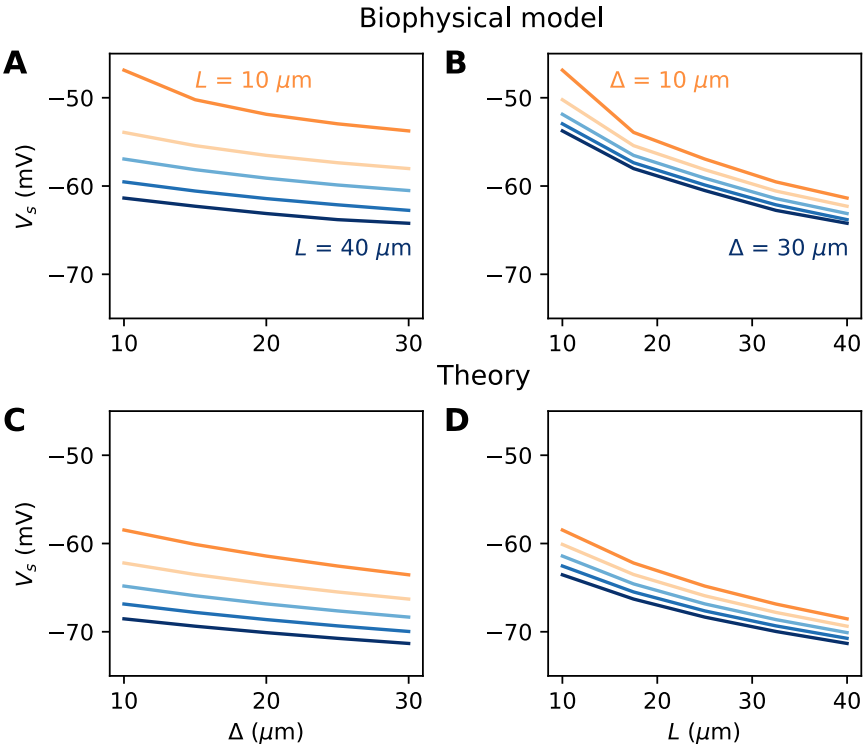

Figure 2.7: Relation between AIS geometry and voltage threshold in the biophysical model with constant Na_v channel density. **A**, Threshold vs. AIS position (distance between soma and AIS start), for different AIS lengths between 10 µm and 40 µm. **B**, Threshold vs. AIS length for different AIS positions between 10 µm and 30 µm. **C**, Theoretical relation between threshold and AIS position (corresponding to panel A). **D**, Theoretical relation between threshold and AIS length (corresponding to panel B).

We can now consider the general case of an extended AIS of length L, placed at distance Δ from the soma. The exact same analytical strategy can be applied, the only difference being the boundary condition at the start of the AIS, which now expresses the fact that the current flowing towards the soma is proportional to the voltage gradient between soma and AIS according to Ohm's law. This can be solved analytically (see Methods), and we find that the spike threshold is almost the same as if the AIS were compressed into a single point at its center ($x_{1/2} = \Delta + L/2$), up to a corrective term $kf(\Delta/L)$. With $k = 5\,\text{mV}$, this corrective term is at most 0.9 mV (see Methods). Figure 2.8 B shows that compressing or extending the AIS around its middle position $x_{1/2}$ without changing the total Na_v conductance has very little effect on the theoretical spike threshold. In the simulated biophysical model, the effect is more significant but remains small (fig. 2.8 C). Therefore, we find that with an extended AIS, the spike threshold is approximately the same as that of the equivalent point AIS placed at the middle position $x_{1/2}$, with the same total Na_v conductance.

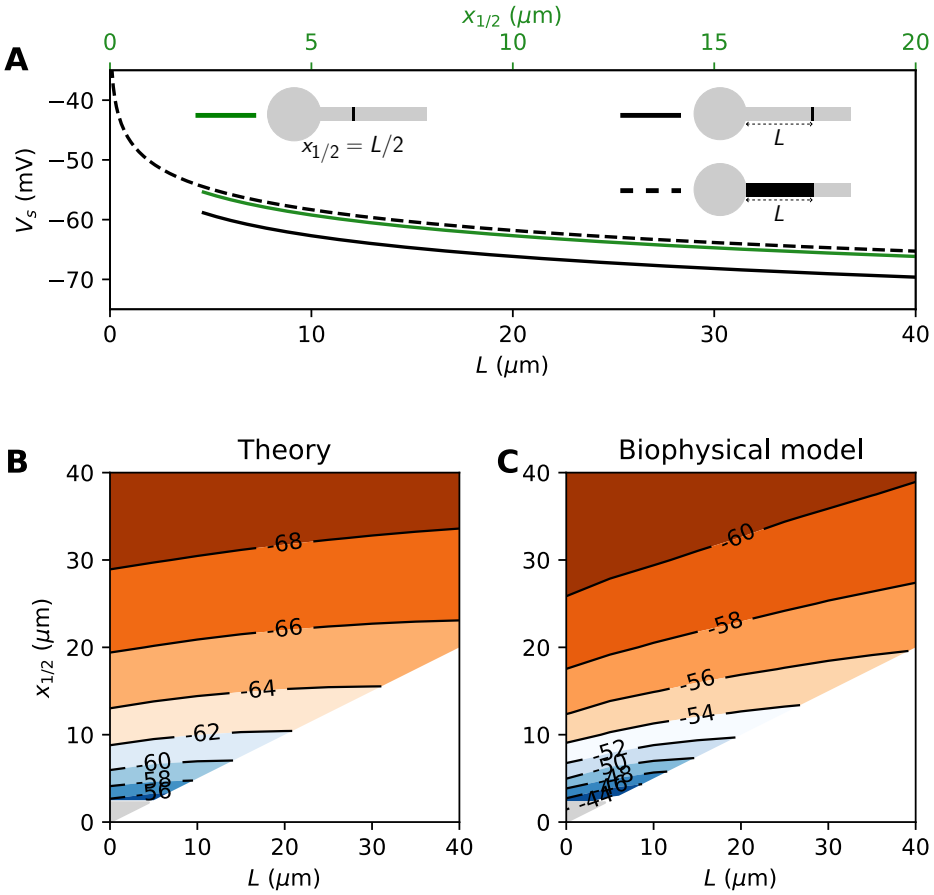

Figure 2.8: Effect of compressing the AIS on spike threshold, with total Na_v conductance held fixed. **A**, Theoretical spike threshold of an AIS of length L starting from the soma (dashed), compared to an equivalent point AIS placed at position $\Delta = L$ (solid black) and at $\Delta = x_{1/2} = L/2$ (solid green). **B**, Theoretical spike threshold (in mV) vs. AIS middle position and length, with fixed total Na_v conductance. The lower right white triangle corresponds to impossible geometries; the lower left shaded triangle is the region where the threshold is undefined in the point model. **C**, Observed relation in the biophysical model.

In summary, we have found a simple theoretical relationship between spike threshold and AIS geometry, as well as Na_v conductance density:

$$V_s = \text{constant} - k\log(g) - k\log(L) - k\log(x_{1/2}) \tag{2.6}$$

The constant term captures the effects of Na_v channel properties, intracellular resistivity and axon diameter (see Discussion). The remarkable finding is that the variation of spike threshold can be separated into three independent contributions. Figure 2.9 indicates that this theoretical finding is essentially valid in the biophysical model. The relation of spike threshold with any of these three factors ($g, L, x_{1/2}$) is essentially the same logarithmic relation when the other two factors are changed, up to a constant shift (i.e., the relations appear as parallel lines). The observed slopes are close to the theoretical prediction $k = 5\,\text{mV}$ for the geometric factors $x_{1/2}$ and L (6 mV to 7 mV), and a little larger for g (8 mV to 9 mV).

We are now in better position to understand fig. 2.7. We noted that the spike threshold changes less than expected when the AIS is moved away. This is because it varies logarithmically with the middle position $x_{1/2}$ and not with the start position Δ. For example, for an AIS of length $L = 40\,\mu m$ placed at position $\Delta = 10\,\mu m$, a displacement of $5\,\mu m$ shifts the middle position from $25\,\mu m$ to $30\,\mu m$. The theory then predicts that the threshold decreases by $0.9\,mV$ (assuming $k = 5\,mV$), close the measurement in the biophysical model ($1.2\,mV$). Thus, the theoretical effect of AIS start position on excitability is significant but moderate.

If we extend the AIS while keeping the same start position, then the spike threshold decreases because of the increase in length (as $-k\log(L)$) and because the AIS middle position moves away (as $-k\log(\Delta + L/2)$). If the AIS is close to the soma, then these terms add up to $-2k\log(L)$. For example, an extension from $40\,\mu m$ to $50\,\mu m$ theoretically lowers the threshold by about $2.2\,mV$. Thus, for realistic changes in position and length, the theory predicts moderate changes in threshold, consistently with empirical observations in structural plasticity studies (see Discussion).

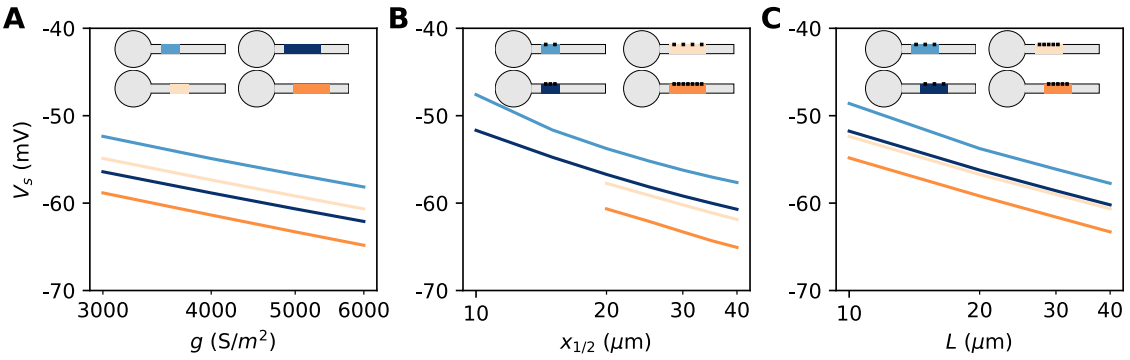

Figure 2.9: Dependence of spike threshold on AIS geometry and Na_v conductance density in the biophysical model. **A**, Spike threshold vs. Na_v conductance density g, for 4 combinations of AIS middle position $x_{1/2}$ and length L (light blue, $x_{1/2} = 20\,\mu m$, $L = 20\,\mu m$, regression slope: $8.4\,mV$; light orange, $x_{1/2} = 20\,\mu m$, $L = 40\,\mu m$, regression slope: $8.3\,mV$; dark blue, $x_{1/2} = 30\,\mu m$, $L = 20\,\mu m$, regression slope: $8.2\,mV$; dark orange, $x_{1/2} = 30\,\mu m$, $L = 40\,\mu m$, regression slope: $8.7\,mV$). **B**, Spike threshold vs $x_{1/2}$ for 4 combinations of g and L (light blue, $g = 3500\,S\,m^{-2}$, $L = 20\,\mu m$, regression slope: $7.1\,mV$; light orange, $g = 3500\,S\,m^{-2}$, $L = 40\,\mu m$, regression slope: $6\,mV$; dark blue, $g = 5000\,S\,m^{-2}$, $L = 20\,\mu m$, regression slope: $6.5\,mV$; dark orange, $g = 5000\,S\,m^{-2}$, $L = 40\,\mu m$, regression slope: $6.4\,mV$). **C**, Spike threshold vs. L for 4 combinations of g and $x_{1/2}$ (light blue, $g = 3500\,S\,m^{-2}$, $x_{1/2} = 20\,\mu m$ regression slope: $6.6\,mV$; light orange, $g = 5000\,S\,m^{-2}$ $x_{1/2} = 20\,\mu m$, regression slope: $6\,mV$; dark blue, $g = 3500\,S\,m^{-2}$, $x_{1/2} = 30\,\mu m$, regression slope: $6.1\,mV$; dark orange, $g = 5000\,S\,m^{-2}$, $x_{1/2} = 30\,\mu m$, regression slope: $6.1\,mV$).

Non-sodium axonal currents

So far, our theoretical analysis predicts that the neuron should be more excitable when the AIS moves away from the soma. Yet the opposite effect has been seen in some model simulations (Grubb and Burrone, 2010; Lezmy et al., 2017). Specifically, Lezmy et al. (2017) observed in a biophysical model that when a strong K_v7 conductance is placed along the AIS, moving the AIS away from the soma makes the neuron less excitable. This effect can be observed in our model if we add a strong hyperpolarizing conductance on the distal half of the AIS (fig. 2.10 A). It contradicts our previous findings, which were based on an analysis of the Na_v channels only. However, it appears that the voltage threshold measured at distal end of the AIS still follows the theoretical prediction, with spikes initiating at lower axonal voltage when the AIS is moved away from the soma (fig. 2.10 B). We now analyze this phenomenon.

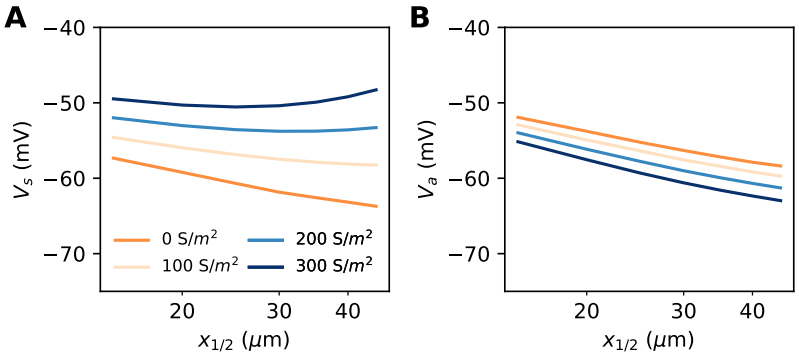

Figure 2.10: Excitability as a function AIS position with hyperpolarizing conductance (biophysical model). The conductance has reversal potential $E = -90\,\text{mV}$ and is uniformly expressed in the distal half of the 30 µm long AIS ($G = 500\,\text{nS}$). **A**, Somatic threshold vs. AIS position for different conductance values (an empirical estimate in layer 5 pyramidal cells is $144\,\text{S}\,\text{m}^{-2}$ (Battefeld et al., 2014)). **B**, Threshold at the distal end of the AIS for different conductance values (logarithmic regression slopes: 5.9 mV to 7.1 mV).

Let us consider a point AIS placed at position , in which a hyperpolarizing current I is injected ($I < 0$). This current could model K_v7 channels or synapses onto the AIS (Wefelmeyer et al., 2015). By resistive coupling, the current will hyperpolarize the AIS relative to the soma by an amount $\Delta V = R_a I = r_a \Delta I$ (r_a is the axial resistance per unit length) (fig. 2.11 A). As shown on fig. 2.11 B, the voltage threshold at the AIS is not substantially affected by this current (see Methods) – although a hyperpolarizing current may indirectly lower the threshold by deinactivating Na_v channels (there is indeed a slight decrease with increasing current amplitude). It follows that the somatic threshold increases linearly with the current, by an amount equal to ΔV. In the absence of hyperpolarizing current, the somatic threshold is theoretically below the AIS threshold by an amount k (about 5 mV). The difference between somatic and AIS threshold is therefore predicted to be $-k - \Delta V$. This prediction holds in the biophysical model, as shown in fig. 2.11 C, which compares the difference between somatic and AIS threshold with the difference between somatic and AIS resting potentials, when intensity and AIS position are varied.

Thus, when the AIS is moved away from the soma, the spike threshold at the AIS decreases as predicted in the previous section, but the somatic threshold differs from it by $-k - \Delta V$, which can make it increase with distance (fig. 2.11D).

Is this effect likely to be substantial in neurons? Empirically, Hu and Bean (2018) found that in layer 5 pyramidal cells, the AIS (more precisely, the axonal bleb) is about 3 mV hyperpolarized relative to the soma. This suggests that the contribution of this effect to threshold variations should be small. For example, suppose that a 45 µm AIS starting 10 µm away from the soma has distal K_v7 channels that hyperpolarize the AIS end by 3 mV. Then moving the AIS away from the soma by 10 µm (a large displacement) would move the AIS end from 55 µm to 65 µm, producing an increase in somatic threshold of about 0.5 mV by the effect discussed in this section (10/55 x 3 mV) – assuming the axonal resting potential is not homeostatically regulated. This increase in threshold would be more than compensated by the decrease due to the displacement of the Na_v channels, of about 1.3 mV (using $k = 5$ mV).

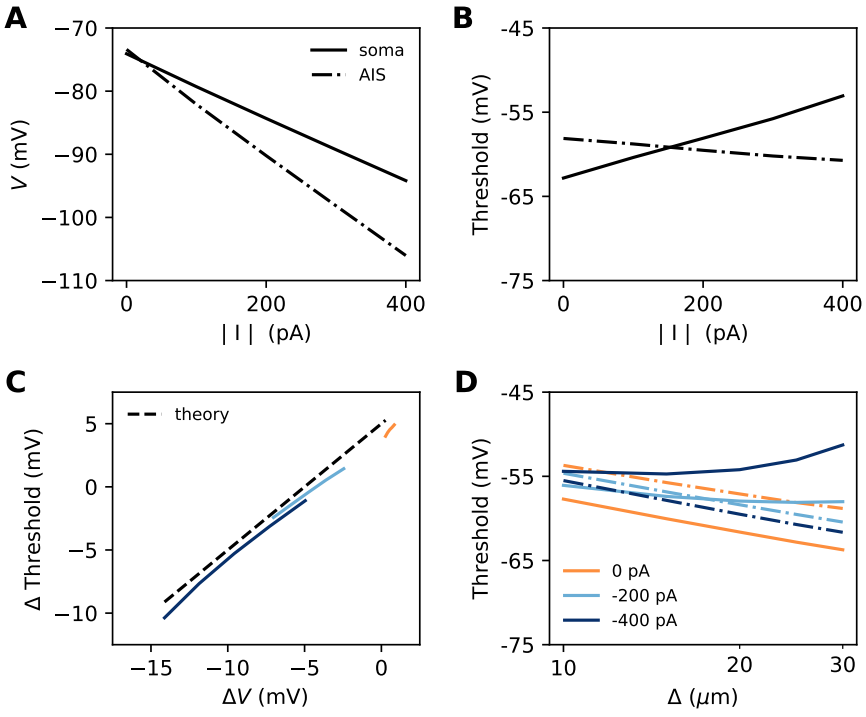

Figure 2.11: Effect of a hyperpolarizing axonal current in the biophysical model with a point AIS. **A**, Resting potential at the soma and AIS as a function of current intensity $|I|$, for an AIS placed 25 µm away from the soma. **B**, Threshold at the AIS and soma as a function of $|I|$. **C**, Difference between AIS and somatic threshold vs. difference between AIS and somatic resting potential. Each curve corresponds to a variable AIS position with a given current intensity (0 pA to −400 pA). **D**, Somatic (solid) and AIS threshold (dashed) vs. when currents are injected at the AIS.

2.3.4 Role of axon morphology

In the previous analysis, we have neglected the role of the distal axon. We now examine the impact of axon morphology on the results.

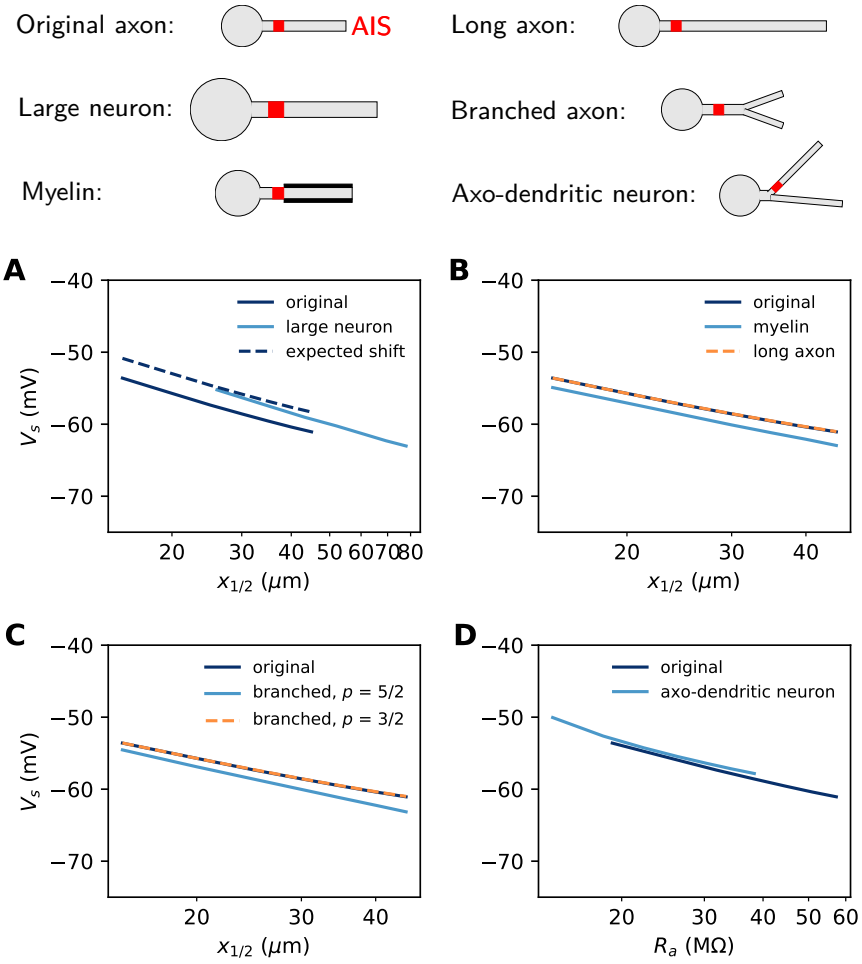

Figure 2.12: Effect of axon morphology on the relation between AIS position and excitability (biophysical model). **Top**: schematics of the different morphologies considered. **A**, Somatic threshold vs. AIS position for a large neuron (light blue; diameter: 3 µm) compared to the original neuron (dark blue; diameter: 1 µm). AIS length is scaled up as the space constant, i.e., by a factor . This scaling results in a theoretical threshold shift of about 2.7 mV (dashed). **B**, Somatic threshold vs. AIS position for a longer axon (dashed orange) and for a myelinated axon (light blue), compared to the original neuron (dark blue). **C**, Somatic threshold vs. AIS position for a branching axon with diameters such that $d_{main}^p = d_1^p + d_2^p$, where $p = 5/2$ (light blue) or $3/2$ (dashed orange). **D**, Somatic threshold vs axial resistance Ra between soma and AIS middle position, in an axo-dendritic neuron (light blue). The axon-carrying dendrite starts with diameter 2 µm from the soma and splits after 7 µm into two branches of equal diameter (such that $d_{main}^{3/2} = d_1^{3/2} + d_2^{3/2}$).

Axon diameter

In the previous simulations, the biophysical models considered a 500 µm long unmyelinated axon of diameter 1 µm. Some neurons can have a much larger AIS: for example, many motoneurons shown in fig. 2.3 have an AIS diameter of about 3 µm. This is not expected to change the electrical situation because, as that figure shows, the size of the soma scales with the size of the AIS. In fig. 2.12 A, we simulated a biophysical model with an axon diameter d_{AIS} = 3 µm and a soma scaled according to the power law: $d_s = d_{AIS}^{3/4}$. All other aspects of the neuron morphology are unchanged. The axonal space constant is increased by a factor $\sqrt{3}$, and therefore we scaled AIS position and length by the same factor. We can see that the spike threshold still varies with AIS position as expected (logarithmic regression slope: 6.8 mV in the original neuron vs. 7.1 mV in the large neuron).

In our theoretical analysis, we have assumed that the AIS diameter d is fixed, but it is possible to take diameter changes into account in our analysis. Diameter contributes in two ways. First, axial resistance scales inversely with the axon section area, i.e., $r_a \propto 1/d^2$. This contributes an additional term $2k\log(d)$ to the threshold. Second, for a fixed surface conductance density, the total conductance scales with axon diameter, $G \propto d$. This contributes an additional term $-k\log(d)$ to the threshold. Therefore, the extended formula reads:

$$V_s = \text{constant} - k\log(g) - k\log(L) - k\log(x_{1/2}) + k\log(d) \tag{2.7}$$

where we neglected the modulation by axonal currents. Thus, for a given AIS position, scaling AIS diameter by a factor 3 and AIS length by a factor $\sqrt{3}$ results in a positive shift of the threshold by $k/2\log(3) \approx 2.7$ mV. This expected shift is shown on fig. 2.12 A (dashed).

Axon length and myelin

In our derivation of the spike threshold, we have ignored the distal axon, that is, we have considered that the resistance towards the distal axon is infinite (very large compared to the resistance towards the soma). More accurately, this resistance is large but finite and depends on the properties of the distal axon. If the 500 µm axon is extended to a 1000 µm axon, then the distal axonal resistance R_{distal} is barely affected and therefore the spike threshold does not change (fig. 2.12 B). However, if the axon is myelinated, so that the specific membrane resistance is increased by a factor 4 (and capacitance decreased by the same factor), then the spike threshold is slightly lowered (fig. 2.12 B, dashed).

To understand this, we can observe that the electrical impact of the distal axon is formally equivalent to a conductance $1/r_{distal}$ applied at the AIS end, with reversal potential equal to the resting potential (neglecting time-dependent effects). Therefore, we can apply the results of the previous section (*Non-sodium axonal currents*). The effect of a finite distal axonal resistance is thus to increase the somatic spike threshold by about:

$$\Delta V = \frac{R_a}{R_{distal}}(V_a - E_L) \tag{2.8}$$

where V_a is the threshold at the AIS and R_a is measured at the AIS end. As $R_{distal} = r_a\lambda$, we have $R_{distal} \propto \sqrt{r_m}$ where r_m is the specific membrane resistance. Therefore, if the axon is

myelinated, then this threshold shift should be halved, which implies that the spike threshold should be lowered. We can make a rough estimate in the case shown on fig. 2.12 B. With the model parameters (table 2.3), we obtain $R_{distal} \approx 780\,\mathrm{M\Omega}$, and $R_a \approx 95\,\mathrm{M\Omega}$ at the end of a 50 µm long AIS placed at position $x_{1/2} = 25\,\mu\mathrm{m}$. With $V_a \approx -55\,\mathrm{mV}$, we obtain $\Delta V \approx 2.4\,\mathrm{mV}$ for an infinite unmyelinated axon. With myelination, this shift is halved: $\Delta V \approx 1.2\,\mathrm{mV}$, and therefore myelination should lower the threshold by about 1.2 mV (this is an imprecise estimate since the axon is not infinite). In the simulation (fig. 2.12 B), this shift was 1.3 mV to 1.9 mV. In summary, the effect of myelination on spike threshold should be limited.

Axon branching

The axon may also display complex branching patterns Wang et al. (2019). The impact of branching on passive electrical properties is well understood from Rall's theory (Rall, 2011). In particular, Rall has shown that an axonal tree is electrically equivalent to an unbranched axon if diameters follow the rule $d_{parent}^{3/2} = d_{daughter1}^{3/2} + d_{daughter2}^{3/2}$. Figure 2.12 C (dashed) shows that indeed in this case the spike threshold is unchanged. Empirically, this relation is not always satisfied: Chklovskii and Stepanyants (2003) report an average exponent of about 5/2, with large variability. In this case, the spike threshold is slightly lowered (fig. 2.12 C, light blue). This shift can be estimated as previously, by calculating R_{distal} with standard cable theory.

Branching can also occur before the AIS, when the AIS sits on an axon-bearing dendrite (Kole and Brette, 2018). In this case, since the diameter is not uniform, one must consider not metric distances but axial resistances: $x_{1/2}$ is then replaced by $R_a(x_{1/2})$ in the equation, where the latter term is the axial resistance between soma and the AIS midpoint. Figure 2.12 D shows the spike threshold as a function of axial resistance between the soma and AIS, for a neuron with a dendrite of 2 µm diameter that splits into two equal branches (according to Rall's law), one of which carrying the AIS. The spike threshold is almost unchanged compared to the original unbranched axon, for a given axial resistance.

Overall, axon morphology appears to have a small impact on excitability.

2.3.5 Relation with experimental observations

We now discuss previous experimental observations in the light of this theoretical work. Not many studies have simultaneously reported changes in voltage threshold (rheobase is often reported instead) and in AIS geometry (position and length). First of all, it is important to stress that those observations cannot be used to directly validate or invalidate the theory, since many other relevant cell properties might also vary between groups (Kole and Brette, 2018), such as axon diameter; density, phosphorylation and inactivation state of Na_v channels; expression level of K_v channels. Rather, we will provide theoretical changes in voltage threshold expected from observed AIS geometry changes, all else being equal (see table 2.1). We will then discuss the discrepancy with observed threshold changes, in particular in terms of the unobserved factors.

We start with the single study of structural AIS plasticity in adult neurons that also reports voltage threshold. In neurons of chick nucleus magnocellularis, the AIS elongates by about 10 µm after 7 days of auditory deprivation, with no significant change in AIS start position (Kuba et al., 2010). It was reported that immunofluorescence intensity did not change, which suggests that at least the structural density of Na_v channels did not change. All else being equal, and in the absence of strong AIS hyperpolarization (e.g. K_v7), we then expect that the spike threshold shifts by -5.2 mV (using $k = 5$ mV; see table 2.1). The reported change was -4 mV (reported with $p<0.05$), a fairly good match.

Another study examined the change in AIS geometry through development in the chick nucleus laminaris (Kuba et al., 2014). The voltage threshold was found to decrease by -12 mV to -14 mV between E15 and P3-7, a very large change. AIS geometry also changed significantly in high frequency neurons, with a distal shift (13 µm to 45 µm, start position) and a shortening (26 µm to 10 µm). As we have seen, these two changes go in opposite directions. When we combine them, we find a theoretical expectation of 0.4 mV for the threshold shift. Similarly, we find expected shifts of 1-3 mV for low and middle frequency neurons. Could the discrepancy be due to the AIS being hyperpolarized by K_v channels? In that case, somatic threshold should increase when the AIS moves distally, contrary to what is observed. We conclude from this analysis that observed changes in threshold are likely due not to changes in AIS geometry but possibly to changes in patterns of expression of ionic channels. For example, it has been observed in other preparations that $Na_v1.6$ channels appear later than $Na_v1.2$ channels during the course of development (Boiko et al., 2003), and the latter activate at lower voltage (Rush et al., 2005).

All the other studies we have examined were in cultured neurons. Chronic depolarization (48h) of cultured hippocampal neurons induces a distal shift of the AIS of about 5 µm (Grubb and Burrone, 2010). This is a small shift because, as we have seen, what determines the excitability change is the relative change in middle AIS position, which is about 25% here. Together with a slight shortening of the AIS, theory then predicts a modest threshold shift of -1.1 mV, therefore slightly increased excitability. The authors observed on the contrary a decrease in excitability as measured by threshold current density, but it was mostly due to a change in input resistance. Nonetheless, the voltage threshold was also reported to raise by about 4.3 mV; this was not statistically significant because of substantial inter-cellular variations in threshold. If confirmed, such a change could in principle be due to the displacement of hyperpolarizing K_v7 channels. However, to raise the threshold by 5 mV with a 25% distal shift of the AIS means requires that the AIS is initially hyperpolarized by 20 mV relative to the soma. This seems very large. Other possible factors are changes in channel expression, phosphorylation, or possibly axon diameter.

In cultured hippocampal dentate granule cells (Evans et al., 2015), 3 hours of depolarization produce a shortening of the AIS, for which we would expect a threshold raised by about 2.4 mV. Instead, the measured threshold is lowered by -1.1 mV in normal condition, and by -1.9 mV in pro-PKA condition (aimed at re-phosphorylating Na_v channels). Both changes

were not statistically significant. However, when AIS length and threshold are compared within groups (with and without chronic depolarization, with and without pro-PKA treatment), a significant negative correlation is found in each case, consistent with theory. This suggests that the observed decrease in threshold (if genuine) might be due to other factors than AIS geometry.

Finally, in cultured dopaminergic interneurons of the olfactory bulb, one day of chronic depolarization produces a proximal shift and a small elongation of the AIS (Chand et al., 2015). As these two factors tend to counteract each other, the theoretical expectation in this case is a small 0.6 mV shift of the threshold. The measured change was -0.49 mV (for the biphasic neurons), which, given the 1.5 mV standard deviation in measurements, appears consistent.

In summary, all studies that we have examined in cultured neurons and in development report changes in AIS geometry that are expected to produce small threshold changes (-1 mV to 2 mV). In cultured neurons, reported changes are not statistically significant, which could be interpreted as consistent with the expectation. It could also simply signal the possibility that larger data sets are necessary to observe such changes. Possibly, these changes might be more clearly observed in individual cells (rather than by comparing groups). In development, there is a large decrease in threshold that seems likely due to changes in expression patterns of ionic channels. In the one study that we could examine on structural AIS plasticity in adults, the observed threshold change (4 mV to 5 mV) was consistent with expectations.

Neuron type	Initial L (µm)	Initial $x_{1/2}$ (µm)	Final L (µm)	Final $x_{1/2}$ (µm)	ΔV_s (mV)	ΔV_s theory (mV)	Reference
Plasticity							
Chicks nucleus magnocellularis	9.6	13.3	19.5	18.4	-4	-5.2	(Kuba et al., 2010)
Hippocampal cultures (only excitatory)	34.8	20.9	33.6	27.2	4.3	-1.1	(Grubb and Burrone, 2010)
Hippocampal dentate granule cells in cultures	19.2	10.4	15.7	7.85	-1.1	2.4	(Evans et al., 2015)
Olfactory bulb dopaminergic neurons in cultures	11.7	21.1	14.2	15.5	-0.4	0.6	(Chand et al., 2015)
Development[1]							
Chicks nucleus laminaris, low	30.3	24.8	23.9	19.9	-12.7	2.3	(Kuba et al., 2014)
Chicks nucleus laminaris, middle	28.8	24.8	14.4	28.3	/	2.8	(Kuba et al., 2014)
Chicks nucleus laminaris, high	26.5	26.6	9.8	50.1	-14.3	1.8	(Kuba et al., 2014)

Table 2.1: Changes in AIS geometry and voltage threshold (V_s) in structural plasticity and development studies, with the theoretical expectation, assuming constant functional Na_v channel density and everything else unchanged (e.g. axon diameter, channel properties). [1] Initial=E15, final=P3-7.

2.4 Discussion

2.4.1 Summary

A number of recent studies have documented changes in AIS geometry across development (Galiano et al., 2012; Gutzmann et al., 2014; Kuba et al., 2014), with activity (Grubb et al., 2011; Jamann et al., 2018), or associated with neurological pathologies (Buffington and Rasband, 2011). The functional effect of these changes is not addressed by the classical theory of excitability, which has focused on isopotential models of spike initiation (Koch, 2004; Tuckwell, 1988b). Spatial aspects of neural biophysics have been studied mainly for dendrites, notably by Rall (2011). Here we have derived an expression for the somatic threshold as a function of geometrical parameters and Nav conductance density, which is well corroborated by simulations of a biophysical model:

$$V_s = \text{constant} - k\log(g) - k\log(L) - k\log(x_{1/2}) - r_a x I \tag{2.9}$$

where k is the activation slope of the Na_v channels, $x_{1/2}$ is the middle position of the AIS, L is the AIS length, g is Na_v conductance density in the AIS, r_a is the axial resistance per unit length, and I is a non-sodium current entering the AIS at position x. Excitability changes caused specifically by changes in the AIS are captured by the somatic voltage threshold, rather than rheobase (which depends on other factors) or axonal threshold (which can remain constant when excitability changes due to AIS currents). According to this theoretical analysis, changes in AIS geometry reported in the literature are expected to produce relatively small changes in threshold (a few mV).

The theory explains seemingly contradictory findings from previous simulation studies. Previous theoretical work (Brette, 2013) and model simulations (Baranauskas et al., 2013; Raghuram et al., 2019; Telenczuk et al., 2017) claimed that the threshold should decrease when the AIS moves away from the soma, because of increased electrical isolation. This claim is valid under two main conditions: 1) that the neuron operates in the resistive coupling regime, meaning that the proximal axon is thin compared to the somatodendritic compartment, 2) that there are no strong subthreshold currents at the AIS. Thus, Gulledge and Bravo (2016) found that the neuron can be more excitable when the AIS is away from the soma when the neuron is small (in that case, the number of dendrites was varied). If axon diameter remains large, then the neuron may indeed not be in the resistive coupling regime any more, in which case there is a positive (but weak) relation between AIS distance and excitability. However, we have shown that, both within and across cell types, smaller neurons tend to also have a thinner AIS. This suggests that the physiological regime is generally the resistive coupling regime (with the qualification that the data we analyzed were not exhaustive, and did not include dendritic size). Lezmy et al. (2017) have found in a pyramidal cell model that the neuron could also be more excitable when the AIS moves distally, but only when K_v7 channels were strongly expressed at the AIS. Indeed, in this case, K_v7 channels produce a hyperpolarizing current, which raises the somatic threshold by an amount proportional to AIS distance (the last term of the formula).

2.4.2 Limitations

To obtain this simple theoretical result, we have made a number of more or less drastic approximations detailed in the Results. Despite these approximations, the formula captures the main aspects of the phenomenon seen in a biophysical model, but there are also some discrepancies. In particular, while the relation between threshold and geometrical factors ($x_{1/2}$ and L) is well predicted quantitatively, the sensitivity of threshold to Nav channel conductance density tends to be underestimated (but still with a correct order of magnitude).

There are also assumptions that we have made both in the theory and in the biophysical model. A few important assumptions are: spikes are initiated in the initial segment and produce a "kink" at somatic spike onset; the somatic membrane potential is constant at the time scale of axonal spike initiation; Na^+ and K^+ currents are temporally separated at spike initiation. These are based on empirical findings (Brette, 2015; Hallermann et al., 2012), but they could differ in particular models, in which case this theory may not apply.

In our calculations, we have also assumed that the AIS is cylindrical, mainly because analytical calculations are not possible in the general case. In reality, the axon tapers near the soma. The AIS can also sit on an axon-bearing dendrite (Kole and Brette, 2018). As explained in the Results (*Role of axon morphology*), one must then consider not metric distances but axial resistances. If the tapering part overlaps with the AIS, then it is not possible to obtain analytical equations anymore; the formula should then be less quantitatively correct. Perhaps the most important point to keep in mind when examining the effect of AIS displacements over a non-uniform axon is that the total Na_v conductance varies if Na_v channel density is fixed. To avoid this confounding factor, the formula with total conductance G should be used: $V^*_{soma} \sim -k\log(x_{1/2}) - k\log(G)$.

The theory also assumes that the AIS is electrically close to the soma (i.e., relative to the axonal space length). In some neurons, such as dopaminergic neurons (González-Cabrera et al., 2017; Meza et al., 2018; Moubarak et al., 2019), this assumption may not hold and specific theoretical developments might be necessary.

Finally, we have essentially ignored changes in Na_v inactivation state. However, these could potentially make an important contribution, in particular for the effect of axonal currents on threshold. As we have seen, a hyperpolarizing current raises the somatic threshold by resistive coupling, by an amount equal to the relative hyperpolarization induced at the AIS. However, this could also deinactivate Na_v channels, which would lower the threshold. This effect would tend to cancel the effect due to resistive coupling, and the magnitude can be similar (Platkiewicz and Brette, 2011).

2.4.3 Changes in axon diameter

Axon diameter can change (slightly) with activity (Chéreau et al., 2017), although this has not been demonstrated at the AIS. It may also change on longer time scales, particularly during

development (Leterrier et al., 2017a). As explained in the Results, it is possible to take diameter changes into account in our analysis, resulting in the following extended formula:

$$V^*_{soma} \sim -k\log(x_{1/2}) - k\log(L) - k\log(g) + k\log(d) \tag{2.10}$$

where we neglected the modulation by axonal currents.

As we have seen, AIS diameter tends to be larger in larger neurons. The above formula indicates that the spike threshold can be maintained constant across cell types of very different sizes if position and length are constant in units of the axonal space length, that is, if they scale as $\sqrt{d}$. This suggests that smaller neurons should also have a smaller AIS in order to regulate the spike threshold. For example, the AIS measures just 5 µm to 10 µm in cerebellar granule cells (Osorio et al., 2010) and about 45 µm in layer 5 pyramidal cortical cells (Hamada et al., 2016). Their respective diameters are 0.1 µm to 0.2 µm and 1 µm to 1.5 µm. In chick nucleus laminaris, low frequency neurons have a large soma and a long AIS, while high frequency neurons have a small soma and short AIS (Kuba et al., 2005, 2006).

Axon diameter can also vary during development and with activity, by the regulation of neurofilaments (Costa et al., 2020; Laser-Azogui et al., 2015; Marszalek et al., 1996). According to the formula, the specific effect of radial growth of the AIS is to raise the threshold (assuming constant surface density of Na_v channels). Naturally, it is more difficult to measure changes in AIS diameter than in length, but this potential source of variation must be kept in mind when interpreting changes in AIS geometry.

2.4.4 Axo-axonic synapses

We have seen that axonal currents can modulate the threshold at the soma. Although we have only discussed K_v7 channels expressed in the AIS, the theory applies also to synaptic currents, in particular those produced at the axo-axonic synapses made by Chandelier cells onto the AIS of pyramidal cortical neurons (Fairen and Valverde, 1980; Somogyi et al., 1977). In this case, the current I in the formula must be understood at threshold, that is: $I = g_s(E_s - V_{threshold})$, where g_s is the synaptic conductance and E_s is the reversal potential. Thus, even if the synaptic currents are depolarizing at rest (values of $E_s = -60$ mV have been reported (Woodruff et al., 2009)), the effect on excitability is still inhibitory, as long as the reversal potential is below axonal threshold. An additional inhibitory effect can be produced if the conductance is strong (specifically, relative to the axial conductance $1/R_a$, see Methods).

In relation to geometry, the effect of an axo-axonic synapse is stronger if the synapse is more distal, up to the AIS position. Beyond the AIS end position, the effect of the synapse does not increase anymore, because it is the voltage gradient between the soma and AIS that modulates excitability. In hippocampal neurons, (Wefelmeyer et al., 2015) observed that chronic depolarization made the AIS move distally, but axo-axonic synapses did not move. As a result, a larger proportion of synapses are between the soma and AIS end, where they can modulate excitability. Thus, theory predicts that the total inhibitory effect is stronger (consistent with that study's conclusions).

2.4.5 Other aspects of electrical function

In this study, we only examined excitability, that is, the ability to trigger an action potential. However, there are others important aspects of electrical function. In many neurons, the action potential is transmitted and regenerated by somatic Na_v channels with higher activation voltage. This could be important for synaptic plasticity (propagating the action potential to the dendrites), but also for intrinsic plasticity (since the nucleus is in the soma). For this transmission to be successful, the current transmitted to the soma at spike initiation must be such as to produce the required depolarization. We have shown theoretically that this current depends primarily on the AIS start position Δ (Hamada et al., 2016); as a first (rough) approximation, it is inversely proportional to AIS position (Ohm's law). Thus, AIS position can modulate the transmitted current very strongly, and indeed this strong modulation appears necessary given the three orders of magnitude of variability in input capacitance of various cell types (3500 pF in some motoneurons (Cormery et al., 2005), about 3 pF in cerebellar granule cells (Cathala et al., 2003)).

In contrast, observed variations in voltage threshold appear rather modest, especially compared to variations in excitability due to changes in input resistance (again 3 orders of magnitude across cell types). An analysis of a large database of electrophysiological recordings reports a standard deviation in voltage threshold of just 6 mV (Tripathy et al., 2015), and this includes considerable variations in methodological conditions (liquid junction potential, measurement method, solutions, etc). This is perhaps to be expected, given that the functional voltage range for electrical function is constrained by the properties of ionic channels (it cannot vary by orders of magnitude). Thus, it is conceivable that AIS position and length are adjusted so that voltage threshold remains stable and transmitted current is adapted to the cell's morphology. This is of course speculative, because other aspects of electrical function could also be considered. For example, action potential speed at the AIS depends on local conductance, which is composed of the axial conductance (therefore AIS position) and of the total Na_v conductance (therefore AIS length). Thus, structural plasticity of the AIS might be related to various aspects of electrical function, beyond excitability in the classical sense.

2.5 Material and methods

2.5.1 Cable theory

Sealed end

We consider a cylindrical semi-infinite axon, with a current injected at distance x from the sealed end (no current passing through). The input resistance decomposes into $R(x)^{-1} = R_{proximal}^{-1} + R_{distal}^{-1}$. R_{distal} is the resistance of a semi-infinite axon: $R_{distal} = r_a\lambda$. $R_{proximal}$ is the resistance of a short segment of axon of size x, with a sealed end. This resistance is (Tuckwell, 1988a):

$$R_{proximal}(x) = \frac{r_a\lambda}{\tanh(x/\lambda)} \tag{2.11}$$

The ratio $R_{proximal}/R_{distal}$ is therefore $\tanh(x\lambda)^{-1}$. Thus, for a short piece of axon ($x << \lambda$),

this ratio is λ/x, a large number. More precisely:

$$R(x) = r_a\lambda\,(1+\tanh(x/\lambda))^{-1} \tag{2.12}$$

and a Taylor expansion gives $R(x) \approx r_a(\lambda - x)$.

Killed end

We consider a cylindrical semi-infinite axon with a killed end (open membrane) (Tuckwell, 1988a). In this case, the resistance of the proximal segment is

$$R_{proximal}(x) = r_a\lambda \tanh(x/\lambda) \tag{2.13}$$

When $x << \lambda$, we have $R_{proximal} \approx r_a x$. The distal axon has resistance $R_{distal} = r_a\lambda$. Therefore, $R_{proximal}/R_{distal} \approx x/\lambda$. A Taylor expansion gives $R(x) \approx r_a x(1 - x/\lambda)$. Thus, the input resistance is approximately proportional to distance.

Large soma

With a large (but not infinitely large) soma, we simply add the resistance of the soma to the proximal resistance, which yields:

$$R(x)^{-1} \approx (r_a x + R_{soma})^{-1} + (r_a\lambda)^{-1}. \tag{2.14}$$

2.5.2 Passive neuron models

Passive models presented in fig. 2.1 and fig. 2.2 consisted of a spherical soma (small: 1 µm; large: 100 µm) and a long and thin cylindrical axon (diameter: 1 µm; length: 2 mm). Specific membrane capacitance is C_m= 0.9 µF cm^{-2}; specific membrane resistance is R_m= 15 000 Ω cm^{-2}; leak reversal potential is $E_L = -75$ mV; intracellular resistivity is R_i = 100 Ω cm. With these values, the characteristic space length is about $\lambda \simeq 600$ µm. Models were simulated with Brian 2 (Stimberg et al., 2019) with 100 µs time step and 2 µm spatial resolution.

2.5.3 Analysis of patch clamp recordings

We analyzed simultaneous patch clamp recordings of soma and axonal blebs in cortical layer 5 pyramidal neurons provided by Hu and Bean (2018) (fig. 2.2 D-F). We analyzed all recordings where the axon bleb is less than 200 µm away from the soma (a distance substantially smaller than the characteristic length) and is stimulated by a current pulse (n = 15), and selected the smallest current pulse in each recording. To calculate the local and somatic depolarizations at $t = 300$ µs, we calculate the median potential between 200 µs and 400 µs and subtract the baseline, defined as the median potential over the 5 ms before the pulse. The resistances are then obtained by dividing by the current amplitude.

2.5.4 Analysis of neuroanatomical data

In fig. 2.3, we extracted measurements of AIS diameter from electron microscopy studies, taken at the end of the AIS. Given the optical diffraction limit, it is necessary to consider electron

rather than optical microscopy measurements, at least for thin axons. Soma diameter was measured with optical or electron microscopy. Four data points correspond to measurements of mean diameters, listed in table 2.2. Soma and AIS diameters were taken from different studies (except cat olivary cells), but with matched cell type and species.

We also digitized individual measurements in 3 studies: anterior horn cells (motoneurons) of human spinal cord, 44-75 years old (Sasaki and Maruyama, 1992); ventral horn cells (motoneurons) cat spinal cord, P0-P16 (Conradi and Ronnevi, 1977); pyramidal, stellate and Martinotti cells of motor and somatosensory cortex of Rhesus monkeys, young adults (Sloper and Powell, 1979).

Adult cat olivary cells	Soma	21.7 µm ± 3.7 µm	(De Zeeuw et al., 1990)
	AIS	1.1 µm ± 0.3 µm	(Ruigrok et al., 1990)
Adult rat CA3 pyramidal cells	Soma	20.9 µm ± 3.2 µm	(Buckmaster, 2012)
	AIS	1.2 µm ± 0.4 µm	(Kosaka, 1980)
Adult rat Purkinje cells	Soma	21.9 µm ± 1.9 µm	(Takacs and Hamori, 1990)
	AIS	0.7 µm ± 0.2 µm	(Somogyu and Hamori, 1976)
Adult mouse cerebellar granule cells	Soma	5.9 µm ± 0.3 µm	(Delvendahl et al., 2015)
	AIS	0.2 µm (no s.d.)	(Palay and Chan-Palay, 2012)

Table 2.2: Mean diameter of soma and AIS in 4 cell types, extracted from electron microscopy studies.

2.5.5 Simplified model

In fig. 2.6 C-D, we used a simplified cable model with only non-inactivating Na_v channels as a first check of analytical expressions, similar to Brette (2013). A spherical soma of diameter 50 µm is attached to an axonal cylinder of diameter 1 µm and length 300 µm (soma diameter is in fact irrelevant as the soma is voltage-clamped). Specific membrane capacitance is C_m= 0.9 µF cm^{-2}; R_m= 15 000 Ω cm^{-2}; leak reversal potential is $E_L = -75$ mV; intracellular resistivity is R_i = 100 Ω cm. Na_v channels are placed at a single position on the axon. We used simple single gate activation dynamics with fixed time constant:

$$\begin{aligned} I_{Na} &= Gm(E_{Na} - V) \\ \tau_m \frac{dm}{dt} &= m_\infty(V) - m \\ m_\infty(V) &= \frac{1}{1 + \exp((V_{1/2} - V/k))} \end{aligned} \tag{2.15}$$

where $E_{Na} = 70\,\text{mV}$, $k = 5\,\text{mV}$, $V_{1/2} = -35\,\text{mV}$ and $\tau_m = 53.6\,\mu\text{s}$ (corresponding to 150 µs before temperature correction, see below). Total conductance G is varied between 200 and 600 nS. To give an order of magnitude, this corresponds to a conductance density of about $2000\,\text{S}\,\text{m}^2$ to $6000\,\text{S}\,\text{m}^2$ for a 30 µm long AIS. The model is simulated in voltage-clamp and an action potential is detected when half the Na_v channels at the AIS are open. We used the Brian 2 simulator (Stimberg et al., 2019) with 5 µs time step and 1 µm spatial resolution.

2.5.6 Biophysical model

The biophysical model has a simple geometry, consisting of a spherical soma (30 µm diameter), a long dendrite (diameter: 6 µm, length: 1000 µm) and a thin unmyelinated axon (diameter: 1 µm, length; 500 µm). When not specified, the AIS extends from 5 µm to 35 µm from the soma. Specific membrane capacitance is C_m= 0.9 µF cm^{-2}; R_m= 15 000 Ω cm^{-2}; leak reversal potential is $E_L = -75\,\text{mV}$; intracellular resistivity is $R_i = 100\,\Omega\,\text{cm}$.

The model includes Na_v and K_v channels based on Hodgkin-Huxley type equations:

$$\begin{aligned} I_{Na} &= g_{Na} m h (E_{Na} - V) \\ I_{Kv1} &= g_{Kv1} n^8 (E_K - V) \\ I_{Kv7} &= g_{Kv7} q (E_K - V) \end{aligned} \tag{2.16}$$

where $E_{Na} = 70\,\text{mV}$, $E_K = -90\,\text{mV}$. K_v7 channels were only included in fig. 2.11. The Na^+ current has a single gate, both for simplicity and because it appears to be empirically adequate (Baranauskas and Martina, 2006). The K^+ current has 8 gates because it matches empirical data for the K_v1 current (Kole et al., 2007). This is important to ensure that the current activates with a delay and thereby does not substantially overlap the Na^+ current at spike initiation. Each gating variable x is governed by a standard kinetic equation:

$$\frac{dx}{dt} = \alpha_x (1 - x) - \beta_x x \tag{2.17}$$

where α_x and β_x are opening and closing rates, respectively. For the voltage-dependent rates, we chose expressions that feature a minimal number of parameters with simple interpretation:

$$\begin{aligned} \alpha_x(V) &= \frac{1}{2 k_x \tau_x^*} \cdot \frac{V - V_x^{1/2}}{1 - e^{-\left(V - V_x^{1/2}\right)/k_x}} \\ \beta_x(V) &= -\frac{1}{2 k_x \tau_x^*} \cdot \frac{V - V_x^{1/2}}{1 - e^{\left(V - V_x^{1/2}\right)/k_x}} \end{aligned} \tag{2.18}$$

where x is m or n. For inactivation (h), opening and closing rates are simply exchanged. These expressions have the following properties: the equilibrium value ($x_\infty(V)$) is a Boltzmann function with half-activation value $V_x^{1/2}$ and slope factor k_x; the voltage-dependent time constant is a bell curve peaking at $V_x^{1/2}$, where its value is τ_x^*.

Parameter values vary substantially between studies. For Na_v channels of proximal axons, empirically measured slope factors vary between 5 mV to 8 mV for activation and 5 mV to 9 mV

for inactivation (Engel and Jonas, 2005; Hu et al., 2009; Kole et al., 2008; Schmidt-Hieber and Bischofberger, 2010). When fitted on the hyperpolarized part important for spike initiation, the activation curve of Na_v channels tend to be lower, as explained in (Platkiewicz and Brette, 2010) (fig. 9) and observed empirically (Baranauskas and Martina, 2006) (fig. 2). Therefore, we simply used rounded values, $k_m = k_h = 5\,\text{mV}$. For half-activation values, we also used rounded values consistent with the literature, with voltage-dependent curves hyperpolarized by 5 mV in the AIS compared to the soma (table 2.3). We used $\tau_m^* = 150\,\mu\text{s}$ as in (Schmidt-Hieber and Bischofberger, 2010), noting that such short time constants are challenging to measure experimentally, especially in axons. For inactivation, we used $\tau_h^* = 5\,\text{ms}$. This value was chosen so that the Na^+ current during the action potential shows a small overlap with the K^+ current, as experimentally observed (Hallermann et al., 2012) (fig. 4E, F). Conductance densities were set as stated in (table 2.3), following experimental and modeling studies (Hallermann et al., 2012; Hu et al., 2009; Kole et al., 2008; Lorincz and Nusser, 2010). Finally, rates were corrected for temperature. Recordings on which parameter values are based were done at T=23 °C, and we set the simulation temperature at 33 °C by applying a temperature factor $Q_{10}^{(33-23)/10}$, with $Q_{10} = 2.8$ (Baranauskas and Martina, 2006).

Densities of K_v1 channels were set similarly to previous studies (Hallermann et al., 2012; Hu et al., 2009; Kole et al., 2008) (see table 2.3). K_v1 channels activate quickly and inactivate slowly (Kole et al., 2007). We did not include inactivation because it has no influence on spike initiation. Parameter values were obtained by least square fitting a Boltzmann function to the activation curve ($n_\infty^8(V)$) obtained from recordings of axonal outside-out blebs of layer 5 pyramidal neurons (Kole et al., 2007). As data were recorded at 33 °C, transition rates were not corrected for temperature.

In fig. 2.11, we added a K_v7 conductance on the distal half of the AIS. K_v7 channels produce the M-current, which activates slowly at low voltage and does not inactivate (Battefeld et al., 2014). We used parameter values rounded from (Battefeld et al., 2014).

2.5.7 Spike threshold with a point AIS

A formula for the spike threshold with a point AIS has been derived in Brette (2013). Here we put a simpler alternative derivation based on a rescaling argument.

In the hyperpolarized range, the Na^+ current changes approximately exponentially with voltage (Baranauskas and Martina, 2006; Hodgkin and Huxley, 1952a): $I_{Na} \simeq G\exp(V/K)(E_{Na} - V_{1/2})$, where V is the axonal membrane potential, G is the total available Na^+ conductance, k is the Boltzmann slope factor of Na_v channels and $V_{1/2}$ is the half-activation voltage of Na_v channels. As the soma is a current sink (hypothesis of resistive coupling theory), this current flows towards the soma as a resistive current: $I_{axial} = (V - V_s)/R_a$, where V_s is the somatic membrane potential and R_a is the axial resistance between soma and AIS. Therefore, we have the following identity:

$$R_a G(E_{Na} - V_{1/2})\exp(V/k) = V - V_s \tag{2.19}$$

Passive properties	R_m	$15\,000\,\Omega\,\mathrm{cm}^{-2}$
	E_L	$-75\,\mathrm{mV}$
	R_i	$100\,\Omega\,\mathrm{cm}$
	C_m	$0.9\,\mu\mathrm{F}\,\mathrm{cm}^{-2}$
Na_v channels	g_{Na}, soma	$250\,\mathrm{S}\,\mathrm{m}^{-2}$
	g_{Na}, dendrites and axon (non AIS)	$50\,\mathrm{S}\,\mathrm{m}^{-2}$
	g_{Na}, AIS	variable (default: $3500\,\mathrm{S}\,\mathrm{m}^{-2}$)
	E_{Na}, soma	$70\,\mathrm{mV}$
	$V_m^{1/2}$, soma	$-30\,\mathrm{mV}$
	$V_h^{1/2}$, soma	$-60\,\mathrm{mV}$
	$V_m^{1/2}$, AIS	$-35\,\mathrm{mV}$
	$V_h^{1/2}$, AIS	$-65\,\mathrm{mV}$
	k_m	$5\,\mathrm{mV}$
	k_h	$5\,\mathrm{mV}$
	τ_m^*	$150\,\mu\mathrm{s}$ (corrected: $54\,\mu\mathrm{s}$)
	τ_h^*	$5\,\mathrm{ms}$ (corrected: $1.8\,\mathrm{ms}$)
K_v1 channels	g_K, soma	$250\,\mathrm{S}\,\mathrm{m}^{-2}$
	g_K, dendrites and axon (non AIS)	$50\,\mathrm{S}\,\mathrm{m}^{-2}$
	g_K, AIS	variable (default: $1500\,\mathrm{S}\,\mathrm{m}^{-2}$)
	E_K, soma	$-90\,\mathrm{mV}$
	$V_n^{1/2}$, soma	$-70\,\mathrm{mV}$
	k_n	$20\,\mathrm{mV}$
	τ_n^*	$1\,\mathrm{ms}$
K_v7 channels	g_{Kv7}	variable
	E_K, soma	$-90\,\mathrm{mV}$

Table 2.3: Parameters values of the biophysical model. Time constants corrected for temperature are indicated in brackets.

With the following change of variables:

$$\begin{aligned} U &= V + k\log(R_a G(E_{Na} - V_{1/2})) \\ U_s &= V_s + k\log(R_a G(E_{Na} - V_{1/2})) \end{aligned} \tag{2.20}$$

we obtain:

$$\exp(U/k) = U - U_s \tag{2.21}$$

This equation is now independent of G and R_a. We denote U^* the threshold for this equation, that is, such that the equation has a bifurcation when $U_s = U^*$. For the original equation, this corresponds to a bifurcation when $V_s = U^* - k\log(R_a G(E_{Na} - V_{1/2}))$.

2.5.8 Spike threshold with an extended AIS starting from the soma

We consider a cylindrical axon of diameter d. The AIS has length L and starts from the somatic end. It has a uniform density of Na_v channels. The total Na_v conductance is

$$G = g\pi dL \tag{2.22}$$

where g is the surface conductance density. We neglect leak and K^+ currents, as well as all time-varying phenomena. The cable equation then becomes:

$$\frac{d^2V}{dx^2} \propto -ge^{V/k} \tag{2.23}$$

with boundary conditions $V(0) = V_s$ (somatic potential) and $V'(L) = 0$ (no axial current flowing towards the distal axon). In units of the AIS length L, this equation reads:

$$\frac{d^2V}{d(x/L)^2} \propto -gL^2e^{V/k} = \exp\left(\frac{V + k\log(gL^2)}{k}\right) \tag{2.24}$$

By the same argument as in the previous section, it follows that the threshold varies with g and L as

$$V_s = \text{constant} - k\log(g) - 2k\log(L) \tag{2.25}$$

This is equivalent to:

$$V_s = \text{constant} - k\log(G) - k\log(L) \tag{2.26}$$

where G is the total Na_v conductance ($G = g\pi dL$ for a cylindrical axon), for a different constant.

We now calculate the constant. With the proportionality factor, the equation is approximately:

$$\frac{d^2V}{d(x/L)^2} = -\pi dr_a gL^2(E_{Na} - V_{1/2})e^{(V-V_{1/2})/k} \tag{2.27}$$

where r_a is resistance per unit length and $V_{1/2}$ is the half-activation voltage of Na_v channels. Here the driving force $(E_{Na} - V)$ has been approximated by $(E_{Na} - V_{1/2})$ as in Brette (2013). We now write the following change of variables:

$$\begin{aligned} U &= \frac{V - V_{1/2}}{k} + \log\left(\pi dr_a gL^2 \frac{E_{Na} - V_{1/2}}{k}\right) \\ y &= x/L \end{aligned} \tag{2.28}$$

and we note $U' = dU/dy$. That is, voltage is in units of k and space is in units of AIS length L. The rescaled cable equation is:

$$U'' + e^U = 0 \tag{2.29}$$

with the boundary conditions:

$$\begin{aligned} U(0) = U_0 &= \frac{V_s - V_{1/2}}{k} + \log\left(\pi d r_a g L^2 \frac{E_{Na} - V_{1/2}}{k}\right) \\ U'(1) &= 0 \end{aligned} \tag{2.30}$$

This equation is analytically solvable, with general solution

$$U(y) = \log\left(\frac{c_1}{2}\right) - 2\log\left(\cosh\left(\frac{1}{2}\sqrt{c_1(y+c_2)^2}\right)\right) \tag{2.31}$$

From $U'(1) = 0$, it follows that $c_2 = -1$. We then obtain for the boundary condition at 0:

$$U(0) = U_0 = \log\left(\frac{c_1}{2}\right) - 2\log\left(\cosh\left(\sqrt{c_1}/2\right)\right) \tag{2.32}$$

which defines c_1 as an implicit function of U_0. We look for a bifurcation, that is, a value of U_0 when the number of solutions changes. This is obtained by setting the derivative of the right hand-side to 0, which gives:

$$\frac{\sqrt{c_1}}{2}\tanh\left(\frac{\sqrt{c_1}}{2}\right) = 1 \tag{2.33}$$

The solution can be calculated: $\sqrt{c_1}/2 \approx 1.2$, giving $c_1 \approx 5.8$. Finally, substituting this value in the above equation gives $U_0 \approx -1.3$. This is the spike threshold for the rescaled cable equation. Back to the original dimensions, we obtain:

$$V_s = V_{1/2} - 0.13k - k\log\left(r_a \frac{E_{Na} - V_{1/2}}{k}\right) - k\log(\pi d g) - 2k\log(L) \tag{2.34}$$

This is the same equation as for a point AIS with the same total conductance G at position L, except that the term $-0.13k$ replaces $-k$. Thus, the difference in threshold between an extended AIS of length L starting from the soma and a point AIS at position L is $0.87k$ (4.3 mV if $k = 5$ mV). Therefore, the threshold of the extended AIS is the same as a point AIS placed at position $x = e^{-0.87}L \approx 0.42L$, which is near the middle of the extended AIS. The error made by placing the equivalent point AIS at the middle point $x = L/2$ is $k\log(0.5/0.42) \approx 0.9$ mV (with $k = 5$ mV).

The expression of $U(y)$ allows us to calculate the potential along the axon at threshold, and in particular at the AIS end, where the expression simplifies: $U(1) = \log(c_1/2) \approx 1.06$. We can see that the threshold at the AIS end is above the somatic threshold by about 1.2 k (1.06+0.13). This is consistent with simultaneous patch clamp measurements at the soma and AIS (Kole and Stuart, 2008).

2.5.9 Spike threshold with an extended AIS starting away from the soma

We apply the same strategy for the more general case where the AIS starts at a distance away from the soma. We choose the origin of x at the AIS start, so that we obtain exactly the same

cable equation as before, except the boundary condition at $x = 0$ now expresses the fact that the piece of axon between the soma and AIS is purely resistive. This implies that the potential varies linearly with distance, and therefore:

$$V(0) = V_s + \Delta \frac{dV}{dx}(0) \tag{2.35}$$

Thus, we obtain the same solution as previously except for the boundary condition at 0:

$$U(0) = U_0 = \log\left(\frac{c_1}{2}\right) - 2\log\left(\cosh\left(\frac{\sqrt{c_1}}{2}\right)\right) - \frac{\Delta}{L}\sqrt{c_1}\tanh\left(\frac{\sqrt{c_1}}{2}\right) \tag{2.36}$$

As before, to find the bifurcation point we set the derivative of the right hand-side (with respect to c_1) to 0, and obtain:

$$f(z) \equiv \left(1 + \frac{\Delta}{L}\right) z\tanh(z) + \frac{\Delta}{L} z^2(1 - \tanh^2(z)) - 1 = 0 \tag{2.37}$$

where $z = \sqrt{c_1}/2$. This defines z, c_1 and therefore U_0 as implicit functions of Δ/L, which can be calculated numerically (which we did in fig. 2.9). The somatic threshold is then:

$$V_s = V_{1/2} + kU_0(\Delta/L) - k\log\left(r_a \frac{E_{Na} - V_{1/2}}{k}\right) - k\log(\pi dg) - 2k\log(L) \tag{2.38}$$

The somatic threshold for a point AIS with the same total conductance placed at the midpoint $x^* = \Delta + L/2$ is:

$$V_s^* = V_{1/2} - k - k\log\left(r_a \frac{E_{Na} - V_{1/2}}{k}\right) - k\log(\pi dgL) - k\log(x^*) \tag{2.39}$$

The difference is:

$$V_s - V_s^* = k\left(U_0\left(\frac{\Delta}{L}\right) + 1 + \log\left(\frac{\Delta}{L} + \frac{1}{2}\right)\right) \equiv kF\left(\frac{\Delta}{L}\right) \tag{2.40}$$

The variable Δ/L varies between 0, where the AIS starts from the soma, and $+\infty$, where the AIS is a single point. Figure 2.13 shows that the function F is a monotonously decreasing function of Δ/L. When $\Delta/L = 0$, the AIS starts from the soma, and we have seen in the previous section, $V_s - V_s^* \approx 0.9\,\text{mV}$ ($0.17\,k$). When $\Delta/L = +\infty$, the AIS is a single point and therefore $V_s = V_s^*$. Thus, the somatic threshold of the extended AIS is approximately equivalent to the threshold of a point AIS with the same total conductance, placed at the midpoint $x_{1/2}$, with a precision of about $0.17k \approx 0.9\,\text{mV}$.

2.5.10 Effect of an axonal current on spike threshold

The effect of an axonal current on the spike threshold of a point AIS has been derived in (Brette, 2013, supplementary text). We show that this extends to an extended AIS, where a current I is injected at the start of the AIS. In that case, the cable equation is unchanged, but the boundary condition at the AIS start ($x = 0$) now includes the current:

$$V(0) = V_s + \Delta \frac{dV}{dx}(0) + R_a I \tag{2.41}$$

where R_a is the axial resistance between soma and AIS start. Thus, inserting this current is equivalent to shifting the somatic potential by an amount I/R_a. Thus, the bifurcation

occurs when $V_s + R_a I = V_s^*$, where V_s^* is the somatic threshold without modulation ($I = 0$). The somatic threshold with modulation is therefore $V_s^* - R_a I$. At threshold, the boundary condition is independent of I, and therefore the axonal voltage at threshold does not depend on I.

If the current is injected at the AIS end, then the boundary condition at the AIS end becomes:

$$\frac{dV}{dx}(L) = r_a I \tag{2.42}$$

The cable equation can still be solved analytically as before. However, it does not lead to any simple expression of threshold as a function of I. It is found numerically that the somatic threshold changes almost (but not exactly) linearly with I, and the threshold at the AIS end varies slightly with I, in the other direction (decreases for a strong hyperpolarizing current).

If current is uniformly injected over the AIS, then boundary conditions are unchanged but the current density is inserted in the cable equation. To our knowledge, it has no analytical solution.

The theoretical analysis above applies to an injected current. The effect of inserting a conductance, i.e., $I = g^*(E - V)$, can be understood in the point AIS model by noting that the conductance g^* is in parallel with the axial resistance R_a. Therefore, it is equivalent to replacing R_a by $(R_a^{-1} + g^*)^{-1}$. As long as g^* is small compared to $1/R_a$, this effect is negligible. That is, the current-based theory holds, with $I = g^*(E - V_{threshold})$, where $V_{threshold}$ is the AIS threshold. If g^* is large, the effective change in R_a must be taken into account.

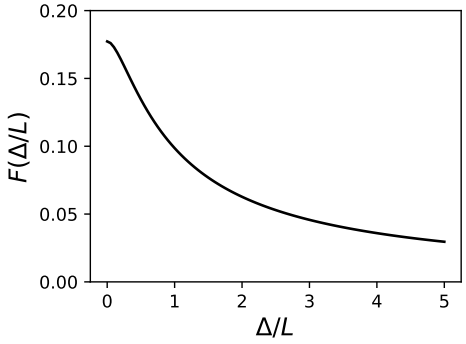

Figure 2.13: Corrective term $F(\Delta/L)$. The threshold of an extended AIS differs from that of point AIS with the same total conductance placed at the midpoint by at most $kF(\Delta/L)$.

2.5.11 Data availability

Code generating all figures is available at:
`https://github.com/romainbrette/AIS-geometry-and-excitability-2019`.

2.5.12 Acknowledgments

We thank Marcel Stimberg for assistance with simulations, Bruce Bean and Wenqin Hu for providing their electrophysiological data, and Christophe Leterrier and Boris Barbour for discussions.

3 Axial current at spike initiation in retinal ganglion cells

In this chapter we present a work supervised by Romain Brette and done in collaboration with Martijn Sierksma, Annabelle Réaux-La Goazigo and Xavier Nicol. At the time of writing this thesis, this chapter will soon be submitted for peer-review in the Elife journal. The electrophysiological recordings were performed by Martijn Sierksma (former post-doc in Xavier Nicol's team at the Vision Institute) and the author of this thesis performed the immunohistochemical labellings, analysed the data and ran the model simulations. The author learned immunohistochemistry with Annabelle Réaux-Le Goazigo (researcher at the Vision Institute).

3.1 Abstract

The action potential (AP) of most vertebrate neurons initiates in the axon initial segment (AIS), and is then transmitted to the soma where it is regenerated by somatodendritic sodium channels. For successful transmission, the AIS must produce a strong axial current, so as to depolarize the soma to the threshold for somatic regeneration. Theoretically, this axial current depends mainly on AIS geometry and Na^+ conductance density. We measured the axial current of mouse RGCs using whole-cell recordings with post-hoc AIS labeling. We found that this current is large, implying high Na^+ conductance density, and carries a charge that covaries with capacitance so as to depolarize the soma by $\sim 30\,\text{mV}$. Additionally, we observed that the axial current attenuates strongly with depolarization, consistent with sodium channel inactivation, but temporally broadens so as to preserve the transmitted charge. Thus, the AIS appears to be organized so as to reliably back-propagate the axonal AP.

3.2 Introduction

In most vertebrate neurons, APs (APs) initiate in the axon initial segment (AIS), a highly organized structure near the soma (Bender and Trussell, 2012), then propagate forward to the axon terminals and backward to the soma and dendrites (Debanne et al., 2011). This backward transmission is functionally important for synaptic plasticity, which requires a precisely timed signal of firing activity at the synapse (Caporale and Dan, 2008). It is also important for long-term intrinsic plasticity since the soma holds the genetic material (Daoudal and Debanne, 2003), and presumably also for structural plasticity of the AIS, which depends on somatic voltage-gated calcium channels (Evans et al., 2013).

At spike initiation, the soma receives an axial current from the AIS, which depolarizes the membrane. When the somatic membrane potential is depolarized about 30 mV above firing threshold, the AP is regenerated by somatic sodium channels (Kole and Stuart, 2008). Hamada et al. (2016) found indirect evidence that the axial current is matched to the capacitance of the somatodendritic compartment, as they observed that larger cortical pyramidal cells tend to have a more proximal AIS. Indeed, theory predicts that a stronger current is produced when the AIS is closer to the soma. However, the axial current was not directly measured.

This measurement could also allow estimating the conductance density of AIS sodium channels, in particular using resistive coupling theory (Brette, 2013; Kole and Brette, 2018). The fact that the AIS, a small structure, must produce a current able to charge a much larger piece of membrane (soma and proximal dendrites), suggests that conductance density should be high, in agreement with immunochemical observations (Lorincz and Nusser, 2010). However, this has remained a somewhat contentious issue (Fleidervish et al., 2010) because direct patch-clamp measurements in the intact AIS indicate low conductance density (Colbert and Pan, 2002), which could be due to the anchoring of channels to the cytoskeleton (Kole et al., 2008).

Finally, it is known that sodium channels can inactivate substantially below threshold, resulting in spike threshold adaptation (Azouz and Gray, 2000; Fontaine et al., 2014; Platkiewicz and Brette, 2011). This suggests that the axial current at spike initiation may also vary substantially. If this is the case, then how can spikes be reliably transmitted to the soma?

To address these questions, we measured the axial current and spontaneous action potentials in ganglion cells of isolated mouse retina (n = 20) followed by ankyrin-G-antibody labelling to measure AIS geometry. We examined the axial current at spike initiation, just below threshold, and with threshold adaptation and compared these results to theoretical predictions.

3.3 Results

3.3.1 The axial current at spike initiation

Action potentials of retinal ganglion cells

Early work on vertebrate motoneurons showed that APs recorded in the soma typically consist of two components (Coombs et al., 1957; Fatt, 1957): an abrupt depolarization due to the axial current originating from the axon initial segment, followed by a regeneration of the AP at a higher potential, by the opening of somatic sodium channels. These two components are clearly distinguished in recordings of spontaneous APs of retinal ganglion cells (RGC) (fig. 3.1). Figure fig. 3.1 A shows a typical AP, rising abruptly from threshold. The voltage derivative dV/dt shows two distinct components (fig. 3.1 B), which appear most clearly when plotted against the membrane potential V (fig. 3.1 C). We define the regeneration threshold as the potential when the acceleration d^2V/dt^2 is maximal (fig. 3.1 D). In n = 10 cells with a stable reference potential, we observed that the spike threshold was -49 $\pm$ 3.8 mV (s.d.) (fig. 3.1

E) while the regeneration threshold is -16 ± 4.6 mV (s.d.) (fig. 3.1 F), about 33 ± 5 mV (s.d.) higher (fig. 3.1 G). This is similar to previous measurements in layer 5 cortical pyramidal cells (Kole and Stuart, 2008).

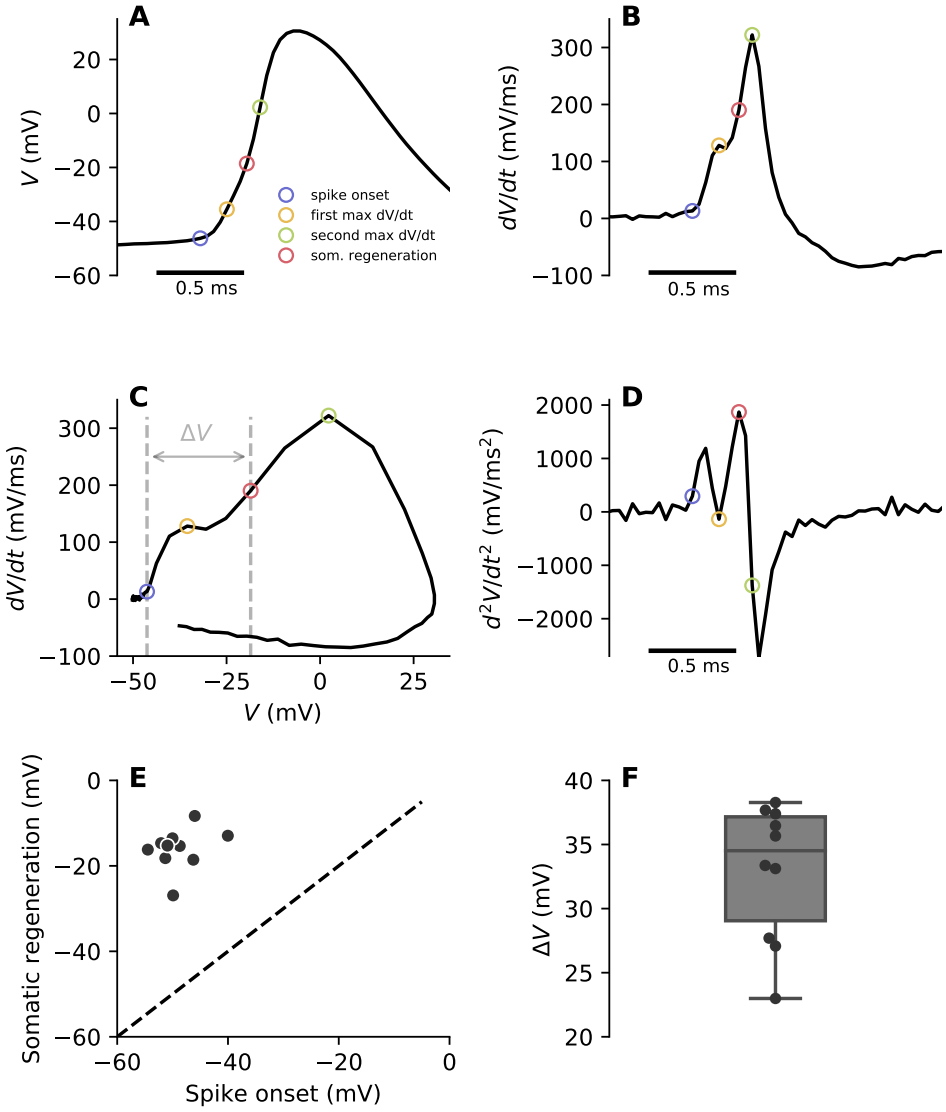

Figure 3.1: Properties of spontaneous APs of retinal ganglion cells. **A**, Spontaneous AP of a RGC, highlighting spike onset (blue), point of maximum dV/dt of the first component (yellow), somatic regeneration threshold (red), point of maximum dV/dt of the second component (green). **B**, Time derivative of the AP trace shown in A. **C**, Phase plot showing dV/dt vs. V. The double arrow shows the difference ΔV between spike onset and regeneration threshold. **D**, Second derivative of the AP trace. Somatic regeneration threshold is defined as the point of maximum acceleration. **E**, Statistics of pike onset over all measured APs (n = 10). **F**, Statistics of somatic regeneration threshold. **G**, Statistics of ΔV.

Measuring the axial current

We measured the axial current with whole-cell voltage clamp by stepping the command potential from $V_0 = -60\,\text{mV}$ to a variable potential V (fig. 3.2). Voltage steps above a threshold value evoke large spikes of inward current (fig. 3.2 A). When the peak current is plotted against voltage, a sharp discontinuity is seen (fig. 3.2 B). Similar recordings have been reported in several cell types in whole-cell patch (Diwakar et al., 2009; Magistretti et al., 2006; Milescu et al., 2010), and also in two-electrode voltage clamp recordings of cat motoneurons (Barrett and Crill, 1980). As argued by Milescu et al. (2010), this abrupt increase in current most likely reflects the axial current produced by the AIS AP. Indeed, the current-voltage curve shows a plateau reflecting the all-or-none axonal spike, followed by an increase at higher potential, most likely reflecting the somatic sodium current. These currents were eliminated by 1 μM tetrodotoxin, a potent sodium channel blocker (2 ± 0.4 % current remaining, n = 4 cells, paired t3 = 4.5, p = 0.02).

Accurate measurement of the axial current is complicated by the presence of the series resistance R_s. Together with the membrane capacitance C, the series resistance forms a RC circuit that low-pass filters the current with a characteristic time constant $\tau = R_s C$. We correct the recorded current by removing the capacitive current $\tau dI/dt$, as described by Traynelis (1998), with the time constant directly estimated from a passive to response to a small voltage step (fig. 3.2 C) (see Methods). Figure 3.2 D shows a recording from a retinal ganglion cell (black). After correction, the peak current is larger (red). We tested the effect of series resistance and the correction in a simple biophysical model of a RGC with an extended AIS, with the electrode modeled as a resistance (see Methods). Figure 3.2 E shows that the peak recorded current decreases substantially when increasing R_s, but this error is well corrected by the method described above. The spike threshold is only marginally affected by the series resistance (fig. 3.2 F; the exact value of the threshold depends on model parameters). We selected cells with residual series resistance smaller than $5\,\text{M}\Omega$ (n = 20). There was a correlation between measured peak axial current I_p and R_s (fig. 3.2 G, Pearson correlation r = 0.43, p = 0.06), but it remained small. We observed no correlation between spike threshold and R_s (fig. 3.2 H, p = 0.25, Pearson test). Therefore, the impact of R_s on our measurements should be moderate.

Transmission of the axial current to the soma

When the soma is not clamped, the axial current at spike initiation charges the somatic capacitance (and proximal dendrites). Therefore, we expect that the axial current measured in voltage clamp is approximately equal to the capacitive current $C \cdot dV/dt$ during the initial rise of an AP recorded in current clamp (more precisely, $C \cdot dV/dt = -I_p$, as I_p is the current from the amplifier to the cell). This equality assumes that the other currents are negligible, which is plausible given the typical amplitude of axial currents (about 9 nA in fig. 3.2 D). Another caveat is that the capacitance is only well defined for an isopotential cell. We estimated the effective capacitance of cells on the first ms of the response to a small current pulse, and measured dV/dt in the initial phase of a spontaneous AP (see Methods).

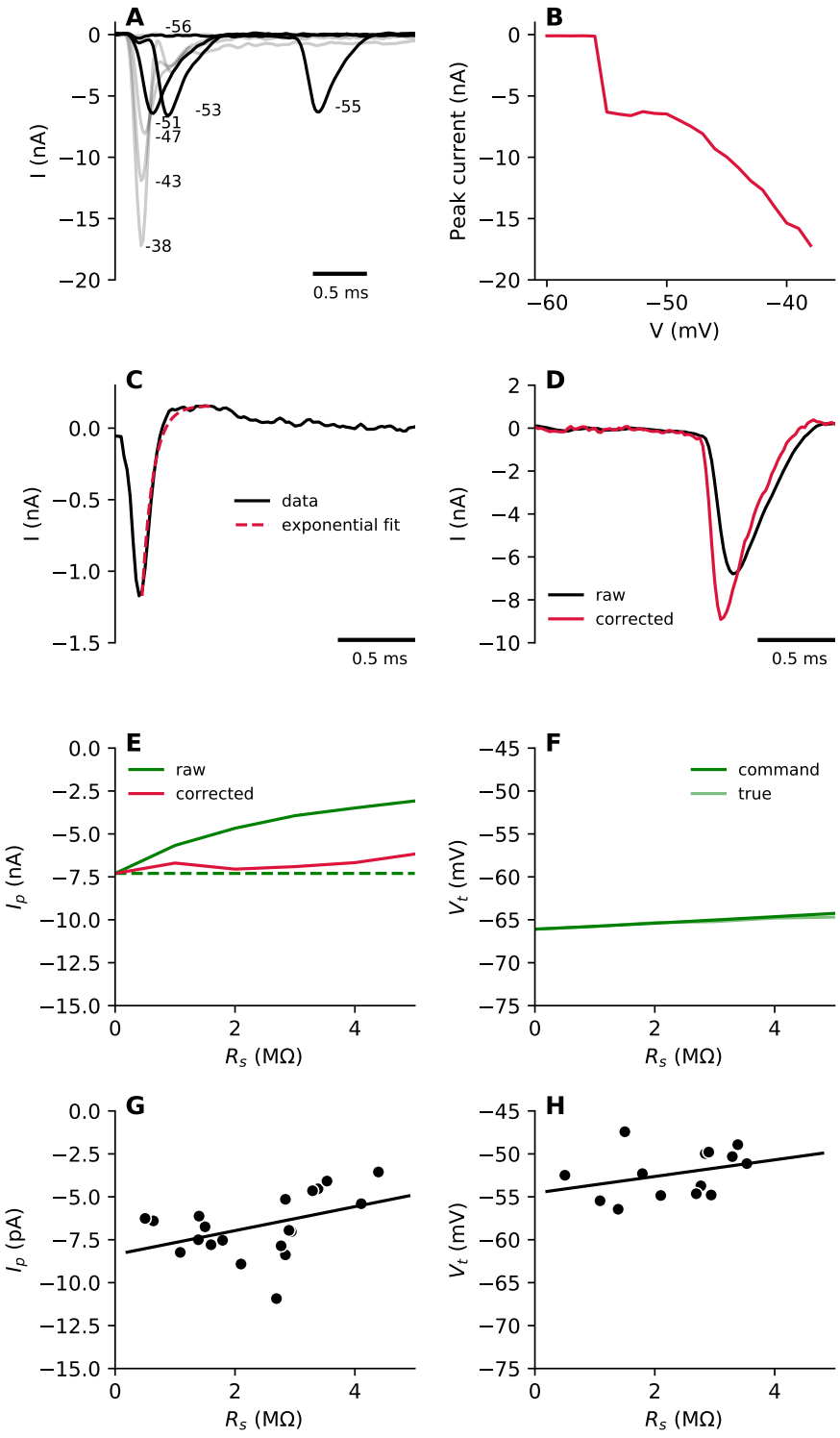

Figure 3.2: Recording the axial current (continued on next page).

Figure 3.2: Recording the axial current (continued). **A**, Raw current recordings (corrected for leak current but no series resistance) in response to voltage steps from $-60\,\mathrm{mV}$ to different target potentials ($-55\,\mathrm{mV}$ to $-38\,\mathrm{mV}$). **B**, Peak current vs. step command potential. The peak current increases abruptly when the potential exceeds some threshold. **C**, Passive response to a $+\,5\,\mathrm{mV}$ voltage step. An exponential function is fitted on the first 0.5 ms, starting from the peak, to estimate the decay time constant (dashed red). **D**, A recorded axial current (black) is corrected by defiltering (red), with residual $R_s = 2.1\,\mathrm{M\Omega}$ and $\tau = 70\,\mu\mathrm{s}$. **E**, Peak current correction in a biophysical model with an extended AIS (5 µm to 30 µm), as a function of series resistance R_s. **F**, Change in measured and actual voltage threshold as a function of R_s in a biophysical model. **G**, Corrected peak axial current at spike initiation vs. series resistance in RGCs (n = 20), showing a weak correlation (Pearson correlation r =0.43, p = 0.06). **H**, Corrected voltage threshold vs. R_s in RGCs (n = 14; 6 cells excluded because the reference potential drifted), with the regression line (p = 0.25, Pearson test).

We found that for most cells, the axial current measured in voltage clamp was indeed close to the capacitive current of a spontaneous AP (fig. 3.3 A; 5 cells were excluded because spontaneous APs or capacitance were not measured). Two cells had a substantially larger capacitive current than expected. As dV/dt was also high in these cells (162 and $201\,\mathrm{V\,s^{-1}}$ compared to an average of $142 \pm 34\,\mathrm{V\,s^{-1}}$, s.d.), it is plausible that AIS Na^+ channels were less inactivated in spontaneous APs than in the voltage clamp measurement at $-60\,\mathrm{mV}$ (see last section). The fact that the magnitude of the axial current is generally consistent with the depolarization observed in current clamp suggests that our measurements are reasonably accurate.

In layer 5 pyramidal cortical cells, Hamada et al. (2016) observed that dV/dt was not very variable across cells, and that the placement of the AIS was consistent with the axial current being proportional to the capacitance. The correlation we observed between axial current and capacitance was not very strong statistically (fig. 3.3 B; Pearson correlation r= 0.47, p = 0.06). This could well be due to the limited precision of our measurements. It may also be due to the variability of dV/dt across the population (coefficient of variation: 0.24). Indeed, the strong functional constraint is not on dV/dt but on the total somatic depolarization induced by the axial current. This depolarization should be $\Delta V = Q/C$, where Q is the total charge transmitted to the soma, i.e., the integral of the axial current. We found a linear correlation between Q and C (fig. 3.3 C; Pearson correlation r = 0.56, p = 0.02), with a slope $\Delta V = 31\,\mathrm{mV}$. This is remarkably close to the difference between spike threshold and regeneration threshold we observed on spontaneous APs (33 mV; fig. 3.1 G). Thus, the transmitted charge appears to be just enough to bring the somatic potential to the voltage where somatic sodium channels open and regenerate the AP.

The axial current duration, defined as the time t_{50} during which the current is above 50% of its peak, did not appear to vary with somatic capacitance (fig. 3.3 D). Excluding the one clear outlier, $t_{50} = 0.36 \pm 0.05\,\mathrm{ms}$, a coefficient of variation of 0.14. Thus, the statistically stronger

correlation observed between Q and C than between I_p and C may simply be due to the fact that the measurement of Q is likely to be more accurate and less noisy than the measurement of I_p, because the integrated current is not affected by the filtering issue discussed above, and integration reduces noise.

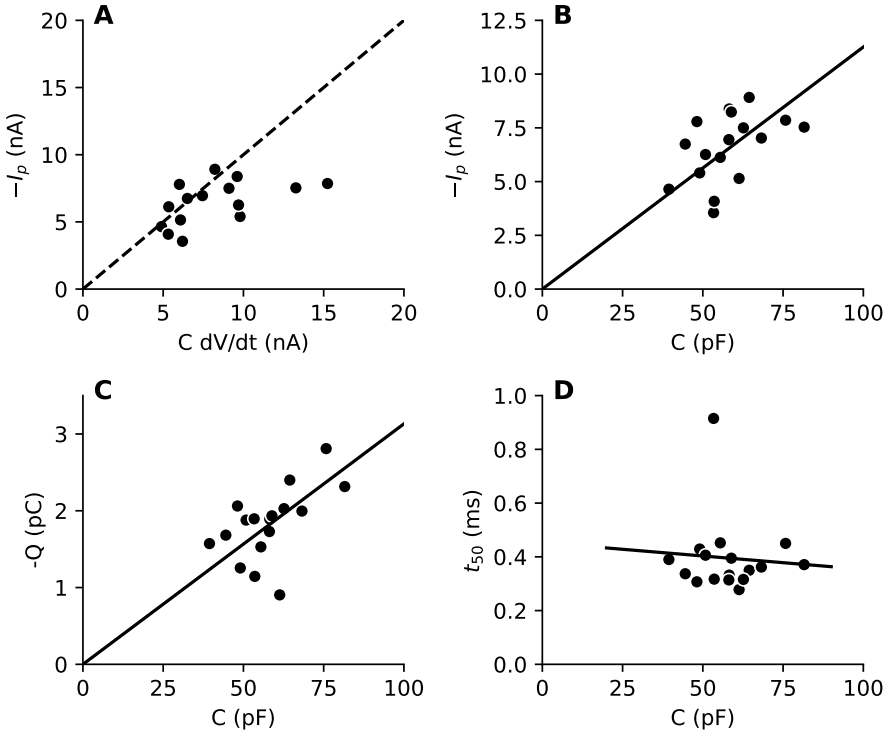

Figure 3.3: Transmission of the axial current to the soma. **A**, Corrected peak axial current at spike initiation measured in voltage clamp vs. capacitive current measured in current clamp (n = 15). The dashed diagonal line represents the identity $-I_p = CdV/dt$ (not a regression line). **B**, Peak axial current measured in voltage clamp vs. somatic capacitance measured in current clamp (n = 17). The solid line is the best linear fit (not affine; i.e., of the form $-I_p = a \cdot C$). **C**, Total transmitted charge vs. somatic capacitance (n = 17). The solid line is the best linear fit, with slope 31 mV. **D**, Axial current duration measured at 50% of peak current, vs. capacitance, with regression line (n= 17).

$\mathbf{Na}_v$ conductance density

The axial current was on average $I_p = -6.7\,\mathrm{nA}$ (s.d. $1.8\,\mathrm{nA}$). From this value, we deduce a lower bound on Na^+ conductance density g_{min} by three methods. The first method uses the fact that the axial current is not greater than the maximum current that can pass through each Na^+ channel. Thus, it produces a lower bound that depends only on axial current and AIS area. The second method consists in calculating the maximum current that a cylindrical axon with uniform conductance density can pass to the soma. Thus, it produces a lower bound that depends on axial current, axon diameter and intracellular resistivity. The third method calculates the axial current based on all biophysical parameters using resistive coupling theory. It is more precise but depends on accurate measurements of AIS geometry and intracellular resistivity.

First, the axial current cannot be greater that the maximum current that all Na^+ channels can pass. This maximum Na^+ current is $G(E_{Na} - V)$, where $E_{Na} \approx 70\,\text{mV}$ is the reversal potential of Na^+, G is the total Na^+ conductance and $V \approx -15\,\text{mV}$ is the local membrane potential at which the current through a Na^+ channel is maximal (based on Na^+ channel properties measured at the AIS of cortical pyramidal cells (Kole and Stuart, 2008)). Therefore, a lower bound for the total Na^+ conductance is $G_{min} = -I_p/(E_{Na} - V) \approx 79\,\text{nS}$.

To estimate the corresponding minimum conductance density, we measured the geometry of the AIS of n = 14 cells by immunolabeling ankyrin-G, while identifying recorded cells using biocytin in the patch pipette (see Methods) (fig. 3.4 A). The AIS was on average 31 µm long (± 6 µm s.d.) and started at 8.6 ± 3.3 µm from the soma (fig. 3.4 B), with no statistically significant correlation between the two measurements (p = 0.59, Pearson test). We also measured the axon diameter at the proximal and distal ends of the AIS. However, it should be kept in mind that these measurements cannot be accurate because of the limitations of conventional light microscopy, and therefore must be considered as rough estimates. The proximal and distal diameters were 0.9 ± 0.3 µm and 0.5 ± 0.2 µm, respectively. For comparison, Raghuram et al. (2019) found by a similar method 1 µm and 0.6 µm on average in α S RGCs of mice, with substantial variability.

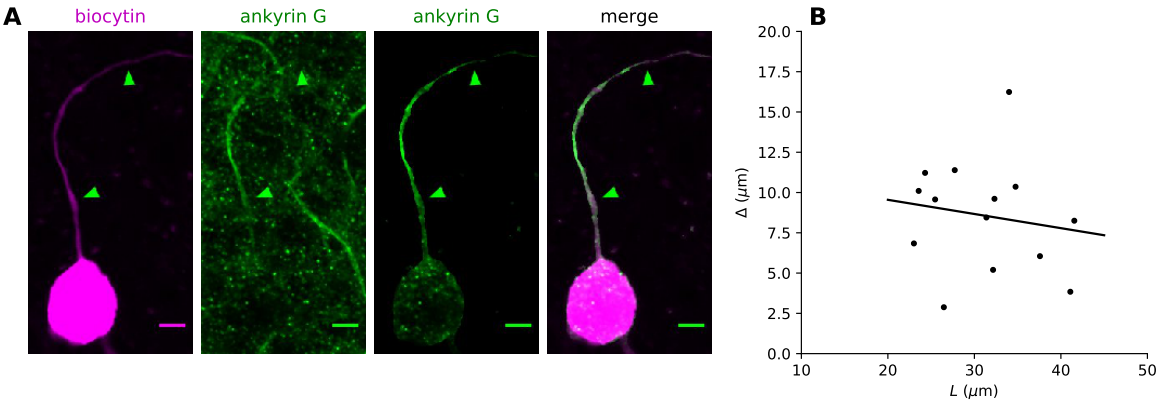

Figure 3.4: Geometry of the AIS. **A left**, Fluorescence image of a RGC labelled with biocytin (pink). The start and end position of the AIS are indicated by green arrowheads. **A middle left**, Fluorescence image of AISs labeled with ankyrin-G antibodies (green). **A middle right**, Fluorescence image of the AIS masked by the neuron morphology. **A right**, Merge of first and third panels. **B**, Distance Δ of the AIS from the soma vs. AIS length L, with the regression line (p = 0.59, Pearson test). **A**, Scale bar is 10 µm.

Using the high estimate of 1 µm for the diameter, the average AIS area was therefore 97 μm^2 (± 19 μm^2 s.d.), which implies a minimum conductance density of 814 $\text{S}\,\text{m}^{-2}$. With a diameter of 0.7 µm, we find a minimum of 1014 $\text{S}\,\text{m}^{-2}$.

This lower bound holds independently of the conditions of propagation of the action potential. In particular, it makes no assumption on intracellular resistivity R_i, which is challenging to measure. We now consider a different constraint, the geometrical mismatch between the small axon and the large soma. Resistive coupling theory provides a quantitative estimate of the axial current, by assuming that current entering the axonal membrane flows resistively towards the soma, which acts as a current sink (Brette, 2013; Goethals and Brette, 2020; Kole and Brette, 2018). We obtain an upper estimate of the axial current by considering open Na^+ channels uniformly distributed along the axon. We then deduce the minimum conductance density necessary to produce an axial current I (see Methods):

$$g_{min} = \frac{4R_i I^2}{\pi^2 \Delta V^2 d_{ais}^3} \tag{3.1}$$

where $\Delta V = E_{Na} - V_t$, with V_t the spike threshold ($\Delta V \approx 120\,\mathrm{mV}$). This lower bound is independent of AIS geometry, but depends on intracellular resistivity R_i. Intracellular resistivity has not been measured directly in the RGC axons. In dendrites of cortical pyramidal cells, it was estimated to be $R_i = 70 - 100\,\Omega\,\mathrm{cm}$ (Stuart and Spruston, 1998). Modeling studies in RGCs assume somewhat higher values, up to about $150\,\Omega\,\mathrm{cm}$ (Fohlmeister et al., 2010; Sheasby and Fohlmeister, 1999), but these are based on model optimization. Taking $R_i = 100\,\Omega\,\mathrm{cm}$, we find $g_{min} = 1263\,\mathrm{S\,m^{-2}}$ for $d = 1\,\mu\mathrm{m}$ and $g_{min} = 2467\,\mathrm{S\,m^{-2}}$ for $d = 0.8\,\mu\mathrm{m}$ (as shown below, it is mostly the geometry of the proximal side that matters for this calculation). With a higher value for R_i, the lower bound on conductance density would be proportionally higher.

Finally, a more precise relation between axial current and conductance density can be estimated using the measured AIS geometry (fig. 3.5) (Hamada et al., 2016). Suppose conductance density is very high, such that the AIS is clamped at E_{Na} when sodium channels open. Then by Ohm's law, the AIS will produce an axial current $I_p = (E_{Na} - V_t)/R_a$, where R_a is axial resistance between the soma and the proximal end of the AIS. Thus, we obtain an inverse relation between axial current and AIS position, independent of AIS length. However, conductance density is finite, which implies that the proximal side of the AIS is pulled towards the somatic potential (fig. 3.5 A). This is equivalent to shifting the AIS distally by an amount δ:

$$I_p = \frac{1}{R_a} \frac{E_{Na} - V_t}{\Delta + \delta} \tag{3.2}$$

where Δ is the distance of the AIS from the soma, r_a is the axial resistance per unit length, and

$$\delta = \sqrt{\frac{d}{4R_i g}} \tag{3.3}$$

Here, AIS length L can be neglected provided that it is substantially larger than δ (see Methods). This is clearly the case because L was $31\,\mu\mathrm{m}$ on average, while a higher estimate of δ using $d = 1.2\,\mu\mathrm{m}$ and $g = 1000\,\mathrm{S\,m^{-2}}$ is $17\,\mu\mathrm{m}$. Thus, in our cells, AIS length should have no impact on axial current. The formula above agrees well with simulations of a simplified model with non-inactivating Na^+ channels (fig. 3.5 B), except when the AIS is very proximal, where it gives an overestimation.

This analysis shows that it is the proximal geometry of the AIS that matters for the calculation of the axial current. Using $d = 1\,\mu m$, we find that the error between the predicted and the measured current varies with g, with a broad minimum at about $5500\,S\,m^2$ (fig. 3.5 C). This is close to the value that Guo et al. (2013) obtained by model optimization on current-clamp recordings ($5000\,S\,m^2$). Figure fig. 3.5 D shows the axial current measured in our cells as a function of AIS position, together with the theoretical predictions using $g = 5500\,S\,m^{-2}$ with diameters $d = 0.8\,\mu m$, $d = 1\,\mu m$ and $d = 1.2\,\mu m$. There is no significant correlation between axial current and AIS position (p = 0.66, Pearson test), but this may simply reflect the variability of AIS diameter, which has a strong impact on this relation.

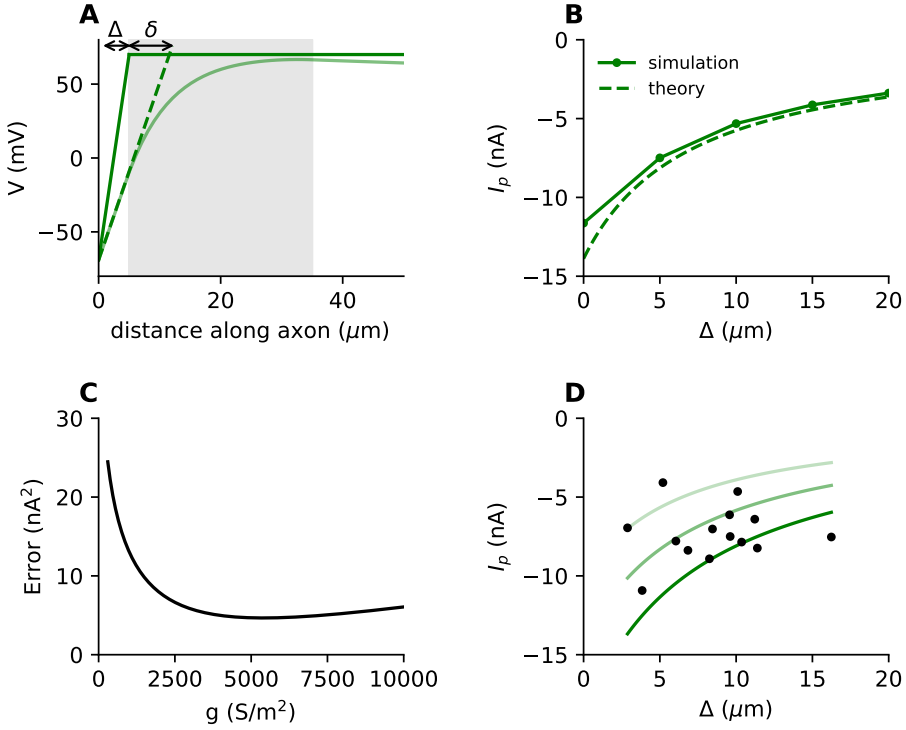

Figure 3.5: Predictions of axial current with resistive coupling theory. **A**, Membrane potential along the axon of a simple model when all Na^+ channels are open along the AIS (red shading), with a voltage clamp of the soma. The proximal side of the AIS is pulled towards the somatic potential, which is equivalent to an AIS clamped at E_{Na} and starting at distance $\Delta + \delta$. **B**, Axial current at spike initiation vs. AIS position Δ in a simple model (solid) compared to theory (dashed). **C**, Mean squared error between predicted and measured current, as a function of conductance density g (with $d = 1\,\mu m$). **D**, Measured axial current vs. Δ, with the theoretical relations for $d = 0.8\,\mu m$, $d = 1\,\mu m$ and $d = 1.2\,\mu m$ (using $g = 5400\,S\,m^{-2}$, the minimum in **C**; n = 14).

3.3.2 The threshold axial current

Variation of axial current near threshold

In a model where the AIS is reduced to a single point, theory predicts that spikes initiate when the sodium current, and therefore the axial current, reaches a threshold $I_t = k/R_a$, where k is the activation slope factor of sodium channels ($k \approx 5\,\text{mV}$) (Brette, 2013). This makes spike initiation distal from the soma efficient because the Na^+ flux below threshold is low. We show in the Methods that the formula is approximately correct in an extended AIS model, if R_a is measured between soma and the middle of the AIS. We tried to estimate I_t in our cells.

To give an order of magnitude, with $d = 1\,\mu\text{m}$ and given that the middle position of the AIS is 24 µm on average, we obtain $R_a \approx 31\,\text{M}\Omega$, which gives $I_t \approx 160\,\text{pA}$ (assuming $k = 5\,\text{mV}$), a small current. Figure 3.6 A shows a recording of the axial current at threshold, which is noisy. We measure the peak current after smoothing. In addition, theory predicts that the axial current increases very steeply near threshold (dI/dV is infinite at threshold), as shown in fig. 3.6 B. This makes the threshold current difficult to measure, and likely leads to an underestimation of the threshold current. We measured the current at different step voltages in steps of 0.5 mV (n = 12). In the example shown in fig. 3.6 C, no increase in current is noticeable up to 3 mV below threshold. More precisely, theory predicts that $V - V_t$ is proportional to $(I/I_t\text{–}1)^2$. This relation is shown in a biophysical model in fig. 3.6 D. In a simplified model (no sodium channel inactivation or potassium channels), the slope β is predicted to be equal to $k/2$. In the more realistic model shown in fig. 3.6 D, the slope is $\beta \approx 4.7\,\text{mV}$, close to k (instead of $k/2$). Our data fitted this quadratic relation well (fig. 3.6 E), with slopes $\beta \approx 4.2\,\text{mV}$ ($\pm$ 1.7 mV), in the expected range.

Threshold vs. AIS geometry

Both the voltage and axial current at threshold are predicted to depend on AIS geometry, namely to decrease when the AIS is shifted away from the soma, all else being equal. We analyzed these relations in n = 10 cells (cells were excluded either because AIS geometry was not measured or reference potential drifted). There was no significant correlation in our data between voltage threshold and either AIS start position (fig. 3.7 A, p = 0.54, Pearson test) or length (fig. 3.7 B, p = 0.14, Pearson test). However, voltage threshold varies theoretically with both quantities as $-k\log(x_{1/2}L)$. The correlation was stronger with $\log(x_{1/2}L)$, although still weak (Pearson correlation r = 0.62, p = 0.06). The regression slope was $k = 4.3\,\text{mV}$, a plausible value (fig. 3.7 C). We note that diameter and perhaps conductance density, which both contribute to the voltage threshold, may also vary across cells. We observed an inverse correlation between axial current threshold and AIS position (fig. 3.7 D, p = 0.04, Pearson test). Theory makes a quantitative prediction: $I_t = k/R_a$, with R_a measured to the middle of the AIS. This may differ by a constant factor in a complex biophysical model (fig. 3.7 E, compare dashed and solid lines). Measured currents are lower than predicted and the inverse correlation is barely significant (Pearson correlation r = -0.65, p = 0.08). As explained above, underestimation and limited precision were expected. Nonetheless, measured currents were close to the expected order of magnitude (92 pA vs. 160 pA on average, with all but two cells

between 70 and 150 pA).

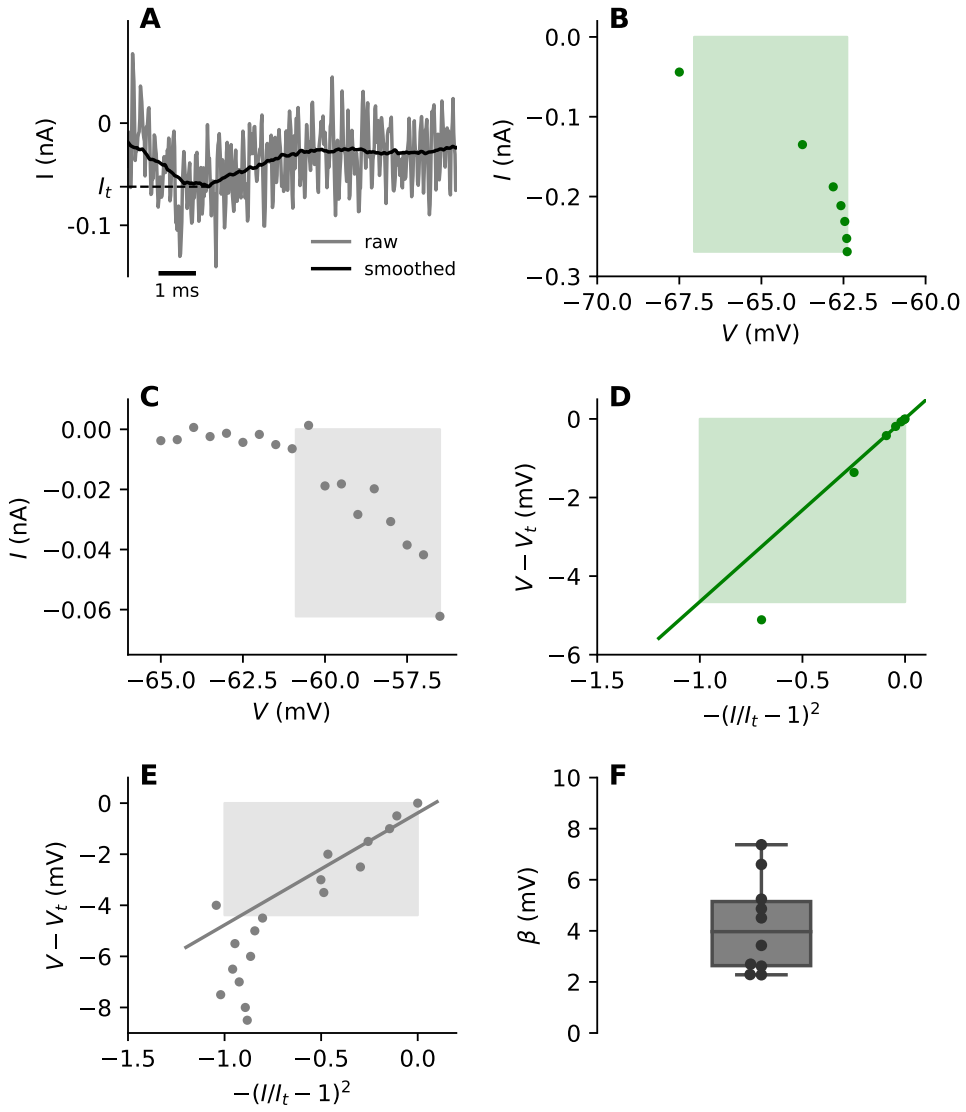

Figure 3.6: Axial current near threshold. **A**, Current recorded at threshold (gray). After smoothing (black), It is the peak value. **B**, Peak current vs. V in a biophysical model with extended AIS. Threshold was measured by bisection for better precision. The shaded box represents the region 3 mV below threshold. **C**, Peak current vs. V measured below threshold in a RGC. **D**, Distance to voltage threshold vs. quadratic normalized current in the biophysical model, with the regression line (slope $\beta = 4.7$ mV). **E**, Same as **D** in the RGC (slope of regression line: $\beta = 4.4$ mV). **F**, Slope of linear regressions shown in **E** over all cells.

3.3.3 Adaptation of the axial current

Properties of adaptation

We observed that the axial current at spike initiation has just the right magnitude to depolarize the soma to the somatic regeneration threshold. What would happen if the availability of sodium channels varied? In many neurons, sodium channels can inactivate substantially below threshold, producing voltage threshold adaptation (Azouz and Gray, 2000; Fontaine et al., 2014; Platkiewicz and Brette, 2011). Threshold adaptation has been observed in current-clamp recordings of salamander RGCs (Mitra and Miller, 2007). If this phenomenon reflects the inactivation of AIS sodium channels, it may compromise the transmission of the AIS spike to the soma.

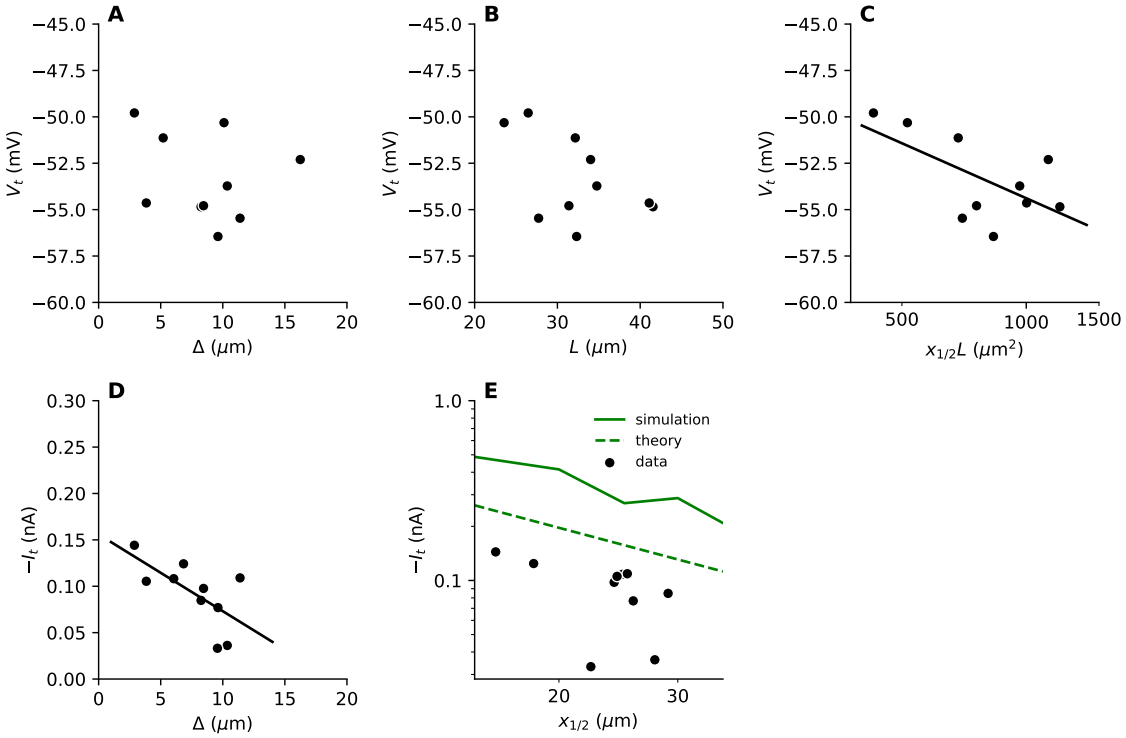

Figure 3.7: Threshold vs. AIS geometry. **A**, Corrected voltage threshold vs. AIS position Δ is RGCs. **B**, Voltage threshold vs. AIS length L. **C**, Voltage threshold vs $x_{1/2}L$ in logarithmic space, with logarithmic regression line (slope $k = 4.3\,\text{mV}$; p = 0.06, Pearson test). **D**, Current at threshold vs. AIS position, with regression line (p = 0.04, Pearson test). **E**, Current at threshold vs. AIS middle position $x_{1/2}$, with theoretical prediction using $d = 1\,\mu\text{m}$ (dashed green) and simulation in a biophysical model (solid).

We examined this issue by holding the neuron at different potentials V_0 before measuring the voltage threshold. We observed that the threshold increases substantially with V_0 (fig. 3.8 A). The relation between V_t and V_0 follows the theoretical expectation for threshold adaptation due to sodium channel inactivation (Fontaine et al., 2014; Platkiewicz and Brette, 2011), where the threshold starts increasing above the baseline V_{min} when V_0 exceeds the half-inactivation voltage V_i of sodium channels, with a slope $k_i/k_a \approx 1$ in the depolarized range (where k_i and

k_a are the inactivation and activation slope factors, respectively). By fitting the theoretical relation, we find $V_i \approx -55.8 \pm 3.1$ mV (fig. 3.8 B), $V_i - V_{min} \approx -0.7 \pm 2.9$ mV (fig. 3.8 C), $k_a \approx 4.1 \pm 2.2$ mV (fig. 3.8 D), and $k_i/k_a \approx 0.9 \pm 0.18$ (fig. 3.8 E). These values are consistent with expectations if threshold adaptation is due to sodium channel inactivation.

We then measured the axial current at spike initiation (just above threshold) as a function of V_0 (note that there are fewer data points because current recordings were discarded when Rs changed by more than 30%). We observed that the current decreased considerably with increasing V_0 (fig. 3.8 F). On average, it attenuates by a factor 12.3 ± 5.1 when V_0 increases from -60 mV to -40 mV (fig. 3.8 G). At V_i, the current is 32 ± 10 % smaller than the maximum current (fig. 3.8 H).

If adaptation of voltage threshold and axial current are both due to sodium channel inactivation, then axial current and voltage threshold should co−vary with V_0. Theoretically, V_t varies with g as $-k \log g$ (Platkiewicz and Brette, 2011). For low g, the axial current I_p is proportional to $\sqrt{g}$. Therefore, V_t should vary with I as $-k \log I_p^2$ or $-2k \log I_p$. We first note that the potential V_i^* at which the axial current is attenuated by $\sqrt{2}$ is indeed close to the half-inactivation voltage V_i estimated from threshold adaptation ($V_i^* = -56.5 \pm 1.9$ mV vs. -55.8 mV) (fig. 3.8 I). Then when we compare V_t with I_p, we find a logarithmic relation (fig. 3.8 J, K) with half-slope $k_a = 2.4 \pm 2.7$ mV (fig. 3.8 L). Note that this average includes one outlier; the median k_a is 3.4 mV (the smaller number of points is due to the fact that exclusion criteria for both V_t and I_p are applied). This strongly suggests that both threshold and axial current adaptation are due to the same phenomenon, sodium channel inactivation.

In contrast, resistive coupling theory predicts that the axial current at threshold (slightly below) depends on AIS geometry but not on sodium conductance. Figure 3.9 A shows current-voltage relations for different V_0 in the same cell. The curves appear to shift horizontally when V_0 is changed, so that the voltage threshold increases with V_0 but the axial current at threshold does not, as shown specifically on fig. 3.9 B. Over all measured cells (n = 6; voltage threshold and current threshold were only measurable with a stable R_s in a few cells), I_t varied by a factor smaller than 2.5 (1.2 ± 0.6) between -60 and -40 mV (fig. 3.9 C), whereas I_p varied by a factor 12.3 on average.

Compensation of axial current attenuation

Figure 3.10 A shows the attenuation of I_p as a function of V_0 in one cell. Here I_p attenuates by a factor 7.3 between -60 and -40 mV. If the axial current at spike initiation attenuates by a factor 10, then we expect the induced somatic depolarization to also attenuate by a factor 7, to about 4 mV, which seems insufficient to reach the threshold for somatic regeneration. However, this is not what we found. In this cell, the total transmitted charge, obtained by integrating the current, attenuates only by a factor 1.7 (fig. 3.10 B). This occurs because current duration increases at high V_0 (fig. 3.10 C). Over all measured cells (n = 7), transmitted charge attenuated by a factor 3.1 ± 1.4 from -60 to -40 mV, compared to 12.3 ± 5.1 for the axial current (fig. 3.10 D). The increase in current duration was observed consistently above -50 mV (fig. 3.10 E).

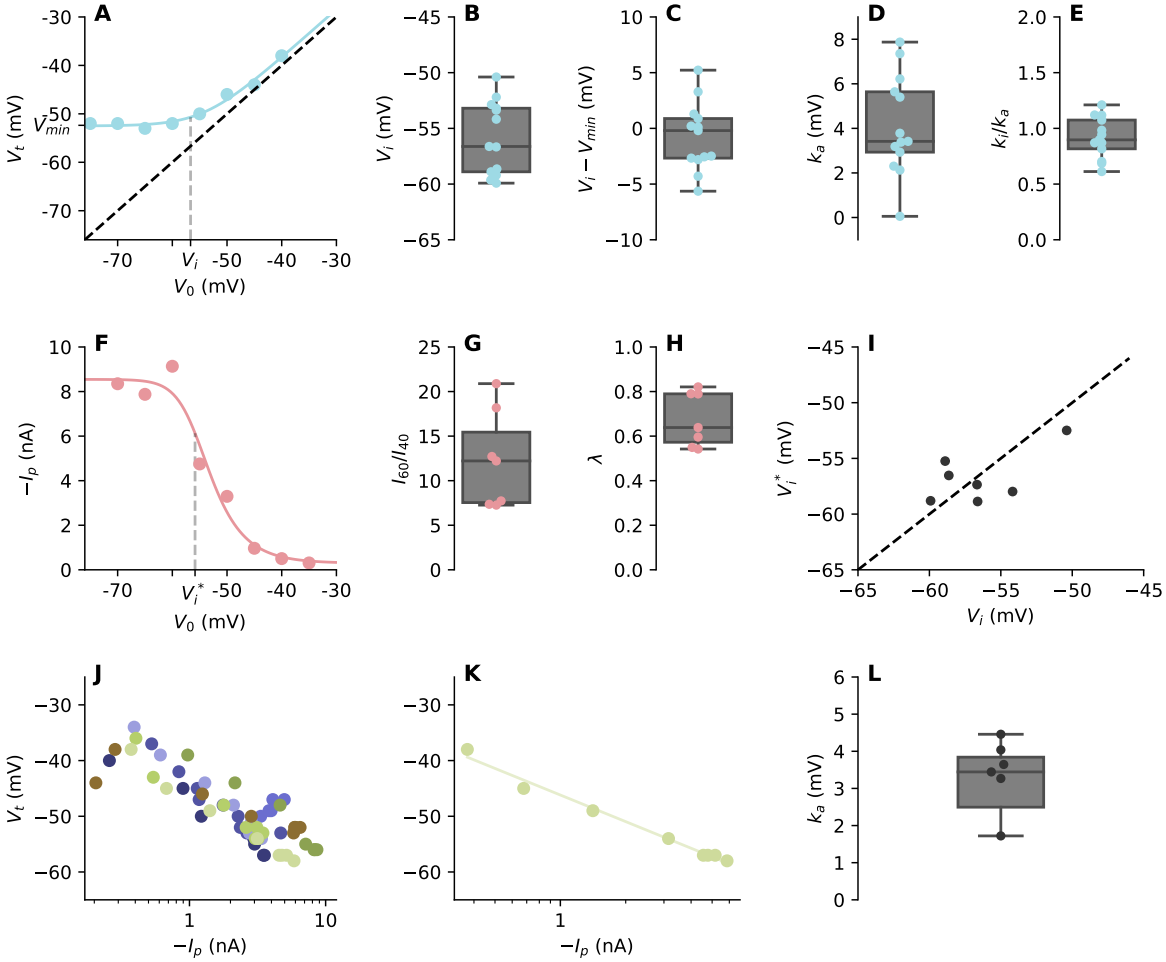

Figure 3.8: Adaptation of the axial current at spike initiation. **A**, Voltage threshold vs. initial holding potential V_0 in a RGC. The dashed line is the identity $V_t = V_0$, and the solid curve is a fit to the theoretical relation. **B**, Statistics of half-inactivation voltage V_i from theoretical fits. **C**, Statistics of $V_i - V_{min}$ from fits. **D**, Statistics of activation slope k_a. **E**, Statistics of k_i/k_a. **F**, Axial current I_p at spike initiation vs. initial holding potential V_0 in a RGC. The dashed line shows the potential V_i^* where I_p is attenuated by $\sqrt{2}$. **G**, Current attenuation I_{60}/I_{40} from $-60\,\text{mV}$ to $-40\,\text{mV}$, over all cells. **H**, Current at half-inactivation voltage V_i, relative to the maximum current. **I**, Statistics of V_i^*. **J**, Voltage threshold V_t vs. axial current in logarithmic space, over all RGCs (n = 9; each color corresponds to one cell). **K**, Voltage threshold V_t vs. axial current for one RGC, with logarithmic regression line (half-slope $k = 3.4\,\text{mV}$, r = 0.99). **L**, Statistics of k_a from logarithmic regressions over all cells.

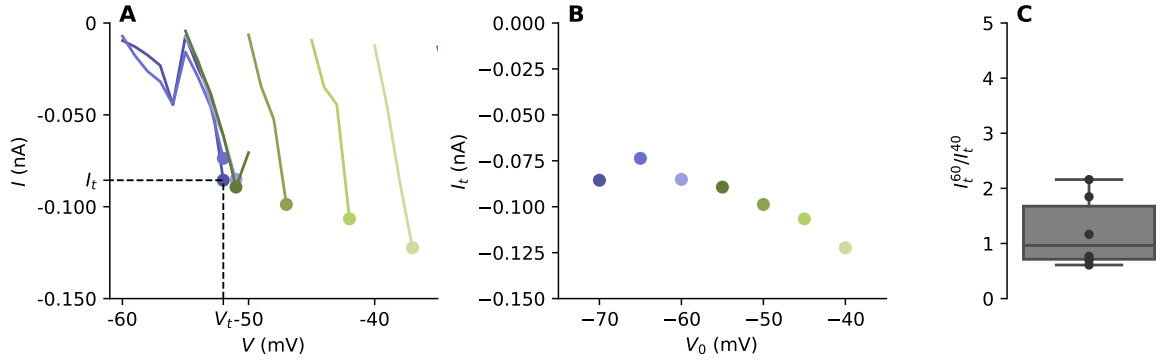

Figure 3.9: Adaptation of the axial current at threshold. **A**, Current vs. somatic potential V a few mV below threshold, shown for different initial holding potentials V_0 (-70, dark purple to -40 mV, light green) in the same RGC. **B**, Current at threshold vs. V_0 in the same cell. **C**, Attenuation of threshold current I_t^{60}/I_t^{40}.

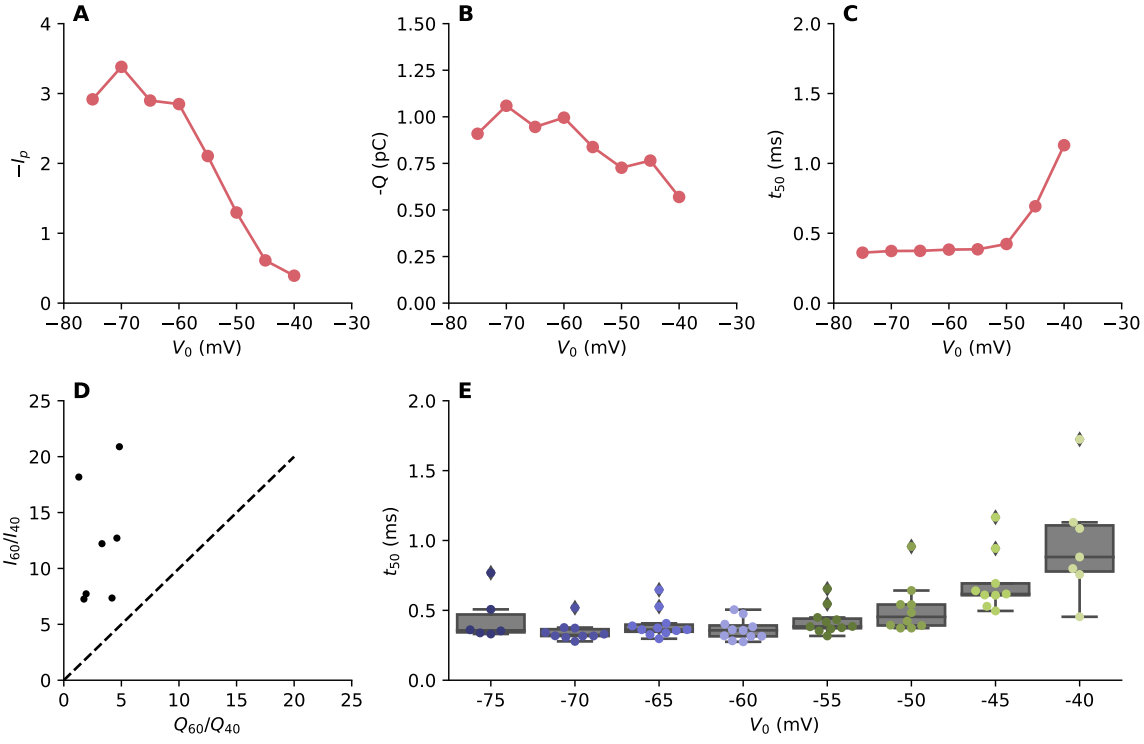

Figure 3.10: Compensation of axial current attenuation. **A**, Axial current at spike initiation vs. initial potential V_0 in a RGC. **B**, Total transmitted charge Q vs. V_0 in the same cell. **C**, Current duration t_{50} vs. V_0 in the same cell. **D**, Current attenuation vs. charge attenuation between -60 and -40 mV, over all cells. **E**, Current duration t_{50} vs. V_0 in all cells.

3.4 Discussion

3.4.1 Summary

In summary, we have observed that the AIS of RGCs produces a large axial current at spike initiation (about 7 nA), which requires a high Na^+ conductance density (most likely several thousand $S\,m^{-2}$). The charge that this current transmits to the soma co-varies with somatic capacitance, in such a way as to produce a depolarization of about 30 mV, the amount necessary to bring the somatic potential to spike regeneration threshold. Theory shows that the axial current is mainly determined by AIS position and diameter, and to some extent by Na^+ conductance density, but perhaps counter-intuitively not by AIS length.

In agreement with resistive coupling theory (Brette, 2013; Kole and Brette, 2018), the axial current is small below threshold (on the order of 100 pA at threshold, and undetectable a few mV below) and decreases when the AIS is further away from the soma, which reduces energy consumption.

We have also observed that the voltage threshold for spike initiation adapts to depolarization, in a way compatible with Na^+ channel inactivation. Consistently, the axial current at spike initiation also decreases when the threshold adapts. This attenuation can reach a factor of 10 or more for large depolarizations, which could potentially compromise spike transmission to the soma. However, we found that this attenuation is compensated by a broadening of the axial current.

3.4.2 Limitations

One of the main technical limitations to interpret the results of this study is that axonal diameter d cannot be measured precisely with conventional optical microscopy. This is an important limitation because theory shows that key properties are very sensitive to diameter. Specifically, axial resistance is inversely proportional to d^2. This results in an error in resistance estimation of around 50% for a 200 nm error in axon diameter estimation (assuming $d \approx 1\,\mu m$). This translates to comparable errors in axial current predictions. This limitation should also be kept in mind when interpreting other studies where changes in AIS geometry are observed (see below). The best way to overcome this limitation would be to measure axonal diameter precisely using either electron microscopy or super-resolution microscopy.

Axial resistance is proportional to intracellular resistivity R_i, but this parameter is difficult to estimate. Ideally, it should be measured by simultaneous recordings in the axon and soma, and a precise estimate requires a precise measurement of axon diameter. Stuart and Spruston (1998) estimated $R_i = 70{-}100\,\Omega\,cm$ in dendrites of cortical pyramidal cells, based on simultaneous recordings in soma and apical dendrite. Although this value is mainly determined by the concentration of the most mobile ions (i.e., mainly K^+), which is not expected vary widely across the cell, it is conceivable that it is higher in thin crowded structures such as the proximal axon. Higher values, up to $150\,\Omega\,cm$, have been used in modeling studies of

RGCs (Fohlmeister et al., 2010; Sheasby and Fohlmeister, 1999), but these are based on model optimization using somatic recordings.

In the theory, we did not take into account axonal tapering. However, in RGCs, axon diameter decreases from soma to AIS, then decreases again along the AIS (Raghuram et al., 2019). The theory assumes a uniform diameter, because general analytical solutions do not exist with variable diameter. For the calculation of the axial current at spike initiation, taking into account tapering would tend to reduce the axial resistance between soma and AIS, as if the AIS were closer to the soma. The diameter in the calculation of δ should be the diameter of the proximal AIS.

We were not able to confirm an inverse relation between AIS position and axial current at spike initiation. A plausible reason is that the axial current is very sensitive to diameter, which might have varied substantially across cells. It is also possible that the available Na^+ conductance density varied across cells. Indeed, our data on adaptation show that half-inactivation voltage (about $-57\,mV$) is close to the initial potential used in our voltage clamp measurements of axial current ($-60\,mV$). Another potential source of variability is that we have studied mice at an age where there are developmental changes in the expression of Na^+ channel subtypes (Boiko et al., 2003; Van Wart et al., 2007), which might have contributed some variability. Finally, series resistance introduces errors that may have been incompletely corrected offline. This issue could be addressed by measuring currents with two electrode voltage-clamp (Barrett and Crill, 1980).

3.4.3 Na^+ conductance density

Whether the AIS has high Na^+ conductance density has been controversial (Colbert and Pan, 2002; Fleidervish et al., 2010; Kole et al., 2008). This question has been typically considered from the viewpoint of excitability: high conductance density has been proposed to account for the fact that the AIS spike initiates about 30 mV below the somatic regeneration threshold. Other contributing factors are the lower activation threshold of axonal sodium channels (Hu et al., 2009; Kole and Stuart, 2008) and the axial resistance between soma and AIS (Brette, 2013). Here we examined another empirical constraint, the axial current that the AIS generates at spike initiation.

By just considering the area of the AIS, to produce a current of 6.7 nA requires a conductance density of about $1000\,S\,m^{-2}$ with $d = 0.7\,\mu m$ or $800\,S\,m^{-2}$ with an upper estimate of $d = 1\,\mu m$. This is a lower bound that neglects considerations of cable theory, namely the fact that the axial current flows from the distal end of the AIS to the soma.

It is possible to calculate the maximum axial current produced by an axon of diameter d and conductance density g. This calculation shows that, to account for a current of 6.7 nA, g must be at least $1200\,S\,m^{-2}$ if $d = 1\,\mu m$, and about $2500\,S\,m^{-2}$ if $d = 0.8\,\mu m$, independently of AIS position. Here the relevant diameter is the diameter of the proximal AIS (about 0.9 µm in our data). Finally, taking into account measured AIS position, the data are consistent with

g around 5000 S m^{-2} (with $d = 1$ µm), although the minimum is broad. Overall, this analysis indicates that g should be several thousand S m^{-2}. This estimate is independent of Na^+ channel kinetics, and in particular it holds even if Na^+ channels cooperate (Naundorf et al., 2006).

Lorincz and Nusser (2010) counted 187 $Na_v1.6$ channels per µm^2 in the AIS of CA1 pyramidal cells. Assuming a unitary conductance of 10 pS to 20 pS per channel (Hille et al., 2001), this amounts to 1870 S m^{-2} to 3740 S m^{-2}. However, this is an estimate of the structural density, not necessarily of the functional density. In a computational model of layer 5 pyramidal cells, a density of 2500 S m^{-2} was necessary to account for the measured initial depolarization speed of somatic APs (Kole et al., 2008). Similarly, optimization of a model of RGCs for AP shape yielded a conductance density of about 5000 S m^{-2} (Guo et al., 2013). Our analysis provides an estimation that is less dependent on model specifics, and confirms these previous studies.

The theoretical analysis indicates that a high conductance density is likely a necessary condition to transmit the AIS spike to the soma in a variety of cell types, due to the drastic geometrical variation at the axosomatic boundary. The minimum conductance density to produce an axial current I is proportional to I^2/d_{AIS}^3. If we assume that the current must scale with the area of the soma, then the minimum g is proportional to d_{soma}^4/d_{AIS}^3. This ratio appears to be approximately conserved across cell types (Goethals and Brette, 2020), and therefore most neurons should face the same constraint requiring a similar conductance density in the AIS.

It should be noted that, despite a high conductance density at the AIS, the total Na^+ influx through the AIS should theoretically have the same order of magnitude as through the soma and proximal dendrites, as observed (Fleidervish et al., 2010). Indeed, the total Na^+ influx at the AIS should match the charge necessary to depolarize the soma by about 30 mV, while the total Na^+ influx at the soma (and proximal dendrites) should account for a further depolarization of a few tens of mV (about 45 mV in our cells). The AIS influx should occur preferentially in the proximal AIS, even if conductance density is uniform, because the driving force of the Na^+ channel is larger there (see fig. 3.5 A). This has indeed been observed in cortical pyramidal cells (Baranauskas et al., 2013).

3.4.4 Structural tuning of the AIS

In layer 5 cortical pyramidal cells, (Hamada et al., 2016) observed that AIS position was inversely related to the diameter of the apical dendrite. Quantitatively, this relation was consistent with a proportionality relation between the axial current produced by the AIS and the somatodendritic capacitance. Here we showed more directly that, in RGCs, the charge transmitted by the AIS covaries with the somatodendritic capacitance, in such a way as to depolarize the soma to the threshold for somatic spike regeneration.

Overall, our measurements are in line with quantitative predictions of resistive coupling theory. However, we did not observe a correlation between AIS position and capacitance.

Theoretically, the structural parameters that determine the axial current are AIS position and diameter (and not AIS length, at least not in the range of observed lengths). Therefore, one would expect a negative correlation between AIS position and capacitance if diameter were homogeneous across cells, or at least uncorrelated to capacitance. In fact, Raghuram et al. (2019) observed a positive correlation between AIS position and soma size in α S RGCs. Such a correlation would be expected if AIS diameter scaled with soma size. The authors did observe a positive correlation between soma size and the diameter of the proximal axon (we note that observing such correlations for the AIS proper, which is below 1 µm in diameter, may not be feasible). It cannot be excluded that the lack of significant inverse correlation between AIS position and capacitance is due to the limited precision of our measurements, especially as we did observe an inverse correlation between AIS position and threshold axial current. It is possible that the availability of Na^+ channels varied across cells. In any case, we stress that axon diameter is a key structural parameter in setting the axial current as well as excitability, and therefore it must be considered to correctly interpret experimental results.

It remains that, in order to produce an axial current of appropriate magnitude from an AIS of a given diameter and conductance density, AIS position must be set appropriately. A number of studies have shown that AIS position can vary across cells (Hamada et al., 2016; Höfflin et al., 2017; Kuba et al., 2006), during development (Galiano et al., 2012; Gutzmann et al., 2014; Kuba et al., 2014), and with activity (Evans et al., 2015; Grubb et al., 2011; Grubb and Burrone, 2010; Jamann et al., 2018; Kuba, 2012; Kuba et al., 2010). These changes have often been suggested to reflect a homeostatic regulation of excitability, but theory predicts a small effect of AIS position on excitability (Goethals and Brette, 2020), and a large effect on axial current. Therefore, it is conceivable that these changes reflect a homeostatic regulation not of excitability per se, but of the axial current required to transmit the AIS spike to the soma. For example, Grubb and Burrone (2010) report that when cultured hippocampal neurons are depolarized with 15 mM KCl, capacitance decreases by about 10% while the AIS shifts away from the soma. This distal shift is consistent a decrease in axial current required to match the decrease in capacitance. Developmental changes in AIS position may also be consecutive of changes in diameter or dendritic area. In neurons of the chick nucleus laminaris, capacitance decreases during development, and this change is accompanied by a distal shift of the AIS. A more precise assessment would require precise information about AIS diameter.

3.4.5 Adaptation

Threshold adaptation has been observed in current-clamp recordings of salamander RGCs (Mitra and Miller, 2007), as well as in many other cell types (reviewed in Platkiewicz and Brette (2011)). We also observed it in mice RGCs and quantified it precisely. The voltage threshold starts increasing when the membrane is depolarized above ≈ -56 mV, and for large depolarizations the slope of the relation between potential and threshold is close to 1. That is, the threshold tracks the membrane potential so as to remain a few mV above it. These observations are consistent with theoretical expectations based on Na^+ channel inactivation (Platkiewicz and Brette, 2011). In layer 5 pyramidal cells, half-inactivation voltage of AIS Na^+ channels is about -61 mV (Kole et al., 2008), which is in line with our observations.

To our knowledge, adaptation of the axial current had not been reported before. Our quantitative analysis shows that the co-variation of axial current and threshold is consistent with AIS Na^+ channel inactivation being the cause of both phenomena. The axial current attenuated by a factor 12 on average over a 20 mV depolarization. This would reduce the charge transmitted to the soma by the same factor if the current spike shape were unchanged, possibly compromising spike transmission to the soma. However, we observed that this attenuation was largely compensated by a broadening of axial currents. This means that the AP at the AIS broadens when the soma is depolarized. In fact, such broadening has been observed in layer 5 pyramidal cells and attributed to the inactivation of K_v1 channels (Kole et al., 2007). As $K_v1.2$ is expressed in the distal AIS of RGCs (Van Wart et al., 2007), this might explain our observations.

In conclusion, our observations indicate that structural and channel properties of the AIS are functionally organized in such a way as to ensure reliable transmission of the AP to the soma.

3.5 Material and Methods

3.5.1 Ethical statement

Timed-pregnant Swiss and C57BL/6NRj mice were purchased from Janvier Labs (Le Genest Saint Isle, France) and housed under controlled conditions (22 $\pm$ 1 °C, 60 $\pm$ 10% relative humidity, 12/12h light/dark cycle, food and water ad libitum). All animal procedures were performed in strict accordance with institutional guidelines and approved by local ethics committees (C2EA-05: Comité d'éthique en expérimentation animale Charles Darwin) and by European Communities Council Directive 2010/63/UE.

3.5.2 Whole-cell electrophysiology of RGCs

Mice were taken at postnatal day 10-12 (P10-12). The pup was rapidly decapitated, the eyes were removed and placed in Ringer's medium containing (in mM): 119 NaCl, 2.5 KCl, 1.0 KH2PO4, 11 glucose, 26.2 NaHCO3, 2 CaCl2 and 1 MgCl2 (290-295 mOsm), bubbled with carbogen (95% O2/5% CO2). The retina was dissected and fixed on filter paper over a small hole (N8895, Sigma-Aldrich) with the RGC layer upwards and continuously perfused with Ringer's solution warmed to 32 °C.

Thick-walled borosilicate pipettes (OD/ID of 1.5/0.87 mm; 30-0060, Harvard Apparatus) were pulled on a P-1000 Flaming/Brown puller (Sutter Instruments). Pipettes were filled with intracellular solution containing (in mM): 128 K-gluconate, 10 HEPES, 16 KCl, 1 EGTA, 2 Mg-ATP, 0.5 Na2-GTP, pH 7.25 with KOH (275 mOsm) and 1-2 mg mL^{-1} biocytin (B4261, Sigma-Aldrich). Open tip resistance was 2.5 MΩ to 4 MΩ. Reported potentials were corrected for a liquid junction potential of −11 mV. Whole-cell recordings were made with a Multiclamp 700B amplifier (Axon Instruments), filtered at 10 kHz and digitized at 50 kHz using a DigiData

1440A (Axon Instruments) and Clampex 10.7 running on Windows 10. High-resistance patch seals (>1 GΩ) were obtained before breaking into the cell. Recordings with a series resistance R_s above 25 MΩ, or with a residual R_s (after compensation) above 5 MΩ, were discarded. The resting membrane potential of the cell was recorded in the first minute after breaking in.

Passive cell properties were recorded by stepping from −70 mV to −80 mV in voltage-clamp mode without whole-cell compensation. Series resistance was electronically compensated 80-95% with a lag of 18 µs. Between protocols we repeated the voltage step without compensation to monitor changes in series resistance, and series resistance compensation was adjusted if necessary. Passive currents were subtracted using a P/n protocol (5 steps of 5 mV) that preceded each protocol. The P/n protocol was missing for a few recordings; we then subtracted the passive response using a 10 mV step.

Adaptation protocols started with a long adaptation step at V_0 (0.5 s, V_0 varied by steps of 5 mV) followed by an activation step (resolution of 1 mV) to elicit an AIS spike. We ensured that the adaptation step was long enough by varying the step duration in a few cells.

In current-clamp mode, bridge balance and pipette capacitance cancellation (6.2 pF to 7.1 pF) were used. A square current injection was performed to measure the cell's capacitance. Next, for n = 16 cells, 5-20 minutes of spontaneous activity were recorded and to analyze spontaneous APs.

At the end of the experiment, the pipette was retracted to obtain an outside-out patch. Outside the retina the tip was cleaned with brief, positive pressure to remove the remaining membrane patch and the potential offset was noted to check for any drift in the reference potential.

The retina was rinsed in 0.12 M PBS, fixed for 15 minutes in 4% paraformaldehyde in 0.12 M phosphate buffer, rinsed again 2 times with 0.12 M PBS and kept in 0.12 M PBS at 4 °C for immunolabeling procedure at a later stage.

3.5.3 Immunohistochemistry

A few days after recording, retinas were washed during 5 minutes in PBS and permeabilized overnight at 4 °C in 5% normal goat serum (NGS, Sigma Aldrich) and 1% Triton-X100 in PBS. Retinas were then incubated with a solution of 0.1M PBS containing the mouse monoclonal anti-Ankyrin G (clone N106/36; 1:250; NeuroMab; ID: AB_2749806) and 1% normal donkey serum (NDS) for 24h at 4 °C. Retinas were washed 4 x 15 minutes in 0.1M PBS and then incubated with a PBS solution containing donkey anti-mouse Alexa Fluor 488 (1:500, Thermo Fisher; ID: AB_141607), Streptavidin Alexa Fluor 594 (1:500, Thermo Fisher, ref. S11227) , 5% NGS and 0.1% Triton-X100 overnight at 4 °C. Retinas were washed 4x15 minutes in PBS and mounted onto Superfrost™slides and coverslipped with Fluoromount. Mounted retinas were stored at 4 °C until confocal imaging.

3.5.4 Confocal imaging

The retinas labelled for biocytin and Ankyrin G were sequentially captured with an inverted laser scanning confocal microscope (FV1000, Olympus) equipped with an Argon (488 nm) ion laser and laser diode (555 nm), filter cubes appropriate for Alexa Fluor 488 and Alexa Fluor 594, and an 40x objective (oil, NA 1.3). Acquisition settings were optimized for each cell. Z-stacks were obtained with a step size of 0.5 µm. Confocal x-y resolution was 0.155 µm, except for three cells for which it was 0.207 µm.

3.5.5 Electrophysiological data analysis

Data were analyzed with custom Python scripts.

Estimation of passive properties

The raw series resistance R_s^* was measured from responses to a test pulse in voltage clamp: $R_s = \Delta V / I_0$, where ΔV is the voltage pulse amplitude and I_0 is the amplitude of the first transient peak. The residual series resistance R_s during a given recording is $R_s = R_s^* - R_{rec}\%_{comp}$ where R_{rec} is the series resistance used for compensation during the experiment and $\%_{comp}$ is the amount of compensation. Effective capacitance is estimated from the response to current pulses, by fitting an exponential to the first ms , which is the time scale of the axial current. This estimation was done in n = 17 cells.

Analysis of APs

The first AP recorded during spontaneous activity was used to measure AP features (fig. 3.1). Spontaneous activity was recorded in 16 cells; 6 of them were excluded from this analysis because the reference potential drifted by more than 3 mV. To compute the phase plots (dV/dt vs V), we ensured that the plotted points are isochronic, by considering that dV/dt corresponds to the derivative midway between two consecutive points, and interpolating the values of V at that midpoint. Spike onset was defined as the potential when dV/dt crosses 20 mV ms^{-1} for the last time before the AP peak. The value of dV/dt for the initial segment component was defined as the first local maximum between spike onset and the global maximum of dV/dt. In a few cells, this was equal to the global maximum. The regeneration threshold is defined as the potential at the point of maximal acceleration d^2V/dt^2 after the initial segment component.

Correction of series resistance error

Axial currents were corrected using a minor adjustment of the method described by Traynelis (1998). The presence of the series resistance results in an error in clamping the somatic potential equal to $-R_s \cdot I_e$, where I_e is the current through the electrode. This produces a capacitive current through the somatic membrane equal to $C \cdot dV/dt = -R_s C dI_e/dt$, which results in filtering the axial current through a low-pass filter with time constant $\tau = R_s C$. We correct the recorded current by subtracting this capacitive current:

$$I^* = I_e + \tau \frac{dI_e}{dt} \tag{3.4}$$

where I^* is the corrected current. The time constant is estimated directly by fitting an exponential to the first 0.5 ms of the response to a voltage step (with the same amplifier tunings as for subsequent recordings). We used the steps from the P/n protocol, except for a few cells with no P/n protocol, where we used a -10 mV test pulse before the axial current recording. We then correct for the loss in driving force due to imperfect clamping as in Traynelis (1998):

$$I = I^* \left(\frac{V_c - E_{Na}}{V_c - I_e R_s - E_{Na}} \right) \tag{3.5}$$

where V_c is the command potential. This is a minor correction.

Threshold

The voltage threshold V_t is defined as the highest command potential where no axonal spike is elicited. The membrane potential at the soma differs slightly from the command potential by $-R_s I_e$. As the axial current at threshold is about 100 pA, this error is smaller than 0.5 mV. 6 cells for which the reference potential drifted by more than 3 mV during the recordings were discarded from voltage threshold analyses.

As the current at threshold is small, we used only the recordings with P/n protocol (n = 15) to ensure accurate leak subtraction. Three additional cells were excluded from the analysis of threshold current because the recordings were either too noisy or with unstable baseline current. Thus, n = 12 cells were used. The current traces below threshold were smoothed with a sliding window (half-window size is 50 points, 1 ms) before peak detection (fig. 3.6 A). The threshold current was then measured as the largest peak current for the data points between $V_t - 1.5$ mV and V_t.

Charge and current duration

The charge Q transferred to the soma at spike initiation is estimated as the integral of I_e in the time window where the current is greater than 10% of its peak value (to avoid integrating noise). Current duration t_{50} is the duration during which the current is greater than 50% of the peak value.

Adaptation

Relations between V_t and V_0 (fig. 3.8) were fitted to the theoretical formula for threshold adaptation with sodium channel inactivation (Fontaine et al., 2014; Platkiewicz and Brette, 2011):

$$V_t = V_{min} + k_a \log \left(1 + e^{(V_0 - V_i)/k_i} \right) \tag{3.6}$$

For the current adaptation analysis, cells were discarded if R_s increased by more than 30% during the protocol. In a few cells, the threshold could not be clearly measured at -40 mV and therefore I_{40} is missing.

3.5.6 Morphological data analysis

Axon tracing in 3D was performed automatically with Vaa3D (Peng et al., 2010) (version 3.2 64-bit ran on MacOSX10.13.6) based on biocytin Z-stacks. The start and end position of the axon

tracing was manually chosen by the researcher to include the entire AIS. Axon coordinates (x, y, z, radius) were stored in SWC files and analyzed with custom Python scripts. Coordinates are interpolated with a finer spacing corresponding to the pixel size (including in the z direction also). Interpolation was performed with B-splines using Scipy (Virtanen et al., 2020) to evaluate the spline at each pixel comprised in the axon profile, and coordinates are rounded at the nearest pixel. The ankyrin G images are then loaded as a 3D stack to get the fluorescence intensity at the interpolated coordinates along the axon profile. The intensity profile is smoothed with a sliding mean (half-width 15 pixels). The AIS start and end position were manually defined using the normalized intensity profile, the 3D stacks and the maximal intensity projection in Fiji (Schindelin et al., 2012). Several cells for which the start or end position were considered too unclear to be determined accurately, were discarded from the analyses, so that morphological measurements were available for n = 14 cells.

3.5.7 Statistics

The box plots in fig. 3.1, 3.6 and 3.8 display the distribution of data in the following way. The central bar shows the median. The lower and upper limit of the box shows the first and third quartiles (Q1 and Q3), respectively. The lower and upper whisker bars show Q1-1.5 IQR (interquartile range, the range between Q1 and Q3) and Q3 + 1.5 IQR, respectively. The data points outside the whiskers are outliers and indicated by diamonds marker.

3.5.8 Theory

Axial current at spike initiation

The axial current at spike initiation has been derived previously based on resistive coupling theory (Hamada et al., 2016):

$$I_p = \frac{E_{Na} - V_t}{r_a(\Delta + \delta)} \tag{3.7}$$

with

$$\begin{aligned} \delta &= \delta' / \tanh(L/\delta') \\ \delta' &= \sqrt{\frac{d}{4R_i g}} \end{aligned} \tag{3.8}$$

where Δ is AIS distance from the soma, L is AIS length, d is AIS diameter, g is Na^+ conductance density, R_i is intracellular resistivity and

$$r_a = \frac{4R_i}{\pi d^2} \tag{3.9}$$

is axial resistance per unit length. The derivation makes the following assumptions: all Na^+ channels are open; channel kinetics are neglected; capacitive and leak currents are considered negligible. These assumptions all tend to overestimate the axial current, but the approximation is generally good (see Fig. 5B). When L is much greater than δ' (which was the case in our measurements), $\delta \approx \delta'$ and the axial current is essentially insensitive to L.

The maximum current across all possible AIS geometries can be calculated by setting $\Delta = 0$and $L = \infty$ (AIS of infinite length starting from the soma):

$$I_p^{max} = \frac{\pi}{2} d^{3/2} \frac{g}{R_i} (E_{Na} - V_t) \tag{3.10}$$

Therefore, the minimum conductance density necessary to produce an axial current I is:

$$g_{min} = \frac{4 R_i I^2}{\pi (E_{Na} - V_t)^2 d_{AIS}^3} \tag{3.11}$$

Axial current at threshold

In a model where the spatial extent of the AIS is neglected (all axonal Na^+ channels clustered at a single point), the axial current at threshold is k/R_a, where k is the Boltzmann activation slope of Na^+ channels and R_a is the axial resistance between soma and AIS (Brette, 2013). It is possible to calculate this current for an AIS of length L starting from the soma.

The axial current at threshold is:

$$I_t = \frac{V'(0)}{r_a} \tag{3.12}$$

where r_a is resistance per unit length. To obtain $V'(0)$, we solve the cable equation in a simple axon model where only the axial current and the Na^+ current are considered, as in (Goethals and Brette, 2020). We consider a cylindrical axon of diameter d. The AIS has length L and starts from the somatic end. It has a uniform density of Na_v channels. The total Na_v conductance is

$$G = g \times \pi d L \tag{3.13}$$

where g is the surface conductance density. We neglect leak and K^+ currents, Na_v channel inactivation, as well as all time-varying phenomena. The cable equation then becomes:

$$\frac{d^2V}{dx^2} = -\pi d r_a g (E_{Na} - V) e^{(V - V_{1/2})/k} \tag{3.14}$$

where $V_{1/2}$ is the half-activation voltage of Na_v channels. The boundary conditions are $V(0) = V_s$ (somatic potential) and $V'(L) = 0$ (no axial current flowing towards the distal axon). In units of the AIS length L, this equation reads approximately:

$$\frac{d^2V}{d(x/L)^2} = -\pi d r_a g L^2 (E_{Na} - V_{1/2}) e^{(V - V_{1/2})/k} \tag{3.15}$$

Here the driving force $(E_{Na} - V)$ has been approximated by $(E_{Na} - V_{1/2})$ as in (Brette, 2013). We now write the following change of variables:

$$\begin{aligned} U &= (V - V_{1/2})/k + \log(\pi d r_a g L^2 (E_{Na} - V_{1/2})) \\ y &= x/L \end{aligned} \tag{3.16}$$

and we note $U' = dU/dy$. That is, voltage is in units of k and space is in units of AIS length L. The rescaled cable equation is:

$$U'' + e^U = 0 \tag{3.17}$$

with the boundary conditions:

$$\begin{aligned} U(0) &= U_0 = (V_s - V_{1/2})/k + \log(\pi d r_a g L^2 (E_{Na} - V_{1/2})) \\ U'(1) &= 0 \end{aligned} \tag{3.18}$$

This equation is analytically solvable, with general solution

$$U(y) = \log\left(\frac{c_1}{2}\right) - 2\log\left(\cosh\left(\frac{1}{2}\sqrt{c_1(y+c_2)^2}\right)\right) \tag{3.19}$$

From $U'(1) = 0$, it follows that $c_2 = -1$. We then obtain for the boundary condition at 0:

$$U(0) = U_0 = \log\left(\frac{c_1}{2}\right) - 2\log\left(\cosh\left(\sqrt{c_1}/2\right)\right) \tag{3.20}$$

which defines c_1 as an implicit function of U_0. We look for a bifurcation, that is, a value of U_0 when the number of solutions changes. This is obtained by setting the derivative of the right hand-side to 0, which gives:

$$\frac{\sqrt{c_1}}{2}\tanh\left(\frac{\sqrt{c_1}}{2}\right) = 1 \tag{3.21}$$

The solution can be calculated: $\sqrt{c_1}/2 \approx 1.2$, giving $c_1 \approx 5.8$. We have $V'(0) = k/LU'(0)$ and

$$U'(y) = -2\frac{\sqrt{c_1}}{2}\tanh\left(\frac{\sqrt{c_1(y-1)^2}}{2}\right) \tag{3.22}$$

so $U'(0) = 2$ and we obtain:

$$I_t = \frac{2k}{r_a L} \tag{3.23}$$

A simple extrapolated formula consistent with the formulae for both point AIS away from the soma and extended AIS starting from the soma is:

$$I_t = \frac{k}{r_a x_{1/2}} \tag{3.24}$$

where $x_{1/2} = \Delta + L/2$ is the middle position of the AIS, relative to the soma. In simulations, we find that this is a good approximation (fig. 3.11).

Axial current near threshold

We calculate the axial current just below threshold as a function of somatic voltage in a point AIS model. We consider a cylindrical axon of diameter d where all the Na_v channels are located at a single location. The AIS contains a total Na_v conductance G. The axial current is

$$I = \frac{V - V_s}{R} \tag{3.25}$$

where V is the axonal voltage, V_s in the somatic voltage, and R is the axial resistance between the soma and the AIS. It must equal the Na^+ current:

$$I_{Na} = G(E_{Na} - V)\exp\left(\frac{V - V_{1/2}}{k}\right) \tag{3.26}$$

which is the exponential approximation near threshold. Near threshold, we have $(E_{Na} - V) \approx (E_{Na} - V_s)$. We consider this driving force as a constant ΔV. We then absorb $V_{1/2}$ into G and take k as the units of voltage. Thus, the equation reads:

$$I = I_{Na} = G\Delta V e^{V} \tag{3.27}$$

Using $V = V_s + RI$, we obtain

$$I = G\Delta V \exp(V_s + RI) \tag{3.28}$$

At the bifurcation (threshold), we have (differentiation with respect to I):

$$1 = GR\Delta V \exp(V_s^* + RI^*) \tag{3.29}$$

where V_s^* is the somatic voltage threshold and I^* is the axial current at threshold. We divide the two previous equations and obtain:

$$1 = \frac{1}{R} \exp(V_s - V_s^* + RI - RI^*) \tag{3.30}$$

In a point AIS, the axial current at threshold is:

$$I^* = 1/R \tag{3.31}$$

Therefore:

$$I = I^* \exp(V_s - V_s^* + I/I^* - 1) \tag{3.32}$$

This can be rewritten as:

$$V_s = V_s^* + 1 - \frac{I}{I^*} + \log\left(\frac{I}{I^*}\right) \tag{3.33}$$

A Taylor expansion gives:

$$V_s \approx V_s^* - \frac{1}{2}\left(1 - \frac{I}{I^*}\right)^2 \tag{3.34}$$

In original units, we obtain:

$$V_s \approx V_s^* - \frac{k}{2}\left(1 - \frac{I}{I^*}\right)^2 \tag{3.35}$$

Relation between voltage threshold and axial current at spike initiation

Theoretically, voltage threshold varies as $-k \log g$ (Brette, 2013; Goethals and Brette, 2020; Platkiewicz and Brette, 2011). The axial current at spike initiation also depends on g, and therefore voltage threshold and axial current co-vary when g is varied. The general relation is complicated, but a simple approximated relation can be obtained by considering the equation for the maximum current I_p^{max} . Since $I_p^{max} \propto \sqrt{g}$, it follows that with this approximation the threshold varies as $-k \log I_p^2$, i.e., as $-2k \log I_p$.

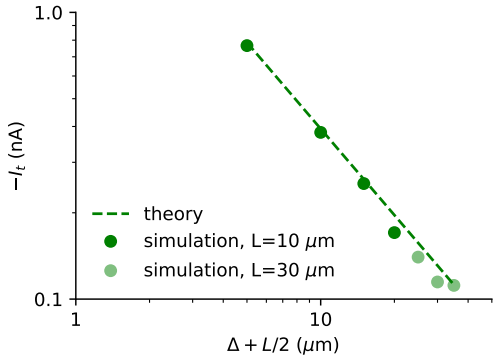

Figure 3.11: Theoretical estimation of axial current at threshold compared to simulations. The simple model (no inactivation, no K_v channels) is simulated with $L = 10\,\mu m$ (dark green dots) and $L = 30\,\mu m$ (light green dots), and the theoretical curve is shown as a dashed line.

3.5.9 Simplified model

In fig. 3.5 A-B and fig. 3.10, we used a simplified model with only non-inactivating Na_v channels to check analytical expressions, similar to (Brette, 2013). A spherical soma of diameter 30 µm is attached to an axonal cylinder of diameter 1 µm and length 500 µm (soma diameter is in fact irrelevant as the soma is voltage-clamped). Specific membrane capacitance is C_m= 0.9 µF cm^{-2}; specific membrane resistance is R_m= 15 000 Ω cm^{-2}; leak reversal potential is E_L = −75 mV; intracellular resistivity is R_i = 100 Ω cm. If not specified, Na_v channels are placed from 5 µm to 35 µm on the axon. In fig. 3.11, the length ranges from 10 µm to 30 µm and the start position from 0 µm to 20 µm. We used simple single gate activation dynamics with fixed time constant:

$$\begin{aligned} I_{Na} &= Gm(E_{Na} - V) \\ \tau_m \frac{dm}{dt} &= m_\infty(V) - m \\ m_\infty(V) &= \frac{1}{1 + \exp((V_{1/2} - V/k))} \end{aligned} \tag{3.36}$$

where E_{Na} = 70 mV, k = 5 mV, $V_{1/2}$ = −35 mV and τ_m = 53.6 µs (corresponding to 150 µs before temperature correction, see (Goethals and Brette, 2020)). For fig. 3.5 A and B, Na^+ conductance density was g = 5000 S m^{-2}. For fig. 3.11, the total Na_v conductance was fixed (G = 350 nS) to keep the total number of Na_v channels fixed when AIS length is varied. This corresponds to conductance densities of about 11 100 and 3700 S m^2 for a 10 and 30 µm long AIS, respectively. The model is simulated in voltage-clamp and the threshold is measured with the bisection method. We used the Brian 2 simulator (Stimberg et al., 2019) with 10 µs time step and 1 µm spatial resolution.

3.5.10 Biophysical model

In fig. 3.2 E-F, fig. 3.6 B-D and fig. 3.7 E, we used a biophysical model of an AP with inactivating Na_v channels and non-inactivating K_v channels, similar to (Goethals and Brette, 2020). The biophysical model has a simple geometry, consisting of a spherical soma (30 µm diameter), a long dendrite (diameter: 6 µm, length: 1000 µm) and a thin unmyelinated axon (diameter:

1 µm, length; 500 µm). The dendrite is irrelevant to most simulations because the soma is voltage-clamped, electrically isolating the dendrites from the axon. It only contributes an additional somatodendritic capacitance when an electrode model is added (fig. 3.2). When not specified, the AIS extends from 5 µm to 35 µm from the soma. Specific membrane capacitance is C_m= 0.9 µF cm^{-2}; specific membrane resistance is R_m= 15 000 Ω cm^{-2}; leak reversal potential is $E_L = -75$ mV; intracellular resistivity is R_i = 100 Ω cm (see table 3.1).

In fig. 3.2 E-F, we inserted an electrode model, which consists of a resistance R_s (0 MΩ to 5 MΩ) between the amplifier and the soma, such that a current $(V_c - V)/R_s$ is injected into the soma (where V_c is the voltage command). The Na_v conductance density g was 7400 S m^{-2}, to obtain peak axonal currents and thresholds comparable to measurements in RGCs.

In fig. 3.6 B-D, the AIS start position was 10 µm, close to the mean AIS start position in our cell population. The threshold was approached with 0.01 mV precision using the bisection method. In fig. 3.7 E, the AIS start position was varied from 0 µm to 20 µm and the AIS length was 30 µm. In these three panels, the Na_v conductance density was $g = 3700$ S m^{-2}.

3.6 Acknowledgments

We thank Marcel Stimberg for assistance with simulations, Elaine Orendorff for assistance with immunochemistry, Stéphane Fouquet for advice and assistance with confocal microscopy, Serge Picaud for access to the electrophysiology setup, and Boris Barbour and Christophe Leterrier for discussions.

Passive properties	R_m	$15\,000\,\Omega\,\mathrm{cm}^{-2}$
	E_L	$-75\,\mathrm{mV}$
	R_i	$100\,\Omega\,\mathrm{cm}$
	C_m	$0.9\,\mu\mathrm{F}\,\mathrm{cm}^{-2}$
Na_v channels	g_{Na}, soma	$250\,\mathrm{S}\,\mathrm{m}^{-2}$
	g_{Na}, dendrites and axon (non AIS)	$50\,\mathrm{S}\,\mathrm{m}^{-2}$
	g_{Na}, AIS	variable ($3500\,\mathrm{S}\,\mathrm{m}^{-2}$ to $7400\,\mathrm{S}\,\mathrm{m}^{-2}$)
	E_{Na}, soma	$70\,\mathrm{mV}$
	$V_m^{1/2}$, soma	$-30\,\mathrm{mV}$
	$V_h^{1/2}$, soma	$-60\,\mathrm{mV}$
	$V_m^{1/2}$, AIS	$-35\,\mathrm{mV}$
	$V_h^{1/2}$, AIS	$-65\,\mathrm{mV}$
	k_m	$5\,\mathrm{mV}$
	k_h	$5\,\mathrm{mV}$
	τ_m^*	$150\,\mu\mathrm{s}$ (corrected: $54\,\mu\mathrm{s}$)
	τ_h^*	$5\,\mathrm{ms}$ (corrected: $1.8\,\mathrm{ms}$)
K_v1 channels	g_K, soma	$250\,\mathrm{S}\,\mathrm{m}^{-2}$
	g_K, dendrites and axon (non AIS)	$50\,\mathrm{S}\,\mathrm{m}^{-2}$
	g_K, AIS	variable (default: $1500\,\mathrm{S}\,\mathrm{m}^{-2}$)
	E_K, soma	$-90\,\mathrm{mV}$
	$V_n^{1/2}$, soma	$-70\,\mathrm{mV}$
	k_n	$20\,\mathrm{mV}$
	τ_n^*	$1\,\mathrm{ms}$

Table 3.1: Parameters values of the biophysical model. Time constants corrected for temperature are indicated in brackets.

4 Axial current at spike initiation in cerebellar granule cells

The author of this thesis did the experimental and theoretical work presented in this chapter.

4.1 Introduction

In many neuron types, APs are initiated at the axon initial segment, a subcellular compartment located in the proximal region of the axon. The elicited spike subsequently propagates to the axon terminal but also back-propagates to the soma to be regenerated and further transmitted in the dendrites. Therefore, the AIS has to produce a sufficiently large current in order to depolarize the soma to the threshold for the opening of somatic Na_v channels. Theory predicts that the axial current that invades the soma at spike initiation decreases when the AIS is more distal (Hamada et al., 2016). In thick-tufted layer 5 pyramidal neurons, the position of the AIS matches the size of the somato-dendritic compartment to normalize the shape of the axonal component of the AP at the soma (Hamada et al., 2016). The larger the somato-dendritic compartment, the more current is needed to charge its capacitance, and the closer the AIS has to be located to the soma. It provides an indirect verification of the theoretical prediction. We here aim at investigating the relationship between the axial current and the AIS geometry directly, by recording the axial current at spike initiation and measuring the geometry of the AIS.

In order to be able to properly record axial currents at spike initiation and relate them to AIS geometry, we turned to cerebellar granule cells (CGC). CGCs are located in the input layer of the cerebellum, the granule cell layer. They are among the smallest neurons in the brain, with a soma diameter of about 6 µm in mice (Delvendahl et al., 2015) and on average 3 to 4 short dendrites (Palay and Chan-Palay, 2012) rarely exceeding 30 µm long in rodents (Delvendahl et al., 2015; Billings et al., 2014). CGCs are particularly suited to our research question for two reasons. First, their AIS is short (Osorio et al., 2010) and their axon is thin (Palay and Chan-Palay, 2012), so we expect the axial current at spike initiation to be small in these cells, and therefore measurable. Second, CGCs are electrotonically compact (Delvendahl et al., 2015), which enables good voltage-clamp. CGCs receive excitatory inputs at the end of their short dendrites from the mossy fibers, the axons entering the cerebellum. These inputs are conveyed to postsynaptic Purkinje cells and stellate cells through the parallel fibers, the CGC's axons. CGCs are therefore a crucial relay in the cerebellum.

As in RGC, the distribution of Na_v channels vary during CGC development. $Na_v1.2$ channels first accumulate at the AIS, while $Na_v1.6$ channels start to appear around P21. $Na_v1.6$ intensity then increases until adulthood and $Na_v1.2$ intensity starts to decrease around P30 (Osorio et al., 2010). By P40-P65 both channels co-localize at the AIS and have their adult distributions. As in rats (Diwakar et al., 2009), no $Na_v1.2$ or 1.6 fluorescence is observed in the soma and dendrites. To our knowledge, AIS length and start position were not measured precisely in CGC. However, optical fluorescence images enable to estimate that the CGC AIS is approximately 5 µm to 10 µm long in adult mice (Osorio et al., 2010; Goldfarb et al., 2007; Diwakar et al., 2009).

We aimed at recording the axial current at spike initiation in CGC, and to relate it to the AIS geometry. We measured the axial current with somatic voltage-clamp experiments in mice aged > 6 weeks to make sure the adult Na_v channels distribution was set. To measure the AIS geometry, the entire neuron morphology was stained by adding biocytin in the patch pipette and the slice was labelled with ankG antibody. In this chapter we present the results of these experiments.

4.2 Results

4.2.1 The axial current at spike initiation in CGC

Measuring the axial current

As was reported in adult mice CGC (Goldfarb et al., 2007) and young rats CGC (Magistretti et al., 2006; Diwakar et al., 2009), we measured a discontinuous current-voltage relationship in CGC (fig. 4.1 A). The soma was held at a resting membrane potential (RMP) of $-94.5\,mV$[1] as the RMP of adult mice CGC *in vitro* has been reported to be low. For instance, the RMP corrected for the liduid junction potential is on average $-99.5\,mV$ in Eshra et al. (2019) at P>70, $-78.6\,mV$ in Cathala et al. (2003) at P39 and $-89\,mV$ in (Chabrol et al., 2015) at P30-60. The soma was then progressively clamped at higher membrane potentials. Above a critical value, the spike initiation threshold, a small inward current of fixed amplitude is first recorded, followed by a larger current whose amplitude increases with voltage (fig. 4.1 B), as was observed in other cell types too (Milescu et al., 2010; Barrett and Crill, 1980). Upon 1 μM TTX application in the bath, these fast inward currents are totally blocked (fig. 4.1 C). The discontinuous IV curve is consistent with the bi-phasic spikes recorded in CGC (see for example fig. 1 and 2 in Eshra et al. (2019)). The spike is initiated remotely from the soma, at the AIS, producing a current of fixed amplitude at the soma until a higher threshold at which somatic Na_v channels open progressively. So the current coming from the AIS has to be large enough to depolarize the soma to the regeneration threshold. In RGC, this depolarization is about 30 mV (see section 3.3.1) and around 28 mV in layer 5 pyramidal cells (Kole and Stuart, 2008).

[1] After correction for a liquid junction potential of 14.5 mV, so during the experiment the cell was held at $-80\,mV$.

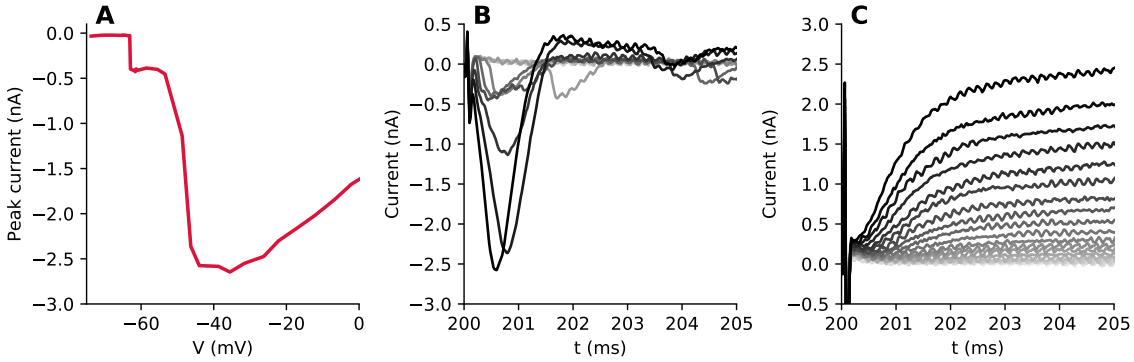

Figure 4.1: Axial currents recorded at the soma in CGC. **A**, Peak current vs. step command voltage. The peak current increases steeply above a voltage threshold. **B**, Raw current traces recorded in response to voltage steps from −74 mV to −44 mV. **C**, Raw current traces recorded in response to voltage steps from −74 mV to 22 mV in the presence of 1 μM TTX in the bath. The transient inward currents are abolished.

The effect of series resistance

Voltage-clamping the cell and recording large currents with the same pipette leads to errors because of the series resistance. It has two effects. First, the series resistance in parallel with the cell capacitance form a RC filter that alters the recorded currents. The characteristic time constant of the filter is $\tau = R_s C$ where R_s is the residual series resistance after on-line compensation (see Methods). In our recording, τ is in the order of $40\,\mathrm{M\Omega} \cdot 4\,\mathrm{pF} = 150\,\mu\mathrm{s}$. Second, the series resistance acts as a voltage divider, causing a voltage drop across the electrode. So true membrane potential differs from the command potential, reducing the driving force. We corrected the currents for these errors using the method described in Traynelis (1998) (see Methods). The capacitive current $\tau dI_e/dt$ is added to the recorded current, were I_e is the recorded current.

We investigated the effect of the series resistance on the voltage threshold and axial current in a biophysical model where the morphology was adapted to the small CGCs (soma diameter: 6 µm (Delvendahl et al., 2015) and axon diameter: 0.2 µm (Palay and Chan-Palay, 2012)). The voltage threshold is barely affected by the series resistance (fig. 4.2 A). The axial current is strongly attenuated when the series resistances increases, but this effect is reduced by the correction (fig. 4.2 C). In our recordings, neither the threshold nor the corrected peak current correlates significantly with the residual series resistance (p=0.18 and p=0.61, respectively, Pearson test) (fig. 4.2 B and D). In consequence, despite the large series resistance during our recordings, we expect a moderate effect of the series resistance. Compared to RGC (see section 3.3.1), the CGC capacitance is roughly one order of magnitude smaller, which compensates for the larger series resistance in the RC time constant.

The peak axial current

The peak axial current is the first current recorded above threshold. In adult mice CGC, the transient inward current has been reported to range from −0.4 nA to −2.5 nA (on average

-1.6 nA) in Osorio et al. (2010) and to be -1 $\pm$ 0.29 nA in Goldfarb et al. (2007). However, these currents were recorded with a cesium-based intracellular solution containing tetraethylammonium (TEA), which progressively blocks K_v channels and depolarizes the cell. In both studies, the extracellular solution contains a low Na^+ concentration (100 mM and 74 mM, respectively), which will tend to reduce Na^+ currents. More importantly, we do not know whether these reported values correspond to peak axial current or if it contains the somatic component of the current too.

We report a peak axial current of -0.75 $\pm$ 0.28 nA (s.d.) at room temperature. Assuming that the AIS starts from 3 µm to 5 µm away from the soma (estimated from fig. 4 of Goldfarb et al. (2007)) and has a diameter of 0.2 µm (Palay and Chan-Palay, 2012), the theory predicts that the peak axial current $I_p = (E_{Na} - V_t)/R_a$ ranges from -1.26 nA to -0.75 nA, using $R_i = 100\,\Omega$ cm for the intracellular resistivity (as in Cathala et al. (2003); Delvendahl et al. (2015)) and $E_{Na} - V_t = 120$ mV. It might be that in some cells the AIS is even located further away from the soma as 40% of CGC are axo-dendritic (Houston et al., 2017), which would reduce even more the peak axial current.

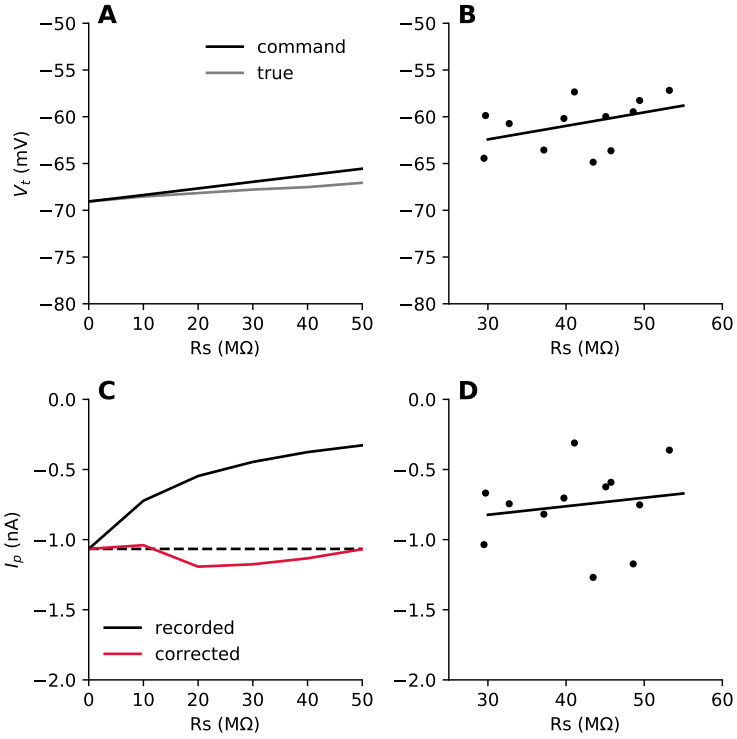

Figure 4.2: Effect of the series resistance on axial currents. **A**, Voltage threshold vs. series resistance in a biophysical model with an extended AIS (from 2 µm to 10 µm). Black, command potential. Gray, true membrane potential. **B**, Voltage threshold vs. residual series resistance in CGC with the regression line (p=0.18, Pearson test, n=12). **C**, Recorded (black) and corrected (red) peak axial current vs. series resistance in a biophysical model. **D**, Corrected peak axial current vs. residual series resistance in CGC with regression line (p=0.61, Pearson test, n=12).

4.2.2 The axial current transmission to the soma

In order to depolarize the soma to the threshold for the opening of somatic Na_v channels, the axial current has to charge the somatic capacitance. Therefore the axial current at spike initiation I_p should equal the capacitive current $C \cdot dV/dt$ during the first component of the spike. This assumes that the axial current is the main source of current at spike initiation, which is plausible given its magnitude. In addition, the capacitance C has to be understood as an effective capacitance charged by the rapid Na^+ currents. The effective capacitance charged by the axial current at spike initiation differs from the input capacitance and should be estimated from the first millisecond of the response to a current pulse, as we did for RGCs (section 3.3.1). The input capacitance is typically estimated from the integral of the response current to a small voltage step over several milliseconds, therefore corresponding to the capacitance of the soma and the proximal dendrites. Another complication arises because the relationship $I_p = C \cdot dV/dt$ is well defined only for an isopotential compartment. Owing to their electrotonic compactness, CGCs form a single electrical compartment and their capacitance is well-defined. The CGC input capacitance is on average 3.87 ± 0.29 pF (s.d.) in our cells, close to reported values in adult mice CGC *in vitro* (Cathala et al., 2003; Goldfarb et al., 2007; Straub et al., 2020) and *in vivo* (Chabrol et al., 2015). However, we can not exclude that the effective capacitance differs from the input capacitance because of the very short time scale of Na^+ currents.

Assuming that dV/dt at the peak of the axonal spike does not vary strongly across cells, we expect the cells with a larger capacitance to have a larger axial current ($I_p = C \cdot dV/dt$). Accordingly, we observe a significant correlation between the peak axial current and the capacitance (p=0.005, Pearson test, fig. 4.3 A). As $I_p = C \cdot dV/dt$, the relationship between I_p and C should be fitted by a linear regression going through the origin, with slope dV/dt. Surprisingly, the linear regression does not fit the data accurately. Its slope dV/dt is $198\,V\,s^{-1}$. In Eshra et al. (2019), the criterion for AP onset is that the first derivative of V crosses $100\,V\,s^{-1}$, suggesting that $198\,V\,s^{-1}$ at the peak of the axonal spike is a reasonable value. In comparison, in RGC, dV/dt at the peak of the axonal spike is $142 \pm 34\,V\,s^{-1}$ (section 3.3.1) and in axo-somatic tick-tufted layer 5 pyramidal neurons, it is $429.7 \pm 11.2\,V\,s^{-1}$ (Hamada et al., 2016).

The depolarization induced at the soma by the axial current, ΔV, can be directly estimated by measuring the charge transferred to the soma: $Q = C\Delta V$. The total charge transferred to the soma is the integral of the axial current and is on average -0.42 $\pm$ 0.15 pC (s.d.) in the recorded cells. We verify that the peak current correlates significantly with the charge to ensures that our measurements of the peak current are consistent (p=0.001, Pearson test, fig. 4.3 B). Indeed, the integral of the current is not altered by the RC filtering explained above. We find that charge correlates also significantly with the total capacitance ($p < 0.001$, Pearson test), and that the linear regression line (going through the origin) has a slope $\Delta V = 111$ mV (fig. 4.3 C). Similarly to the $I_p - C$ relationship, the data are not accurately fitted by the linear regression. In addition, the slope $\Delta V = 111$ mV is larger than expected. Indeed, the depolarization between the spike onset and the regeneration threshold is roughly 20 - 25 mV at 36 °C in CGC

(Eshra et al., 2019) and 33 mV at 32 °C in RGC (section 3.3.1), much smaller than the value we find.

The current duration is on average 0.73 ± 0.1 ms and does not correlate with the cell capacitance (p=0.16, Pearson test, fig. 4.3 D).

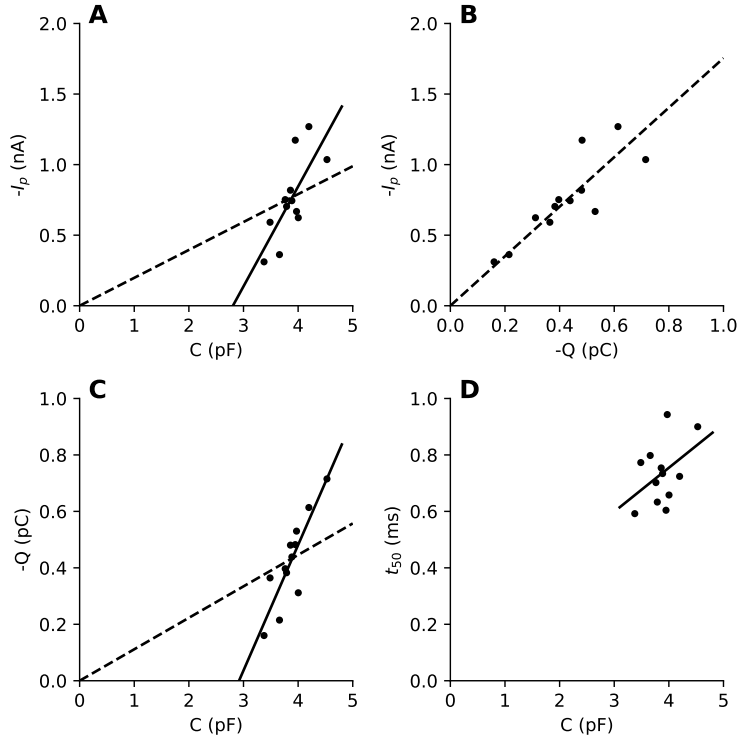

Figure 4.3: Transmission of the axial current to the soma (n=12). **A**, Peak axial current vs. total capacitance with regression line (solid line, Pearson correlation: r=0.75, p=0.005) and the best linear fit (dashed line). **B**, Peak axial current vs. transferred charge, measured as the integrated current, with the best linear fit (dashed line). Pearson correlation (not shown): r=0.85, p=0.001. **C**, Charge vs. total capacitance with regression line (solid line, Pearson correlation: r=0.87, p< 0.001) and the best linear fit (dashed line). **D**, Current duration at 50% of the peak vs. total capacitance with regression line (Pearson correlation: r=0.44, p=0.16).

The large estimation of ΔV that we report might be related to the recording temperature. We recorded axial currents at room temperature (RT) (21 - 22 °C), well below the physiological temperature. We performed a few recordings (n=6) at higher temperature ($\sim$ 32 °C). First, we noticed that the current duration remains approximately constant across cells and that currents are shorter compared to RT (0.29 ± 0.03 ms (s.d.), fig. 4.4 A), consistent with faster channels dynamics. Second, the axial current I_p correlates with the charge Q (p=0.001, Pearson test, fig. 4.4 B). The mean charge at 32 °C is -0.22 ± 0.074 pC (s.d.), almost half the charge transmitted at RT. If less charge is transmitted to the soma, the depolarization ΔV should be smaller. Indeed, the slope of the linear regression (going through the origin) fitted to the charge - capacitance relationship has a slope of 65 mV (fig. 4.4 C). This value is still larger than the depolarization between the AP onset and the regeneration threshold reported in

different cell types. However, based on the decrease in charge from RT to 32 °C, we can speculate that at physiological temperature (∼ 37 °C), the charge is even lower and therefore, ΔV too.

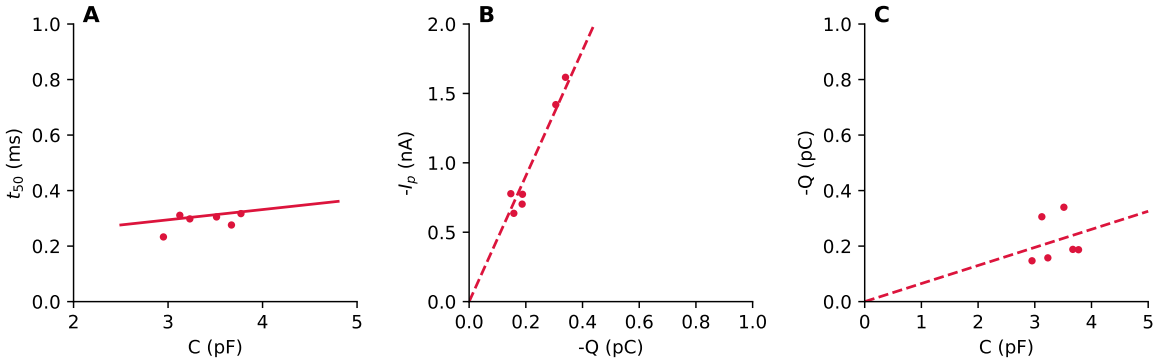

Figure 4.4: Transmission of the axial current to the soma at 32 °C (n=6). **A**, Current duration at 50% of the peak vs. total capacitance with regression line (Pearson correlation: r=0.52, p=0.29). **B**, Peak axial current vs. charge with the best linear fit. Pearson correlation (not shown): r=0.98, p=0.001. **C**, Charge vs. capacitance with the best linear fit.

4.2.3 Axial current and AIS geometry

Staining the CGC full morphology was more challenging than expected. In a large majority of the experiments, the cell could not be found after biocytin revelation. It is known that closing small cells at the end of a patch-clamp experiment is tricky (Stephen Brickley, personal communication). Even when the cell could be found in the slice, the axon was often not stained, putatively because of weak biocytin diffusion in the very thin axon (a successful example is illustrated on fig. 4.5 left). In addition, because of the very high density of CGC in the granule cell layer, the number of AISs around a cell body is very large, as illustrated on fig. 4.5 (right). On top of the absent/very dim axon labelling, linking a cell body to its AIS was very complicated. In consequence, we could not perform the analysis of the relationship between the AIS geometry and electrical properties in CGC.

4.2.4 Adaptation

The voltage threshold, the membrane potential above which a spike is triggered, vary with the membrane potential, a phenomenon referred to as *threshold adaptation* (Azouz and Gray, 2000; Platkiewicz and Brette, 2011; Fontaine et al., 2014). Among the possible causes of threshold adaptation, the Na_v channels inactivation is particularly important (Platkiewicz and Brette, 2011), as it will modify the AIS Na_v channels availablility at subthreshold potential. A slight depolarization of the resting membrane potential results in more inactivated channels, which should increase the threshold for spike initiation, as the number of available Na_v channels decreases. We investigated threshold adaptation by holding the membrane potential at different voltage V_0 during 200 ms and then measuring the threshold. Examples of IV curves recorded at different V_0 are illustrated in fig. 4.6 A. When the holding potential V_0 becomes more depolarized, the shape of the IV curve changes importantly: the axial current is reduced,

the voltage threshold shifts and the somatic currents become smaller too. All reported voltages are corrected for the liquid junction potential.

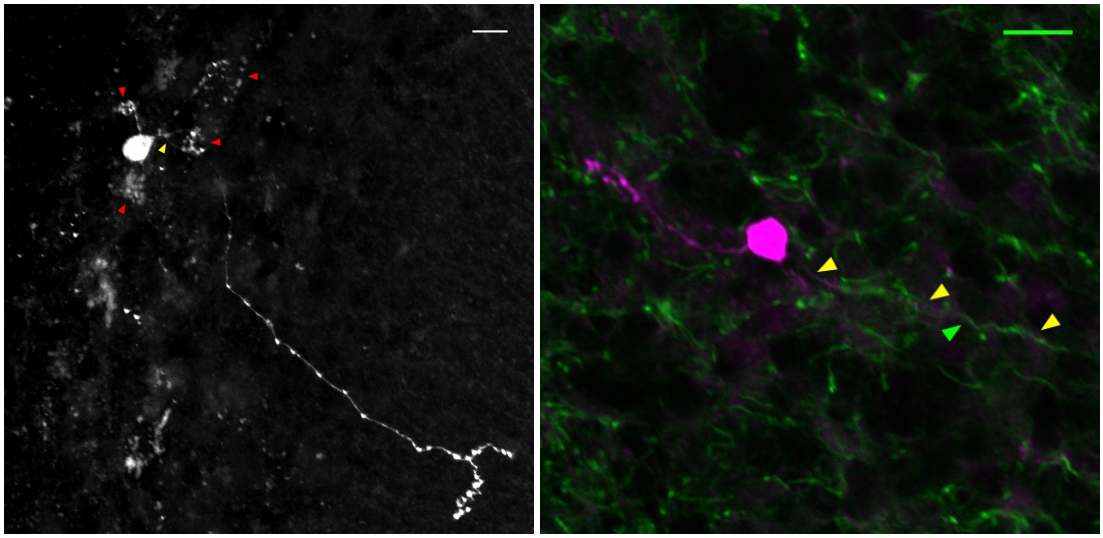

Figure 4.5: Full morphology and AIS labelling in CGC. **Left**, Example of a cell filled with biocytin during patch-clamp recording (maximal intensity z-projection). The four dendrites with their rosette ending are visible (red arrowheads). The axon originates from a dendrite (yellow arrowhead) and ends in the molecular layer (lower right). Scale bar: 10 µm. **Right**, Biocytin-filled granule cell (magenta) and AIS (green) in the z-stack where the axon is visible (yellow arrowheads). Several short green processes are superimposed on the axon (an example is indicated by the green arrowhead), making the attribution of an AIS to the cell complicated. Scale bar:10 µm.

Threshold adaptation

We indeed observe that the threshold adapts in all cells (n=8 at room temperature and n=3 at 32 °C), as illustrated by an example in fig. 4.6 A and B, and that adaptation seems to occur in two regimes. First, from -94.5 mV to -74.5 mV for the illustrated cell, the threshold decreases with V_0. Second, from -74.5 mV for the illustrated cell, the threshold increases with V_0, remaining just above it. If the adaptation was only due to Na_v inactivation, we would expect the threshold to be roughly constant until a value of V_0 close to the half-inactivation voltage, where it would start to increase with V_0, as observed in RGC (section 3.3.3). It suggests that another depolarizing/hyperpolarizing conductance at the AIS activates/inactivates respectively in the range where the threshold decreases with V_0. We recorded the adaptation protocol with 100 nM dendrotoxin-I (DTX-I, a blocker of $K_v1.1$ and $K_v1.2$ channels) in the bath in one cell, with no clear suppression of the first regime of threshold adaptation (data not shown). It is not surprising since K_v1 channels activate at higher voltage in the AIS (-24 mV in layer 5 cortical pyramidal cells; Kole et al. (2007)) and underlie a hyperpolarizing current at the AIS.

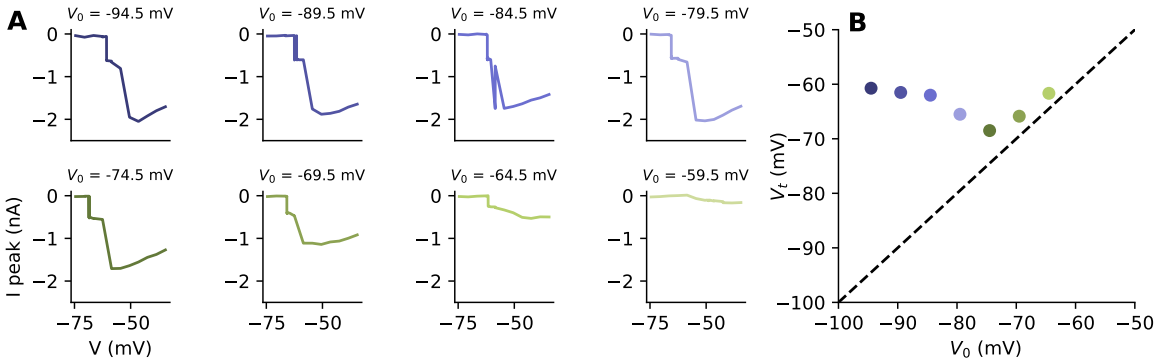

Figure 4.6: Threshold adaptation in CGC. **A**, Peak current vs. step command voltage for different V_0 in an example cell. **B**, Voltage threshold vs. V_0 in the same cell and the identity $V_t = V_0$ (dashed line).

Axial current adaptation

The peak current also adapts, decreasing substantially when V_0 increases (fig. 4.7 A). For this analysis, we considered both the cells recorded at room and higher temperature but cells for which the series resistance increased by more than 30% during the adaptation protocol were not included. Over a 30 mV depolarization range (from -89.5 mV to -59.5 mV), the peak axial current decreases on average 2.69 $\pm$ 0.51 (s.d.) fold (n=6, fig. 4.7 B), except for one cell (the one illustrated on fig. 4.7 A) that has a 6.17 fold attenuation. The small attenuation found in most of the cells probably comes from the fact that we did not explore adaptation at V_0 above -54.5 mV.

If the peak current adaptation and the threshold adaptation in the second regime are both due to Na_v inactivation, we would expect the threshold and the current to co-vary. Indeed, $V_t \sim -k_a \log(g_{Na})$ and $I_p \sim \sqrt{g_{Na}}$ which leads to a relationship between the threshold and the peak axial current: $V_t \sim -2k_a \log(I_p)$. It is indeed what we observe in the range of potential where the threshold increases with V_0, i.e. where the adaptation is most probably due to Na_v inactivation (fig. 4.7 C and D). The factor k_a, the slope of activation, has values close to expectations ($k_a = 4.34 \pm 1.07$ mV (s.d.), n=7, fig. 4.7 G). In cultured mice CGC, k_a has been reported to be 5.2 mV (Goldfarb et al., 2007) and 4.8 mV in young rats CGC (Magistretti et al., 2006). This result supports the hypothesis that threshold adaptation in the depolarized region and peak axial current adaptation are explained in a large part by the same phenomenon, Na_v inactivation.

Is the spike reliably transmitted to the soma upon adaptation? Successful spike transmission to the soma is required to ensure somatic spike regeneration. Is it maintained when the peak axial current attenuates? The decrease in peak current could be partly compensated by an increase in current duration, such that the total transmitted charge is conserved, as observed in RGC (section 3.3.3). Within the range of V_0 that was explored, the charge attenuation is very similar to current attenuation (charge attenuation: 2.28 $\pm$ 0.59 (s.d.), n=6, except for one cell with charge attenuation 7.67). Current and charge adaptation are illustrated in an example cell on fig. 4.8 A and B and compared across cells in fig. 4.8 C. The current duration remains

almost constant upon adaptation in the range of V_0 that was explored (mean change: 0.88 $\pm$ 0.09 (s.d.), n=5), as exemplified on fig. 4.8 D.

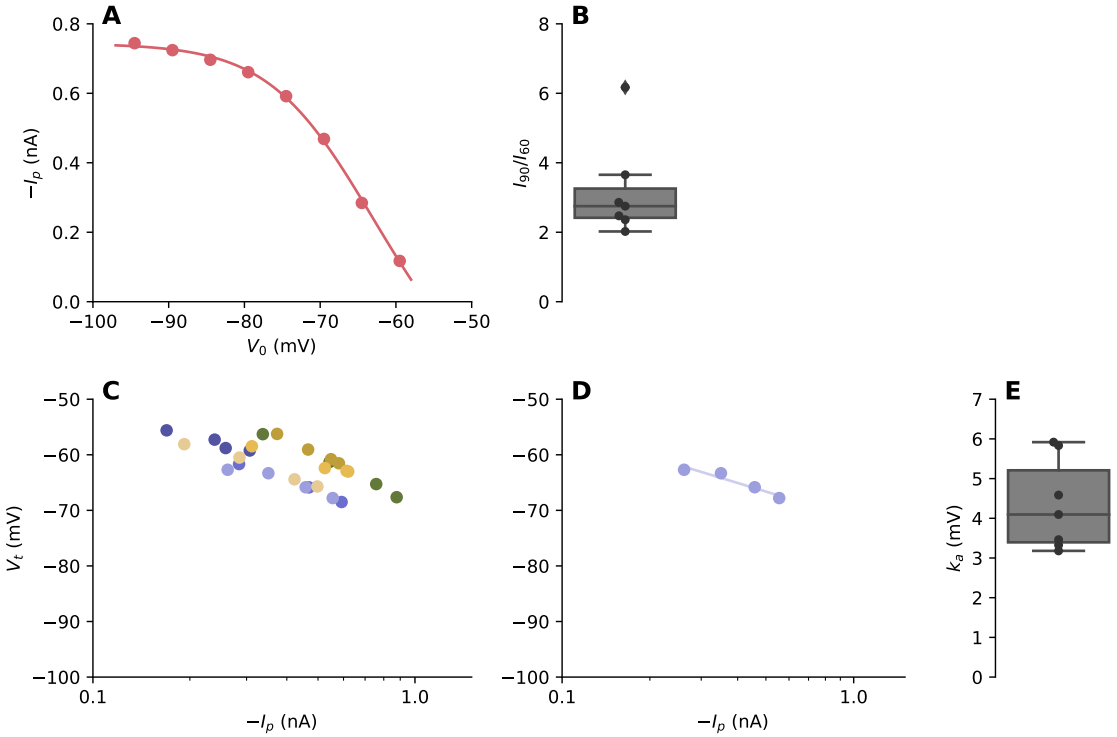

Figure 4.7: Peak axial current adaptation in CGC. **A**, Peak axial current vs. holding potential V_0 in an example cell. **B**, Statistics of the current attenuation from $-89.5\,\text{mV}$ to $-59.5\,\text{mV}$. **C**, Voltage threshold vs. peak axial current in the range where the threshold increases with V_0 (each color corresponds to one cell, n=7). **D**, Voltage threshold vs. peak axial current in the range where the threshold increases with V_0 in an example cell with logarithmic regression line ($k_a = 3.46\,\text{mV}$, Pearson correlation: r=0.96, p=0.038). **E**, Statistics of k_a from logarithmic regression in each cell ($k_a = 4.34 \pm 1.07\,\text{mV}$, n=7).

To summarize, in the range of V_0 that we explored, current and charge attenuation are very similar, and the current duration remains almost constant. However, we can not exclude that charge attenuation would be different from current attenuation, and that the current duration would have changed if more depolarized V_0 would have been investigated. The axial current depolarizes the soma to a voltage $V = V_t + Q/C$. At $-89.5\,\text{mV}$, the depolarization induced by the peak axial current ($\Delta V = Q/C$) ranges from 51 mV to 130 mV (n=7), more than what is necessary to reach the regeneration threshold. Among the 7 cells, one was recorded at 32 °C and it is the cell with the smallest ΔV, consistently with the lower amount of charge transmitted to the soma at higher temperature. At $-59.5\,\text{mV}$, the depolarization induced by the peak axial current ranges from 26 mV to 60 mV (38.5 $\pm$ 15.1 mV, n=6), except for the cell with larger attenuation for which $\Delta V = 15\,\text{mV}$. These values of Q/C are closer to the observed depolarization between initiation and regeneration thresholds.

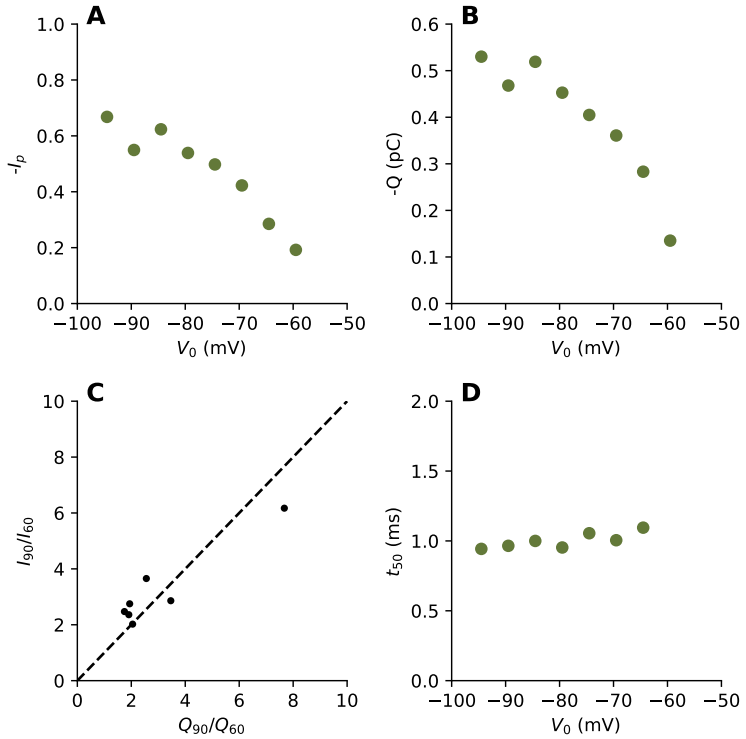

Figure 4.8: Axial current transmission to the soma during adaptation in CGC. **A**, Peak axial current vs. V_0 in an example cell. **B**, Charge vs. V_0 in an example cell. **C**, Peak axial current vs. charge attenuation from -90 mV to -60 mV with the identity (n=7). **D**, Current duration at 50% of the peak vs. V_0 in an example cell.

4.2.5 Suppression threshold

The threshold for spike initiation corresponds to a saddle-node bifurcation (Brette, 2013). It is the somatic voltage at which the axonal voltage suddenly jumps from resting membrane potential to a much larger value. This dynamical system undergoes hysteresis (see Methods, fig. 4.10). If the system is originally in a spiking configuration, decreasing the somatic membrane potential will block the spike below a threshold that is lower than the threshold for spike initiation. We call this somatic membrane potential below which the axonal spike is blocked the *suppression threshold*. In other terms, a bifurcation occurs at a different somatic membrane potential than the bifurcation corresponding to spike initiation.

To bring the system in a spiking situation, we elicited a spike with a very brief prepulse and then looked for the potential below which no spike is recorded. We used the following protocol of deactivation in voltage-clamp (fig. 4.9 A, compare with the protocol used to measure initiation threshold in fig. 4.9 B). The cell was very briefly (0.1 ms) clamped at a potential above the initiation threshold and the voltage was stepped from -50 mV to resting membrane potential or 10 mV below. We could record a deactivation protocol in 12 cells, among which 5 cells have a suppression threshold that is similar to the initiation threshold and 3 show a significantly lower suppression threshold compared to initiation threshold (fig. 4.9 C and D). For 4 other cells, the initiation threshold was not measured but the suppression threshold is well below the average initiation threshold across the population (shown on fig. 4.9 C). Note

that for 4 cells, the suppression threshold is actually below the indicated value because it was not reached by the protocol.

The theory predicts that

$$\frac{V_t^* + V_t}{2} = V_{1/2} - \frac{R_a I_p}{2} \tag{4.1}$$

where V_t is the initiation threshold and V_t^* the suppression threshold (see Methods). In mice cultured cerebellar cells, the half-activation threshold $V_{1/2}$ has been measured in whole-cell somatic patch clamp recordings to be -33.3 $\pm$ 4.2 mV (Goldfarb et al., 2007). From cell-attached recordings at the AIS in layer 5 pyramidal neurons, $V_{1/2} \approx -31.1$ mV (Kole et al., 2008). So we use $V_{1/2} = -35$ mV as a rounded value. Using $R_i = 100\,\Omega$cm and $d = 0.2\,\mu$m, the axial resistance per unit length is $31.83\,\mathrm{M\Omega\,\mu m^{-1}}$. With the mean I_p measured in our cells population and the AIS start position ranging from 3 µm to 5 µm, the predicted $(V_t^* + V_t)/2$ ranges from -70.8 mV to -94.7 mV. For 6 cells, $(V_t^* + V_t)/2$ is below -75 mV (fig. 4.9 E). But the values of R_i and $V_{1/2}$ could be different.

The observations, that, in a few cells within the population studied here, there exists a threshold below which the spike is blocked and that is much lower than the initiation threshold is a new support for modelling spike initiation as a saddle-node bifurcation.

4.3 Discussion

4.3.1 Summary

We measured an axial current at spike initiation in CGC (on average -0.75 nA) that is consistent with theoretical predictions. The axial current, as well as the total charge transferred to the soma just above spike initiation threshold, correlates with the cell capacitance. As in RGC, the transmitted charge correlates with the somato-dendritic capacitance. However, these relationships predict surprisingly large somatic depolarization ΔV and initial dV/dt. It is probably explained by the recording temperature during our experiments. As the axial current is strongly determined by the AIS start position and the axon diameter at the start of the AIS (Hamada et al., 2016), the strong correlations between axial current/transmitted charge and capacitance suggests that the AIS start position and/or the AIS diameter covary with the somato-dendritic geometry. Furthermore, we report that the initiation threshold adapts and that the axial current attenuates in parallel, probably because of Na_v inactivation but we lack data to confirm this hypothesis. The charge transferred to the soma attenuates approximately as much as the axial current in the voltage range that was tested. Finally, we could find a suppression threshold below which APs are blocked.

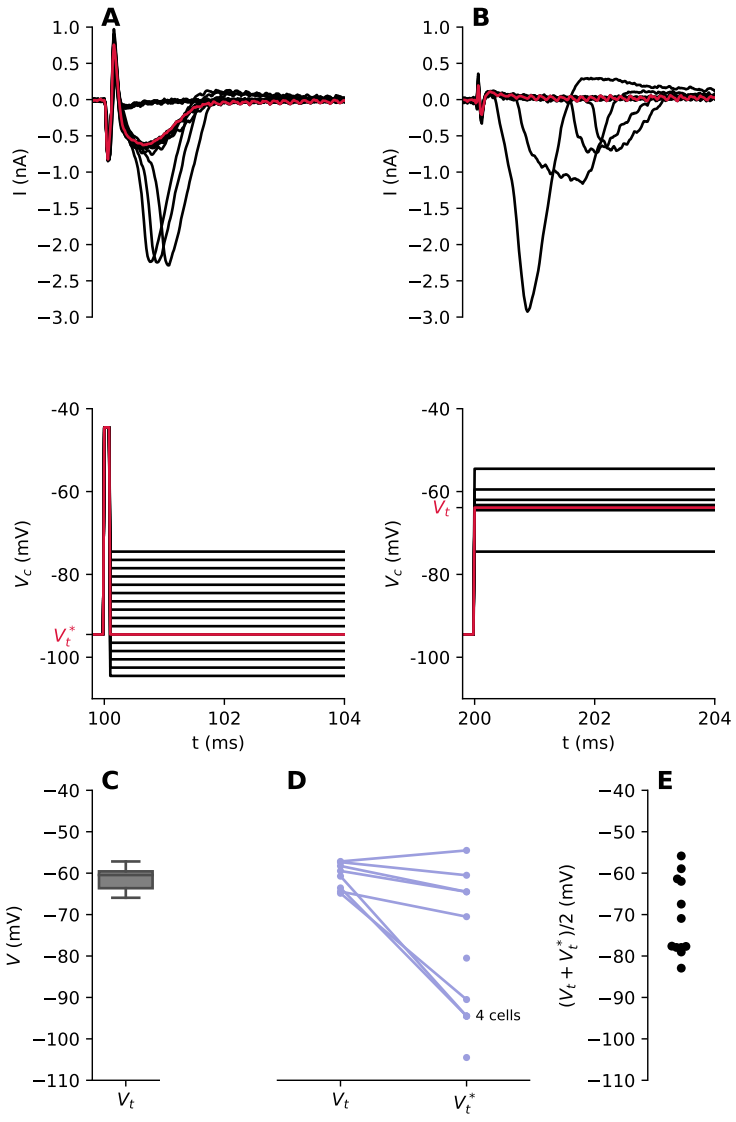

Figure 4.9: Suppression threshold in CGC. **A**, Bottom, voltage-clamp protocol used to measure the suppression threshold V_t^* (indicated in red). Top, current response to the protocol. The last recording with a large transient current, corresponding to V_t^*, is shown in red. **B**, Bottom, voltage-clamp protocol used to measure the initiation threshold V_t (indicated in red). Top, current response to the protocol. The last recording without a large transient current, corresponding to V_t, is shown in red. **C**, Statistics of the initiation threshold across all the population (-61.36 $\pm$ 2.92 mV (s.d.), n=18). **D**, Comparison of the initiation threshold V_t (left) with the suppression threshold V_t^* (right). 4 cells have $V_t^* \leq -94.5$ mV. **E**, The midpoint between the initiation and suppression thresholds.

4.3.2 Limitations

Our results are limited for several reasons. First, we could not investigate the relationship between axial current at spike initiation and the AIS start position directly, as most of the cells were not properly filled with biocytin after the patch-clamp experiments. Secondly, no test pulse with the same compensation settings as during the axial current recordings were recorded in most of the cells, preventing a proper estimation of the effective capacitance. In addition, using a leak subtraction protocol would have been useful to subtract the leak component of the currents, even if the leak current is very small in CGC. Third, the resting membrane potential at which the cells were clamped was certainly too low. Using $-80\,\mathrm{mV}$ after LJP correction would have been more correct. Fourth, for the adaptation protocols, higher prepulse potential V_0 should have been explored, to assess whether axial current attenuation and charge attenuation are similar or not. Fifth, recording action potentials would have helped the analysis of the axial current transmission to the soma. The cells were usually lost or the patch became very damaged after the adaptation and the deactivation protocols were ran (approximately 15 minutes), preventing the switch to current-clamp mode.

4.3.3 Effect of the recording temperature on AP transmission to the soma

We report that transient Na^+ currents in CGCs are significantly shorter and transmit less charge at $\sim 32\,^\circ\mathrm{C}$ compared to room temperature (charge: 1.9 fold smaller at $32\,^\circ\mathrm{C}$; current duration: 3.9 fold smaller at $32\,^\circ\mathrm{C}$). Consequently, the predicted depolarization ΔV at the soma at spike initiation is larger at RT than at $32\,^\circ\mathrm{C}$ ($108.5\,\mathrm{mV}$ vs. $65.3\,\mathrm{mV}$ using $\Delta V = Q/C$ with the mean capacitance and charge at each temperature). Recordings at $20\,^\circ\mathrm{C}$ and $37\,^\circ\mathrm{C}$ in rat myelinated nerve fibres show that the temperature affects the kinetics of Na_v channels activation and inactivation, by increasing their time constant $\tau_m(V)$ and $\tau_h(V)$, respectively (Schwarz and Eikhof, 1987). On the contrary, the steady-state activation $m_\infty(V)$ and inactivation $h_\infty(V)$ are not affected by the temperature, as well as the voltage dependence of the time constants of activation and inactivation. Similarly, in rat prefrontal pyramidal neurons, the kinetics of Na_v channels activation and inactivation is altered by temperature, but not their voltage dependence (Baranauskas and Martina, 2006). The dependence of channels kinetics on temperature can be expressed with the Q_{10} factor. Schwarz and Eikhof (1987) reports a Q_{10} of 2.2 for Na_v activation and 2.9 for Na_v inactivation. Baranauskas and Martina (2006) use 2.8. With the latter value, we obtain that the temperature factor for switching from $22\,^\circ\mathrm{C}$ to $32\,^\circ\mathrm{C}$ is $Q_{10}^{(32-22)/10}$, meaning that the rates of transition between the opened and closed states are 2.8 times faster at $32\,^\circ\mathrm{C}$, and that the time constant τ_m and τ_h are 2.8 times smaller. The gating variables m and h scale exponentially with their respective time constant. So if the axial current kinetics is determined by the kinetics of m and h, its duration and thereby the transmitted charge vary the same way, as $\exp(-1/Q_{10})$. In the Hodgkin-Huxley model, the Na^+ charge decreases exponentially with the temperature (Yu et al., 2012). As a result, less charge will flow to the soma at spike initiation, consistently with the reduction of transmitted charge we find when switching from RT to $32\,^\circ\mathrm{C}$. It follows that the charge transmitted to the soma at physiological temperature ($\sim 37\,^\circ\mathrm{C}$) is even smaller. From $32\,^\circ\mathrm{C}$ to $37\,^\circ\mathrm{C}$, the temperature factor is $\sqrt{2.8}$. Therefore, the depolarization induced by the axial current at the

soma at spike initiation in CGC *in vivo* is likely less important than the one we estimated form *in vitro* recordings at 32 °C. It is interesting since a vast majority of *in vitro* recordings are performed at 32 °C. As the voltage dependence of Na_v channels activation does not change with temperature (Schwarz and Eikhof, 1987), the depolarization we measured in RGC at 32 °C is also likely to be smaller at physiological temperature and therefore may not be sufficient to reach the threshold for the opening of the somatic Na_v channels.

This supposition provides new elements in the discussion about spikelets. Spikelets are small all-or-none AP-like events observed in several neuron types. Distinct types of spikelets have been reported in the literature, we here focus on 10 mV to 30 mV amplitude orthodromic spikelets reported *in vivo* ((see e.g. Epsztein et al., 2010; Coletta et al., 2018)), the first type described in Michalikova et al. (2019). Spikelets origin is resolved in some neuron types, but is an ongoing debate in cortical pyramidal cells (for details see the review of Michalikova et al. (2019)). As already suggested in early electrophysiological studies (Coombs et al., 1957), our results and others strongly suggest that, in many cases, orthodromic spikelets represent the passive propagation of the axonal spike to the soma (Michalikova et al., 2017; Hu et al., 2009). Notably, orthodromic spikelets in cortical pyramidal neurons were mostly reported *in vivo* (Michalikova et al., 2019). As most *in vitro* recordings are performed at 32 °C, our observations suggest that the charge transferred to the soma is larger than in physiological conditions, which could preclude axonal AP propagation failure and thereby the observations of orthodromic spikelets at the soma. At 37 °C, AP propagation failure might occur more frequently because of the decreased amount of charge transferred to the soma, explaining the spikelets recorded *in vivo* (Epsztein et al., 2010; Coletta et al., 2018).

4.4 Material and methods

4.4.1 Electrophysiology

C57B1/6J mice aged $>$ 6 weeks/42 days were decapitated and the cerebellum quickly detached from the forebrain and placed in ice-cold high sucrose slicing solution containing (in mM): 2.5 KCl, 0.5 $CaCl_2$, 4 $MgCl_2$, 24 $NaHC0_3$, 1.25 NaH_2PO_4, 25 D-glucose, 230 sucrose (Chabrol et al., 2015). Acute parasagittal slices (250 µm) were cut from the vermis using a Vibratome (Leica VT1000 S) in the ice-cold slicing solution. They were then directly transferred in an incubation chamber containing the incubation solution (in mM): 85 NaCl, 2.5 KCl, 0.5 $CaCl_2$, 4 $MgCl_2$, 24 $NaHC0_3$, 1.25 NaH_2PO_4, 25 D-glucose, 75 sucrose (Chabrol et al., 2015) at 32 °C for 30 min. Slices were then transferred to the extracellular recording solution containing (in mM): 125 NaCl, 2.5 KCl, 1.5 $CaCl_2$, 1.5 $MgCl_2$, 25 $NaHC0_3$, 1.25 NaH_2PO_4, 25 D-glucose and kept at room temperature. All solutions were bubbled with carbogen (95% O_2 /5% CO_2). 1 μM Tetrodotoxin (TTX, Alomone Laboratories) or 0.1 μM Dendrotoxin-I (DTX-I, Alomone Laboratories) were added in the extracellular solution during some cell recordings.

Thick-walled borosilicate capillaries (OD: 1.5 mm, ID: 0.86 mm, Harvard Apparatus) were pulled on a P-1000 Flaming/Brown puller (Sutter Instruments). Pipettes were filled

with an intracellular solution containing (in mM): 150 K gluconate, 10 NaCl, 10 HEPES, 0.3 GTP-Na, 3 ATP-Mg (Delvendahl et al., 2015), pH adjusted to 7.25 with KOH (305 mOsm) and supplemented with 1 mg μl^{-1} biocytin (B4261, Sigma-Aldrich). The pipette tip resistance was 5.5 MΩ to 10.5 MΩ. Reported voltages were corrected for a calculated liquid junction potential of +14.5 mV (similar to (Delvendahl et al., 2015; Eshra et al., 2019)).

Whole-cell recordings were performed at room temperature, except for 6 cells recorded at 32 °C, with a Multiclamp 700B amplifier (Axon Instruments), Bessel-filtered at 10 kHz and digitized at 40 or 50 kHz with an analog-to-digital converter (USB-6343, National Instruments), controlled by custom Python program (`https://github.com/romainbrette/clampy`). Upon tight seal formation, gentle suction was applied to break into the cell (Hamill et al., 1981). Series resistance R_s^{tot} was 45 MΩ to 70 MΩ and electronically compensated for 15% to 55% and often monitored during the experiment, to adjust compensation if necessary. The residual series resistance is $R_s = R_s^{tot} - \%_{comp} \cdot R_{rec}$ where $\%_{comp}$ is the amount of online series resistance compensation and R_{rec} is the series resistance used for compensation during the recording. Recordings with residual series resistance larger than 60 MΩ where discarded from the analysis. The cell capacitance and R_s^{tot} were estimated from the response to a voltage step from −94.5 mV to −99.5 mV. The series resistance is the amplitude of the peak current divided by the amplitude of the voltage step. The cell capacitance is $C_m = Q/\Delta V \cdot R_{in}/(R_s^{tot} + R_{in})$ where Q is the integral under the peak current (contribution of the current due to the input resistance was subtracted) and ΔV is the voltage step amplitude (Platzer and Zorn-Pauly, 2016).

To accurately measure the voltage threshold and the peak axial current, we designed different voltage-clamp protocols. First, the threshold was roughly estimated with the bisection method. Second, starting at this inaccurate value of the threshold, a second protocol was used to precisely determine the threshold. In some cells, regular voltage steps of small amplitude (0.2 mV) were used. In another group of cells, we used the staircase method based on accelerated stochastic approximation to estimate the threshold (Kesten et al., 1958). To measure threshold adaptation, the cell was first held at a potential V_0 ranging from −94.5 mV to −59.5 mV with 5 mV steps during 200 ms and then the threshold was measured. The suppression threshold was measured by eliciting an axonal spike with a very short prepulse (100 µs at −30 mV). The clamping voltage was subsequently stepped from −30 mV to −90 mV (illustrated on fig. 4.9 A).

At the end of the recordings, the patch pipette was gently retracted from the cell membrane in order to pull an outside-out patch and retain the biocytin within the cell. The slice was fixed for 10 min to 15 min in 4% paraformaldehyde in 0.12 M phosphate buffer and kept in 0.12 M PBS at 4 °C for immunolabeling procedure at a later stage.

4.4.2 Immunohistochemistry

A few days after recording, slices were washed during 5 minutes in PBS and permeabilized for 2 h at room temperature in 5% normal goat serum (NGS, Sigma Aldrich) and 2% Triton-X100 in PBS. Slices were then incubated with a solution of 0.1M PBS containing the mouse

monoclonal anti-Ankyrin G (clone N106/36; 1:250; NeuroMab; ID: AB_2749806) and 1% normal donkey serum (NDS) over the week-end at 4 °C. Slices were washed 3 x 10 minutes in 0.1M PBS and then incubated with a PBS solution containing donkey anti-mouse Alexa Fluor 488 (1:500, Thermo Fisher; ID: AB_141607) and Streptavidin Alexa Fluor 594 (1:500, Thermo Fisher, ref. S11227) for 2 h at room temperature. Slices were washed 3 x 10 minutes in PBS and mounted onto Superfrost™slides and coverslipped with Fluoromount. Mounted slices were stored at 4 °C until confocal imaging.

4.4.3 Confocal imaging

The slices labelled for biocytin and Ankyrin G were sequentially captured with an inverted laser scanning confocal microscope (FV1000, Olympus) equipped with an Argon (488 nm) ion laser and laser diode (555 nm), filter cubes appropriate for Alexa Fluor 488 and Alexa Fluor 594, and an 40x objective (oil, NA 1.3). Acquisition settings were optimized for each cell. Z-stacks were obtained with a step size of 0.5 µm. Confocal x-y resolution was 150.5 nm.

4.4.4 Data analysis

Data were analyzed with custom written Python scripts.

Correction of series resistance errors

Axial currents were corrected using a minor adjustment of the method described by Traynelis (1998). The presence of the series resistance results in an error in clamping the somatic potential equal to $-R_s \cdot I_e$, where I_e is the current through the electrode. This produces a capacitive current through the somatic membrane equal to $CdV/dt = -R_s C dI_e/dt$, which results in filtering the axial current through a low-pass filter with time constant $\tau = R_s C$. We correct the recorded current by subtracting this capacitive current:

$$I^* = I_e + \tau \frac{dI_e}{dt} \tag{4.2}$$

where I^* is the corrected current. The capacitance and residual series resistance were estimated as explained above. We then correct for the loss in driving force due to imperfect clamping as in Traynelis (1998):

$$I = I^* \left(\frac{V_c - E_{Na}}{V_c - I_e R_s - E_{Na}} \right) \tag{4.3}$$

where V_c is the command potential.

Thresholds

The voltage threshold V_t is defined as the highest command potential where no axonal spike is elicited. The membrane potential at the soma differs slightly from the command potential by $-R_s I_e$. As the axial current at threshold is about 20 pA, this error is smaller than 1 mV and we did not corrected the presented values. As the reference potential never drifted by more than $\pm$ 1.1 mV, it was not an inclusion criterion.

The suppression voltage threshold V_t^* is defined as the lowest command potential where an axonal spike is elicited by a very short prepulse.

Charge and current duration

The charge Q transferred to the soma at spike initiation is estimated as the integral of I_e in the time window where the current is greater than 10% of its peak value (to avoid integrating noise). Current duration t_{50} is the duration during which the current is greater than 50% of the peak value.

Axonal current adaptation

Cells for which the series resistance increased by more than 30% during the adaptation protocol were not included in the analysis of the axonal current adaption.

4.4.5 Theory

Suppression threshold

Following resistive coupling theory (Brette, 2013), the axial current that flows towards the soma at spike initiation has to match the Na^+ current entering the AIS $f(V_a)$:

$$f(V_a) = \frac{V_a - V_s}{R_a} \tag{4.4}$$

where V_a is the membrane potential at the AIS and V_s is the membrane potential at the soma. The Na^+ current is:

$$f(V_a) = g_{Na}(E_{Na} - V_a)\frac{1}{1 + \exp\left(-\frac{V_a - V_{1/2}}{k_a}\right)} \tag{4.5}$$

Solving eq. (4.4), we obtain that at a critical value of the somatic membrane potential (the bifurcation parameter), there is a saddle-node bifurcation (number of solutions changes from 3 to 1). The threshold for spike initiation V_t corresponds to this critical value at which the axonal voltage suddenly jumps from resting membrane potential to a much large potential. As illustrated on the bifurcation diagram (fig. 4.10), another bifurcation occurs when the system is originally in a spiking situation (high V_a) and the number of solutions changes from 3 to 1 when the somatic membrane potential decreases. The somatic membrane potential at this bifurcation is the suppression threshold.

At the peak of the Na^+ current (close to the suppression threshold), the activation function can be approximated by an exponential, so we obtain:

$$\frac{V_a - V_s}{R_a} = g_{Na}(E_{Na} - V_a)\left(1 - \exp\left(-\frac{V_a - V_{1/2}}{k_a}\right)\right) \tag{4.6}$$

At the bifurcation, we assume that at the peak of the current $E_{Na} - V_a^* \simeq E_{Na} - V_{1/2}$ so the bifurcation condition (Brette, 2013) is:

$$\frac{1}{R_a} = g_{Na}(E_{Na} - V_{1/2})\left(\frac{1}{k_a}\exp\left(\frac{V_{1/2} - V_a^*}{k_a}\right)\right) \tag{4.7}$$

The axonal membrane potential at the bifurcation is therefore

$$V_a^* = V_{1/2} + k_a \log\left(g_{Na} R_a \frac{E_{Na} - V_{1/2}}{k_a}\right) \tag{4.8}$$

and we see that the bifurcation diagram is symetric around $V_{1/2}$ in the y-direction. From eq. (4.4) and eq. (4.5) we also have:

$$V_a - V_s = g_{Na} R_a (E_{Na} - V_{1/2}) - g_{Na} R_a (E_{Na} - V_{1/2}) \exp\left(\frac{V_{1/2} - V_a}{k_a}\right) \tag{4.9}$$

and at the threshold, using the bifurcation condition, we obtain that

$$k_a = V_s^* - V_a^* + g_{Na} R_a (E_{Na} - V_{1/2}) \tag{4.10}$$

The somatic suppression threshold is therefore

$$\begin{aligned} V_s^* &= V_a^* + k_a - g_{Na} R_a (E_{Na} - V_{1/2}) \\ &= V_{1/2} + k_a + k_a \log\left(g_{Na} R_a \frac{E_{Na} - V_{1/2}}{k_a}\right) - g_{Na} R_a (E_{Na} - V_{1/2}) \\ &= 2V_{1/2} - V_s - g_{Na} R_a (E_{Na} - V_{1/2}) \end{aligned} \tag{4.11}$$

so that

$$\frac{V_s^* + V_s}{2} = V_{1/2} - \frac{g_{Na} R_a (E_{Na} - V_{1/2})}{2} = V_{1/2} - \frac{R_a I_p}{2} \tag{4.12}$$

The difference between the suppression and the initiation threshold is

$$V_s^* - V_s = 2k_a + 2k_a \log\left(g_{Na} R_a \frac{E_{Na} - V_{1/2}}{k_a}\right) - g_{Na} R_a (E_{Na} - V_{1/2}) \tag{4.13}$$

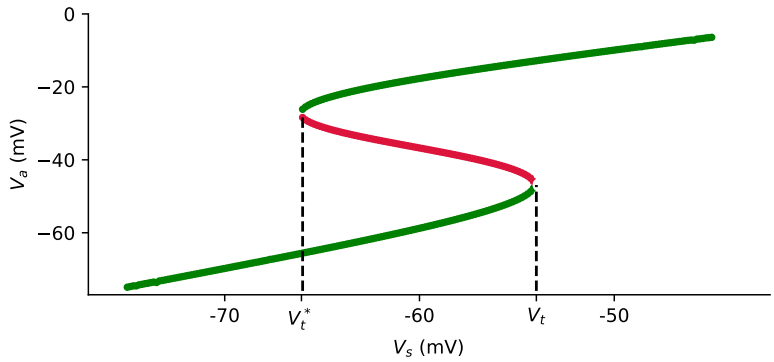

Figure 4.10: Bifurcation diagram. The solutions V_a of eq. (4.4) as a function of the bifurcation parameter V_s. Stable fixed points are shown in green and unstable fixed points in red. The suppression threshold V_t^* is lower than the initiation threshold V_t.

4.4.6 Biophysical model

For fig. 4.2 A and C, we used a previously published biophysical model (Goethals and Brette, 2020). The morphology was adapted to that of CGC: the soma diameter is 6 µm, the axon diameter is 0.2 µm and the dendrite diameter is 2 µm (the size of the soma and the dendrite are not relevant as the soma is voltage-clamped). The AIS starts at 2 µm away from the soma and ends at 10 µm. It contains a total Na_v conductance density of 150 nS. All the other parameters are identical to (Goethals and Brette, 2020).

5 Conclusion

In this thesis we investigated theoretically and experimentally the relationship between the AIS geometry and two of the neuron's fundamental electrical properties, namely excitability and AP transmission to the soma.

The theoretical predictions presented in this thesis were developed in the framework of resistive coupling theory (RCT) (Brette, 2013). As the site of spike initiation is approximately an order of magnitude smaller than the soma, the former responds more quickly to a current entering the axon and this response depends on the axial resistance between the soma and the initiation site. Thereby, spike initiation occurs through a decoupling of the membrane potential at the soma and at the AIS. When the somatic membrane potential reaches a threshold, Na_v channels at the AIS open, generating a spike. This current flows towards the soma, resulting in an all-or-none current at the soma. RCT was initially developed in a two-compartment electrical model consisting of a voltage-clamped soma connected through a resistor to the initiation site, which contains non-inactivating Na_v channels (Brette, 2013). It was later shown that RCT describes accurately spike initiation in multicompartmental biophysical models (Telenczuk et al., 2017). Experimental support for RCT is reviewed in Telenczuk et al. (2017). As an example, RCT predicts that AIS Na_v channels open abruptly as a function of the somatic membrane potential. It is verified in the discontinuous IV curves recorded in voltage-clamp at the soma. RCT was further empirically tested with the pinching experiments described in the introduction of this thesis. When the axial resistance between the soma and the initiation site is increased by pinching the axon with two glass pipettes, voltage threshold decreases, as predicted by RCT (Fekete, 2018). In this work we bring additional evidence that neurons follow the resistive coupling regime. Regarding the requirement that the soma is much larger than the AIS, we collected geometrical data and found that, in the considered neuron types, the soma has a much larger diameter than the AIS. Next, we compared the response to a current injected in the proximal axon at the soma and at the injection site, and observed a voltage gradient, as predicted. Furthermore, the input resistance at the injection site increases with its position, supporting the modelling of the soma-injection site region as resistive.

5.1 Summary

Building on this we show that the most appropriate parameter to describe the impact of AIS geometry on excitability is the somatic voltage threshold for spike initiation. It captures the effect of structural changes such as elongation or shift along the axon, but also variations in Na_v conductance and hyperpolarizing currents at the AIS. We hope this will help to standardize how the impact of AIS plasticity on excitability will be investigated in the future, to ease the comparison between different studies. Our theoretical approach allows to separate the influence of each specific parameter on the voltage threshold. In particular, we predict that the neuron is more excitable when the AIS is more distal. It is in line with the idea that the AIS is the site of spike initiation because it is electrically isolated from the soma (Baranauskas et al., 2013; Brette, 2013).

Although theory predicts a moderate effect of a change in AIS geometry on the voltage threshold, it predicts a strong impact on the axial current transmitted to the soma at spike initiation. Consistently, in layer 5 pyramidal neurons, the start position of the AIS matches the size of the somato-dendritic compartment to normalize the speed of the spike at the peak of the axonal spike (first max of dV/dt), suggesting that the AIS start position is tuned to ensure spike transmission to the soma (Hamada et al., 2016). In this work we studied this phenomenon more directly by measuring the axial current at spike initiation in retinal ganglion cells. First, we deduced that a high density of Na_v channels at the AIS is required in order to produce the current that we recorded, adding a new element to the ongoing debate (see section 1.2.3). Second, we found that the amount of charge transferred to the soma at spike initiation covaries with the somato-dendritic capacitance in order to depolarize the soma to the regeneration threshold. This results is particularly remarkable as we did not distinguish between the RGC subtypes. RGCs constitute a diversified neuron population that encompasses many sub-populations of neurons characterized by their size, dendritic arbor shape and function (Seung and Sümbül, 2014; Sanes and Masland, 2015), strengthening the idea that the AIS position-soma size is a fundamental relationship. Finally, when the axial current attenuates in parallel to threshold adaptation, it is compensated by current broadening. As a result, the amount of charge transferred to the soma remains sufficient to regenerate the spike. It suggests that he AIS geometry and channel properties at the AIS are probably tuned to produce the right amount of charge.

Altogether, as discussed in section 2.4.5, the results summarized above challenge the usual interpretation of AIS plasticity as a homeostatic mechanism that regulates excitability (see e.g. Grubb et al., 2011; Yamada and Kuba, 2016; Wefelmeyer et al., 2016).

5.2 Modelling the structural tuning of the AIS

The covariation between the AIS start position and the somato-dendritic capacitance that we report raises numerous questions. Could it be that it is a fundamental characteristic of all

multipolar neurons? It is possible, at least for neurons that regenerate the spike at the soma. We report similar results in two very different neuron types, which is significant. Interestingly, in the chick nucleus laminaris, the AIS moves away from the soma and shortens during development. In parallel, the capacitance of high and low CF neurons decreases. However, at least in middle and high CF neurons, the APs are not regenerated at the soma (Kuba et al., 2005). They have small amplitude and small maximal rate-of-rise. These neurons also bear very short dendrites (5 µm to 30 µm long, Smith and Rubel (1979)). Similarly, NM neurons are adendritic and high and middle CF neurons do not regenerate the AP at the soma. The fact that APs are not regenerated at the soma in NM and NL neurons could be attributable to their function, as a relay between the auditory nerve and the NL, and as a coincidence detector, respectively. On the contrary, ensuring reliable transmission of the AP to the axon terminal might by crucial for these neurons. Assuming that the membrane potential at the end of the AIS at AP peak must remain constant and that the density of channels is constant, we obtain a relationship between the AIS start position and length (Appendix A). If the AIS is located far from the soma, it has to be shorter, while if it is located close to the soma it has to be longer. In the NL, high CF neurons have a distal and short AIS, while low-CF neurons have a long and proximal AIS, which corresponds to the predicted trade-off between start position and length. In conclusion, the AIS of NL neurons could be structured to normalize the spike that is transmitted along the axon. The AIS start position and length in the chicks NM and NL neurons seems to be precisely adjusted (reviewed in Kuba (2012)), a pattern that progressively appears during development (Kuba et al., 2014). Whether it is to preserve a fundamental electrical property or for a reason that is more specific to their function still needs to be determined.

It is becoming clear from our results and others (Jamann et al., 2018; Kuba, 2012; Kole and Brette, 2018) that the AIS does not have a random position and length in the proximal axon but is accurately located for a functional purpose. The latter might depend on the neuron types and its specific function. In layer 5 pyramidal neurons and RGC, the AIS geometry seems to be tuned for successful AP regeneration at the soma. In the NM and NL, the AIS geometry is putatively adapted to the different input the neuron receives. The question that emerges is, how is the tuning achieved? How does the neuron know how and where to place its AIS? In NL neurons, cochlea ablation reduces the AIS shortening that occurs during development in middle and high CF neurons (Kuba et al., 2014), indicating that spontaneous activity refines AIS localization. In neurons where the AIS position matches the size of the SD compartment, how is this established? Does the neuron know from the beginning where to place its AIS? Or does it learn by trial-and-error for instance?

As a continuation of this work, one could develop a model for the tuning mechanism. To get more insights into the possible mechanisms that determine the AIS geometry, we can start with the ones that drive AIS plasticity. Depending on the neuron type, different kinase and phosphatase are implied. For instance, in dissociated hippocampal neurons, activity-dependent relocation of the AIS is triggered by L-type voltage-gated calcium channels (VGCC) and mediated by calcineurin (Evans et al., 2013; Grubb and Burrone, 2010). Calcineurin is a molecule that is sensitive to changes in calcium concentration. Interestingly, L-type VGCC

and calcineurin are concentrated at the soma and proximal dendrites and not at all at the AIS (Evans et al., 2013). It suggests that AIS relocation is triggered in the somatodendritic compartment and it is in line with the idea that AIS position is tuned for successful spike transmission and regeneration at the soma. AIS plasticity in inhibitory olfactory bulb neurons is also triggered by L-type VGCC but is not mediated by calcineurin (Chand et al., 2015). In hippocampal CA1 pyramidal neurons, the fast (4 hours) relocation of Na_v and K_v7 channels triggered by M-current inhibition is not dependant on L-type VGCC (Lezmy et al., 2017). M-current inhibition also induces a slower (2 days) relocation of ankyrin G and whether this relies on L-type VGCC has not been tested (Lezmy et al., 2017).

Therefore, based on these observations and on the idea that the spike has to be successfully regenerated at the soma, we can think of a model for the adjustment of AIS localization. The aim could be to find the minimal axial current that elicits a spike at the soma. The model would comprise two sensors that monitor the spiking activity at the soma and the AIS, that can communicate and trigger changes in AIS geometry. The results on AIS plasticity suggest that the sensors could be calcic sensors that monitor the intracellular calcium concentration. If a signal is triggered at the AIS but not at the soma: the somatic sensor triggers a movement of the AIS towards the soma to increase the axial current. If a signal is triggered at the soma and the AIS, the sensor at the AIS shifts the AIS away from the soma to decrease the axial current. This feedback mechanism would continue until the minimal axial current that regenerates the spike at the soma is reached. AP regeneration at the soma is one criterion, another could be to maintain the threshold for spike initiation, as it was observed not to vary substantially (discussed in Goethals and Brette (2020)).

For such a model to be accurate, the right amount of voltage-gated channels has to be inserted in the AIS. Na_v channels density at the AIS has been explored using different techniques (detailed in sections 1.2.3 and 3.4.3) but none allows to estimate precisely the density of functional Na_v channels at the AIS. In particular, we do not know whether it changes with AIS plasticity. The functional density of Na_v channels at the AIS results from the interplay of lateral diffusion, channels turnover and channels phosphorylation.

The specific structure of the AIS cytoskeleton constrains the membrane protein number, as well as their diffusion along the membrane. The number of Na_v channels is presumably limited by the size of the ankyrin G binding domain. Moreover, once inserted in the AIS, the mobility of Na_v channels is hindered, constrained by the mobility of the ankG terminal. The latter assertion is supported by results from single particle tracking studies. The diffusion coefficient of channels anchored to ankG is, depending on the exact technique used, $0.001\,\mu m^2\,s^{-1}$ (Brachet et al., 2010) or $0.01\,\mu m^2\,s^{-1}$ (Nakada et al., 2003) in mature neurons. It is small compared to some other membrane proteins whose diffusion coefficient usually lays between 0.01 and $1\,\mu m^2\,s^{-1}$ (reviewed in (Groc and Choquet, 2008)).

If the density of Na_v channels at the AIS is strongly limited by the AIS cytoskeleton structure, it might not be substantially variable. Therefore, if we know the dimensions of

the AIS components, we might be able to estimate the maximal number of (functional) Na_v channels at the AIS. Together with the minimal estimate obtained from the axial current (section 3.3.1), this could be included in the aforementioned model.

5.3 Perspectives

In addition to developing a model of the AIS geometry tuning mechanism, we can think of different follow-ups of this work, which are listed below.

- To overcome some of the limitations of our study in RGC, I would suggest recording axial currents at AP initiation in adult neurons, labelling ankyrin G and Na_v channels, and imaging the AIS with super resolution microscopy as for example in Schlüter et al. (2019). Thereby, the axial current could be related to the two geometrical parameters that influence it strongly: the AIS start position and the AIS diameter. In addition, using adult animal neurons would avoid possible heterogeneity in channels expression during development, and therefore minimize the other factors that influence the axial current. For instance, dentate granule cells from the hippocampus are small neurons and could therefore be an appropriate choice.

- RCT predicts that the AIS and the soma form a dipole at spike initiation. It could be tested we high density multi-electrode array (MEA) recordings, associated with AP recording in whole-cell patch clamp and AIS labelling, for example the data presented in Bakkum et al. (2019). Indeed, the spatial resolution of high-density MEA (17.8 µm pitch) is close to the dimensions of the AIS (Obien et al., 2015). However, this analysis is very likely to be complicated by unwanted electrical interactions between the electrodes and the neuronal membrane.

- In line with the previous point, taking the AIS into account to understand the neuronal responses evoked by electrical stimulation could be helpful. For instance, to explain the unexpected shape of percepts induced by retinal implants. Upon focal electrode stimulation, patients see distorted patches, whose shape and size vary from one trial and one patient to the other, for the same stimulation (references listed in Beyeler et al. (2019)). It has been attributed to the activation of axon fibers passing close to the electrode. A model including the topographical organization of axon bundles in the retina reproduces some of the distorted shapes with moderate accuracy (Beyeler et al., 2019). Refining this model with spike initiation at the AIS might improve the performance of the model and help unravel the mechanism behind these surprising visual percepts.

To conclude, we hope this work advanced the knowledge about the mechanism of spike initiation, and more precisely how it is influenced by the properties of the axon initial segment and constrained by the morphology of the somatodendritic compartment.

A Action potential at AIS distal end

In this appendix we derive a formula for the amplitude of the AP at the end of the AIS. We consider a cylindrical model of an axon with constant diameter d, which is voltage-clamped at its end, corresponding to the effect of the soma. The AIS starts at a distance Δ from the soma and has a length L. Sodium channels are uniformly distributed in the AIS and do not inactivate. We consider that they are all open because we examine the membrane potential at the peak of the AP. The cable equation is:

$$\frac{1}{r_a}\frac{d^2V}{dx^2} = -g(E_{Na} - V) \tag{A.1}$$

with

$$\begin{aligned} r_a &= \frac{4R_i}{\pi d^2} \\ g &= \pi d g^* \end{aligned} \tag{A.2}$$

where g^* is the surface conductance density in the AIS and R_i is the intracellular resistivity. The boundary conditions are $V(0) = V_s$ (voltage-clamp at the soma) and $V'(\Delta + L) = 0$ (no axial current flowing towards the distal axon). Following (Goethals and Brette, 2020), we set the origin of x at the AIS start position. As the region between the soma and the AIS start is purely resistive, the potential varies linearly with the distance and it implies that the boundary condition at the start of the axon translates to a boundary condition at the AIS start:

$$V(0) = V_s + V'(0) \cdot \Delta \tag{A.3}$$

The second boundary condition becomes:

$$V'(L) = 0 \tag{A.4}$$

We use $\tilde{g} = \frac{4R_i}{d_{ais}} g^*$ and $U = V - E_{Na}$ and the cable equation now reads:

$$\frac{d^2U}{dx^2} = \tilde{g}U \tag{A.5}$$

The solution is a sum of exponential functions:

$$U(x) = ae^{\sqrt{\tilde{g}}x} + be^{-\sqrt{\tilde{g}}x} \tag{A.6}$$

From the first boundary condition, we obtain b:

$$b = \frac{V_s - a(1 - \sqrt{\tilde{g}}\Delta)}{1 + \sqrt{\tilde{g}}\Delta} \tag{A.7}$$

and from the second we have:

$$a = \frac{V_s e^{-\sqrt{\tilde{g}}L}}{(1+\sqrt{\tilde{g}}\Delta)e^{\sqrt{\tilde{g}}L} + (1-\sqrt{\tilde{g}}\Delta)e^{-\sqrt{\tilde{g}}L}} \tag{A.8}$$

Therefore:

$$U(L) = \frac{V_s}{\cosh(\sqrt{\tilde{g}}L) + \sqrt{\tilde{g}}\Delta\sinh(\sqrt{\tilde{g}}L)} \tag{A.9}$$

and, in original units, the membrane potential at the end of the AIS is:

$$V(L) = \frac{V_s - E_{Na}}{\cosh\left(\sqrt{\frac{4R_i}{d}g^*}L\right) + \sqrt{\frac{4R_i}{d}g^*}\Delta\sinh\left(\sqrt{\frac{4R_i}{d}g^*}L\right)} + E_{Na} \tag{A.10}$$

If we assume that the membrane potential at the end of the AIS at AP peak is normalized, we obtain a relationship between the AIS start position and its length, as illustrated on fig. A.1 A. This relationship resembles the one reported in the chick nucleus laminaris neurons, as illustrated on fig. A.1 B.

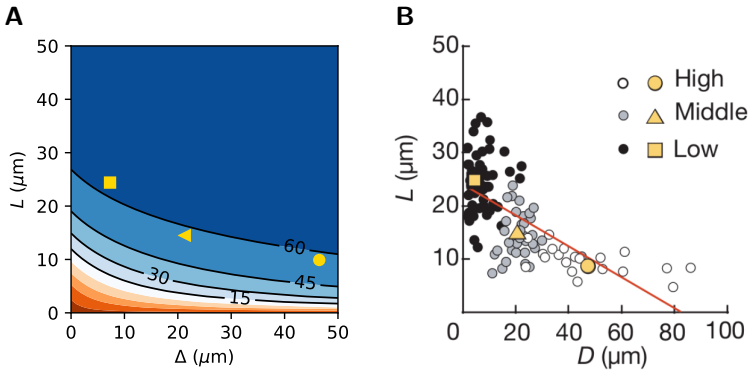

Figure A.1: Voltage at AIS end. **A**, Theoretical prediction for the membrane potential at the end of the AIS just after spike initiation, for different AIS start position Δ and length L. Numbers indicate the membrane potential in mV. Yellow square, triangle and dot illustrate the mean Δ and L of low, middle and high CF neurons, respectively. Values of the parameters are $R_i = 100\,\Omega\,\mathrm{cm}$, $g^* = 3500\,\mathrm{S\,m^{-2}}$, $d = 1\,\mu\mathrm{m}$, $E_{Na} = 70\,\mathrm{mV}$ and $V_s = -50\,\mathrm{mV}$. **B**, AIS length vs. start position in high, middle and low CF neurons from the chicks nucleus laminaris (adapted from Kuba et al. (2006)).

B Sodium current along the AIS

We are interested in the distribution of the Na^+ current along the proximal axon at spike initiation. Therefore, we calculate the Na^+ current that enters the AIS at any location. We consider an axon model identical to the one used in Appendix A. The AIS starts at a position Δ, has a length L and contains a uniform density of Na_v channels. They do not inactivate and are considered all open. The sodium current in the AIS is $I = g(E_{Na} - V(x))$, where g is the sodium conductance density per unit length. Similarly to Appendix A we choose the origin of x at the start of the AIS and solve the cable equation A.1 in the AIS with the boundary conditions A.3 and A.4 and the same change of variables. The solution of the problem is:

$$U(x) = V_s \frac{\cosh\left(\sqrt{\tilde{g}}(x - L)\right)}{\cosh\left(\sqrt{\tilde{g}}L\right) + \sqrt{\tilde{g}}\Delta \sinh\left(\sqrt{\tilde{g}}L\right)} \tag{B.1}$$

It results that the Na^+ current along the AIS is, in original units:

$$I_{Na}(x) = g(E_{Na} - V_s) \frac{\cosh\left(\sqrt{\frac{4R_i}{d}g^*}(x - L)\right)}{\cosh\left(\sqrt{\frac{4R_i}{d}g^*}L\right) + \sqrt{\frac{4R_i}{d}g^*}\Delta \sinh\left(\sqrt{\frac{4R_i}{d}g^*}L\right)} \tag{B.2}$$

where V_s is the somatic voltage, R_i is the intracellular resistivity, d is the axon diameter and E_{Na} is the reversal potential of Na^+. The maximal Na^+ current occurs at $x = 0$, i.e. at the start of the AIS with our definition of the origin of x, and decreases with the distance, as illustrated for different start positions in fig. B.1. Indeed, the proximal axon undergoes the effect of the nearby very large soma and its membrane potential is pulled by the somatic membrane potential, as explained in Hamada et al. (2016) and illustrated on ?? (fig RGC paper). It follows that the membrane potential in the proximal axon is further away from E_{Na} and thereby the driving force is larger, which increases the current.

This theoretical prediction is in close correspondence with the distribution of the Na^+ flux along the proximal axon recorded during an AP in cortical layer 5 pyramidal neurons (Baranauskas et al., 2013). As shown on fig. 1.11, the Na^+ flux is maximal in the region corresponding to the beginning of the AIS and decreases with the distance in the distal AIS. The authors suggest that it reflects a difference in Na_v channels density within the AIS but we argue that this distribution is more correctly explained by a variation of driving force with distance.

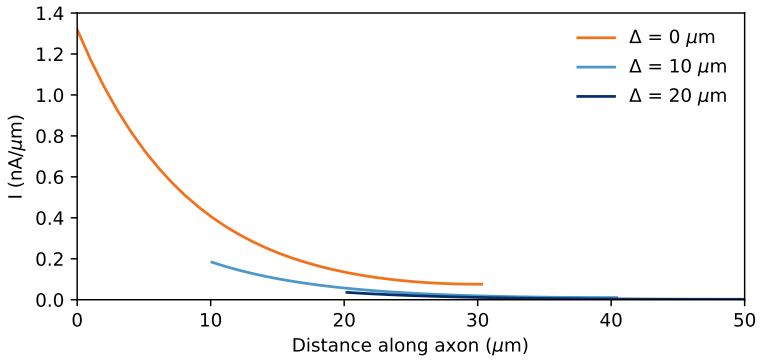

Figure B.1: Theoretical prediction for the Na^+ current along the AIS for different AIS start positions Δ and a fixed length $L = 30\,\mu m$. Values of the parameters are $R_i = 100\,\Omega\,cm$, $g^* = 3500\,S\,m^{-2}$, $d = 1\,\mu m$, $E_{Na} = 70\,mV$ and $V_s = -50\,mV$.

List of Figures

List of Tables

Bibliography

D. Albrecht, C. M. Winterflood, M. Sadeghi, T. Tschager, F. Noé, and H. Ewers. Nanoscopic compartmentalization of membrane protein motion at the axon initial segment. *Journal of Cell Biology*, 215(1):37–46, 2016.

K. J. Angelides, L. W. Elmer, D. Loftus, and E. Elson. Distribution and lateral mobility of voltage-dependent sodium channels in neurons. *The Journal of cell biology*, 106(6):1911–1925, 1988.

E. Angelino and M. P. Brenner. Excitability constraints on voltage-gated sodium channels. *PLoS computational biology*, 3(9), 2007.

R. Azouz and C. M. Gray. Dynamic spike threshold reveals a mechanism for synaptic coincidence detection in cortical neurons in vivo. *Proceedings of the National Academy of Sciences*, 97 (14):8110–8115, 2000.

L. Badel, S. Lefort, R. Brette, C. C. Petersen, W. Gerstner, and M. J. Richardson. Dynamic iv curves are reliable predictors of naturalistic pyramidal-neuron voltage traces. *Journal of Neurophysiology*, 99(2):656–666, 2008.

D. J. Bakkum, M. E. J. Obien, M. Radivojevic, D. Jäckel, U. Frey, H. Takahashi, and A. Hierlemann. The axon initial segment is the dominant contributor to the neuron's extracellular electrical potential landscape. *Advanced biosystems*, 3(2):1800308, 2019.

G. Baranauskas and M. Martina. Sodium currents activate without a hodgkin and huxley-type delay in central mammalian neurons. *Journal of Neuroscience*, 26(2):671–684, 2006.

G. Baranauskas, Y. David, and I. A. Fleidervish. Spatial mismatch between the na+ flux and spike initiation in axon initial segment. *Proceedings of the National Academy of Sciences*, 110 (10):4051–4056, 2013.

B. Barbour. Electronics for electrophysiologists. *Barel, O., SA Shalev, R. Ofir, A. Cohen, J. Zlotogora, Z. Shorer, G. Mazor, G. Finer, S. Khateeb, N. Zilberberg and OS Birk (2008)." Maternally inherited Birk Barel mental retardation dysmorphism syndrome caused by a mutation in the genomically imprinted potassium channel KCNK9." Am J Hum Genet*, 83(2):193–199, 2014.

J. Barrett and W. Crill. Voltage clamp of cat motoneurone somata: properties of the fast inward current. *The Journal of physiology*, 304(1):231–249, 1980.

A. Battefeld, B. T. Tran, J. Gavrilis, E. C. Cooper, and M. H. Kole. Heteromeric kv7. 2/7.3 channels differentially regulate action potential initiation and conduction in neocortical myelinated axons. *Journal of Neuroscience*, 34(10):3719–3732, 2014.

B. P. Bean. The action potential in mammalian central neurons. *Nature Reviews Neuroscience*, 8 (6):451–465, 2007.

E. Bearer and T. Reese. Association of actin filaments with axonal microtubule tracts. *Journal of neurocytology*, 28(2):85–98, 1999.

Y. Ben-Ari, J.-L. Gaiarsa, R. Tyzio, and R. Khazipov. Gaba: a pioneer transmitter that excites immature neurons and generates primitive oscillations. *Physiological reviews*, 87(4):1215–1284, 2007.

K. J. Bender and L. O. Trussell. The physiology of the axon initial segment. *Annual review of neuroscience*, 35:249–265, 2012.

S. L. Berger, A. Leo-Macias, S. Yuen, L. Khatri, S. Pfennig, Y. Zhang, E. Agullo-Pascual, G. Caillol, M.-S. Zhu, E. Rothenberg, et al. Localized myosin ii activity regulates assembly and plasticity of the axon initial segment. *Neuron*, 97(3):555–570, 2018.

J. Bernstein. Elektrobiologie. *Die Lehre von den elektrischen Vorgangen im Organismus auf moderner Grundlage dargestellt*, 1912.

M. Beyeler, D. Nanduri, J. D. Weiland, A. Rokem, G. M. Boynton, and I. Fine. A model of ganglion axon pathways accounts for percepts elicited by retinal implants. *Scientific reports*, 9(1):1–16, 2019.

G. Billings, E. Piasini, A. Lőrincz, Z. Nusser, and R. A. Silver. Network structure within the cerebellar input layer enables lossless sparse encoding. *Neuron*, 83(4):960–974, 2014.

T. Boiko, M. N. Rasband, S. R. Levinson, J. H. Caldwell, G. Mandel, J. S. Trimmer, and G. Matthews. Compact myelin dictates the differential targeting of two sodium channel isoforms in the same axon. *Neuron*, 30(1):91–104, 2001.

T. Boiko, A. Van Wart, J. H. Caldwell, S. R. Levinson, J. S. Trimmer, and G. Matthews. Functional specialization of the axon initial segment by isoform-specific sodium channel targeting. *Journal of Neuroscience*, 23(6):2306–2313, 2003.

A. Brachet, C. Leterrier, M. Irondelle, M.-P. Fache, V. Racine, J.-B. Sibarita, D. Choquet, and B. Dargent. Ankyrin g restricts ion channel diffusion at the axonal initial segment before the establishment of the diffusion barrier. *Journal of Cell Biology*, 191(2):383–395, 2010.

R. Brette. Sharpness of spike initiation in neurons explained by compartmentalization. *PLoS computational biology*, 9(12), 2013.

R. Brette. What is the most realistic single-compartment model of spike initiation? *PLoS computational biology*, 11(4), 2015.

J. W. Brown, E. Bullitt, S. Sriswasdi, S. Harper, D. W. Speicher, and C. J. McKnight. The physiological molecular shape of spectrin: a compact supercoil resembling a chinese finger trap. *PLoS computational biology*, 11(6), 2015.

P. S. Buckmaster. Mossy cell dendritic structure quantified and compared with other hippocampal neurons labeled in rats in vivo. *Epilepsia*, 53:9–17, 2012.

S. A. Buffington and M. N. Rasband. The axon initial segment in nervous system disease and injury. *European Journal of Neuroscience*, 34(10):1609–1619, 2011.

R. L. Calabrese and D. Kennedy. Multiple sites of spike initiation in a single dendritic system. *Brain research*, 82(2):316–321, 1974.

N. Caporale and Y. Dan. Spike timing–dependent plasticity: a hebbian learning rule. *Annu. Rev. Neurosci.*, 31:25–46, 2008.

E. Carmeliet. From bernstein's rheotome to neher-sakmann's patch electrode. the action potential. *Physiological reports*, 7(1):e13861, 2019.

L. Cathala, S. Brickley, S. Cull-Candy, and M. Farrant. Maturation of epscs and intrinsic membrane properties enhances precision at a cerebellar synapse. *Journal of Neuroscience*, 23(14): 6074–6085, 2003.

W. A. Catterall. Localization of sodium channels in cultured neural cells. *Journal of Neuroscience*, 1(7):777–783, 1981.

W. A. Catterall. From ionic currents to molecular mechanisms: the structure and function of voltage-gated sodium channels. *Neuron*, 26(1):13–25, 2000.

M. S. Cembrowski, S. M. Logan, M. Tian, L. Jia, W. Li, W. L. Kath, H. Riecke, and J. H. Singer. The mechanisms of repetitive spike generation in an axonless retinal interneuron. *Cell reports*, 1(2):155–166, 2012.

F. P. Chabrol, A. Arenz, M. T. Wiechert, T. W. Margrie, and D. A. DiGregorio. Synaptic diversity enables temporal coding of coincident multisensory inputs in single neurons. *Nature neuroscience*, 18(5):718, 2015.

A. N. Chand, E. Galliano, R. A. Chesters, and M. S. Grubb. A distinct subtype of dopaminergic interneuron displays inverted structural plasticity at the axon initial segment. *Journal of Neuroscience*, 35(4):1573–1590, 2015.

R. Chéreau, G. E. Saraceno, J. Angibaud, D. Cattaert, and U. V. Nägerl. Superresolution imaging reveals activity-dependent plasticity of axon morphology linked to changes in action potential conduction velocity. *Proceedings of the National Academy of Sciences*, 114(6):1401–1406, 2017.

D. B. Chklovskii and A. Stepanyants. Power-law for axon diameters at branch point. *BMC neuroscience*, 4(1):18, 2003.

C. M. Colbert and E. Pan. Ion channel properties underlying axonal action potential initiation in pyramidal neurons. *Nature neuroscience*, 5(6):533–538, 2002.

S. Coletta, R. Zeraati, K. Nasr, P. Preston-Ferrer, and A. Burgalossi. Interspike interval analysis and spikelets in presubicular head-direction cells. *Journal of Neurophysiology*, 120(2):564–575, 2018.

S. Conradi. Ultrastructural specialization of the initial axon segment of cat lumbar motoneurons. preliminary observations. *Acta Societatis Medicorum Upsaliensis*, 71(5):281, 1966.

S. Conradi and L.-O. Ronnevi. Ultrastructure and synaptology of the initial axon segment of cat spinal motoneurons during early postnatal development. *Journal of neurocytology*, 6(2): 195–210, 1977.

J. Coombs, D. Curtis, and J. Eccles. The interpretation of spike potentials of motoneurones. *The Journal of Physiology*, 139(2):198–231, 1957.

E. C. Cooper. Made for "anchorin": Kv7. 2/7.3 (kcnq2/kcnq3) channels and the modulation of neuronal excitability in vertebrate axons. In *Seminars in cell & developmental biology*, volume 22, pages 185–192. Elsevier, 2011.

B. Cormery, E. Beaumont, K. Csukly, and P. Gardiner. Hindlimb unweighting for 2 weeks alters physiological properties of rat hindlimb motoneurones. *The Journal of physiology*, 568 (3):841–850, 2005.

A. R. Costa, S. C. Sousa, R. Pinto-Costa, J. C. Mateus, C. D. Lopes, A. C. Costa, D. Rosa, D. Machado, L. Pajuelo, X. Wang, et al. The membrane periodic skeleton is an actomyosin network that regulates axonal diameter and conduction. *eLife*, 9:e55471, 2020.

G. Daoudal and D. Debanne. Long-term plasticity of intrinsic excitability: learning rules and mechanisms. *Learning & memory*, 10(6):456–465, 2003.

C. De Zeeuw, T. Ruigrok, J. Holstege, M. Schalekamp, and J. Voogd. Intracellular labeling of neurons in the medial accessory olive of the cat: Iii. ultrastructure of axon hillock and initial segment and their gabaergic innervation. *Journal of Comparative Neurology*, 300(4):495–510, 1990.

D. Debanne, E. Campanac, A. Bialowas, E. Carlier, and G. Alcaraz. Axon physiology. *Physiological reviews*, 91(2):555–602, 2011.

I. Delvendahl, I. Straub, and S. Hallermann. Dendritic patch-clamp recordings from cerebellar granule cells demonstrate electrotonic compactness. *Frontiers in cellular neuroscience*, 9:93, 2015.

J. J. Devaux, K. A. Kleopa, E. C. Cooper, and S. S. Scherer. Kcnq2 is a nodal k+ channel. *Journal of Neuroscience*, 24(5):1236–1244, 2004.

S. Diwakar, J. Magistretti, M. Goldfarb, G. Naldi, and E. D'Angelo. Axonal na+ channels ensure fast spike activation and back-propagation in cerebellar granule cells. *Journal of neurophysiology*, 101(2):519–532, 2009.

Y. Dzhashiashvili, Y. Zhang, J. Galinska, I. Lam, M. Grumet, and J. L. Salzer. Nodes of ranvier and axon initial segments are ankyrin g–dependent domains that assemble by distinct mechanisms. *The Journal of cell biology*, 177(5):857–870, 2007.

E. D'Este, D. Kamin, F. Göttfert, A. El-Hady, and S. W. Hell. Sted nanoscopy reveals the ubiquity of subcortical cytoskeleton periodicity in living neurons. *Cell reports*, 10(8):1246–1251, 2015.

E. D'Este, D. Kamin, C. Velte, F. Göttfert, M. Simons, and S. W. Hell. Subcortical cytoskeleton periodicity throughout the nervous system. *Scientific reports*, 6(1):1–8, 2016.

D. Engel and P. Jonas. Presynaptic action potential amplification by voltage-gated na+ channels in hippocampal mossy fiber boutons. *Neuron*, 45(3):405–417, 2005.

J. Epsztein, A. K. Lee, E. Chorev, and M. Brecht. Impact of spikelets on hippocampal ca1 pyramidal cell activity during spatial exploration. *Science*, 327(5964):474–477, 2010.

A. Eshra, P. Hirrlinger, and S. Hallermann. Enriched environment shortens the duration of action potentials in cerebellar granule cells. *Frontiers in cellular neuroscience*, 13:289, 2019.

M. D. Evans, R. P. Sammons, S. Lebron, A. S. Dumitrescu, T. B. Watkins, V. N. Uebele, J. J. Renger, and M. S. Grubb. Calcineurin signaling mediates activity-dependent relocation of the axon initial segment. *Journal of Neuroscience*, 33(16):6950–6963, 2013.

M. D. Evans, A. S. Dumitrescu, D. L. Kruijssen, S. E. Taylor, and M. S. Grubb. Rapid modulation of axon initial segment length influences repetitive spike firing. *Cell reports*, 13(6):1233–1245, 2015.

G. Eyal, H. D. Mansvelder, C. P. de Kock, and I. Segev. Dendrites impact the encoding capabilities of the axon. *Journal of Neuroscience*, 34(24):8063–8071, 2014.

A. Fairen and F. Valverde. A specialized type of neuron in the visual cortex of cat: a golgi and electron microscope study of chandelier cells. *Journal of Comparative Neurology*, 194(4): 761–779, 1980.

P. Fatt. Sequence of events in synaptic activation of a motoneurone. *Journal of Neurophysiology*, 20(1):61–80, 1957.

A. Fekete. *Les déterminants du seuil du potentiel d'action dans les neurones corticaux*. PhD thesis, Aix-Marseille, 2018.

S. Finger. *Origins of neuroscience: a history of explorations into brain function*. Oxford University Press, USA, 2001.

R. FitzHugh. Mathematical models of threshold phenomena in the nerve membrane. *The bulletin of mathematical biophysics*, 17(4):257–278, 1955.

I. A. Fleidervish, N. Lasser-Ross, M. J. Gutnick, and W. N. Ross. Na+ imaging reveals little difference in action potential–evoked na+ influx between axon and soma. *Nature neuroscience*, 13(7):852, 2010.

J. F. Fohlmeister, E. D. Cohen, and E. A. Newman. Mechanisms and distribution of ion channels in retinal ganglion cells: using temperature as an independent variable. *Journal of neurophysiology*, 103(3):1357–1374, 2010.

B. Fontaine, J. L. Peña, and R. Brette. Spike-threshold adaptation predicted by membrane potential dynamics in vivo. *PLoS Comput Biol*, 10(4):e1003560, 2014.

N. Fourcaud-Trocmé, D. Hansel, C. Van Vreeswijk, and N. Brunel. How spike generation mechanisms determine the neuronal response to fluctuating inputs. *Journal of Neuroscience*, 23(37): 11628–11640, 2003.

A. Fréal, C. Fassier, B. Le Bras, E. Bullier, S. De Gois, J. Hazan, C. C. Hoogenraad, and F. Couraud. Cooperative interactions between 480 kda ankyrin-g and eb proteins assemble the axon initial segment. *Journal of Neuroscience*, 36(16):4421–4433, 2016.

A. Fréal, D. Rai, R. P. Tas, X. Pan, E. A. Katrukha, D. van de Willige, R. Stucchi, A. Aher, C. Yang, A. M. Altelaar, et al. Feedback-driven assembly of the axon initial segment. *Neuron*, 104(2): 305–321, 2019.

S. I. Fried, A. C. Lasker, N. J. Desai, D. K. Eddington, and J. F. Rizzo 3rd. Axonal sodium-channel bands shape the response to electric stimulation in retinal ganglion cells. *Journal of neurophysiology*, 101(4):1972–1987, 2009.

M. R. Galiano, S. Jha, T. S.-Y. Ho, C. Zhang, Y. Ogawa, K.-J. Chang, M. C. Stankewich, P. J. Mohler, and M. N. Rasband. A distal axonal cytoskeleton forms an intra-axonal boundary that controls axon initial segment assembly. *Cell*, 149(5):1125–1139, 2012.

E. Galliano, E. Franzoni, M. Breton, A. N. Chand, D. J. Byrne, V. N. Murthy, and M. S. Grubb. Embryonic and postnatal neurogenesis produce functionally distinct subclasses of dopaminergic neuron. *Elife*, 7:e32373, 2018.

A. Ganguly, Y. Tang, L. Wang, K. Ladt, J. Loi, B. Dargent, C. Leterrier, and S. Roy. A dynamic formin-dependent deep f-actin network in axons. *Journal of Cell Biology*, 210(3):401–417, 2015.

J. J. Garrido, P. Giraud, E. Carlier, F. Fernandes, A. Moussif, M.-P. Fache, D. Debanne, and B. Dargent. A targeting motif involved in sodium channel clustering at the axonal initial segment. *Science*, 300(5628):2091–2094, 2003.

J.-M. Goaillard, E. Moubarak, M. Tapia, and F. Tell. Diversity of axonal and dendritic contributions to neuronal output. *Frontiers in Cellular Neuroscience*, 13, 2019.

S. Goethals and R. Brette. Theoretical relation between axon initial segment geometry and excitability. *Elife*, 9:e53432, 2020.

M. Goldfarb, J. Schoorlemmer, A. Williams, S. Diwakar, Q. Wang, X. Huang, J. Giza, D. Tchetchik, K. Kelley, A. Vega, et al. Fibroblast growth factor homologous factors control neuronal excitability through modulation of voltage-gated sodium channels. *Neuron*, 55(3):449–463, 2007.

R. H. Goldstein, O. Barkai, A. Íñigo-Portugués, B. Katz, S. Lev, and A. M. Binshtok. Location and plasticity of the sodium spike initiation zone in nociceptive terminals in vivo. *Neuron*, 102(4):801–812, 2019.

C. Golgi. The neuron doctrine: theory and facts. *Nobel lecture*, 1921:190–217, 1906.

C. González-Cabrera, R. Meza, L. Ulloa, P. Merino-Sepúlveda, V. Luco, A. Sanhueza, A. Oñate-Ponce, J. P. Bolam, and P. Henny. Characterization of the axon initial segment of mice substantia nigra dopaminergic neurons. *Journal of Comparative Neurology*, 525(16):3529–3542, 2017.

J. Götz, G. Halliday, and R. M. Nisbet. Molecular pathogenesis of the tauopathies. *Annual Review of Pathology: Mechanisms of Disease*, 14:239–261, 2019.

L. Groc and D. Choquet. Measurement and characteristics of neurotransmitter receptor surface trafficking. *Molecular membrane biology*, 25(4):344–352, 2008.

M. S. Grubb and J. Burrone. Activity-dependent relocation of the axon initial segment fine-tunes neuronal excitability. *Nature*, 465(7301):1070–1074, 2010.

M. S. Grubb, Y. Shu, H. Kuba, M. N. Rasband, V. C. Wimmer, and K. J. Bender. Short-and long-term plasticity at the axon initial segment. *Journal of Neuroscience*, 31(45):16049–16055, 2011.

A. T. Gulledge and J. J. Bravo. Neuron morphology influences axon initial segment plasticity. *eNeuro*, 3(1), 2016.

T. Guo, D. Tsai, J. W. Morley, G. J. Suaning, N. H. Lovell, and S. Dokos. Cell-specific modeling of retinal ganglion cell electrical activity. In *2013 35th Annual International Conference of the IEEE Engineering in Medicine and Biology Society (EMBC)*, pages 6539–6542. IEEE, 2013.

A. Gutzmann, N. Ergül, R. Grossmann, C. Schultz, P. Wahle, and M. Engelhardt. A period of structural plasticity at the axon initial segment in developing visual cortex. *Frontiers in neuroanatomy*, 8:11, 2014.

S. Hallermann, C. P. De Kock, G. J. Stuart, and M. H. Kole. State and location dependence of action potential metabolic cost in cortical pyramidal neurons. *Nature neuroscience*, 15(7):1007, 2012.

M. S. Hamada, S. Goethals, S. I. de Vries, R. Brette, and M. H. Kole. Covariation of axon initial segment location and dendritic tree normalizes the somatic action potential. *Proceedings of the National Academy of Sciences*, 113(51):14841–14846, 2016.

O. P. Hamill, A. Marty, E. Neher, B. Sakmann, and F. Sigworth. Improved patch-clamp techniques for high-resolution current recording from cells and cell-free membrane patches. *Pflügers Archiv*, 391(2):85–100, 1981.

M. Hammarlund, E. M. Jorgensen, and M. J. Bastiani. Axons break in animals lacking β-spectrin. *The Journal of cell biology*, 176(3):269–275, 2007.

R. J. Hatch, Y. Wei, D. Xia, and J. Götz. Hyperphosphorylated tau causes reduced hippocampal ca1 excitability by relocating the axon initial segment. *Acta neuropathologica*, 133(5):717–730, 2017.

M. Häusser, G. Stuart, C. Racca, and B. Sakmann. Axonal initiation and active dendritic propagation of action potentials in substantia nigra neurons. *Neuron*, 15(3):637–647, 1995.

J. He, R. Zhou, Z. Wu, M. A. Carrasco, P. T. Kurshan, J. E. Farley, D. J. Simon, G. Wang, B. Han, J. Hao, et al. Prevalent presence of periodic actin–spectrin-based membrane skeleton in a broad range of neuronal cell types and animal species. *Proceedings of the National Academy of Sciences*, 113(21):6029–6034, 2016.

K. L. Hedstrom, X. Xu, Y. Ogawa, R. Frischknecht, C. I. Seidenbecher, P. Shrager, and M. N. Rasband. Neurofascin assembles a specialized extracellular matrix at the axon initial segment. *The Journal of cell biology*, 178(5):875–886, 2007.

K. L. Hedstrom, Y. Ogawa, and M. N. Rasband. Ankyring is required for maintenance of the axon initial segment and neuronal polarity. *The Journal of cell biology*, 183(4):635–640, 2008.

S. Herculano-Houzel. The human brain in numbers: a linearly scaled-up primate brain. *Frontiers in human neuroscience*, 3:31, 2009.

B. Hille et al. Ion channels of excitable membranes (sinauer, sunderland, ma), 2001.

A. L. Hodgkin and A. F. Huxley. Action potentials recorded from inside a nerve fibre. *Nature*, 144(3651):710–711, 1939.

A. L. Hodgkin and A. F. Huxley. Currents carried by sodium and potassium ions through the membrane of the giant axon of loligo. *The Journal of physiology*, 116(4):449–472, 1952a.

A. L. Hodgkin and A. F. Huxley. A quantitative description of membrane current and its application to conduction and excitation in nerve. *The Journal of physiology*, 117(4):500–544, 1952b.

F. Höfflin, A. Jack, C. Riedel, J. Mack-Bucher, J. Roos, C. Corcelli, C. Schultz, P. Wahle, and M. Engelhardt. Heterogeneity of the axon initial segment in interneurons and pyramidal cells of rodent visual cortex. *Frontiers in cellular neuroscience*, 11:332, 2017.

C. M. Houston, E. Diamanti, M. Diamantaki, E. Kutsarova, A. Cook, F. Sultan, and S. G. Brickley. Exploring the significance of morphological diversity for cerebellar granule cell excitability. *Scientific reports*, 7:46147, 2017.

A. Howard, G. Tamas, and I. Soltesz. Lighting the chandelier: new vistas for axo-axonic cells. *Trends in neurosciences*, 28(6):310–316, 2005.

W. Hu and B. Bean. Responses to axonal current injection in cortical layer 5 pyramidal neurons, Nov. 2019. URL `https://doi.org/10.5281/zenodo.3539297`.

W. Hu and B. P. Bean. Differential control of axonal and somatic resting potential by voltage-dependent conductances in cortical layer 5 pyramidal neurons. *Neuron*, 97(6):1315–1326, 2018.

W. Hu, C. Tian, T. Li, M. Yang, H. Hou, and Y. Shu. Distinct contributions of na v 1.6 and na v 1.2 in action potential initiation and backpropagation. *Nature neuroscience*, 12(8):996, 2009.

M. Igarashi, M. Nozumi, L.-G. Wu, F. C. Zanacchi, I. Katona, L. Barna, P. Xu, M. Zhang, F. Xue, and E. Boyden. New observations in neuroscience using superresolution microscopy. *Journal of Neuroscience*, 38(44):9459–9467, 2018.

M. Inan, L. Blázquez-Llorca, A. Merchán-Pérez, S. A. Anderson, J. DeFelipe, and R. Yuste. Dense and overlapping innervation of pyramidal neurons by chandelier cells. *Journal of Neuroscience*, 33(5):1907–1914, 2013.

N. Jamann, M. Jordan, and M. Engelhardt. Activity-dependent axonal plasticity in sensory systems. *Neuroscience*, 368:268–282, 2018.

N. Jamann, D. Dannehl, R. Wagener, C. Corcelli, C. Schultz, J. Staiger, M. H. Kole, and M. Engelhardt. Sensory input drives rapid homeostatic scaling of the axon initial segment in mouse barrel cortex. *bioRxiv*, 2020.

S. M. Jenkins and V. Bennett. Ankyrin-g coordinates assembly of the spectrin-based membrane skeleton, voltage-gated sodium channels, and l1 cams at purkinje neuron initial segments. *The Journal of cell biology*, 155(5):739–746, 2001.

S. Jhaveri and D. Morest. Neuronal architecture in nucleus magnocellularis of the chicken auditory system with observations on nucleus laminaris: a light and electron microscope study. *Neuroscience*, 7(4):809–836, 1982.

S. L. Jones and T. M. Svitkina. Axon initial segment cytoskeleton: architecture, development, and role in neuron polarity. *Neural plasticity*, 2016, 2016.

S. L. Jones, F. Korobova, and T. Svitkina. Axon initial segment cytoskeleton comprises a multiprotein submembranous coat containing sparse actin filaments. *Journal of Cell Biology*, 205 (1):67–81, 2014.

E. Katz, O. Stoler, A. Scheller, Y. Khrapunsky, S. Goebbels, F. Kirchhoff, M. J. Gutnick, F. Wolf, and I. A. Fleidervish. Role of sodium channel subtype in action potential generation by neocortical pyramidal neurons. *Proceedings of the National Academy of Sciences*, 115(30):E7184–E7192, 2018.

H. Kesten et al. Accelerated stochastic approximation. *The Annals of Mathematical Statistics*, 29 (1):41–59, 1958.

E. J. Kim, C. Feng, F. Santamaria, and J. H. Kim. Impact of auditory experience on the structural plasticity of the ais in the mouse brainstem throughout the lifespen. *Frontiers in cellular neuroscience*, 13:456, 2019.

A. N. King, C. F. Manning, and J. S. Trimmer. A unique ion channel clustering domain on the axon initial segment of mammalian neurons. *Journal of Comparative Neurology*, 522(11): 2594–2608, 2014.

C. Koch. *Biophysics of computation: information processing in single neurons*. Oxford university press, 2004.

M. H. Kole and R. Brette. The electrical significance of axon location diversity. *Current opinion in neurobiology*, 51:52–59, 2018.

M. H. Kole and G. J. Stuart. Is action potential threshold lowest in the axon? *Nature neuroscience*, 11(11):1253, 2008.

M. H. Kole and G. J. Stuart. Signal processing in the axon initial segment. *Neuron*, 73(2):235–247, 2012.

M. H. Kole, J. J. Letzkus, and G. J. Stuart. Axon initial segment kv1 channels control axonal action potential waveform and synaptic efficacy. *Neuron*, 55(4):633–647, 2007.

M. H. Kole, S. U. Ilschner, B. M. Kampa, S. R. Williams, P. C. Ruben, and G. J. Stuart. Action potential generation requires a high sodium channel density in the axon initial segment. *Nature neuroscience*, 11(2):178–186, 2008.

E. Kordeli, S. Lambert, and V. Bennett. Ankyrin a new ankyrin gene with neural-specific isoforms localized at the axonal initial segment and node of ranvier. *Journal of Biological Chemistry*, 270(5):2352–2359, 1995.

T. Kosaka. The axon initial segment as a synaptic site: ultrastructure and synaptology of the initial segment of the pyramidal cell in the rat hippocampus (ca3 region). *Journal of neurocytology*, 9(6):861–882, 1980.

G. J. Kress, M. J. Dowling, L. N. Eisenman, and S. Mennerick. Axonal sodium channel distribution shapes the depolarized action potential threshold of dentate granule neurons. *Hippocampus*, 20(4):558–571, 2010.

M. Krieg, A. R. Dunn, and M. B. Goodman. Mechanical control of the sense of touch by β-spectrin. *Nature cell biology*, 16(3):224–233, 2014.

M. Krieg, J. Stühmer, J. G. Cueva, R. Fetter, K. Spilker, D. Cremers, K. Shen, A. R. Dunn, and M. B. Goodman. Genetic defects in β-spectrin and tau sensitize c. elegans axons to movement-induced damage via torque-tension coupling. *Elife*, 6:e20172, 2017.

H. Kuba. Structural tuning and plasticity of the axon initial segment in auditory neurons. *The Journal of physiology*, 590(22):5571–5579, 2012.

H. Kuba and H. Ohmori. Roles of axonal sodium channels in precise auditory time coding at nucleus magnocellularis of the chick. *The Journal of physiology*, 587(1):87–100, 2009.

H. Kuba, R. Yamada, I. Fukui, and H. Ohmori. Tonotopic specialization of auditory coincidence detection in nucleus laminaris of the chick. *Journal of Neuroscience*, 25(8):1924–1934, 2005.

H. Kuba, T. M. Ishii, and H. Ohmori. Axonal site of spike initiation enhances auditory coincidence detection. *Nature*, 444(7122):1069–1072, 2006.

H. Kuba, Y. Oichi, and H. Ohmori. Presynaptic activity regulates na+ channel distribution at the axon initial segment. *Nature*, 465(7301):1075–1078, 2010.

H. Kuba, R. Adachi, and H. Ohmori. Activity-dependent and activity-independent development of the axon initial segment. *Journal of Neuroscience*, 34(9):3443–3453, 2014.

H. Kuba, R. Yamada, G. Ishiguro, and R. Adachi. Redistribution of kv1 and kv7 enhances neuronal excitability during structural axon initial segment plasticity. *Nature communications*, 6(1):1–12, 2015.

A. Laser-Azogui, M. Kornreich, E. Malka-Gibor, and R. Beck. Neurofilament assembly and function during neuronal development. *Current opinion in cell biology*, 32:92–101, 2015.

E. Lazarov, M. Dannemeyer, B. Feulner, J. Enderlein, M. J. Gutnick, F. Wolf, and A. Neef. An axon initial segment is required for temporal precision in action potential encoding by neuronal populations. *Science advances*, 4(11):eaau8621, 2018.

B. Le Bras, A. Fréal, A. Czarnecki, P. Legendre, E. Bullier, M. Komada, P. J. Brophy, M. Davenne, and F. Couraud. In vivo assembly of the axon initial segment in motor neurons. *Brain Structure and Function*, 219(4):1433–1450, 2014.

S. C. Leite, P. Sampaio, V. F. Sousa, J. Nogueira-Rodrigues, R. Pinto-Costa, L. L. Peters, P. Brites, and M. M. Sousa. The actin-binding protein α-adducin is required for maintaining axon diameter. *Cell reports*, 15(3):490–498, 2016.

C. Leterrier. The axon initial segment, 50 years later: a nexus for neuronal organization and function. In *Current topics in membranes*, volume 77, pages 185–233. Elsevier, 2016.

C. Leterrier. The axon initial segment: an updated viewpoint. *Journal of Neuroscience*, 38(9): 2135–2145, 2018.

C. Leterrier. A dual role for βii-spectrin in axons. *Proceedings of the National Academy of Sciences*, 116(31):15324–15326, 2019.

C. Leterrier, H. Vacher, M.-P. Fache, S. A. d'Ortoli, F. Castets, A. Autillo-Touati, and B. Dargent. End-binding proteins eb3 and eb1 link microtubules to ankyrin g in the axon initial segment. *Proceedings of the National Academy of Sciences*, 108(21):8826–8831, 2011.

C. Leterrier, J. Potier, G. Caillol, C. Debarnot, F. R. Boroni, and B. Dargent. Nanoscale architecture of the axon initial segment reveals an organized and robust scaffold. *Cell reports*, 13(12): 2781–2793, 2015.

C. Leterrier, N. Clerc, F. Rueda-Boroni, A. Montersino, B. Dargent, and F. Castets. Ankyrin g membrane partners drive the establishment and maintenance of the axon initial segment. *Frontiers in cellular neuroscience*, 11:6, 2017a.

C. Leterrier, P. Dubey, and S. Roy. The nano-architecture of the axonal cytoskeleton. *Nature Reviews Neuroscience*, 18(12):713, 2017b.

J. Lezmy, M. Lipinsky, Y. Khrapunsky, E. Patrich, L. Shalom, A. Peretz, I. A. Fleidervish, and B. Attali. M-current inhibition rapidly induces a unique ck2-dependent plasticity of the axon initial segment. *Proceedings of the National Academy of Sciences*, 114(47):E10234–E10243, 2017.

H. Lodish, A. Berk, C. A. Kaiser, M. Krieger, M. P. Scott, A. Bretscher, H. Ploegh, P. Matsudaira, et al. *Molecular cell biology*. Macmillan, 2008.

D. N. Lorenzo, A. Badea, R. Zhou, P. J. Mohler, X. Zhuang, and V. Bennett. βii-spectrin promotes mouse brain connectivity through stabilizing axonal plasma membranes and enabling axonal organelle transport. *Proceedings of the National Academy of Sciences*, 116(31):15686–15695, 2019.

A. Lorincz and Z. Nusser. Cell-type-dependent molecular composition of the axon initial segment. *Journal of Neuroscience*, 28(53):14329–14340, 2008.

A. Lorincz and Z. Nusser. Molecular identity of dendritic voltage-gated sodium channels. *Science*, 328(5980):906–909, 2010.

J. C. Magee and D. Johnston. A synaptically controlled, associative signal for hebbian plasticity in hippocampal neurons. *Science*, 275(5297):209–213, 1997.

J. Magistretti, L. Castelli, L. Forti, and E. D'Angelo. Kinetic and functional analysis of transient, persistent and resurgent sodium currents in rat cerebellar granule cells in situ: an electrophysiological and modelling study. *The Journal of physiology*, 573(1):83–106, 2006.

Z. F. Mainen, J. Joerges, J. R. Huguenard, and T. J. Sejnowski. A model of spike initiation in neocortical pyramidal neurons. *Neuron*, 15(6):1427–1439, 1995.

E. Maratou and G. Theophilidis. An axon pacemaker: diversity in the mechanism of generation and conduction of action potentials in snail neurons. *Neuroscience*, 96(1):1–2, 2000.

J. R. Marszalek, T. L. Williamson, M. K. Lee, Z. Xu, P. N. Hoffman, M. W. Becher, T. O. Crawford, and D. W. Cleveland. Neurofilament subunit nf-h modulates axonal diameter by selectively slowing neurofilament transport. *The Journal of cell biology*, 135(3):711–724, 1996.

D. A. McCormick, Y. Shu, and Y. Yu. Hodgkin and huxley model—still standing? *Nature*, 445 (7123):E1–E2, 2007.

P. Meyrand, J. M. Weimann, and E. Marder. Multiple axonal spike initiation zones in a motor neuron: serotonin activation. *Journal of Neuroscience*, 12(7):2803–2812, 1992.

R. C. Meza, L. López-Jury, C. C. Canavier, and P. Henny. Role of the axon initial segment in the control of spontaneous frequency of nigral dopaminergic neurons in vivo. *Journal of Neuroscience*, 38(3):733–744, 2018.

M. Michalikova, M. W. Remme, and R. Kempter. Spikelets in pyramidal neurons: Action potentials initiated in the axon initial segment that do not activate the soma. *PLoS computational biology*, 13(1), 2017.

M. Michalikova, M. W. Remme, D. Schmitz, S. Schreiber, and R. Kempter. Spikelets in pyramidal neurons: generating mechanisms, distinguishing properties, and functional implications. *Reviews in the Neurosciences*, 31(1):101–119, 2019.

L. S. Milescu, B. P. Bean, and J. C. Smith. Isolation of somatic na+ currents by selective inactivation of axonal channels with a voltage prepulse. *Journal of Neuroscience*, 30(22):7740–7748, 2010.

P. Mitra and R. F. Miller. Mechanism underlying rebound excitation in retinal ganglion cells. *Visual neuroscience*, 24(5):709, 2007.

Molecular Devices. The axon guide, a guide to electrophysiology & biophysics laboratory techniques. *Sunnyvale: MDS Analytical Technologies*, 2008.

E. Moubarak, D. Engel, M. A. Dufour, M. Tapia, F. Tell, and J.-M. Goaillard. Robustness to axon initial segment variation is explained by somatodendritic excitability in rat substantia nigra dopaminergic neurons. *Journal of Neuroscience*, 39(26):5044–5063, 2019.

J. Muir and J. T. Kittler. Plasticity of gabaa receptor diffusion dynamics at the axon initial segment. *Frontiers in cellular neuroscience*, 8:151, 2014.

C. Nakada, K. Ritchie, Y. Oba, M. Nakamura, Y. Hotta, R. Iino, R. S. Kasai, K. Yamaguchi, T. Fujiwara, and A. Kusumi. Accumulation of anchored proteins forms membrane diffusion barriers during neuronal polarization. *Nature cell biology*, 5(7):626–632, 2003.

A. I. Nascimento, F. M. Mar, and M. M. Sousa. The intriguing nature of dorsal root ganglion neurons: Linking structure with polarity and function. *Progress in neurobiology*, 168:86–103, 2018.

B. Naundorf, F. Wolf, and M. Volgushev. Unique features of action potential initiation in cortical neurons. *Nature*, 440(7087):1060–1063, 2006.

E. Neher and B. Sakmann. Single-channel currents recorded from membrane of denervated frog muscle fibres. *Nature*, 260(5554):799–802, 1976.

A. D. Nelson and P. M. Jenkins. Axonal membranes and their domains: assembly and function of the axon initial segment and node of ranvier. *Frontiers in cellular neuroscience*, 11:136, 2017.

M. E. J. Obien, K. Deligkaris, T. Bullmann, D. J. Bakkum, and U. Frey. Revealing neuronal function through microelectrode array recordings. *Frontiers in neuroscience*, 8:423, 2015.

I. Ogiwara, H. Miyamoto, N. Morita, N. Atapour, E. Mazaki, I. Inoue, T. Takeuchi, S. Itohara, Y. Yanagawa, K. Obata, et al. Nav1. 1 localizes to axons of parvalbumin-positive inhibitory interneurons: a circuit basis for epileptic seizures in mice carrying an scn1a gene mutation. *Journal of Neuroscience*, 27(22):5903–5914, 2007.

N. Osorio, L. Cathala, M. H. Meisler, M. Crest, J. Magistretti, and P. Delmas. Persistent nav1. 6 current at axon initial segments tunes spike timing of cerebellar granule cells. *The Journal of physiology*, 588(4):651–670, 2010.

S. L. Palay and V. Chan-Palay. *Cerebellar cortex: cytology and organization*. Springer Science & Business Media, 2012.

S. L. Palay, C. Sotelo, A. Peters, and P. M. Orkand. The axon hillock and the initial segment. *The Journal of cell biology*, 38(1):193–201, 1968.

L. M. Palmer and G. J. Stuart. Site of action potential initiation in layer 5 pyramidal neurons. *Journal of Neuroscience*, 26(6):1854–1863, 2006.

Z. Pan, T. Kao, Z. Horvath, J. Lemos, J.-Y. Sul, S. D. Cranstoun, V. Bennett, S. S. Scherer, and E. C. Cooper. A common ankyrin-g-based mechanism retains kcnq and nav channels at electrically active domains of the axon. *Journal of neuroscience*, 26(10):2599–2613, 2006.

A. Pan-Vazquez, W. Wefelmeyer, V. G. Sabater, G. Neves, and J. Burrone. Activity-dependent plasticity of axo-axonic synapses at the axon initial segment. *Neuron*, 2020.

H. Peng, Z. Ruan, F. Long, J. H. Simpson, and E. W. Myers. V3d enables real-time 3d visualization and quantitative analysis of large-scale biological image data sets. *Nature biotechnology*, 28(4):348–353, 2010.

J. A. Perge, J. E. Niven, E. Mugnaini, V. Balasubramanian, and P. Sterling. Why do axons differ in caliber? *Journal of Neuroscience*, 32(2):626–638, 2012.

A. Peters, C. C. Proskauer, and I. R. Kaiserman-Abramof. The small pyramidal neuron of the rat cerebral cortex: the axon hillock and initial segment. *The Journal of cell biology*, 39(3):604–619, 1968.

A. Peters, C. C. Proskauer, and C. E. Ribak. Chandelier cells in rat visual cortex. *Journal of Comparative Neurology*, 206(4):397–416, 1982.

J. Platkiewicz and R. Brette. A threshold equation for action potential initiation. *PLoS computational biology*, 6(7), 2010.

J. Platkiewicz and R. Brette. Impact of fast sodium channel inactivation on spike threshold dynamics and synaptic integration. *PLoS computational biology*, 7(5), 2011.

D. Platzer and K. Zorn-Pauly. Letter to the editor: Accurate cell capacitance determination from a single voltage step: a reminder to avoid unnecessary pitfalls. *American Journal of Physiology-Heart and Circulatory Physiology*, 311(4):H1072–H1073, 2016.

A. Prokop. Cytoskeletal organization of axons in vertebrates and invertebrates. *Journal of Cell Biology*, 219(7), 2020.

V. Raghuram, P. Werginz, and S. I. Fried. Scaling of the ais and somatodendritic compartments in α s rgcs. *Frontiers in cellular neuroscience*, 13:436, 2019.

W. Rall. Core conductor theory and cable properties of neurons. *Comprehensive physiology*, pages 39–97, 2011.

M. N. Rasband. The axon initial segment and the maintenance of neuronal polarity. *Nature Reviews Neuroscience*, 11(8):552–562, 2010a.

M. N. Rasband. Clustered k+ channel complexes in axons. *Neuroscience letters*, 486(2):101–106, 2010b.

G. Rinetti-Vargas, K. Phamluong, D. Ron, and K. J. Bender. Periadolescent maturation of gabaergic hyperpolarization at the axon initial segment. *Cell reports*, 20(1):21–29, 2017.

M. M. Rolls and T. J. Jegla. Neuronal polarity: an evolutionary perspective. *Journal of Experimental Biology*, 218(4):572–580, 2015.

M. M. Rolls, D. Satoh, P. J. Clyne, A. L. Henner, T. Uemura, and C. Q. Doe. Polarity and intracellular compartmentalization of drosophila neurons. *Neural development*, 2(1):7, 2007.

M. Royeck, M.-T. Horstmann, S. Remy, M. Reitze, Y. Yaari, and H. Beck. Role of axonal nav1. 6 sodium channels in action potential initiation of ca1 pyramidal neurons. *Journal of neurophysiology*, 100(4):2361–2380, 2008.

T. Ruigrok, C. De Zeeuw, J. Van Der Burg, and J. Voogd. Intracellular labeling of neurons in the medial accessory olive of the cat: I. physiology and light microscopy. *Journal of comparative neurology*, 300(4):462–477, 1990.

A. M. Rush, S. D. Dib-Hajj, and S. G. Waxman. Electrophysiological properties of two axonal sodium channels, nav1. 2 and nav1. 6, expressed in mouse spinal sensory neurones. *The Journal of physiology*, 564(3):803–815, 2005.

W. Rushton. A theory of the effects of fibre size in medullated nerve. *The Journal of physiology*, 115(1):101–122, 1951.

N. Sánchez-Soriano, W. Bottenberg, A. Fiala, U. Haessler, A. Kerassoviti, E. Knust, R. Löhr, and A. Prokop. Are dendrites in drosophila homologous to vertebrate dendrites? *Developmental biology*, 288(1):126–138, 2005.

J. R. Sanes and R. H. Masland. The types of retinal ganglion cells: current status and implications for neuronal classification. *Annual review of neuroscience*, 38:221–246, 2015.

S. Sasaki and S. Maruyama. Increase in diameter of the axonal initial segment is an early change in amyotrophic lateral sclerosis. *Journal of the neurological sciences*, 110(1-2):114–120, 1992.

J. Schindelin, I. Arganda-Carreras, E. Frise, V. Kaynig, M. Longair, T. Pietzsch, S. Preibisch, C. Rueden, S. Saalfeld, B. Schmid, et al. Fiji: an open-source platform for biological-image analysis. *Nature methods*, 9(7):676–682, 2012.

A. Schlüter, S. Rossberger, D. Dannehl, M. Janssen, S. Vorwald, J. Hanne, C. Schultz, D. Mauceri, and M. Engelhardt. Dynamic regulation of synaptopodin and the axon initial segment in retinal ganglion cells during postnatal development. *Frontiers in cellular neuroscience*, 13:318, 2019.

C. Schmidt-Hieber and J. Bischofberger. Fast sodium channel gating supports localized and efficient axonal action potential initiation. *Journal of Neuroscience*, 30(30):10233–10242, 2010.

J. R. Schwarz and G. Eikhof. Na currents and action potentials in rat myelinated nerve fibres at 20 and 37 c. *Pflügers Archiv*, 409(6):569–577, 1987.

H. S. Seung and U. Sümbül. Neuronal cell types and connectivity: lessons from the retina. *Neuron*, 83(6):1262–1272, 2014.

E.-A. Seyfarth. Julius bernstein (1839–1917): pioneer neurobiologist and biophysicist. *Biological cybernetics*, 94(1):2–8, 2006.

B. W. Sheasby and J. F. Fohlmeister. Impulse encoding across the dendritic morphologies of retinal ganglion cells. *Journal of neurophysiology*, 81(4):1685–1698, 1999.

Y. Shu, A. Hasenstaub, A. Duque, Y. Yu, and D. A. McCormick. Modulation of intracortical synaptic potentials by presynaptic somatic membrane potential. *Nature*, 441(7094):761–765, 2006.

Y. Shu, A. Duque, Y. Yu, B. Haider, and D. A. McCormick. Properties of action-potential initiation in neocortical pyramidal cells: evidence from whole cell axon recordings. *Journal of neurophysiology*, 97(1):746–760, 2007.

J. Sloper and T. P. S. Powell. A study of the axon initial segment and proximal axon of neurons in the primate motor and somatic sensory cortices. *Philosophical Transactions of the Royal Society of London. B, Biological Sciences*, 285(1006):173–197, 1979.

D. J. Smith and E. W. Rubel. Organization and development of brain stem auditory nuclei of the chicken: dendritic gradients in nucleus laminaris. *Journal of comparative neurology*, 186(2): 213–239, 1979.

J.-M. Sobotzik, J. M. Sie, C. Politi, D. Del Turco, V. Bennett, T. Deller, and C. Schultz. Ankyring is required to maintain axo-dendritic polarity in vivo. *Proceedings of the National Academy of Sciences*, 106(41):17564–17569, 2009.

P. D. Sohn, T. E. Tracy, H.-I. Son, Y. Zhou, R. E. Leite, B. L. Miller, W. W. Seeley, L. T. Grinberg, and L. Gan. Acetylated tau destabilizes the cytoskeleton in the axon initial segment and is mislocalized to the somatodendritic compartment. *Molecular neurodegeneration*, 11(1):47, 2016.

P. D. Sohn, C. T.-L. Huang, R. Yan, L. Fan, T. E. Tracy, C. M. Camargo, K. M. Montgomery, T. Arhar, S.-A. Mok, R. Freilich, et al. Pathogenic tau impairs axon initial segment plasticity and excitability homeostasis. *Neuron*, 104(3):458–470, 2019.

P. Somogyi, T. Freund, and A. Cowey. The axo-axonic interneuron in the cerebral cortex of the rat, cat and monkey. *Neuroscience*, 7(11):2577–2607, 1982.

P. Somogyi et al. A specific 'axo-axonal'interneuron in the visual cortex of the rat. *Brain Res*, 136(2):345–350, 1977.

P. Somogyu and J. Hamori. A quantitative electron microscopic study of the purkinje cell axon initial segment. *Neuroscience*, 1(5):361–IN3, 1976.

J. Spurrier, A. K. Shukla, T. Buckley, S. Smith-Trunova, I. Kuzina, Q. Gu, and E. Giniger. Expression of a fragment of ankyrin 2 disrupts the structure of the axon initial segment and causes axonal degeneration in drosophila. *Molecular neurobiology*, 56(8):5689–5700, 2019.

Y. Srinivasan, L. Elmer, J. Davis, V. Bennett, and K. Angelides. Ankyrin and spectrin associate with voltage-dependent sodium channels in brain. *Nature*, 333(6169):177–180, 1988.

M. Stimberg, R. Brette, and D. F. Goodman. Brian 2, an intuitive and efficient neural simulator. *Elife*, 8, 2019.

I. Straub, L. Witter, A. Eshra, M. Hoidis, N. Byczkowicz, S. Maas, I. Delvendahl, K. Dorgans, E. Savier, I. Bechmann, et al. Gradients in the mammalian cerebellar cortex enable fourier-like transformation and improve storing capacity. *Elife*, 9:e51771, 2020.

G. Stuart and N. Spruston. Determinants of voltage attenuation in neocortical pyramidal neuron dendrites. *Journal of Neuroscience*, 18(10):3501–3510, 1998.

G. Stuart, J. Schiller, and B. Sakmann. Action potential initiation and propagation in rat neocortical pyramidal neurons. *The Journal of physiology*, 505(3):617–632, 1997.

J. Szabadics, C. Varga, G. Molnár, S. Oláh, P. Barzó, and G. Tamás. Excitatory effect of gabaergic axo-axonic cells in cortical microcircuits. *Science*, 311(5758):233–235, 2006.

J. Takacs and J. Hamori. Morphological plasticity of dendrites in adult brain. *Acta neurobiologiae experimentalis*, 50(4-5):109–114, 1990.

M. Telenczuk, B. Fontaine, and R. Brette. The basis of sharp spike onset in standard biophysical models. *PLoS One*, 12(4), 2017.

C. Thome, T. Kelly, A. Yanez, C. Schultz, M. Engelhardt, S. B. Cambridge, M. Both, A. Draguhn, H. Beck, and A. V. Egorov. Axon-carrying dendrites convey privileged synaptic input in hippocampal neurons. *Neuron*, 83(6):1418–1430, 2014.

S. F. Traynelis. Software-based correction of single compartment series resistance errors. *Journal of neuroscience methods*, 86(1):25–34, 1998.

L. C. Triarhou. Axons emanating from dendrites: phylogenetic repercussions with cajalian hues. *Frontiers in neuroanatomy*, 8:133, 2014.

J. S. Trimmer. Subcellular localization of k+ channels in mammalian brain neurons: remarkable precision in the midst of extraordinary complexity. *Neuron*, 85(2):238–256, 2015.

S. J. Tripathy, S. D. Burton, M. Geramita, R. C. Gerkin, and N. N. Urban. Brain-wide analysis of electrophysiological diversity yields novel categorization of mammalian neuron types. *Journal of Neurophysiology*, 113(10):3474–3489, 2015.

S. Trunova, B. Baek, and E. Giniger. Cdk5 regulates the size of an axon initial segment-like compartment in mushroom body neurons of the drosophila central brain. *Journal of Neuroscience*, 31(29):10451–10462, 2011.

H. C. Tuckwell. *Introduction to theoretical neurobiology. Vol. 1, Linear cable theory and dendritic structure*. Cambridge University Press, 1988a.

H. C. Tuckwell. *Introduction to theoretical neurobiology: volume 2, nonlinear and stochastic theories*, volume 8. Cambridge University Press, 1988b.

S. F. van Beuningen, L. Will, M. Harterink, A. Chazeau, E. Y. Van Battum, C. P. Frias, M. A. Franker, E. A. Katrukha, R. Stucchi, K. Vocking, et al. Trim46 controls neuronal polarity and axon specification by driving the formation of parallel microtubule arrays. *Neuron*, 88(6): 1208–1226, 2015.

A. Van Wart, J. S. Trimmer, and G. Matthews. Polarized distribution of ion channels within microdomains of the axon initial segment. *Journal of Comparative Neurology*, 500(2):339–352, 2007.

S. Vassilopoulos, S. Gibaud, A. Jimenez, G. Caillol, and C. Leterrier. Ultrastructure of the axonal periodic scaffold reveals a braid-like organization of actin rings. *Nature Communications*, 10 (1):1–13, 2019.

S. Veitinger. The patch-clamp technique. 2011.

M. L. Veruki, L. Oltedal, and E. Hartveit. Electrical coupling and passive membrane properties of aii amacrine cells. *Journal of neurophysiology*, 103(3):1456–1466, 2010.

M. Vicente-Manzanares, X. Ma, R. S. Adelstein, and A. R. Horwitz. Non-muscle myosin ii takes centre stage in cell adhesion and migration. *Nature reviews Molecular cell biology*, 10(11): 778–790, 2009.

P. Virtanen, R. Gommers, T. E. Oliphant, M. Haberland, T. Reddy, D. Cournapeau, E. Burovski, P. Peterson, W. Weckesser, J. Bright, et al. Scipy 1.0: fundamental algorithms for scientific computing in python. *Nature methods*, 17(3):261–272, 2020.

G.-Y. Wang, G.-M. Ratto, S. Bisti, and L. M. Chalupa. Functional development of intrinsic properties in ganglion cells of the mammalian retina. *Journal of neurophysiology*, 78(6):2895–2903, 1997.

Y. Wang, P. Xie, H. Gong, Z. Zhou, X. Kuang, Y. Wang, A.-a. Li, Y. Li, L. Liu, M. B. Veldman, et al. Complete single neuron reconstruction reveals morphological diversity in molecularly defined claustral and cortical neuron types. *bioRxiv*, page 675280, 2019.

W. Wefelmeyer, D. Cattaert, and J. Burrone. Activity-dependent mismatch between axo-axonic synapses and the axon initial segment controls neuronal output. *Proceedings of the National Academy of Sciences*, 112(31):9757–9762, 2015.

W. Wefelmeyer, C. J. Puhl, and J. Burrone. Homeostatic plasticity of subcellular neuronal structures: from inputs to outputs. *Trends in neurosciences*, 39(10):656–667, 2016.

E. T. Whittaker. *A History of the Theories of Aether and Electricity from the Age of Descartes to the Close of the Nineteenth Century*. Longmans, Green and Company, 1910.

A. Woodruff, Q. Xu, S. A. Anderson, and R. Yuste. Depolarizing effect of neocortical chandelier neurons. *Frontiers in neural circuits*, 3:15, 2009.

A. R. Woodruff, S. A. Anderson, and R. Yuste. The enigmatic function of chandelier cells. *Frontiers in neuroscience*, 4:201, 2010.

C. Wu, E. Ivanova, J. Cui, Q. Lu, and Z.-H. Pan. Action potential generation at an axon initial segment-like process in the axonless retinal aii amacrine cell. *Journal of Neuroscience*, 31(41): 14654–14659, 2011.

K. D. Wyatt, P. Tanapat, and S. S.-H. Wang. Speed limits in the cerebellum: constraints from myelinated and unmyelinated parallel fibers. *European Journal of Neuroscience*, 21(8):2285–2290, 2005.

K. Xu, G. Zhong, and X. Zhuang. Actin, spectrin, and associated proteins form a periodic cytoskeletal structure in axons. *Science*, 339(6118):452–456, 2013.

S. R. y Cajal. *Histology of the nervous system of man and vertebrates*, volume 1. Oxford University Press, USA, 1995.

S. R. y Cajal and D. Sanchez. *Contribución al conocimiento de los centros nerviosos de los insectos*. Imprenta de Hijos de Nicolás Moya, 1915.

R. Yamada and H. Kuba. Structural and functional plasticity at the axon initial segment. *Frontiers in cellular neuroscience*, 10:250, 2016.

Y. Yang, Y. Ogawa, K. L. Hedstrom, and M. N. Rasband. βiv spectrin is recruited to axon initial segments and nodes of ranvier by ankyring. *The Journal of cell biology*, 176(4):509–519, 2007.

J. Z. Young. The structure of nerve fibres in cephalopods and crustacea. *Proceedings of the Royal Society of London. Series B-Biological Sciences*, 121(823):319–337, 1936.

Y. Yu, Y. Shu, and D. A. McCormick. Cortical action potential backpropagation explains spike threshold variability and rapid-onset kinetics. *Journal of Neuroscience*, 28(29):7260–7272, 2008.

Y. Yu, A. P. Hill, and D. A. McCormick. Warm body temperature facilitates energy efficient cortical action potentials. *PLoS Comput Biol*, 8(4):e1002456, 2012.

X. Zhang and V. Bennett. Restriction of 480/270-kd ankyrin g to axon proximal segments requires multiple ankyrin g-specific domains. *The Journal of cell biology*, 142(6):1571–1581, 1998.

Y. Zhang, K. Abiraman, H. Li, D. M. Pierce, A. V. Tzingounis, and G. Lykotrafitis. Modeling of the axon membrane skeleton structure and implications for its mechanical properties. *PLoS computational biology*, 13(2):e1005407, 2017.

G. Zhong, J. He, R. Zhou, D. Lorenzo, H. P. Babcock, V. Bennett, and X. Zhuang. Developmental mechanism of the periodic membrane skeleton in axons. *Elife*, 3:e04581, 2014.

D. Zhou, S. Lambert, P. L. Malen, S. Carpenter, L. M. Boland, and V. Bennett. Ankyring is required for clustering of voltage-gated na channels at axon initial segments and for normal action potential firing. *The Journal of cell biology*, 143(5):1295–1304, 1998.